BEHAVIOUR OF SAND UNDER SIMULTANEOUS INCREASE IN STRESS RATIO AND ROTATION OF PRINCIPAL STRESSES

by

DHARMAPRIYA WIJEWICKREME

B. Sc. (Eng) Hons., University of Peradeniya, Sri Lanka

M. A. Sc., University of British Columbia, Canada

A THESIS SUBMITTED IN PARTIAL FULFILLMENT OF

THE REQUIREMENTS FOR THE DEGREE OF

DOCTOR OF PHILOSOPHY

in

THE FACULTY OF GRADUATE STUDIES

DEPARTMENT OF CIVIL ENGINEERING

We accept this thesis as conforming

to the required standard

THE UNIVERSITY OF BRITISH COLUMBIA

August, 1990

In presenting this thesis in partial fulfilment of the requirements for an advanced degree at the University of British Columbia, I agree that the Library shall make it freely available for reference and study. I further agree that permission for extensive copying of this thesis for scholarly purposes may be granted by the head of my department or by his or her representatives. It is understood that copying or publication of this thesis for financial gain shall not be allowed without my written permission.

Department of CIVIL ENGINEERING

The University of British Columbia
Vancouver, Canada

Date 15 AUGUST 1990.

Abstract

Drained behaviour of sands under simultaneous increase in stress ratio and principal stress rotation is investigated. The hollow cylinder torsional (HCT) device which permits independent control of four stress parameters: mean normal stress σ'_m, stress ratio R, intermediate principal stress parameter b and the inclination α_σ of σ'_1 to the vertical, is adopted as the testing device.

In order to conduct complex stress path testing in the HCT device, a new automatic stress path control system is developed. The stress non-uniformities due to the curvature of the HCT specimen is assessed using an incremental elastic representation of sand behaviour, in order to delineate the domain of stress space that could reliably be explored using the HCT device. It is shown that previous assessments of stress non-uniformities assuming linear elastic soil grossly overestimate the stress non-uniformities in a HCT sand specimen. A much larger domain of stress space with acceptable levels of non-uniformities is apparent from the results of incremental elastic analysis. New domain of stress space for reliable exploration using the HCT device is delineated and the testing program is developed so that all stress paths lie within these acceptable limits. Tests are carried out on pluviated sand under saturated drained conditions.

The deformations under increasing R and α_σ is shown to be path independent, if the final stress state is within the approximate bounds of $R \leq 2$ and $\alpha_\sigma \leq 45°$, regardless of the b or relative density D_r, levels. With increasing stress ratio R and/or principal stress rotation α_σ, the deformations gradually become path dependent. Once loaded to a stress state within the domain $R \leq 2$ and $\alpha_\sigma \leq 45°$, the strain response under subsequent principal stress rotation is shown to be independent of

the previous loading history. It is demonstrated that the strain response under any general increasing R - α path in the domain of $R \leq 2$ and $\alpha_\sigma \leq 45°$ can be predicted using the results of a limited number of tests characterizing that domain. It is shown that these concepts can be extended to loading paths which involve simultaneous increase of three stress parameters.

Strain increment direction $\alpha_{\Delta\epsilon}$ is shown to be approximately coincident with and totally governed by the stress increment direction $\alpha_{\Delta\sigma}$ when the stress increment direction $\alpha_{\Delta\sigma}$ is more inclined towards the vertical deposition direction. When the stress increment direction is inclined closer to the bedding plane, the strain increment direction depends in addition, on other parameters such as R, α_σ and D_r etc.

Under any stress path involving principal stress rotation, the deformations decrease with increasing density and therefore the principal stress rotation is more crucial in loose sands. Deformations increase with the level of stress ratio R. Level of b parameter does not affect deformations under principal stress rotation, if the rotations are small. However, with increasing α_σ deformations due to principal stress rotation tend to increase with decreasing b value.

Table of Contents

List of Tables

List of Figures

List of Symbols

σ - Normal stress

τ - Shear stress

Δ - Prefix indicating an increment

σ'_1 - Major effective principal stress

σ'_2 - Intermediate effective principal stress

σ'_3 - Minor effective principal stress

R - Effective principal stress ratio ($= \sigma'_1/\sigma'_3$)

σ'_m - Effective mean normal stress ($= \frac{\sigma'_1+\sigma'_2+\sigma'_3}{3}$)

b - Intermediate principal stress parameter ($= \frac{\sigma'_2-\sigma'_3}{\sigma'_1-\sigma'_3}$)

α_σ - Direction of σ'_1 with respect to the deposition direction

$\alpha_{\Delta\sigma}$ - Direction of $\Delta\sigma'_1$ with respect to the deposition direction

ε - Normal strain

γ - Shear strain

ε_1 - Major principal strain

ε_2 - Intermediate principal strain

ε_3 - Minor principal strain

ε_v - Volumetric strain ($= \varepsilon 1 + \varepsilon 2 + \varepsilon 3$)

γ_{max} - Maximum shear strain ($= \varepsilon_1 - \varepsilon_3$)

$\{\varepsilon_v\}_{\sigma'_m}$, $\{\gamma_{max}\}_{\sigma'_m}$ - Volumetric and maximum shear strains under hydrostatic loading ($R = 1$; b and α_σ undefined).

$\{\varepsilon_v\}_R$, $\{\gamma_{max}\}_R$ - Volumetric and maximum shear strains due to changes in R only, with $\alpha_\sigma = 0°$. (b and σ'_m held constant).

$\{\varepsilon_v\}_\alpha$, $\{\gamma_{max}\}_\alpha$ - Volumetric and maximum shear strains due to changes in α_σ only, with R, b and σ'_m held constant.

$\alpha_{\Delta\varepsilon}$ - Direction of $\Delta\varepsilon_1$ with respect to the deposition direction

T_h - Torque about the vertical axis

F_z - Vertical Force

P_i, P_e - Internal and external confining pressures

R_i, R_e - Internal and external specimen radii

H - Specimen height

D_r - Relative density

β_R - Stress non-uniformity coefficient

R path - Stress path with variation of R only, with fixed values of σ'_m, b, and α_σ.

α path - Stress path with variation of α_σ only, with fixed values of σ'_m, b, and R.

$R-\alpha$ path - Stress path with simultaneous variation of R and α_σ, with fixed values of σ'_m and b.

$\sigma'_m - R - \alpha$ path - Stress path with simultaneous variation of σ'_m, R and α_σ, with a fixed value of b.

Acknowledgement

I wish to express my sincere gratitude to my supervisor Professor Y.P. Vaid for his guidance, valuable suggestions and the encouragement throughout this research.

Special thanks are due to members of my examining/supervisory committee, Professors P.M. Byrne, W.D.L. Finn, Y.P. Vaid, R.G. Campanella, D.L. Anderson, S.M. Calisal and P.V. Lade and Dr. M.K.W. Lee for their helpful criticism and suggestions.

Assessment of stress non-uniformities would not have been possible without the 3-D finite element program 3DSLB developed by my colleague Francisco Salgado, and his valuable assistance during program execution. Assistance and advice given by Dr. D. Negussey during my graduate studies at U.B.C. is deeply appreciated. I would also like to thank my colleagues Alberto, Mustapha, Ralph, Carlos, Sasi and Hendra for their helpful discussions.

Sincere thanks are extended to Mr. S. Jackson and Mr. R. Nussbaumer of the electronic workshop for their co-operation in the development of the stress path control system, and Mr. A. Brookes and H. Schrempp of the mechanical workshop for their skills in making several improvements to the HCT apparatus.

The Izaak Walton Killam Graduate Fellowship (1986-1987) and the University of B.C. Graduate Fellowship (1988-1989) awards, which provided the financial support during my doctoral program, are gratefully acknowledged.

Finally, I would like to extend very special thanks to my wife Nilmini for her continuous encouragement and support throughout this research.

Chapter 1

Introduction

Field loading of soils is frequently associated with rotation of principal stresses. Since most sedimentary deposits are inherently anisotropic, rotation of principal stresses alone would produce volumetric and shear deformations in a soil mass. The ability to characterize behaviour under such loading conditions is essential for satisfactory geotechnical design of structures.

The influence of anisotropy has largely been neglected in the modelling of soil behaviour, primarily because of its complexity and general unavailability of data under generalized stress path loading. In order to study the anisotropic behaviour and the effects of principal stress rotation, the laboratory testing devices should have the ability to exercise control on both the directions and magnitudes of principal stresses. As a result of research work over two decades, two testing devices have emerged that could impose continuous rotation of principal stresses on a soil specimen: viz. the directional shear cell (DSC) (Arthur et al., 1977) and the hollow cylinder torsional (HCT) device (Hight et al., 1983). The DSC in its present state of development can operate only under plane strain conditions and at low confining pressures. On the other hand, in the HCT device independent control of three principal stresses and rotation of principal stresses in one plane can be exercised. Frequently, an alternate set of equivalent stress parameters: effective mean normal stress $\sigma'_m = (\sigma'_1+\sigma'_2+\sigma'_3)/3$, shear stress $q = (\sigma'_1 - \sigma'_3)$ (or stress ratio $R = \sigma'_1 \ / \ \sigma'_3$), intermediate principal stress parameter $b = (\sigma'_2 - \sigma'_3) \ / \ (\sigma'_1 - \sigma'_3)$, and the inclination of major principal stress to the vertical (angle α_σ of σ'_1 with deposition direction) are used to interpret HCT test

results. Since these parameters describe completely the stress states involving two dimensional principal stress rotation, the HCT device has the versatility of simulating many practical stress path loadings that actually occur in the field.

In early research under generalized stress path loading, the interest focused mainly on the strength behaviour of sand. Stress ratios mobilized under general working conditions typical of deformation problems in geotechnical engineering are at a much lower level than at the failure state. Comprehensive knowledge of the effects of principal stress rotations at such moderate stress ratios is very limited. The only contributions to this area of research have come from the laboratory studies on sands using the HCT device (Symes et al., 1984, 1988; Sayao, 1989).

Real field loading generally involves increase in several stress parameters simultaneously. Laboratory investigations have, however been restricted to stress paths in which only one stress parameter is increased at a given time (Sayao, 1989; Hight et al., 1983; Symes et al., 1988). No attempts have been made to carry out stress path tests where simultaneous increase of more than one stress parameter occurs in a controlled manner.

It is widely recognized that sand behaviour is stress path dependent. Yet, not enough is known about the stress path dependent strain response, particularly under principal stress rotations. It has also been suggested that the initial deposition anisotropy governs sand behaviour if the associated strains on loading are moderate, regardless of the stress path. These conclusions have been arrived at from the results of only a limited number of tests.

Lack of knowledge and understanding regarding sand behaviour under generalized stresses led to the evolution of the main theme of this research. As such, a comprehensive investigation on the drained behaviour of sand under simultaneous increase in stress ratio and principal stress rotation is carried out using the HCT device. The results are compared with those from stress paths in which only one stress parameter

is permitted to increase. Possible path independent domain of the stress space is identified based on these comparisons. Hence a procedure for predicting stress strain response under simultaneous increase of stress ratio and principal stress rotation is proposed using the observed behaviour from stress paths, wherein the principal stress rotations occurred at constant levels of stress ratio.

A systematic testing program was designed in order to achieve the above objectives. All tests were carried out using reconstituted specimens of saturated sand under drained conditions. Sand behaviour is examined predominantly at medium loose relative density D_r of 30% in which principal stress rotation effects are expected to be most pronounced. Stress ratio levels were mainly restricted to those below 2.0. Tests were carried out to delineate the effects of mean normal stress σ'_m and intermediate principal stress parameter b under otherwise identical stress paths. Behaviour of denser sand with $D_r = 50\%$ and 70% was also investigated. For all stress paths the directional changes in principal stress increment in response to applied stress increment and stress directions is also investigated, in order to understand possible changes in inherent anisotropy during loading.

The accomplishment of these objectives required complex stress path tests, which may involve simultaneous increase in all four surface tractions in the HCT device. The manual control of these tractions together is a difficult, if not impossible task. This necessitated the development of a new automatic stress path testing facility with a feed back control system.

Another important consideration in the use of the HCT device is the level of stress non-uniformities across the wall of the specimen that arise due to the curvature of the specimen. A proper assessment of these non-uniformities is essential in evaluating the quality of data from HCT tests. It is necessary to identify the domain of stress space which may result in unacceptable stress non-uniformities and hence constitute the "no-go" regions. Previously, stress non-uniformities in HCT specimens have been

assessed, mostly with the assumption that the soil behaviour is linear elastic. Stress non-uniformities determined from linear elastic assumptions lead to overestimation of actual stress non-uniformities if the soil is non-linear. No systematic analysis of stress non-uniformities in HCT specimens has been made which recognizes non-linear soil behaviour. Hence a reevaluation of stress non-uniformities in the HCT specimens using a nonlinear elastic representation of soil behaviour was undertaken, as a prerequisite to the experimental investigation.

Chapter 2

Review of Sand Behaviour Under General Stress Path Loading

2.1 Introduction

Even though experimental evidence suggests anisotropic behaviour, sand is traditionally characterized based on the assumption of isotropy. This is primarily (i) to preserve simplicity in modelling and (ii) need for complex testing devices for characterizing behaviour of anisotropic material.

In general, the state of stress at a point in a sand deposit can be expressed in terms of six parameters: three principal stresses $\sigma'_1, \sigma'_2, \sigma'_3$ and their inclinations to a set of orthogonal coordinate axes (Fig. 2.1). An equivalent set of parameters, mean effective stress $\sigma'_m = (\sigma'_1 + \sigma'_2 + \sigma'_3)/3$; effective stress ratio $R = \sigma'_1/\sigma'_3$; intermediate principal stress parameter $b = (\sigma'_2 - \sigma'_3)/(\sigma'_1 - \sigma'_3)$ are commonly used instead of σ'_1, σ'_2 and σ'_3. One of the reference coordinate directions is normally taken as the vertical deposition direction. Controlled changes in the magnitudes of stresses and their inclinations to the reference directions are extremely important in the study of anisotropic material behaviour.

In most soil testing devices such as conventional triaxial, true triaxial and plain strain, principal stresses are fixed in direction and at most, only an interchange of principal directions (called jump rotations) can be imposed. No device has yet been developed which allows principal stress rotation in three dimensions. The only devices that allow controlled rotation of principal stresses in one plane are the directional

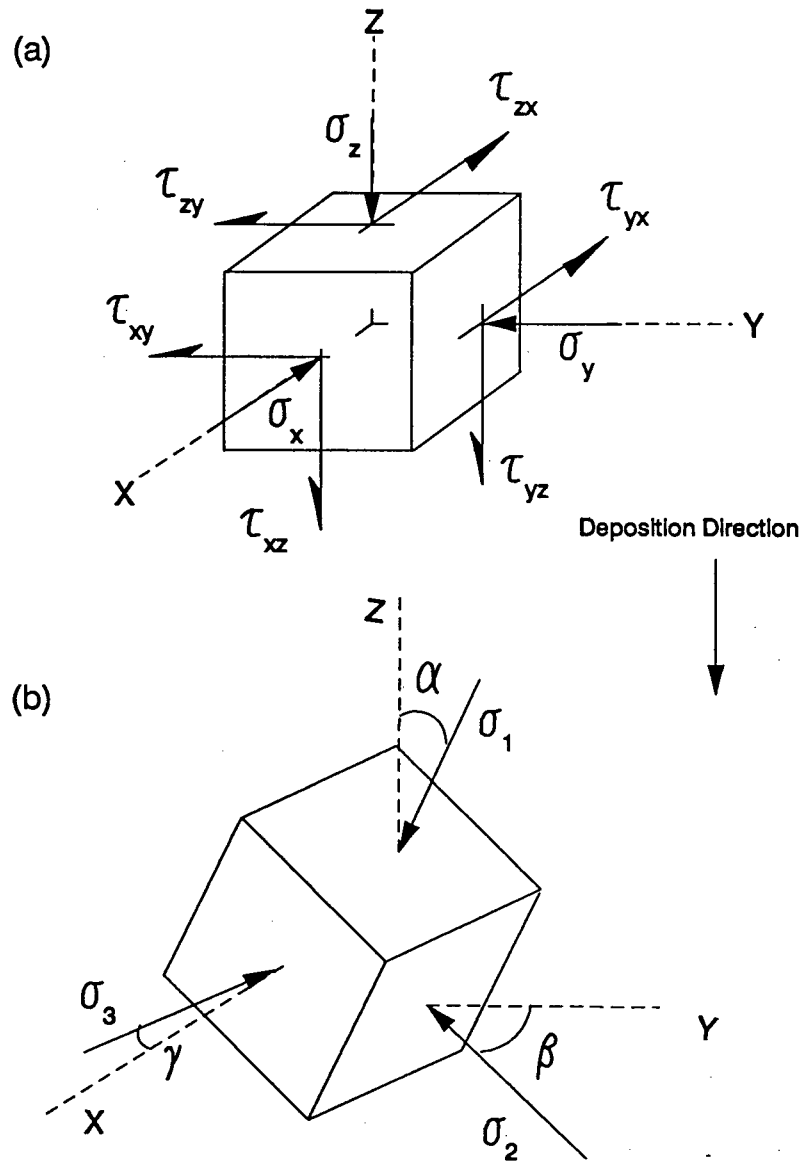

Figure 2.1: Expression of stress at a point

shear cell (DSC) (Arthur et al., 1977) and the hollow cylinder torsional (HCT) device (Hight et al., 1983; Vaid et al. 1990). The HCT device has the added advantage of being the only apparatus that allows independent control of the magnitudes of all stress parameters σ'_m, R, b, and α_σ (inclination of σ'_1 with vertical deposition direction).

In this chapter conceptual and experimental evidence in support of anisotropic nature of sand is first presented. The measured deformation response of sands is then critically reviewed, with emphasis placed on drained behaviour. Only pre-failure behaviour is considered which is central to the solution of deformation as opposed to stability problems in sands. The interpretation of hollow cylinder data close to failure could be questionable due to potentially excessive stress non-uniformities across the wall of the specimen (see Chapter 3).

The new directions in research that would enhance the current understanding of the behaviour of sand as an anisotropic material are identified and a research program is proposed to accomplish these objectives.

2.2 Anisotropic Nature of Sand

The discrete nature of particles and their spatial arrangement characterizes the mechanical behaviour of a sand mass. Casagrande and Carillo (1944) distinguished between two types of anisotropy in soils, viz. inherent and induced. Inherent anisotropy was defined as a physical characteristic inherent in the material before any deformations are imposed. On the other hand, the anisotropy due exclusively to the strain associated with the applied stress was called induced anisotropy.

Although the above distinction gave a convenient means of classifying anisotropy, Saada (1981) correctly pointed out that any current state of a sand can be treated as an inherently anisotropic state for the next loading increment. Additional definitions such as initial anisotropy (Symes et al., 1984) have thus evolved, which takes into

account both the induced anisotropy due to past events and the inherent anisotropy.

2.2.1 Inherent Anisotropy

2.2.1.1 Particle Fabric

During the origin of a sand deposit, individual grains assume a position in the sand mass depending on the mode of deposition and the shape of grains. The term fabric has been used to describe the spatial arrangement of solid particles and the associated voids in a granular mass.

Oda (1972) investigated the grain structure of sand by examining thin sections of both natural and reconstituted sand samples. The thin sections were obtained after infiltrating a resin binder into the voids of the sand specimen. The results indicated that during deposition under gravity, non spherical sand grains preferred to rest with their long axis oriented in a nearly horizontal direction. Oda also found that the majority of particle contact normals were oriented in a direction parallel to that of deposition. These observations revealed that the preferred alignment of non spherical particles as well as the preferred orientation of particle contacts, contributed towards creating an anisotropic fabric after deposition.

Several investigations have shown that sand specimens comprised of even spherical grains, when deposited under gravity exhibit anisotropic behaviour (Haruyama, 1981; Oda, 1981; Shibuya and Hight, 1987). Since there is no longitudinal axis in the case of spheres, this anisotropic behaviour has been attributed solely to the preferred orientation of particle contact normals in the direction of deposition.

The anisotropy in sand revealed by examining the grain structure has been further corroborated by laboratory stress-strain response observations. In the earliest laboratory experiments, Kjellman (1936) reported significant differences in the three principal strains during hydrostatic compression of cubical sand specimens.

The anisotropy in natural sand deposits has been reported by Ladd et al. (1977) using undisturbed triaxial samples of loose Niigata sand obtained by a freezing technique. They observed that under hydrostatic compression in the conventional triaxial cell, the radial strains induced were more than twice the vertical strains. Miura and Toki (1984) conducted drained triaxial compression and extension tests on undisturbed samples (obtained using a freezing technique) from two relatively homogeneous sand deposits. The results indicated that the vertical direction insitu was less compressible than the horizontal direction.

Due to the difficulties in undisturbed sampling of sand, the anisotropic behaviour of sands has been studied mainly using laboratory reconstituted samples. Oda et al. (1978) have shown that the sand specimens prepared by laboratory pluviation (i.e. deposition under gravity) closely simulate the sedimentation process and the resulting fabric of water deposited sands insitu. They also demonstrated the anisotropic nature of pluviated Toyoura sand by testing tilted specimens in the plane strain device. Miura and Toki (1984) carried out triaxial tests on pluviated sand in a manner identical to their tests on undisturbed samples (see previous paragraph). Their results also showed very similar stress-strain characteristics between the undisturbed and the water pluviated sand. Reconstituted pluviated specimens thus enable a convenient means of studying the behaviour of water deposited insitu sands.

2.2.1.2 Stress Strain Behaviour

Several investigations reflecting inherent anisotropy in pluviated sands can be found in literature. The observations showing loading direction dependent behaviour of pluviated Ottawa sand made by Sayao (1989) using the HCT device are reproduced in Fig. 2.2. Each sample was loaded with a fixed inclination (α_σ) to the direction of deposition while σ'_m and b were held constant. Such loading tests were carried out at several angles α_σ of σ'_1 to the deposition direction. A profound effect of

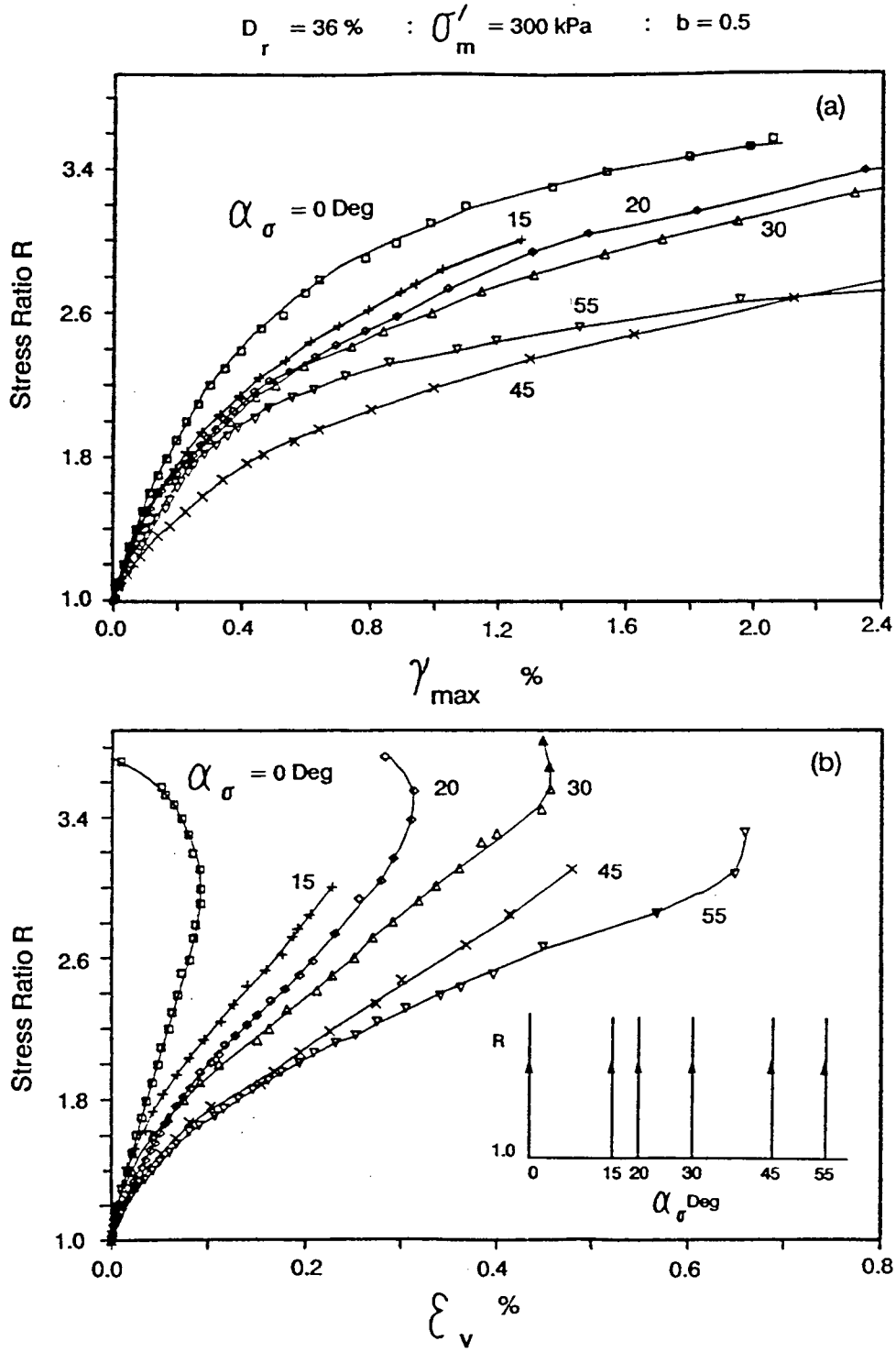

Figure 2.2: Inherent anisotropy of pluviated Ottawa sand - after Sayao (1989)

initial anisotropic fabric of sand is apparent in both volumetric and shear strain responses (Fig. 2.2). The stiffest response is seen for loading in the vertical ($\alpha_\sigma = 0°$) deposition direction. In general, the strain response becomes softer with increasing values of α_σ. But, at lower stress ratios, shear with $\alpha_\sigma = 55°$ shows a stiffer strain response than that obtained at $\alpha_\sigma = 45°$. Sayao (1989) noted that similar observations have also been made by Miura (1985), who explained this observation using the concept of mobilized planes of Matsuoka (1974). It was suggested that the maximum deformability occurs when the mobilized planes (i.e. plane of maximum stress obliquity) and the bedding plane are coincident. At lower R values (i.e. lower mobilized friction angles), the mobilized plane is inclined to the major principal stress direction by approximately 45°[1]. As such, when the inclination of the major principal stress α_σ is 45° to the vertical, the mobilized plane at lower R values would make an angle of $\approx 90°$ with the vertical. This indicates approximate coincidence of bedding and mobilized planes, and thus affirming the maximum deformability oberved at $\alpha_\sigma = 45°$.

Results in support of the general increase in deformability of sand with increasing α_σ have also been reported by Symes et al. (1988) in HCT tests, Arthur and Menzies (1972) in cubical triaxial tests on tilted samples and Arthur et al. (1981) in directional shear cell (DSC) tests.

The mechanical behaviour of pluviated sands is generally considered to be cross anisotropic. This implies, that the behaviour should be symmetrical about the vertical axis. Miura (1985) reported HCT tests on two identical samples of pluviated sand. One sample was loaded with a fixed inclination of major principal stress α_σ measured clockwise to the direction of deposition and the other was loaded with the same magnitude of α_σ but inclined in the anticlockwise sense to the vertical. He observed an identical strain response, indicating the symmetrical nature of pluviated sand about

[1]mobilized plane is inclined to the major principal direction by an angle of $(45° + \phi/2)$

the direction of deposition. Wong and Arthur (1985) reported DSC tests on sand samples loaded, so that the plane of σ_1'-σ_3' is coincident with the bedding plane. They observed that the strain response was unaffected by the orientation of σ_1' in the horizontal bedding plane. Although the tests were aimed at checking the performance of DSC, the results demonstrated that the pluviated sands are cross anisotropic and the behaviour is symmetrical about the vertical deposition axis. It should be noted that the foregoing laboratory observations on stress strain behaviour strongly corroborate the concepts of anisotropic particle fabric proposed by Oda (1972).

2.2.2 Induced Anisotropy

Oda et al. (1985) observed that the spatial arrangement of solid particles and the associated voids in sand undergo progressive changes when subjected to shearing stresses. They found that the contact normals concentration tend to increase along the direction of σ_1' while the elongated grains align in a direction perpendicular to the direction of σ_1'. They also noted that a new fabric of the sand continuously evolves in response to the applied stresses.

Arthur et al. (1980, 1981) investigated such stress induced anisotropy of Leighton Buzzard sand using the DSC. Some of their results are reproduced in Fig. 2.3. The DSC specimens were presheared in the original plane of isotropy (i.e. the plane normal to the deposition direction) until $R = 6$ with $\sigma_3' = 14$ kPa and fixed directions of principal stresses (N.B. Since DSC is a plane strain device the value of σ_2' could not be controlled). Then the specimens were unloaded back to the condition $\sigma_1' = \sigma_3' = 14$ kPa in the horizontal plane and were subsequently reloaded with different angles (α) to the direction of initial loading. They observed that the stiffness of sand progressively decreases with increasing angle α to the previous loading direction, which is a reflection of the induced anisotropy due to preshear in the plane which was initially isotropic.

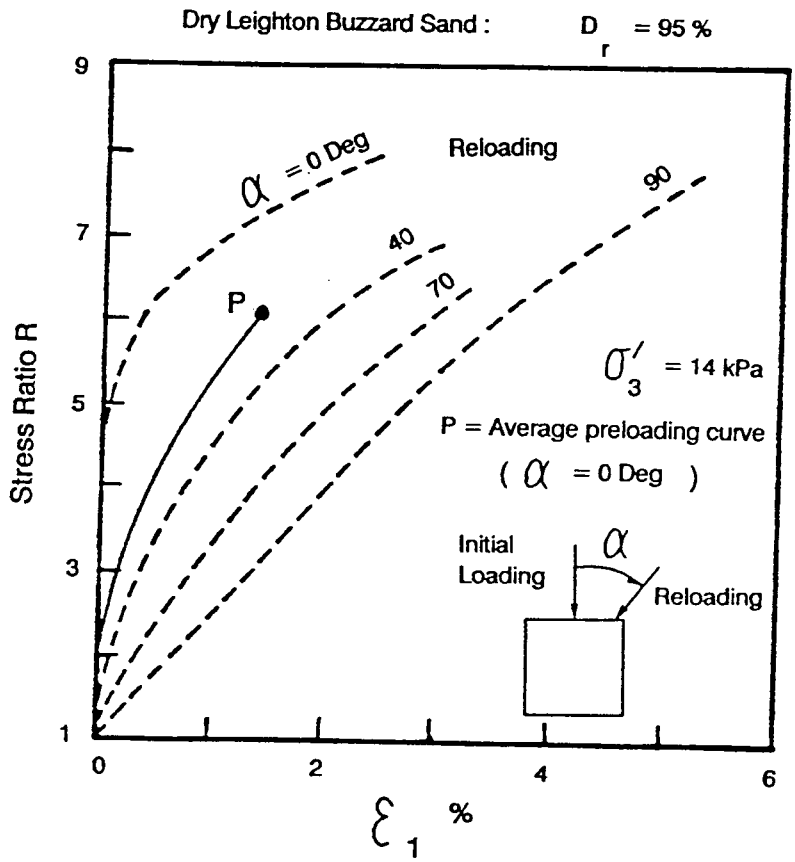

Figure 2.3: Induced anisotropy on initially isotropic sand - after Arthur et al. (1981)

Mould et al. (1982) also reported results in support of induced anisotropy in Leighton Buzzard sand, tested in the cubical triaxial device. This device can impose only jump rotations of 90°. The samples were initially sheared in the original plane of isotropy upto a stress ratio R of 4.5 with $\sigma'_2 = \sigma'_3 = 14$ kPa and fixed principal stress directions. They were then unloaded back to hydrostatic state before reloading in a direction perpendicular to the preshear direction. A marked reduction in the stiffness of sand was noted during reloading compared to that under virgin loading. When the specimen was again unloaded and reloaded in the original preshear direction, the strain response was much similar to that of the first reloading, although the loading directions had changed by 90°. Even though Mould et al. did not offer a detailed explanation for the observed behaviour, the results clearly demonstrated the profound changes that could occur in a granular fabric due to a simple loading process.

2.3 Deformations due to Continuous Rotation of Principal Stresses

2.3.1 General Stress Strain Behaviour

Arthur et al. (1979, 1980) reported deformations under cyclic rotation of principal stresses with constant stress ratio R on dense sand using the directional shear device (DSC). They observed that the major principal strain accumulated continuously with cyclic rotation of principal stresses. Cyclic stress rotations in the DSC were achieved by maintaining boundary shear stresses constant. The normal stresses in the $\sigma'_1 - \sigma'_3$ plane were controlled so as to achieve constant R conditions. Since the DSC is a plane strain device, the sand experiences fluctuations in the mean normal effective stress σ'_m as well as the b parameter during shear. Therefore, the isolated influence of the principal stress rotations on the sand behaviour cannot be investigated in the DSC.

The HCT apparatus is the only device which allows independent control of the stress parameters σ'_m, b, R and α_σ. Drained HCT tests where the magnitudes of the principal stresses (and hence σ'_m, b and R) were kept constant and only α_σ was varied, have been reported by Symes et al. (1982, 1988), Miura (1985), and Sayao (1989).

Symes et al. (1982) reported a principal stress rotation test carried out on dense ($D_r = 88\%$) Ham river sand. A relatively high stress ratio ($R = 3.5$) was used with $b = 0.5$ and $\sigma'_m = 200$ kPa. They observed that at the initial stages of principal stress rotation ($\alpha_\sigma < 35°$) contractive deformations developed, but at larger rotations the deformations became dilative and the specimen eventually failed (reached very large strains) at $\alpha_\sigma \approx 65°$. On the other hand, Miura (1985) reported results from similar tests on dense Toyoura sand ($D_r = 82\%$) carried out with $R = 4$, $b = 0.5$ and $\sigma'_m = 98$ kPa which contradict observations of Symes et al (1982). He observed an initial dilative behaviour for rotations upto $\alpha_\sigma \approx 120°$ followed by steady contraction. Both Ham river and Toyoura sands are similar, being uniform sands of mainly subangular quartz particles with D_{50} of 0.18 and 0.3 mm respectively. The only difference between the two tests was in the values of R and σ'_m. This disparity alone cannot possibly explain the above contrasting results.

It is important to point out that results described above have been obtained for principal stress rotations on very dense samples, at rather high R values. As will be shown in Chapter 3, the stress non-uniformities across the HCT specimen wall are likely to be much more severe in the case of dense samples, especially at higher stress ratios. Therefore confidence in these results become questionable. Moreover, Sayao (1989) pointed out that stress non-uniformity effects are likely to be more severe in Miura's HCT results, because of his smaller specimen dimensions and the higher R value ($R = 4$) used. It is probable that the differences in stress non-uniformities could have led to the reported differences between the observed strain responses. Such results illustrate the importance of identifying the domain of stress space in a given

HCT device that leads to unacceptable stress non-uniformities, and classifying these as the 'no go' regions of stress space for the purpose of studying deformation response under general stress paths.

The effect of principal stress rotations on the undrained response of sand have been examined by Symes et al. (1984). HCT tests were performed with constant total principal stresses while the direction of σ_1 was rotated on medium loose Ham river sand. A progressive increase in pore water pressure was observed with increasing angle of principal stress rotation. Based on these undrained results Symes et al. (1984) proposed a unified framework to understand the effects of initial anisotropy and principal stress rotation on sand behaviour. This consisted of the concept of a state boundary surface originally proposed by Roscoe et al. (1958) but modified to include α_σ as an additional parameter. Symes et al. (1984) constructed a bounding surface (BS) in the 3-D space comprising q - α_σ - σ'_m, for each constant void ratio and b conditions. (N.B. $q = (\sigma'_1 - \sigma'_3)/2$)

The BS was divided into two main regions: (a) contractant region (b) dilatant region. The contractant region was further subdivided into post-peak and pre-peak zones (Fig. 2.4). If the sand state is on the pre-peak zone of the BS, it would be stable. On the other hand in the post-peak zone unstable response would occur under stress controlled conditions. This is usually followed by a tendency to dilate (i.e. drop in pore pressures).

For an element of soil which exists on the BS, "loading" and "unloading" was distinguished by the direction of the effective stress increment vector in the q-α_σ-σ'_m space. If the stress increment vector is directed towards the outside of the BS, or in the limiting case where the stress increment is tangential to the BS, the path was considered as "loading". If the stress increment vector is directed towards the inside of the BS, the path was considered as "unloading".

Symes et al. (1984) made qualitative predictions of pore pressure response under

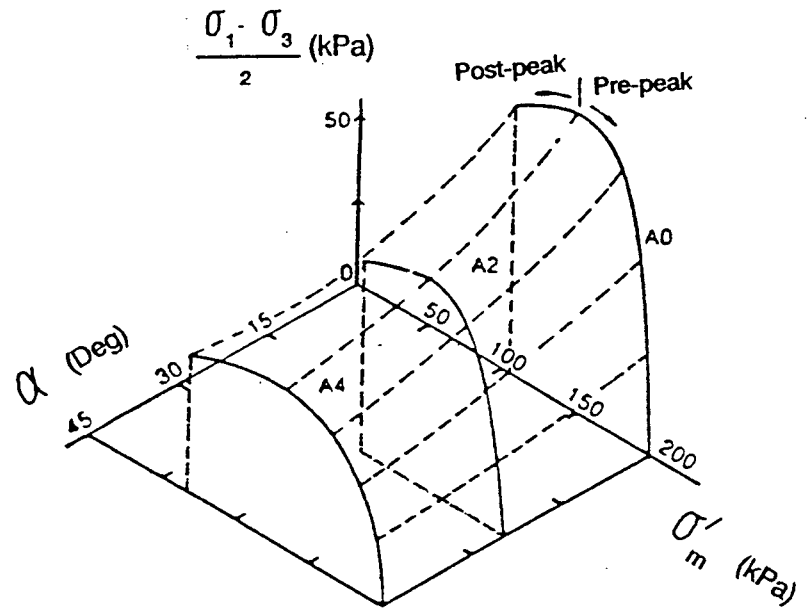

(a) Contractant Region

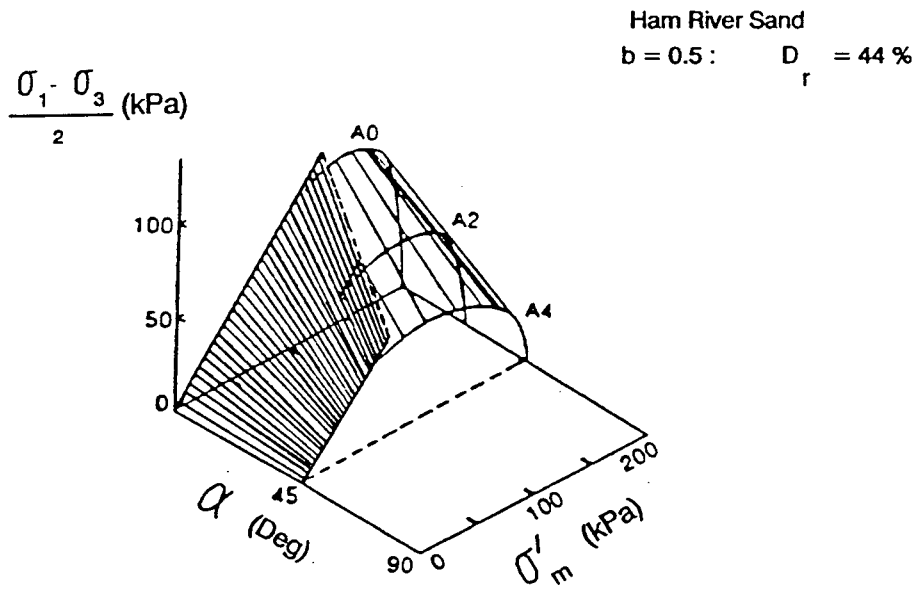

(b) Complete Surface

Figure 2.4: State boundary surface of sand - after Symes et al. (1984)

a given stress increment, based on the position of effective stress path (ESP) with respect to the BS. When the ESP was beneath the BS, pore pressure development was small. On the other hand, large pore pressures were observed when ESP was on the BS.

Initially the validity of BS concept was shown limited only for undrained principal stress rotations up to 45° from the deposition direction. Shibuya and Hight (1987), using undrained HCT tests on Ham river sand demonstrated that the concept of BS is applicable to the complete domain of rotations $-90° < \alpha_\sigma < +90°$, if the "shear strains are small" so that the induced anisotropy effects are negligible. However no guidelines were presented as to what constitutes "small strains". The BS approach for undrained response was further supported by the results from HCT tests on pluviated glass ballotini.

In their recent work, Symes et al. (1988) using a limited number of tests, extended the concept of the BS to drained loading by taking into account the volume changes occurring during drained principal stress rotation. The void ratio changes in drained tests were incorporated into the BS by using an equivalent effective mean normal stress σ'_{me}; defined as $\sigma'_{me} = \exp\left(\frac{e_o - e_i}{\lambda}\right)$, where e_o = void ratio at σ'_m = unity, e_i = current void ratio and λ = slope of the virgin hydrostatic consolidation line. Unlike clays, the value of λ for sands is generally quite low, and not even constant with stress level (Chern, 1985). Therefore λ value derived from laboratory tests will be susceptible to questionable interpretations. As such, the positioning of the BS will also be questionable due to the difficulties in evaluation of λ.

To highlight some of the observations under drained loading, typical results from Symes et al. (1988) on Ham river sand are reproduced in Fig. 2.5. In tests LR1 and LR3, specimens were initially sheared upto $R = 1.55$ and $R = 2.6$ respectively with $\alpha_\sigma = 0°$. Then the principal stresses were rotated from $\alpha_\sigma = 0°$ to 45° at constant R, σ'_m and b. Finally the value of R was increased until failure at constant

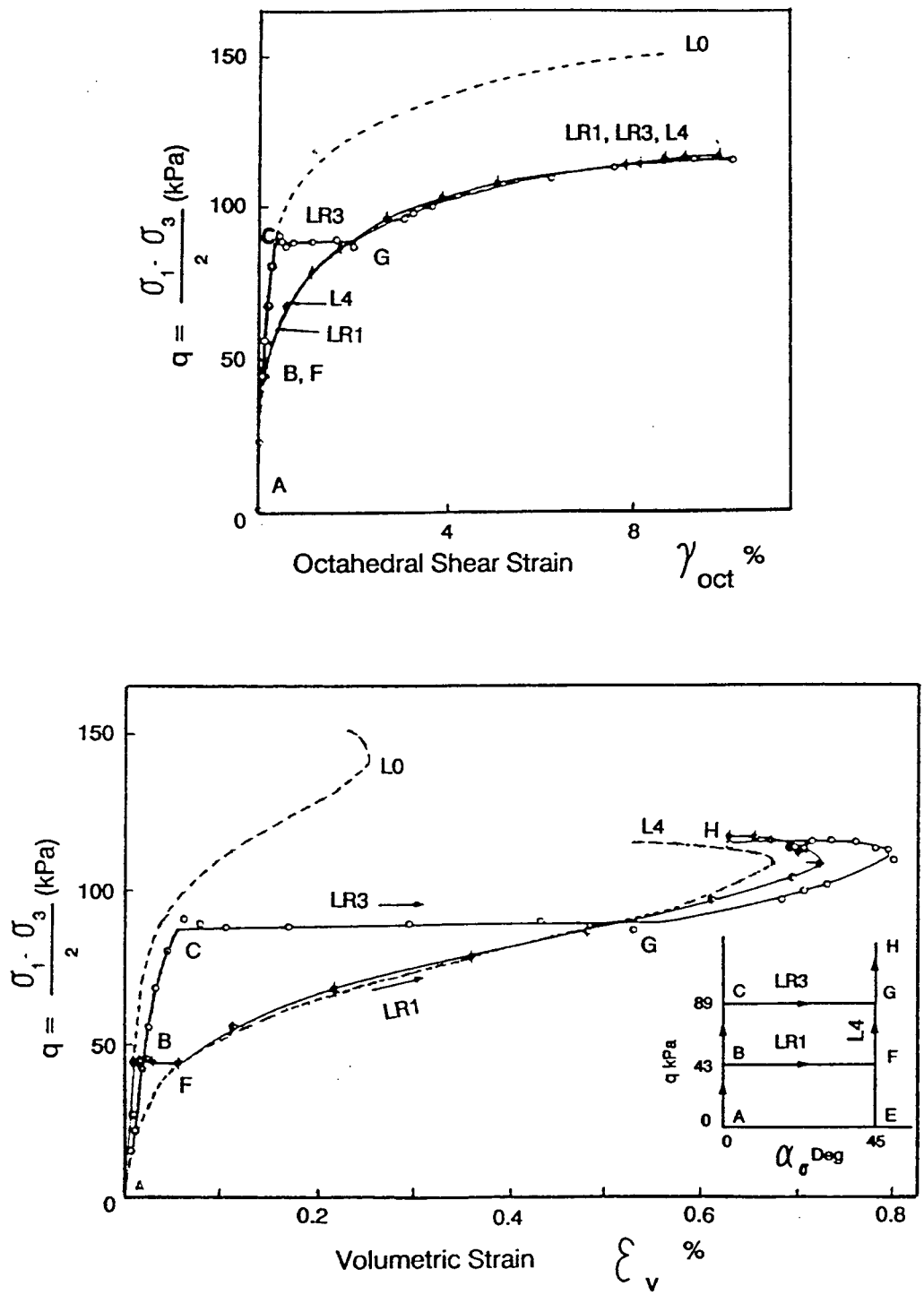

Figure 2.5: Drained principal stress rotation tests - after Symes et al. (1988)

σ'_m, b and $\alpha_\sigma = 45°$. In this last phase of the tests LR1 and LR3, the stress path was identical to that of L4 where R was increased from hydrostatic stress state to failure with $\alpha_\sigma = 45°$. All tests were carried out with constant $b = 0.5$ and $\sigma'_m = 300$ kPa. It was noted that both volumetric and shear strains in tests LR1 and LR3 matched closely the strains in L4 at common stress states F and G respectively. This indicates a stress path independent behaviour, although such stress path independence is not apparent in their earlier results (Hight et al., 1983). Furthermore, in shear loading with $\alpha_\sigma = 45°$ subsequent to principal stress rotation, specimens LR1 and LR3 exhibited strain response very similar to those of specimen L4. It is to be noted that in these stress paths, neither R nor α_σ experienced decrease during the course of the test. Symes et al. (1988) suggested that these tests imply a total loading condition and the stress paths would lie on the BS. They concluded that the initial anisotropy is the overriding factor in determining the behaviour of sand for stress paths involving "moderate amount of shear strain", but no limits on these strain levels were suggested.

It is important to emphasize that the validity of the BS for drained loading has been tested using few tests carried out at limited R levels and the stress rotations α_σ restricted to 45°. There is no experimental evidence to support the uniqueness of BS concept at larger principal stress rotations under drained conditions. Sayao and Vaid (1989) correctly pointed out that the effects of induced anisotropy and previous stress history effects are intrinsically neglected when the BS is considered unique in its position and/or shape. The observations on the BS have also been limited to constant σ'_m and b values of 200 kPa and 0.5 respectively. Thus the concept of bounding surface should be applied with caution, in spite of the attractiveness which comes as a result of its conceptual simplicity in describing principal stress rotation effects in sand.

Sayao (1989) noted that very little is known about the effects of principal stress rotation on sand response at moderate levels of stress ratio. He carried out a comprehensive investigation on the behaviour of Ottawa sand under rotations of principal

stresses using the HCT device. Volumetric and maximum shear strain response in two way ($\alpha_\sigma = 0° \rightarrow \pm 60°$) cyclic principal stress rotation on a loose sample by Sayao (1989) are reproduced in Fig. 2.6. Steady contractive deformations are observed regardless of whether the α_σ is increased or decreased on either side of the vertical direction. Larger volumetric strains develop for the increasing phases of α_σ than for the decreasing phases. This is in accordance with the BS concepts of Symes et al. (1988). However it was observed that the hardening effects usually associated with one way rotation cycles are greatly reduced in the case of two way cyclic rotations, suggesting inapplicability of the BS concept under such conditions. Although some recovery of the maximum shear strains is observed during the decreasing α_σ phase, the residual maximum shear strains increase with each cycle. Furthermore, the rate of strain per cycle decrease as the number of cycles increase. These drained cyclic rotation results from Sayao (1989) would imply a progressive pore pressure build up under cyclic undrained principal stress rotation.

Effect of the level of stress ratio at which principal stress rotation is imposed, on the strain development is shown in Fig. 2.7 (Sayao, 1989). With increasing α_σ, both ε_v and γ_{max} increase with the level of R. Thus principal stress rotations occurring at higher stress ratios could lead to large undesirable deformations in a sand mass.

2.3.2 Effects of Intermediate Principal Stress

Most of the investigations on the effects of σ_2' on deformation response have been carried out in terms of parameter $b = (\sigma_2' - \sigma_3')/(\sigma_1' - \sigma_3')$, which defines the relative magnitude of σ_2' with respect to σ_1' and σ_3'. This parameter was first introduced by Habib (1953) in investigating strength characteristics of clays and sands in torsional triaxial tests. Bishop (1966) suggested that the influence of σ_2' on soil response can be well portrayed in terms of b rather than σ_2' itself. Sayao (1989) noted that although large number of investigations are reported on the effect of b on strength parameters

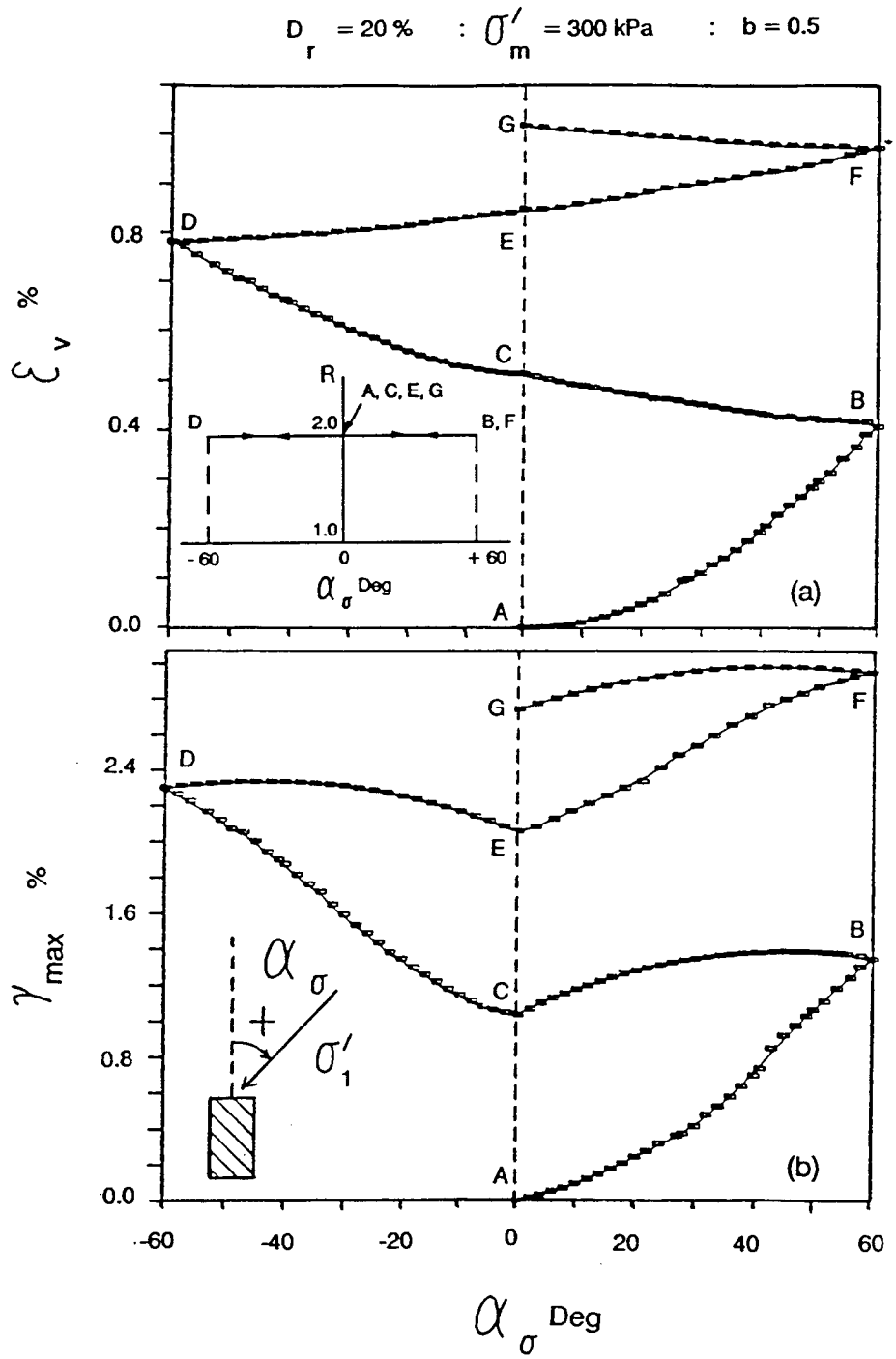

Figure 2.6: Strain development due to cyclic principal stress rotation - after Sayao (1989)

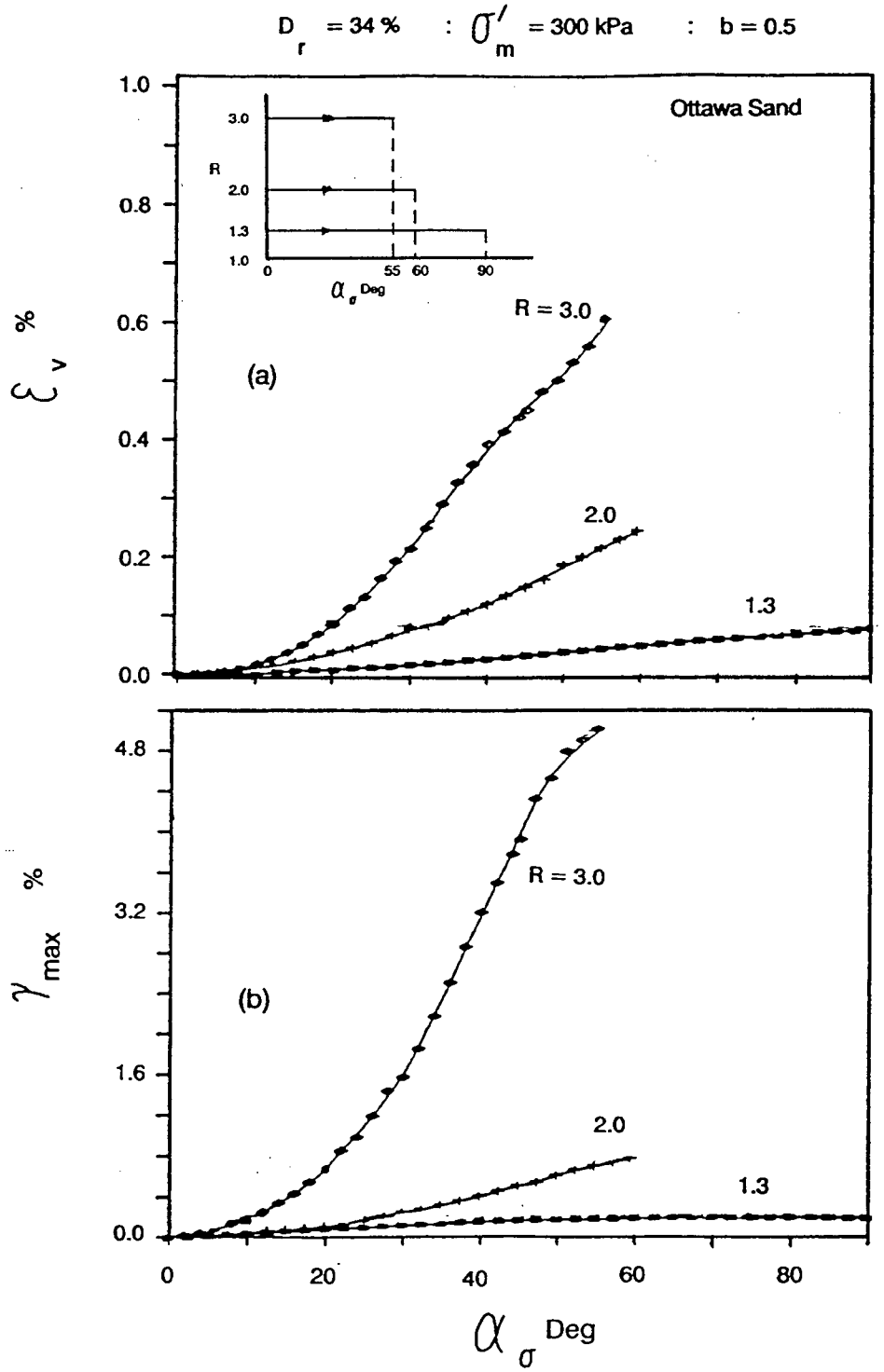

Figure 2.7: Effect of stress ratio on strain development due to principal stress rotation - after Sayao (1989)

(Bishop, 1966; Sutherland and Mesdary, 1969; Green, 1971; Lade and Duncan, 1973; Haruyama, 1981), there was very little work done on its effects on pre-failure stress strain behaviour.

Sayao (1989) carried out a comprehensive investigation on the effects of b on deformations along several stress paths, including those with principal stress rotation. From shear tests (increasing R) with constant σ'_m, b, and α_σ it was observed that the softest response occurred at $b = 0$ and the stiffest at $b = 0.3$. It was noted that the plain strain problems ($b \approx 0.3$) may have their deformations largely overpredicted when data from triaxial tests ($b = 0$) is used.

From HCT tests with continuously changing b parameter under constant R, α_σ and σ'_m conditions, Sayao (1989) observed a progressive accumulation of strains in medium loose sand. However, in the range of $b = 0$ to 0.4 which corresponds to most loading conditions in the field, the sensitivity of strains to the changes in b was found to be relatively low.

2.3.3 Effect of Mean Normal Stress and Relative Density

The increasing contractant behaviour under increasing confining pressure at constant relative density and decreasing relative density at constant confining pressure are a well recognized characteristic of granular materials (Lee and Seed, 1967; Vesic and Clough, 1979).

Sayao (1989) observed that this observation is valid even for stress paths involving principal stress rotation with fixed R, b, σ'_m and D_r. Some of his results are reproduced in Figs. 2.8 and 2.9 to illustrate these features. Sands tend to become more isotropic with increasing relative density (El-Sohby and Andrawes, 1972). Therefore, principal stress rotations would induce lesser strains at higher relative densities. The results reproduced in Figs. 2.8 and 2.9 also show that the rotation of principal stresses in general induces progressively larger volume contractions regardless of the relative

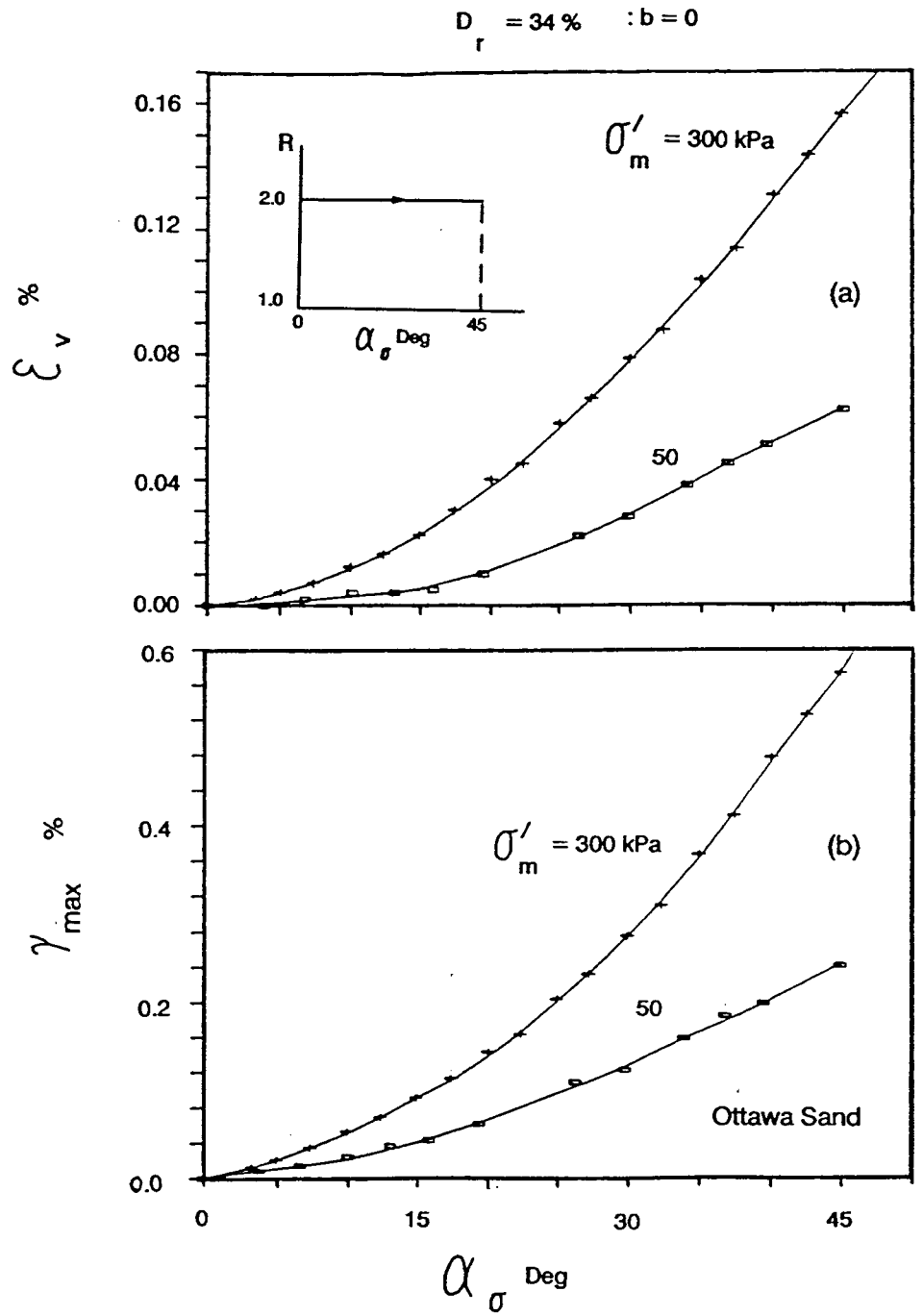

Figure 2.8: Effect of σ'_m on strain development due to principal stress rotation - after Sayao (1989)

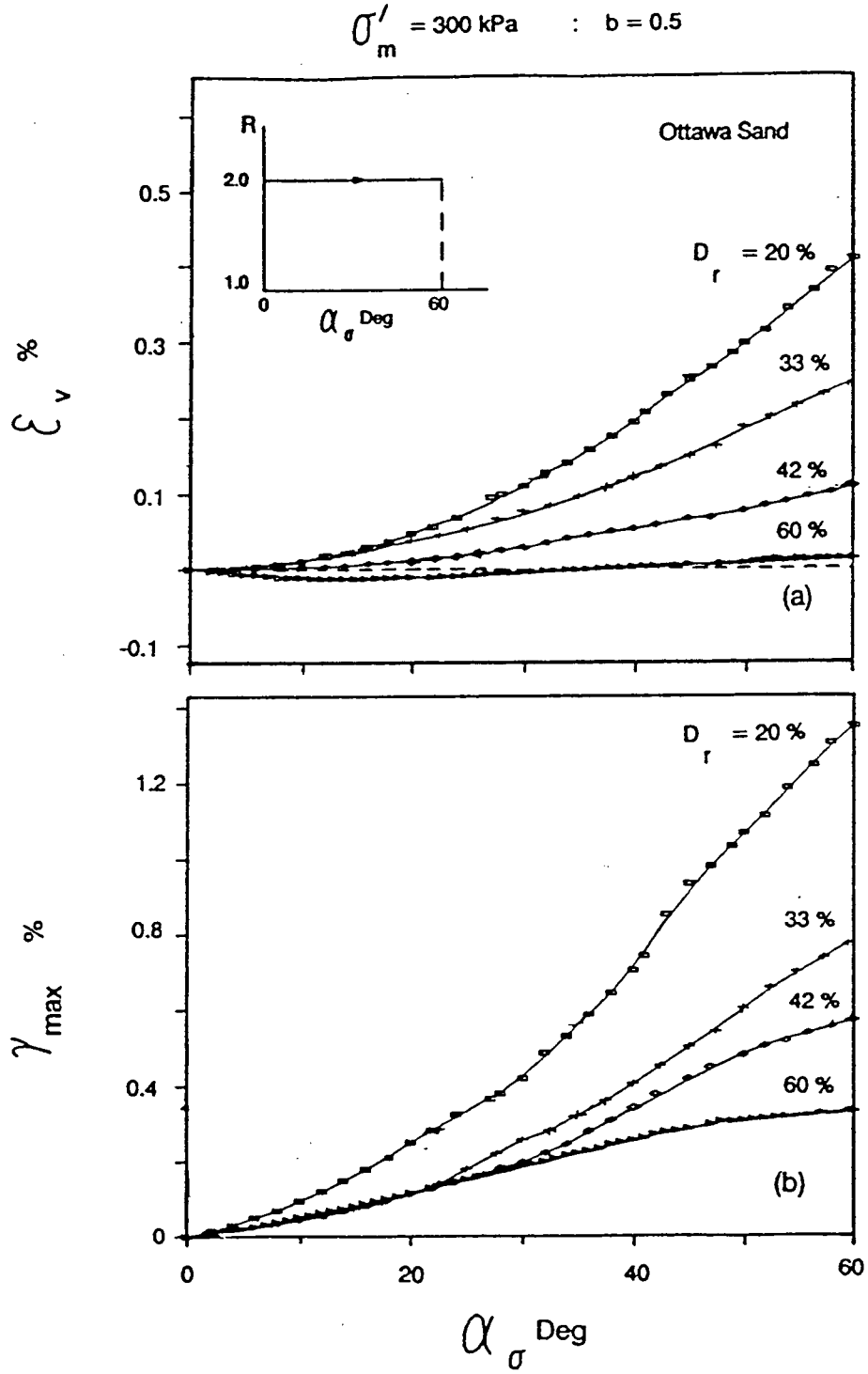

Figure 2.9: Effect of D_r on strain development due to principal stress rotation - after Sayao (1989)

density (except at the highest $D_r = 60\%$) and the mean normal stress.

As discussed in the foregoing sections, valuable research has been carried out on the isolated effect of each stress parameter on sand behaviour. Under general field loading situations however, simultaneous changes in all stress parameters R, σ'_m, b and α_σ generally occur. Therefore, it would be of great importance to examine whether the separate effects of each stress parameter on sand response could be combined to obtain behaviour under stress paths, where more than one stress parameter changes. Hight et al. (1983) and Symes et al. (1988) have reported only two HCT tests in which the stress ratio and the direction of principal stress α_σ was varied simultaneously. No attempts have been made to study comprehensively the behaviour of sand under simultaneous changes in the magnitude and directions of principal stresses.

2.3.4 Direction of Strain Increment

Any stress path could be viewed as a combination of a series of discrete stress increments. Therefore the strain increment direction $\alpha_{\Delta\epsilon}$ in relation to the directions of the applied stress α_σ and the stress increment $\alpha_{\Delta\sigma}$, always provide a better insight on the sand behaviour than that obtained from the examination of total strain response alone. In studies of material behaviour in the HCT device, the directions of stress and strain increments ($\alpha_{\Delta\sigma}$ and $\alpha_{\Delta\epsilon}$) are also expressed with reference to the same vertical deposition axis to which direction α_σ of σ_1 is referred to (Fig. 2.10).

Symes et al. (1988) examined the relationships between α, $\alpha_{\Delta\epsilon}$ and $\alpha_{\Delta\sigma}$, in drained principal stress rotation tests on medium loose Ham river sand. They observed that for stress paths which involved "loading"[2] in terms of the bounding surface, the strain increment direction $\alpha_{\Delta\epsilon}$ was lying between the stress direction α_σ and stress increment direction $\alpha_{\Delta\sigma}$. For loading paths at higher stress ratios, $\alpha_{\Delta\epsilon}$ was much closer to α_σ than $\alpha_{\Delta\sigma}$. On the other hand, for unloading (in terms of the BS) stress paths, $\alpha_{\Delta\epsilon}$

[2]loading and unloading is defined in section 2.3.1

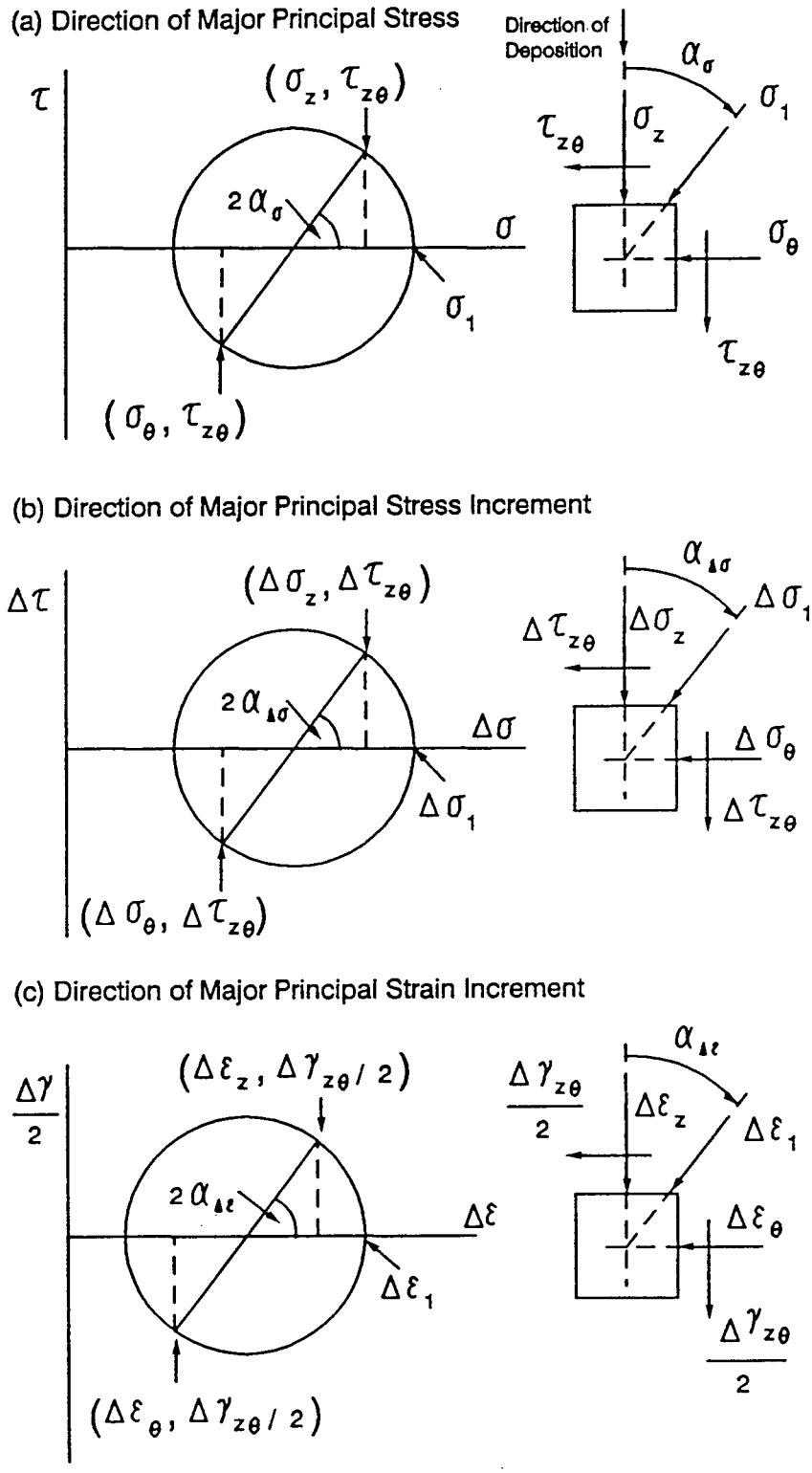

Figure 2.10: Definition of stress and strain increment directions

was lying close to $\alpha_{\Delta\sigma}$ irrespective of the magnitude of α_σ and the level of stress ratio R. They attributed the inequality of $\alpha_{\Delta\epsilon}$ and $\alpha_{\Delta\sigma}$ to the more irrecoverable strains induced during "loading paths". The agreement between $\alpha_{\Delta\epsilon}$ versus $\alpha_{\Delta\sigma}$ during "unloading paths" was alternatively suggested to be due to the high recoverable strains associated with unloading.

It has already been demonstrated that the sand is inherently anisotropic. It is therefore important to examine whether the coincidence of stress and strain increment directions could be directly viewed as a reflection of the recoverability of strains. If, for example, the material behaviour is isotropic elastic, the stress and strain increment directions would coincide. On the other hand, if it is cross anisotropic, even under ideal elastic conditions the coincidence of $\alpha_{\Delta\epsilon}$ and $\alpha_{\Delta\sigma}$ is not a necessity. It can be demonstrated that in a given cross anisotropic elastic material, the stress and strain increment directions will coincide only under a unique loading condition (Appendix A). It is therefore important that any correspondence between $\alpha_{\Delta\epsilon}$ and $\alpha_{\Delta\sigma}$ should be interpreted only with due consideration given to material anisotropy. The interpretations based on ideas directly applicable to isotropic elasticity will be of little assistance to the understanding behaviour of a material which is known to be anisotropic.

The examination of strain increment directions during deformation is still important, since it can be used as a qualitative indicator of the changes in anisotropy during stress path loading. Sayao (1989) examined the relation between $\alpha_{\Delta\epsilon}$ and $\alpha_{\Delta\sigma}$ under cyclic rotation of principal stresses at constant R, b and σ'_m. Typical results for a loose sand are reproduced in Fig. 2.11. The increasing phases of α_σ (α_σ from 0° to $\pm 60°$), always resulted in larger differences between $\alpha_{\Delta\epsilon}$ and $\alpha_{\Delta\sigma}$. On the other hand decreasing α_σ towards zero from either side of its maximum amplitude resulted in $\alpha_{\Delta\epsilon}$ close to $\alpha_{\Delta\sigma}$. As such, the strain increment directions clearly reflected the changes in anisotropy that took place during cyclic principal stress rotation.

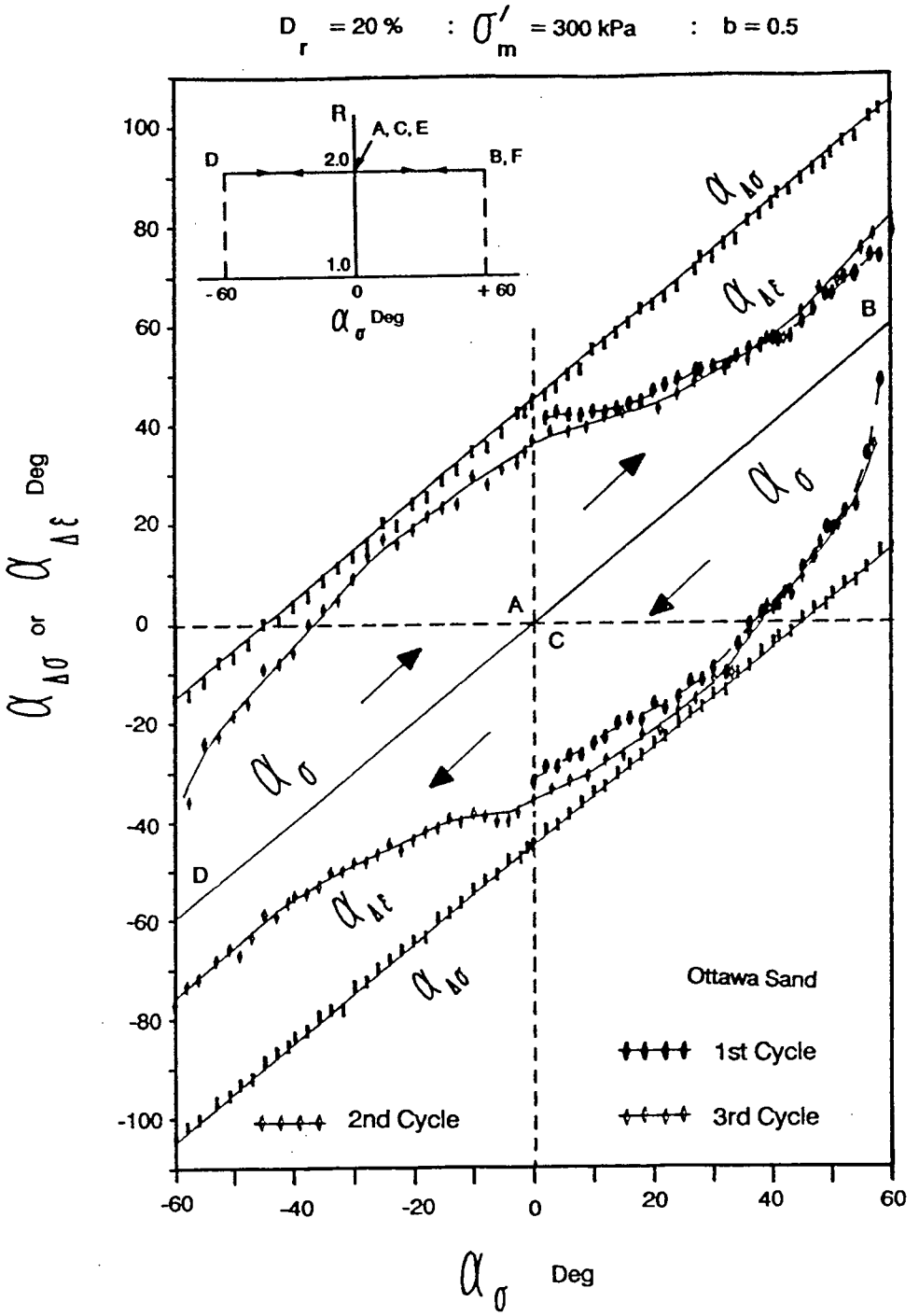

Figure 2.11: Strain increment directions during cyclic principal stress rotation - after Sayao (1989)

2.4 Summary

The foregoing literature review indicates that major advances have been made in the understanding of the separate effects of principal stress rotation and other stress parameters on the behaviour of cross anisotropic sands. The behaviour under general field loading conditions involve simultaneous changes in all six stress parameters σ'_m, R, b and the inclinations of the principal stress to the three cordinate axes fixed in the material. The HCT device enables an independent control of σ'_m, R, b, and principal stress rotation α_σ in one plane and hence a systematic study of material behaviour that includes principal stress rotation in one plane. The previous research using the HCT has concentrated on deformation due to changes in only one of these parameters at a given time. No comprehensive study has been made to investigate the behaviour of sands under simultaneous increase of these stress parameters in a controlled manner.

It has been suggested that the initial anisotropy governs the behaviour under principal stress rotation, if the induced strains are small. These conclusions have been based on a limited number of tests which envelopes only a small domain of the stress space.

Serious stress non-uniformities can develop in the HCT specimens of a given geometry under certain loading conditions. Thus it is imperative to delineate the domain of stress space available to the HCT device, for confident exploration of sand response under generalized stress path loading (see Chapter 3). Stress non-uniformities have been assessed mostly assuming sand to be linear elastic. Sands, however, are non-linear in their stress strain response. In order to delineate the domain of stress space that could be reliably explored using the HCT, the non-uniformities assessed on the basis of non-linear soil behaviour are therefore essential. No such assessment has so far been made which uses stress ratio R as the index of stress non-uniformity.

It is the purpose of this thesis to explore further some of the unanswered territories

of stress strain behaviour of cross anisotropic sands. The University of B.C. HCT apparatus is used in accomplishing this task. A detailed assessment of the stress non-uniformities in the HCT specimen having the geometry used at UBC is carried out assuming an incremental elastic hyperbolic representation of sand behaviour. The domain of stress space that could reliably be explored without introducing serious stress non-uniformities is thus identified. The stress paths for the experimental testing program are chosen so that they would lie within this domain. The testing program was designed particularly to study the effects of simultaneous increase in more than one stress parameter on sand response, and investigate possible interrelationships between this response and the response from tests in which only one stress parameter was varied.

Chapter 3

Stress Non-uniformities in the Hollow Cylinder Torsional Device

3.1 Introduction

The stress distribution within a hollow cylindrical torsional (HCT) specimen is non-uniform due to the curvature of the specimen wall as well as end restraint effects. The latter is common to most soil testing devices and could be minimized by selecting sufficiently long specimens together with end platens that reduce radial shear at the ends (Saada and Townsend, 1981; Hight et al., 1983; Vaid et al., 1990). On the other hand, stress non-uniformities due to the curvature of the specimen can occur even when the boundary stresses are uniformly applied.

Investigations into the stress non-uniformities due to curvature of the wall in HCT specimens have been reported by Hight et al. (1983) and Sayao and Vaid (1988). Hight et al. examined stress non-uniformities across the wall of the specimen in terms of the distribution of individual stress components. Sayao and Vaid argued that the assessment of stress non-uniformities should be based on the variation of effective stress ratio R across the specimen wall, because the deformation behaviour of granular material is intimately linked to the level of R and not to individual stress components. Their analysis revealed that although the level of stress non-uniformities according to Hight et al.'s criterion were in the acceptable range, serious non-uniformities were in fact present in terms of the distribution of R. Based on these studies, Sayao and Vaid delineated the domain of stress space that could reliably be explored using the

hollow cylinder device of a given geometry.

The assessment of stress non-uniformities in the HCT apparatus have been mostly carried out assuming that sand behaviour is linear elastic. This was mainly due to the readily obtainable closed form solutions to describe the stress distributions in a linear elastic hollow cylinder. In general, the assumption of linear elastic behaviour permits the presence of large stress gradients and hence high stress non-uniformities. Since the soil behaviour is non-linear (modulus degradation associated with increasing shear) the results emanating from a linear elastic analysis would generally overestimate stress non-uniformities. Although this would provide a conservative upper bound on the non-uniformities, it is important to point out that this conservatism is achieved at the expense of severely limiting the domain of the general stress space that could reliably be explored. A rational assessment of stress non-uniformities should be based on a material stress strain law which models the deformation modulus degradation characteristics of soils.

Hight et al. (1983) did report a limited study on stress non-uniformities in HCT specimens assuming a strain hardening elasto-plastic material behaviour. Since the non-uniformities were assessed for individual stress components, their results did not reflect the non-uniformity of stress ratio R across the wall of the specimen, a measure most crucial in the case of granular material. So far there has not been any detailed examination of the stress non-uniformities in terms of R, which takes the non-linearity of the sand behaviour into account.

In order to interpret data from a HCT test, relationships have to be established between average stresses and the surface tractions (see section 3.2). Like stress non-uniformity evaluation, the average stresses are commonly estimated with the assumption that the sand response is linear elastic. It is therefore important to investigate the validity of the linear elastic assumptions in the estimation of average stresses even if soil is assumed non-linear in assessing stress non-uniformities. No attempts have

been made to examine this important aspect, upon which the entire concept of stress path testing and interpretation of data in a HCT device is based.

In this chapter the stress non-uniformities arising due exclusively to the curvature of the HCT specimen are examined using the finite element (FE) analysis. An incremental elastic hyperbolic stress strain law is used to model sand behaviour. These results are then compared with the stress non-uniformities obtained if the soil was assumed linear elastic. The domain of stress space that could reliably be explored without introducing unacceptable stress non-uniformities is identified based on the results from the FE analysis. The effects of confining pressure and relative density of sand on stress non-uniformities are also examined. Finally, the average stresses obtained from linear elastic analysis are compared with those derived from FE analysis, in order to verify the validity of linear elastic assumption for the computation of average stresses.

3.2 Definitions of Average Stresses, Strains and Non-uniformity Parameters

In order to follow a given stress path, four surface tractions applied to the HCT specimen need be varied in a prescribed manner. They are: vertical force F_z, torque T_h, external and internal pressures: P_e and P_i respectively (Fig. 3.1). At any given point in the HCT specimen these tractions induce stresses σ_z, σ_r, σ_θ and $\tau_{z\theta}$ as shown in Fig. 3.1. In response to these stresses four non-zero strain components ϵ_z, ϵ_r, ϵ_θ and $\epsilon_{z\theta}$ develop.

3.2.1 Average Stresses

Interpretation of results from HCT tests is made by considering the entire specimen as a single element, deforming as a right circular cylinder. In order to compute

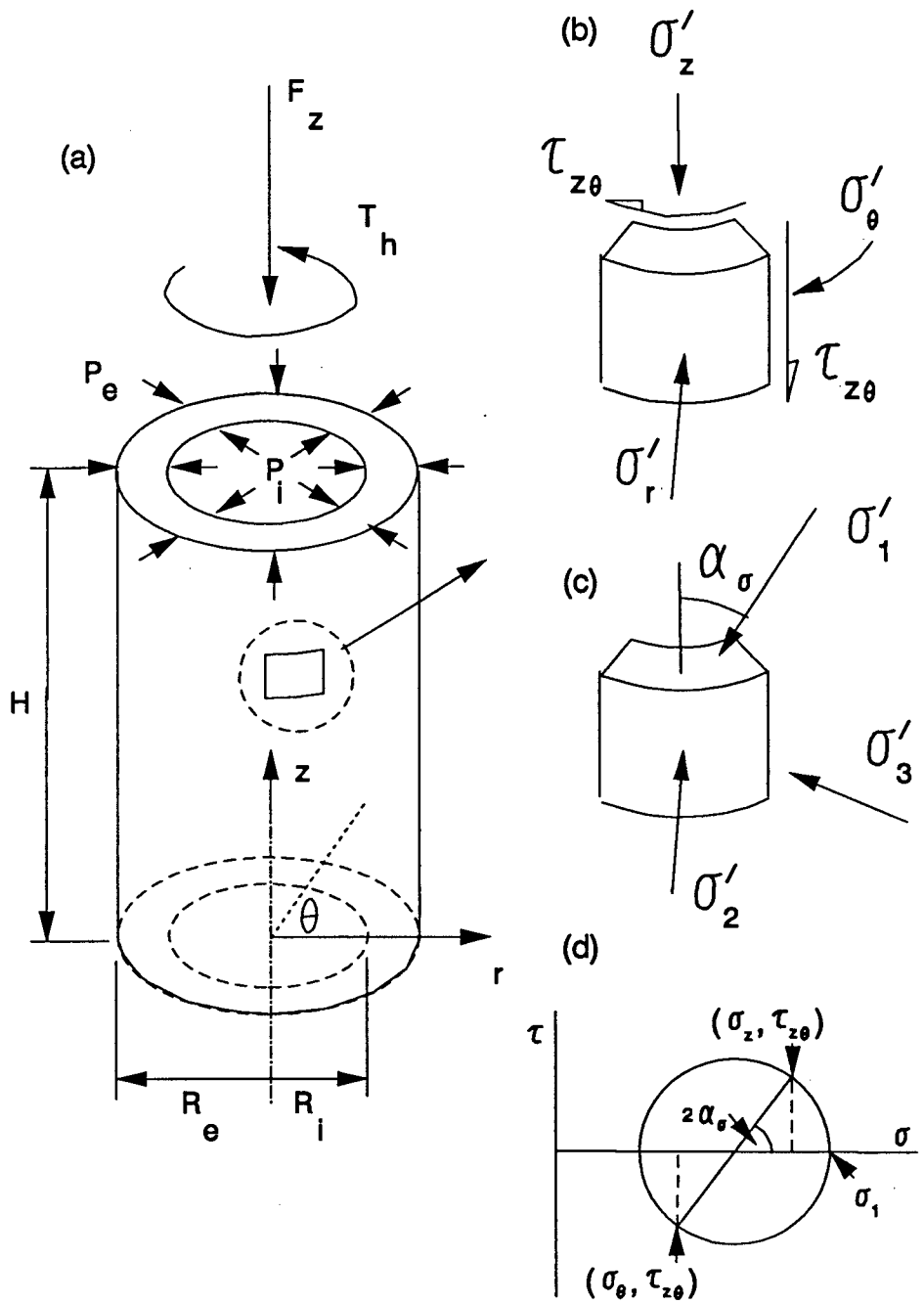

Figure 3.1: Loading and stress conditions in HCT specimens

surface tractions for following a given stress path or vice versa, average stresses are usually computed assuming a linear elastic isotropic material (Hight et al., 1983; Sayao, 1989). The expressions for σ_r, σ_θ and $\tau_{z\theta}$ are obtained by averaging the stresses over the volume of the specimen. The vertical stress σ_z is assumed to be distributed uniformly across the cross section, and thus obtained using equilibrium considerations only. The resulting expressions are:

$$\sigma_z = \frac{F_z + \pi(P_e R_e^2 - P_i R_i^2)}{\pi(R_e^2 - R_i^2)} \tag{3.1}$$

$$\begin{matrix}\sigma_r \\ \sigma_\theta\end{matrix} = \frac{(P_e R_e^2 - P_i R_i^2)}{(R_e^2 - R_i^2)} \mp \frac{2(P_e - P_i) R_e^2 R_i^2 \ln(R_e/R_i)}{(R_e^2 - R_i^2)^2} \tag{3.2}$$

$$\tau_{z\theta} = \frac{4T_h(R_e^3 - R_i^3)}{3\pi(R_e^4 - R_i^4)(R_e^2 - R_i^2)} \tag{3.3}$$

where,

R_e - External Radius of the HCT specimen

R_i - Internal Radius of the HCT specimen

The radial stress σ_r is usually the intermediate principal stress σ_2 in HCT tests. Using the Mohr's circle on σ_z, σ_θ and $\tau_{z\theta}$, the major σ_1 and minor σ_3 principal stresses and the inclination α_σ of the major principal stress σ_1 to the vertical can be calculated (Fig. 3.1).

3.2.2 Average Strains

The average strain components in the specimen are calculated using the following expressions.

$$\varepsilon_z = -\frac{\Delta H}{H} \tag{3.4}$$

$$\varepsilon_r = -\left(\frac{\Delta R_e - \Delta R_i}{R_e - R_i}\right) \tag{3.5}$$

$$\varepsilon_\theta = -\left(\frac{\Delta R_e + \Delta R_i}{R_e + R_i}\right) \tag{3.6}$$

$$\gamma_{z\theta} = \frac{2\Delta\theta\,(R_e^3 - R_i^3)}{3H\,(R_e^2 - R_i^2)} \tag{3.7}$$

where,

$H, \Delta H$ - Height and change in height of the specimen

$\Delta\theta$ - Angular displacement at the base of the specimen

The change in the inner radius ΔR_i is obtained from the measured values of ΔH and volume change of the inner chamber. The external radius change ΔR_e can then be computed from the measured values of ΔH, volume change of the sample and the derived value of ΔR_i.

3.2.3 Degree of Stress Non-uniformity

The degree of stress non-uniformity in the HCT specimen is assessed in terms of the variation of stress ratio across the wall (Sayao and Vaid, 1988) and is given by the non-uniformity coefficient,

$$\beta_R = \frac{(R_{max} - R_{min})}{R_{av}} \tag{3.8}$$

where,

R_{max} - Maximum stress ratio across the wall of the specimen

R_{min} - Minimum stress ratio across the wall of the specimen

R_{av} - Average stress ratio across the wall of the specimen

3.3 Finite Element Program and Mesh

3.3.1 Finite Element Program

The three dimensional FE program 3DSLB developed at UBC by Salgado (1990) was employed for stress analysis in the HCT specimen. The program uses cubical isoparametric elements ("brick" elements) with 8 nodes per element. Each node can assume 6 degrees of freedom: viz. 3 displacements and 3 rotations. The program also has the ability to include beam elements in the FE mesh, thus making provision to accomodate the feature of soil structure interaction.

Although the program has the capability of using complex stress strain models, an isotropic incremental elastic hyperbolic model as proposed by Duncan et al. (1980) was used. Soil modelling using such a constitutive law has been claimed to result in deformation predictions which agree favourably with measured deformations in the field (NSF/NSERC Workshop, 1980). Soil parameters used in hyperbolic modelling are given in Fig. 3.2 and the relevant equations signifying parameter usage are:

$$E_t = \left\{1 - \frac{R_f(1-\sin\phi)(\sigma_1' - \sigma_3')}{2\sigma_3' \sin\phi}\right\}^2 E_i \tag{3.9}$$

$$E_i = k_E P_a \left(\frac{\sigma_3'}{P_a}\right)^n \tag{3.10}$$

$$B_t = k_B P_a \left(\frac{\sigma_3'}{P_a}\right)^m \tag{3.11}$$

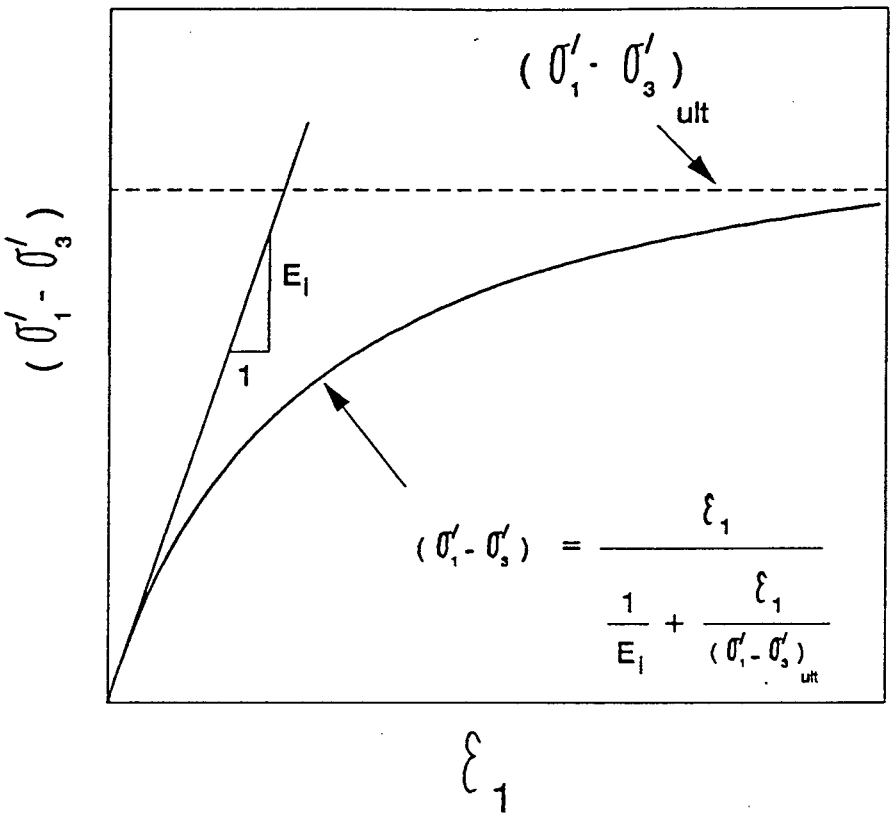

Parameter	Name	Function
$(\sigma_1' - \sigma_3')_{ult}$	Asymptotic deviator stress	
$(\sigma_1' - \sigma_3')_f$	Failure deviator stress	
E_i	Initial tangent modulus	
B_t	Tangent bulk modulus	
k_E	Modulus Number	Relate E_i to σ_3'
n	Modulus exponent	
ϕ_1, $\Delta\phi$	Friction angle parameters	Relate $(\sigma_1' - \sigma_3')_f$ to σ_3'
R_f	Failure ratio	Relate $(\sigma_1' - \sigma_3')_{ult}$ to $(\sigma_1' - \sigma_3')_f$
k_B	Bulk modulus number	Value of B_t/P_a at $\sigma_3' = P_a$
m	Bulk modulus exponent	

Figure 3.2: The definition of parameters for the hyperbolic model - after Duncan et al. (1980)

Table 3.1: Hyperbolic Soil Parameters used in the Analysis

D_r %	k_E	n	k_B	m	ϕ_1	$\Delta\phi$	R_f
30	500	0.5	300	0.25	33	0	0.9
75	900	0.5	500	0.25	41	4	0.7
100	1500	0.5	900	0.25	50	9	0.6

$$\phi = \phi_1 - \Delta\phi \log\left(\frac{\sigma_3'}{P_a}\right) \tag{3.12}$$

In the FE program two independent incremental elastic moduli, the tangent Young's modulus E_t and the tangent bulk modulus B_t define the stress strain relationship. The values of E_t and B_t for a given sand depend upon the stress level as shown in the above equations. The parameters to compute these moduli are usually obtained from conventional triaxial tests. Since the aim of this study was to assess the stress non-uniformities in the HCT test for a general sand specimen, representative values of soil parameters were obtained as suggested by Byrne et al. (1987). These are listed in Table 3.1 for three relative density states.

3.3.2 Mesh Used

The hollow cylinder specimen was simulated using an axisymmetric polygonal cross section with 12 sectors as shown in Fig. 3.3. The dimensions of the mesh was chosen to represent the University of B.C. HCT device. The UBC-HCT has the following dimensions: external diameter = 152 mm (6.0 in), internal diameter = 102 mm (4.0 in) and height = 305 mm (12.0 in). The effects of end platens were simulated by having a series of beam elements at the top and bottom ends of the FE mesh as shown in Fig. 3.4. The beam elements connect the nodes lying on a radial line from

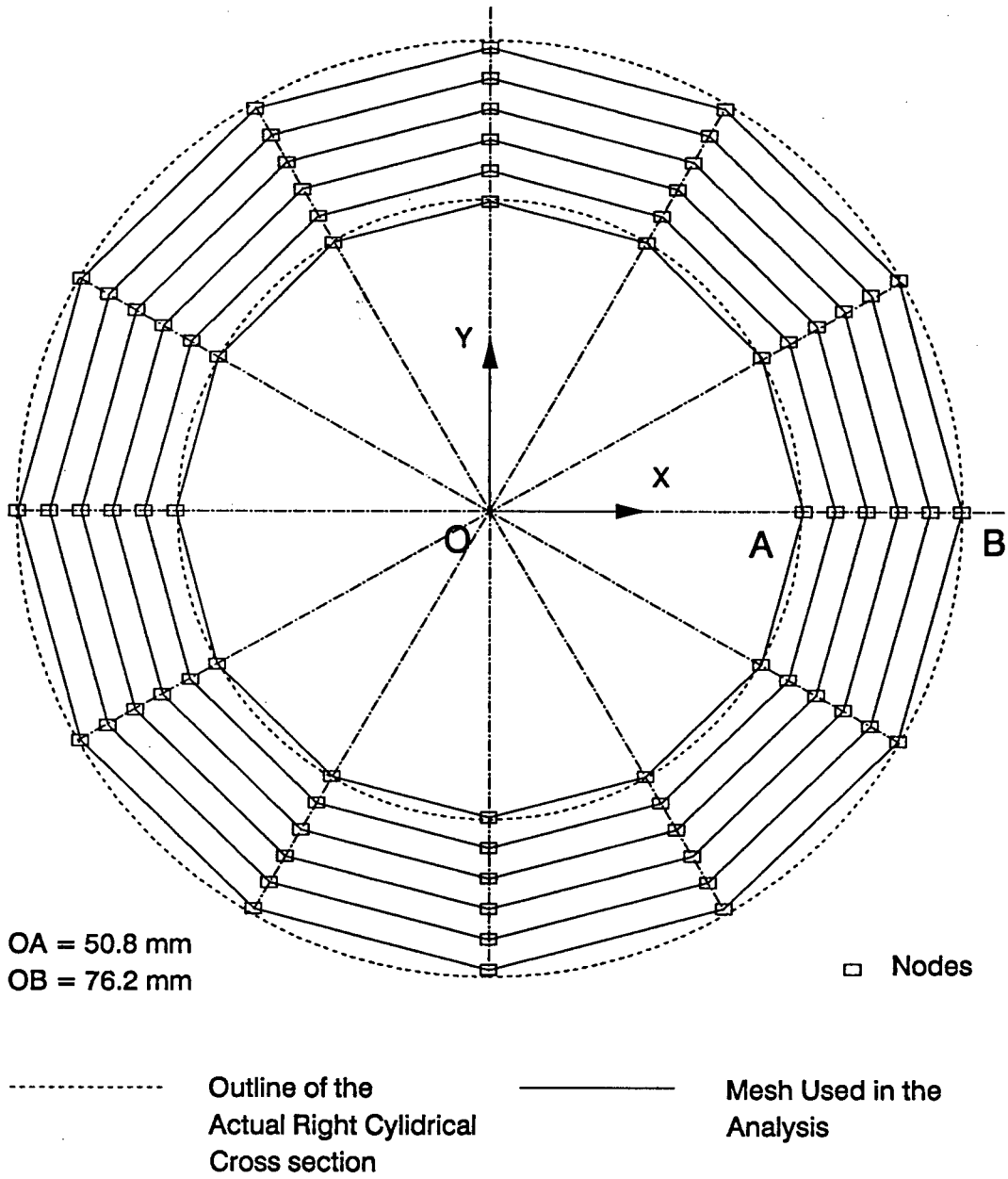

Figure 3.3: Cross section of the FE mesh used

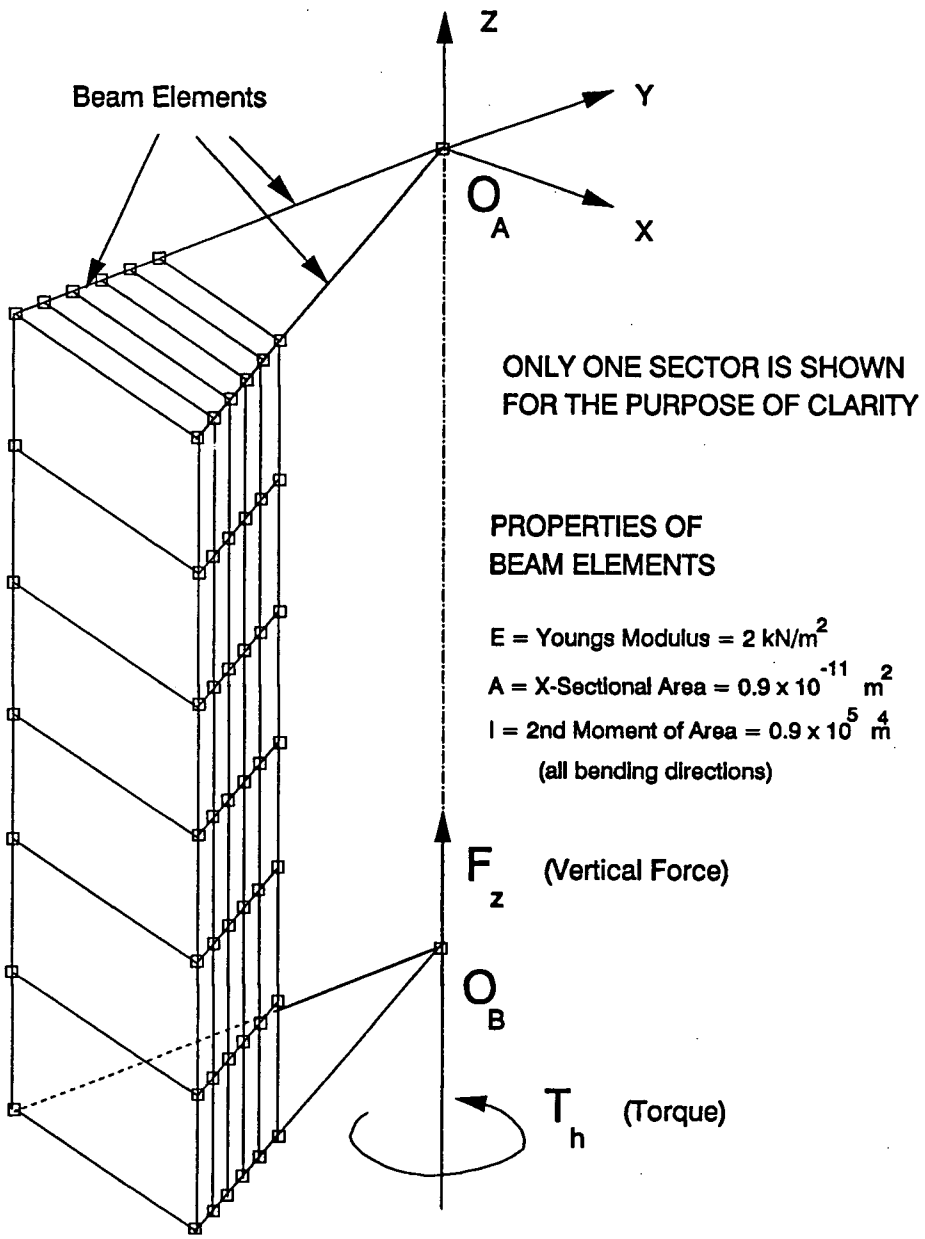

Figure 3.4: One sector of the FE mesh with end beam elements

the central node which is at the central axis of the specimen (O_A and O_B in Fig. 3.4). Each end platen is simulated by 12 such radial lines in order to match the selected number of sectors. Each radial line has 6 nodes in addition to the central node, thus requiring 6 beam elements for interconnecting these nodes.

Since the analytical study was aimed at investigating stress non-uniformities arising due only to the curvature of the specimen, it was necessary to specify boundary conditions so that the effect of specimen curvature alone contributed to the non-uniformities. This was achieved by satisfying the following end conditions in the FE analysis.

1. At the top and bottom end platens (simulated by beam elements) there is no restraint to the movement of the soil in the radial direction (no radial end restraint).

2. Both end platens act as rigid bodies against any mode of deformation which involves bending of the beam elements. Full friction should develop between the end platens and the soil to arrest any slip in the circumferential direction. (i.e. soil elements in contact with end platen undergo an angular movement about the central axis O_AO_B, which is identical to the angular movement of the end platen itself).

3. Vertical (i.e. axial) displacement and rotation about the vertical axis of the top platen is held fixed, whereas the bottom platen is allowed to move any desired amount in these two modes of motion.

The first requirement was achieved by having beam elements with very low cross sectional area so that the axial stiffness of the beams was neglegibly small (value of EA = 1.8×10^{-11} N). This made the relative movements of the nodes in the radial direction of the mesh to be unaffected by the presence of these structural elements, thus satisfying the zero *radial* end restraint condition.

The second boundary condition was simulated by increasing the flexural rigidity of the beam elements (in all directions of bending) to a significantly high value (value of EI = 1.8×10^5 Nm^2), and connecting each beam element to its end nodes with full moment resisting capacity. Thus, due to the high flexural rigidity and the imposed end fixity conditions for the beam elements, the nodes lying on a radial line at the beginning of loading remained radial during any stage of loading. This ensured a rigid end platen condition against torsional mode of loading. Since the soil and beam elements had common nodes at the top and bottom ends, the soil elements automatically experienced an angular displacement identical to that of the end platens, thus accomplishing the no *circumferential* slip condition at the ends.

The third boundary condition requires the top end platen to be held fixed against the vertical (axial) movement and rotation about the vertical axis. The zero vertical displacement requirement at the top end platen was achieved by prescribing all the nodes lying on the horizontal cross section through O_A (Fig. 3.4) to have zero displacement in the vertical direction. In arresting the rotational movement of the top platen, only node O_A was held fixed against rotation about the vertical axis. Due to the rigid beam element assembly (as described in the previous paragraph), the other nodes lying on that cross section through O_A were automatically held against rotation. On the other hand, all nodes at the bottom end platen were given the freedom to move both in the vertical and rotational modes.

Finally, in order to keep the vertical axis O_AO_B aligned and vertical under any loading condition, the movement of the nodes O_A and O_B in the horizontal plane was not permitted.

As described previously the hollow cylindrical specimen is loaded by applying four surface tractions. In order to load the specimen along a desired stress path, the surface tractions are back calculated from the average stresses obtained from linear elastic considerations (i.e. equations 3.1 to 3.3). In simulating these tractions in

the FE analysis, the external vertical force and the torque about the vertical axis is applied at the bottom of the specimen at the central node O_B (Fig. 3.4). On the other hand, the internal and external pressures on the specimen walls are distributed by applying equivalent nodal loads on the interior and exterior vertical faces of the mesh.

The full cylinder was modelled by six 2.0 in. (5.0 cm) high elements in the vertical direction (Fig. 3.4).

In order to check the validity of the numerical analog in computing stresses in the hollow cylindrical specimen, two loading cases in classical linear elasticity were simulated, and the results compared with closed form solutions. The loading cases selected were:

1. hollow cylinder subjected to pure torque only

2. hollow cylinder subjected to different internal and external pressures only

Figures 3.5 and 3.6 illustrate comparisons between the FE and closed form solutions for the two loading cases considered. The close agreement between the two solutions gives credibility to the use of this polygonal mesh, and the stiffness parameters selected for the beams, for numerically simulating the actual hollow cylindrical specimen. Furthermore, the FE analysis results show that all elements located at a given radius have identical stress states, confirming the expected perfect symmetry of stresses about the vertical axis. The stress state is dependent only on the radial location (not dependent on θ) and independent of the vertical location of the elements. (i.e. an element neighbouring an end platen has a stress state identical to that of an element located away from the ends, provided both are at the same radial location). This confirmed that the selected parameters for the beam elements effectively simulated the zero radial end restraint condition, which was an important requirement to be met in this analysis.

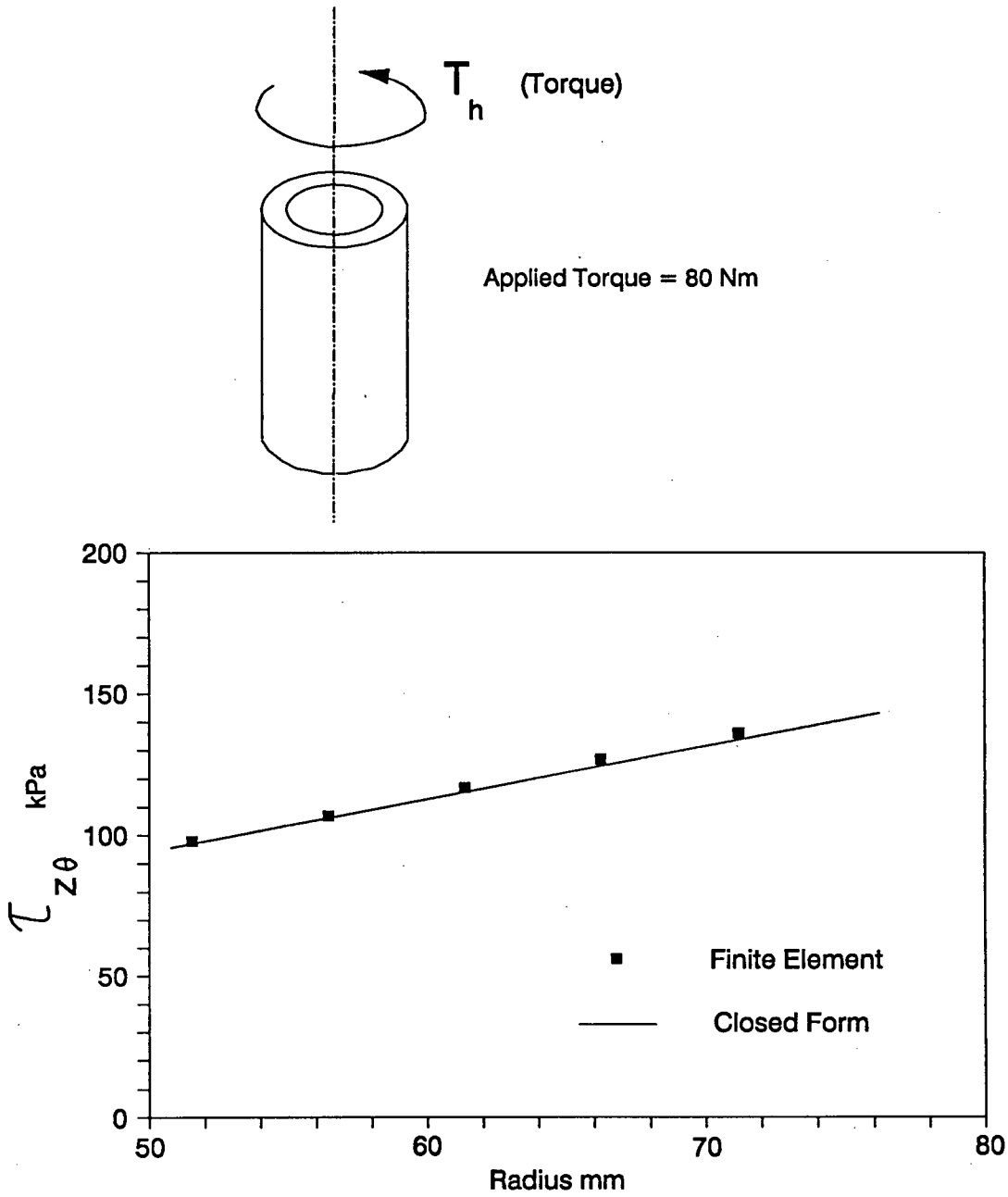

Figure 3.5: Distribution of $\tau_{z\theta}$ across the wall under pure torque - Linear elastic material

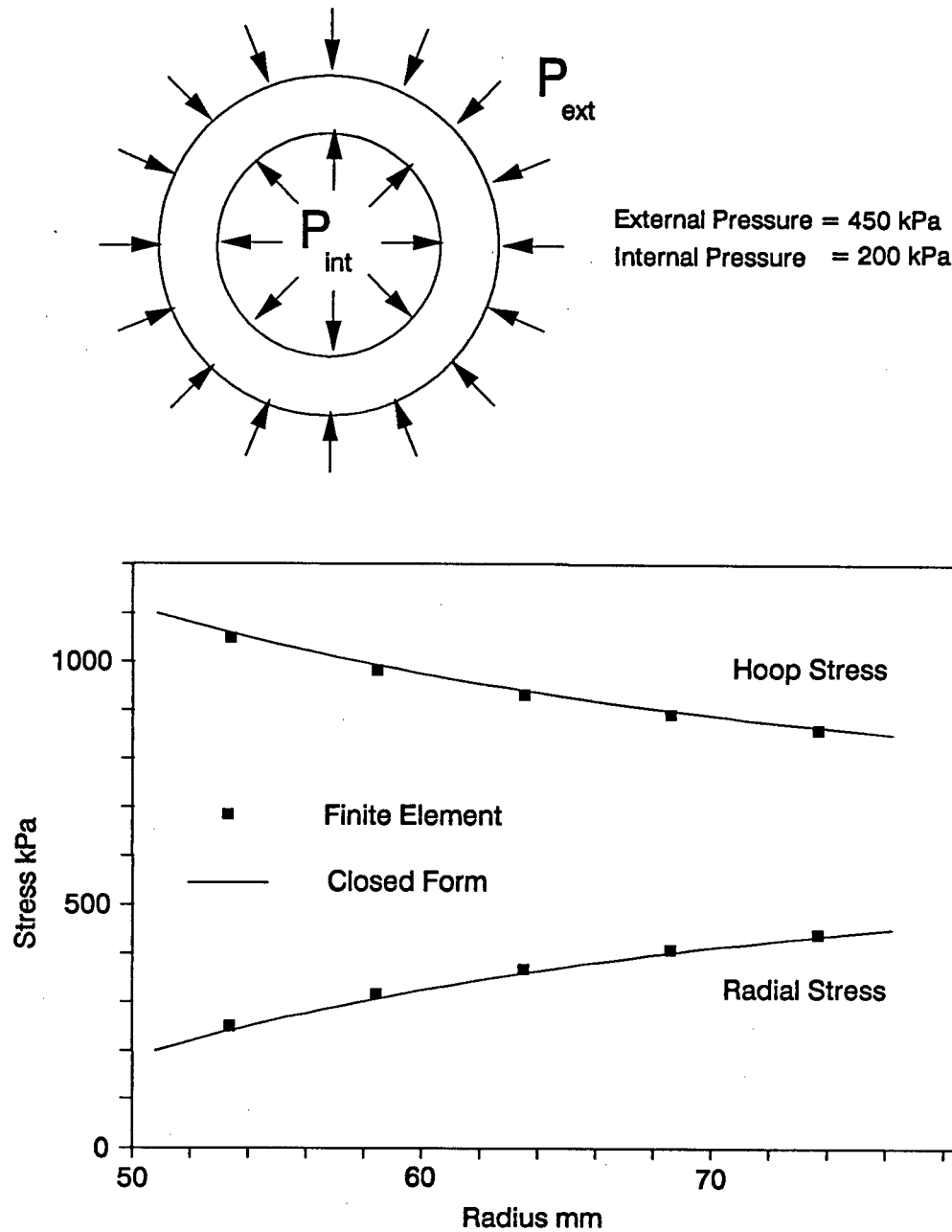

Figure 3.6: Distribution of σ_r and σ_θ across the wall under different external and internal pressures - Linear elastic material

The imposed zero end restraint condition implies that under a given loading condition, the stress distributions across the wall would be independent of the height of the specimen. Thus, stress non-uniformities due to the curvature of the specimen wall could possibly be assessed with a lesser number of elements in the longitudinal (vertical) direction of the FE mesh, resulting in very large savings in computational effort.

It was therefore decided to investigate the feasibility of replacing the full cylinder mesh with a concise FE mesh (Fig. 3.7) that contains only one element in the longitudinal direction. Other than the difference in the number of elements in the longitudinal direction, the concise FE mesh is identical to the full mesh in terms of the beam element assembly and the end boundary conditions. With concise and the full FE mesh idealizations, the HCT specimen was subjected to identical loading conditions as given below, and the resulting stress distribution across the wall compared for the two representations.

1. Hollow cylinder specimen of linear elastic isotropic material under,
   - a pure torque of 80 Nm
   - external and internal pressures of 450 and 200 kPa respectively
2. Hollow cylinder specimen of incremental elastic loose sand ($D_r = 30\%$) in a stress path loading in which the stress ratio R is increased from 1 to 2 with,
   - $b = 0.0$; $\alpha_\sigma = 45°$ and $\sigma'_m = 300$ kPa
   - $b = 0.5$; $\alpha_\sigma = 0°$ and $\sigma'_m = 300$ kPa
   - $b = 0.5$; $\alpha_\sigma = 45°$ and $\sigma'_m = 300$ kPa

The first two loading cases for the linear elastic material (item No. 1 above) are identical to those presented in Figs. 3.5 and 3.6. The stress path loadings simulated

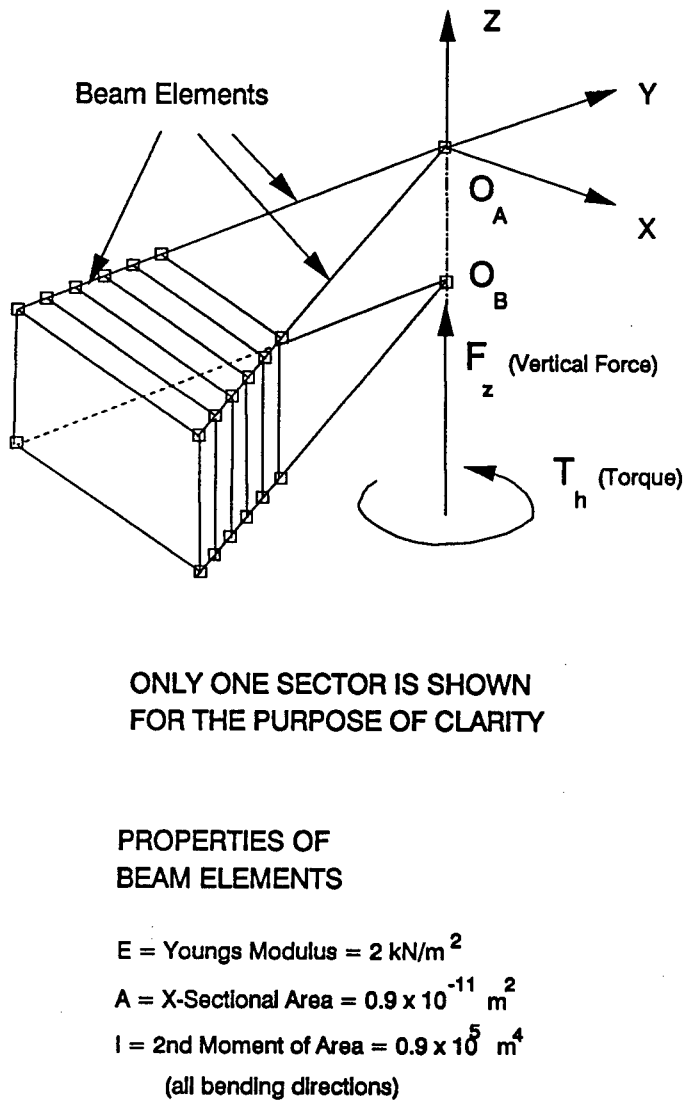

Figure 3.7: One sector of the concise FE mesh with end beam elements

(item No. 2 above) were selected directly from the main stress non-uniformity investigation program described in section 3.4. In this manner the suitability of using the concise mesh was checked for both linear elastic and incremental elastic representations.

Fig. 3.8 compares the stress distribution across cylinder wall using the concise mesh with that from the full FE mesh for loading of the linear elastic material. Similar comparisons of the distribution of stress ratio R across the wall for loading of the incremental linear elastic material are presented in Fig. 3.9. Excellent agreement between the results show that the zero end restraint conditions are fully satisfied with the use of concise mesh. Thus, the concise mesh only was used in the assessment of stress non-uniformities **due exclusively to the curvature of the specimen**.

3.4 Stress Non-uniformities Under General Stress States in Non-linear Soil

Stress non-uniformities in the HCT specimen were assessed predominantly for loose sand ($D_r = 30\%$). Loose density was selected because the effects of principal stress rotation have been found to be more profound in loose sands (Sayao, 1989).

Theoretically an infinite number of stress paths can be followed in loading to a given stress state, defined by the parameters σ'_m, R, b and α_σ. Because of the non-linearity of the selected constitutive law, the stress non-uniformities at the target stress state will depend on the stress path executed to that stress state. This prompted some preliminary analyses to investigate the dependence of the degree of stress non-uniformity coefficient β_R on the stress path followed.

Results of these analyses are presented in Fig. 3.10, which also shows different stress paths followed to identical target stress states. It may be observed that the stress non-uniformities do depend on the stress path followed to the target stress

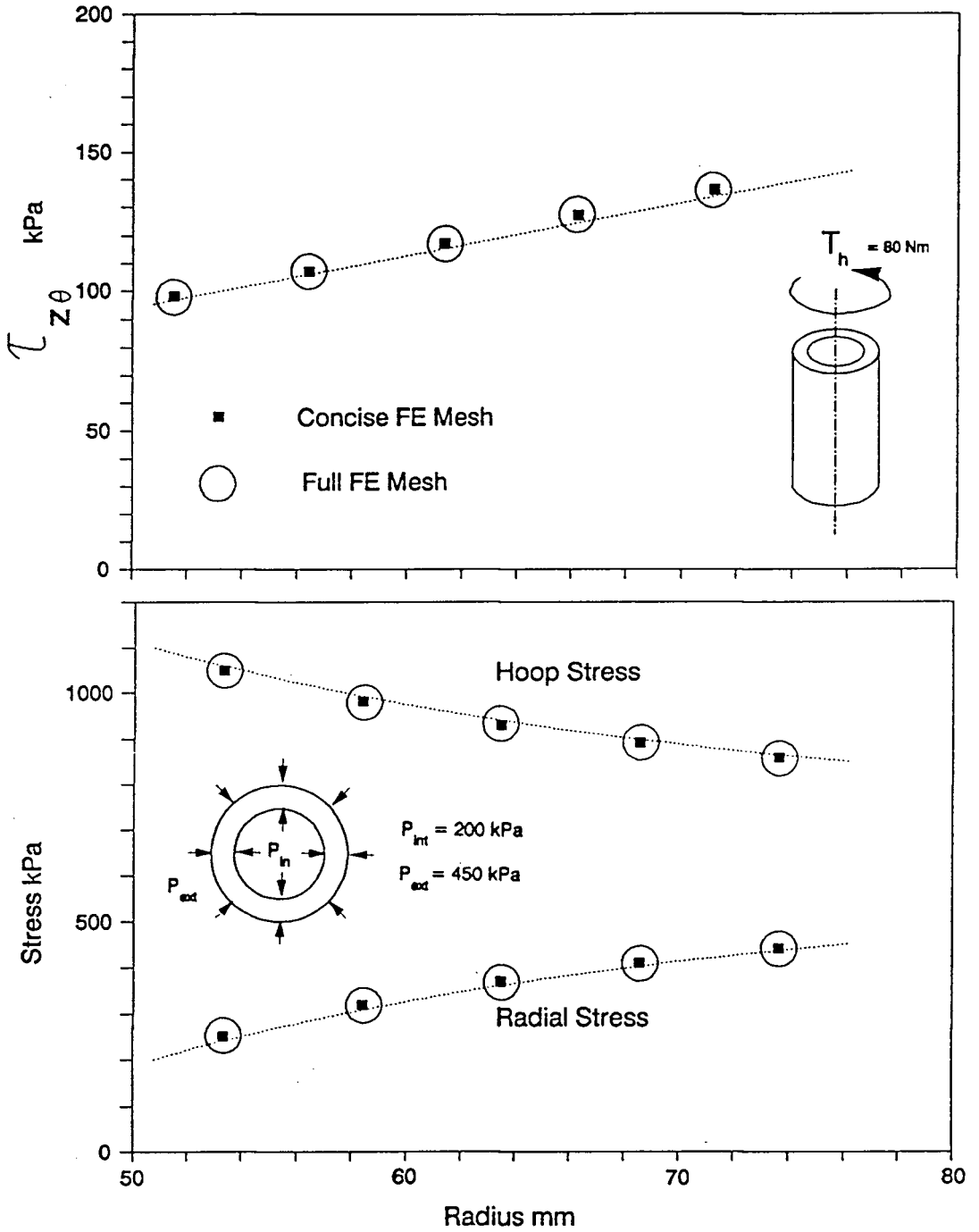

Figure 3.8: Comparison of stress distributions across the specimen wall from the full FE mesh versus concise FE mesh - Linear elastic material

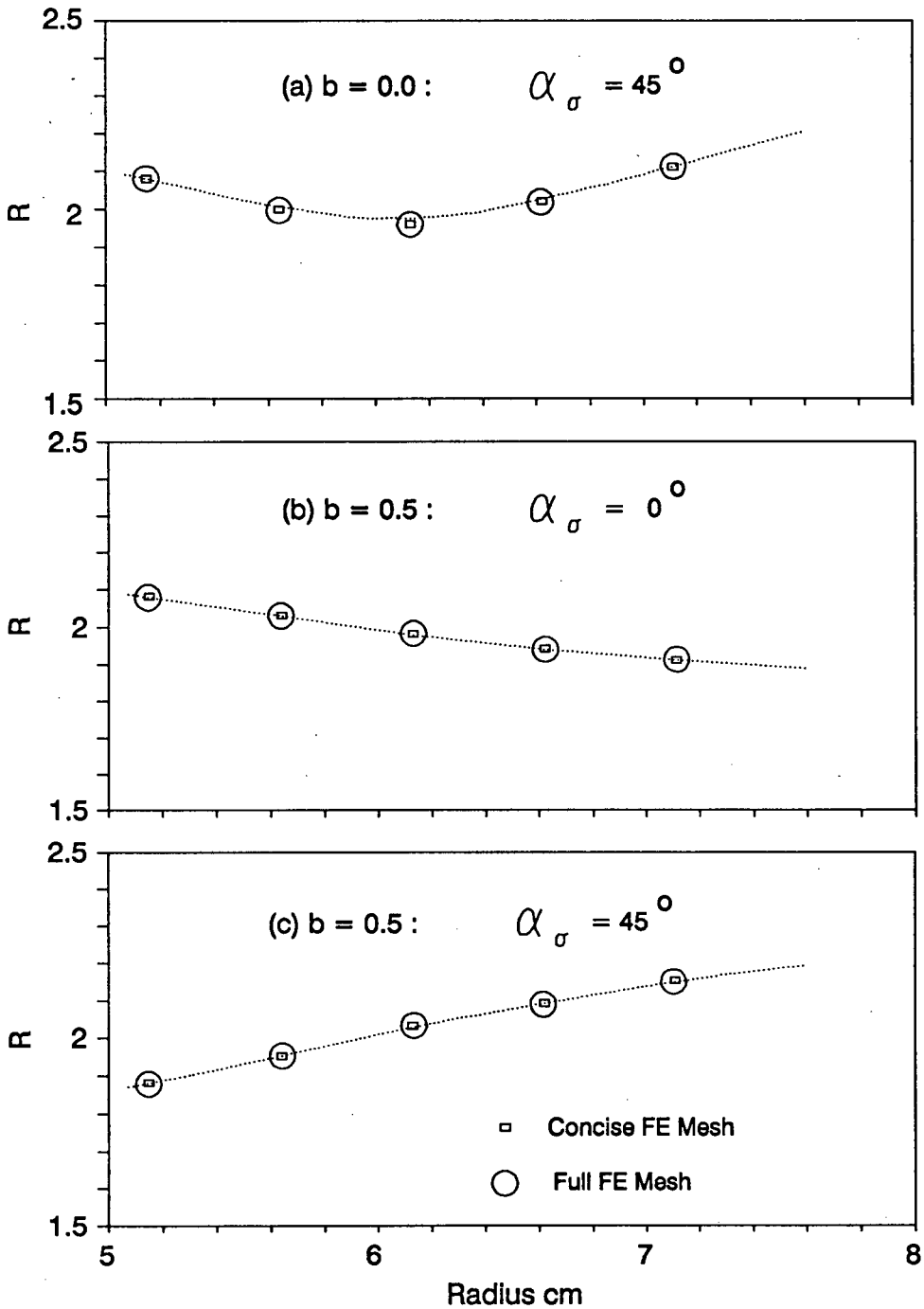

Figure 3.9: Comparison of stress distributions across the specimen wall from the full FE mesh versus concise FE mesh - Incremental elastic material

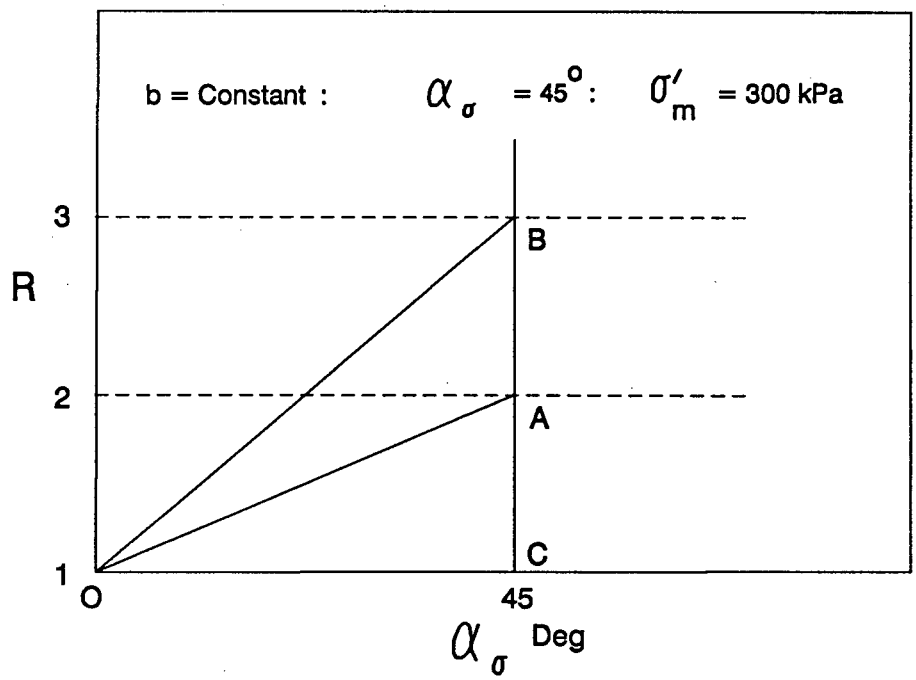

		Stress Path			
β_R	b	OA	CA	OB	CB
	0.0	0.077	0.078	0.066	0.091
	0.5	0.133	0.145	0.070	0.090
	1.0	0.060	0.052	0.032	0.029

Figure 3.10: Dependence of β_R on the stress path

state. β_R values along stress paths CA and CB are larger than those obtained along paths OA and OB respectively, for b values of 0.0 and 0.5. However for $b = 1.0$ the reverse is true. It is virtually impossible to assess β_R for every stress path to the target stress state. Based on the above limited path dependence study, only increasing R stress paths with all other stress parameters held constant (i.e. similar to CA and CB) were selected for a detailed exploration of stress non-uniformities in the (R, b, α_σ) stress space. Figure 3.11a illustrates one such path in the generalized stress space. Along all stress paths, for a given D_r the value of σ'_m was held constant while different combinations of b and α_σ were used for each stress path. Fig. 3.11b shows combinations of b and α_σ selected for the analysis.

The non-uniformity coefficients at different R values along R paths are computed and compared with those obtained assuming linear elastic isotropic material. The effect of mean normal stress on β_R is then assessed for loose sand at selected b, α_σ combinations. Finally, the influence of increasing relative density on β_R is examined for a limited combinations of σ'_m, b and α_σ.

3.4.1 Stress Non-uniformities in Loose Sand HCT Specimens

3.4.1.1 Comparison with Linear Elastic Material

Figure 3.12 compares the distribution of stress ratio R across the wall of the HCT specimen for the incrementally linear and linear elastic analyses. The comparisons are made at three arbitrarily selected stress states: (a) $\sigma'_m = 300$ kPa, $R = 2.0$, $b = 0.0$, $\alpha_\sigma = 45°$; (b) $\sigma'_m = 300$ kPa, $R = 2.0$, $b = 0.5$, $\alpha_\sigma = 0°$; and (c) $\sigma'_m = 300$ kPa, $R = 2.0$, $b = 0.5$, $\alpha_\sigma = 45°$. Similar comparisons made at a higher stress ratio $R = 3$ for otherwise identical σ'_m, b and α_σ conditions are shown in Fig. 3.13. It may be noted that for all stress states, linear elastic material shows large variations of stress

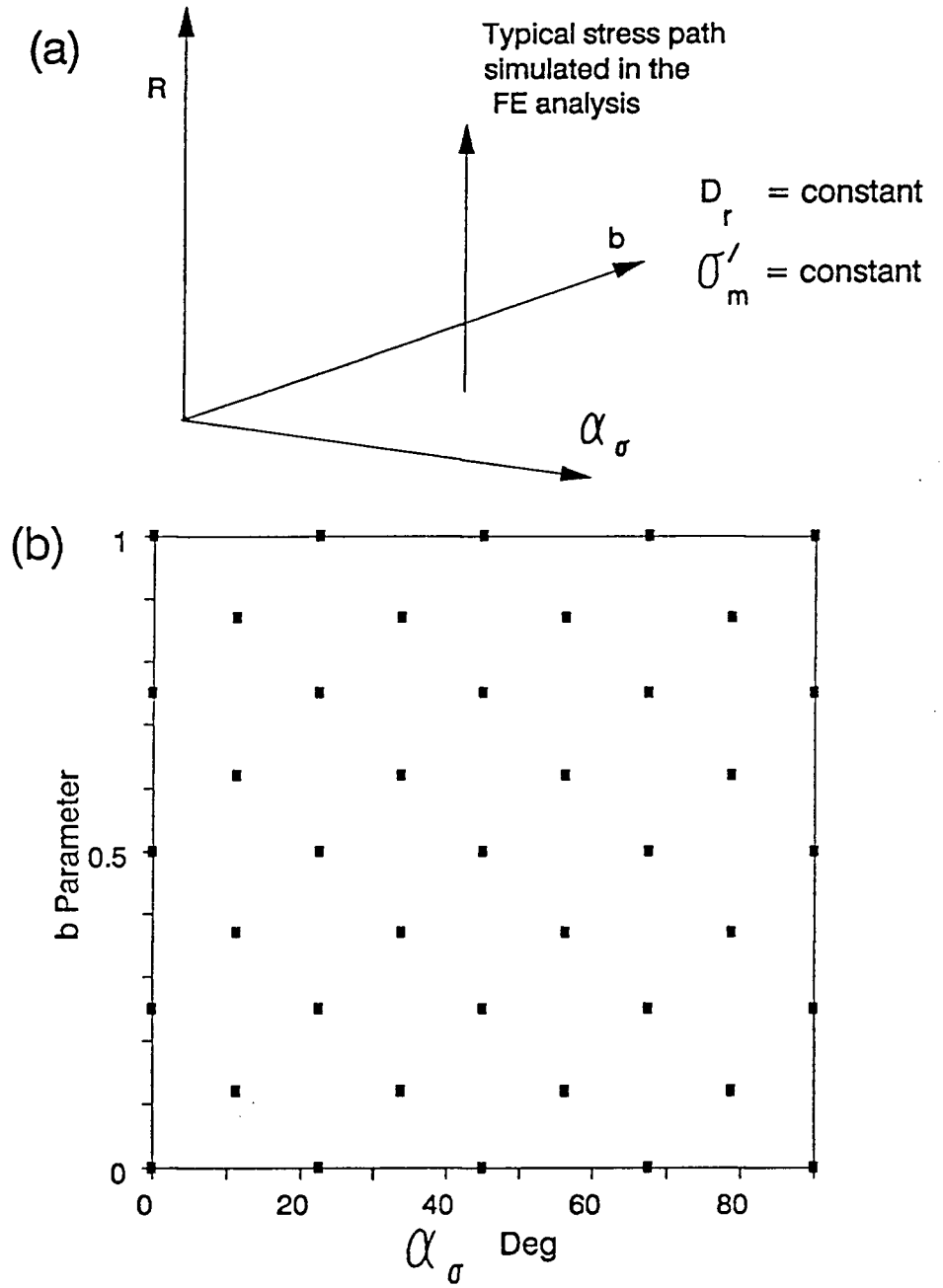

Figure 3.11: Stress paths used in the FE analysis

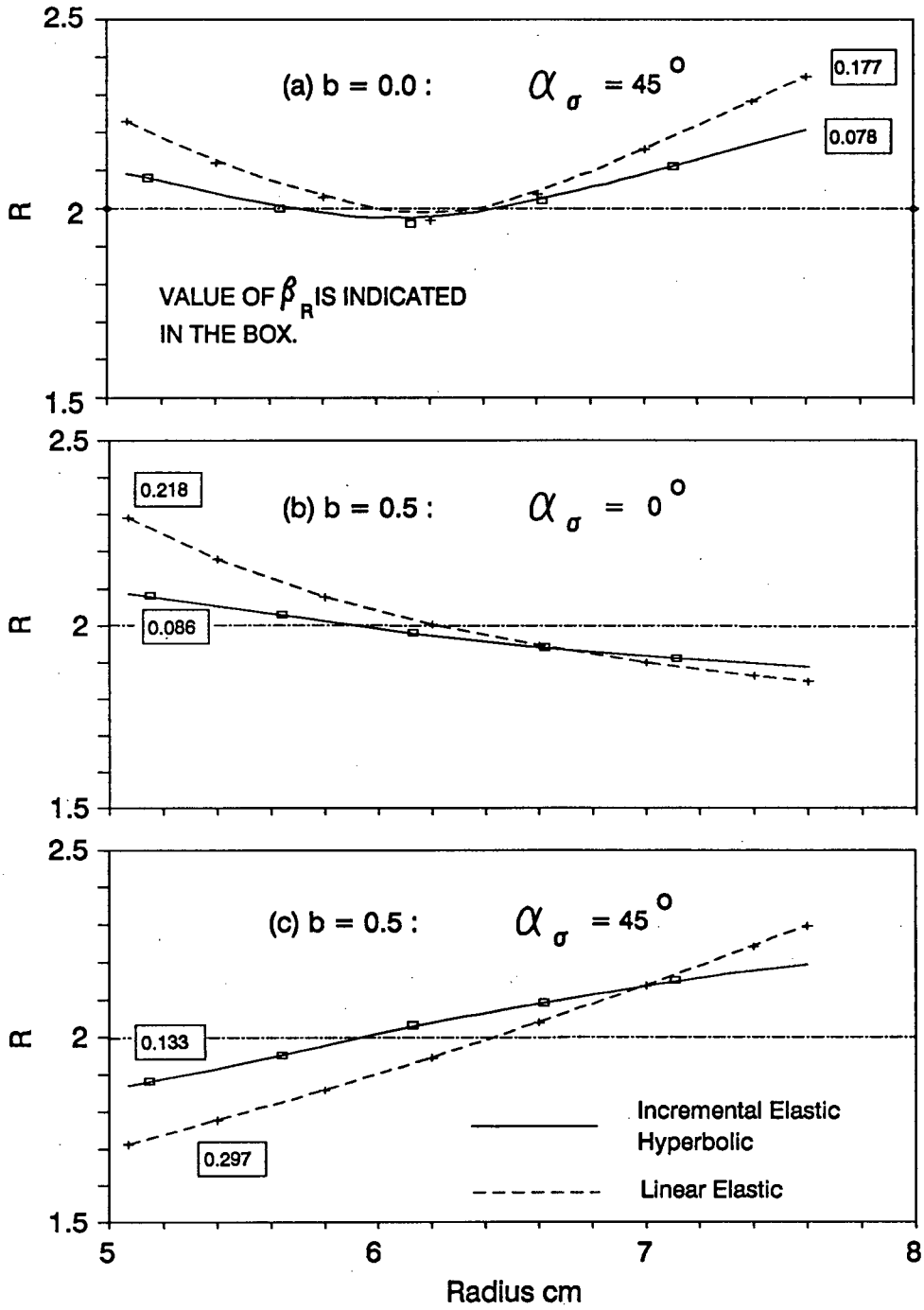

Figure 3.12: Distribution of stress ratio across the wall of the specimen with material behaviour: σ'_m = 300 kPa; R = 2.0; D_r = 30%

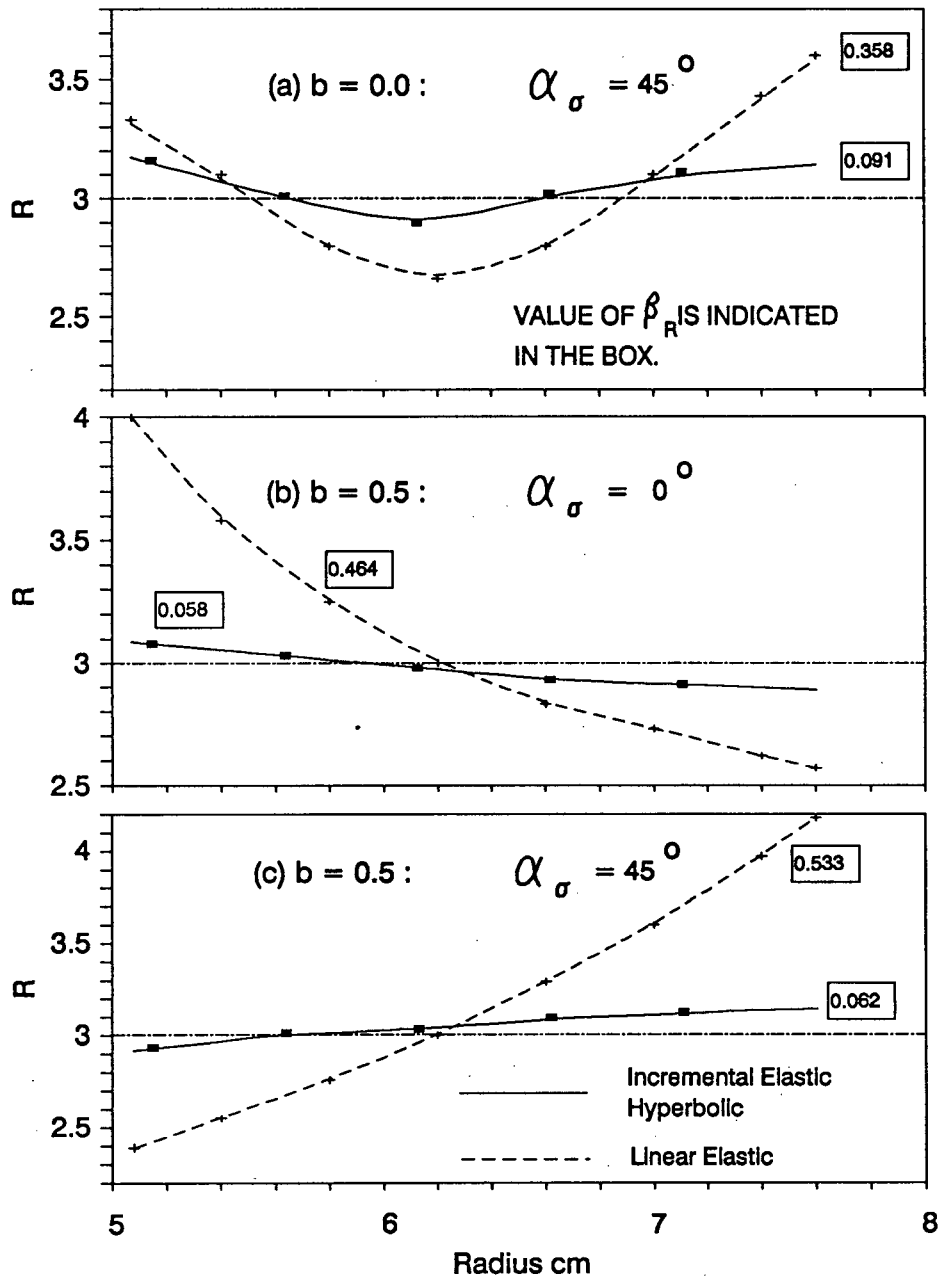

Figure 3.13: Distribution of stress ratio across the wall of the specimen with material behaviour: $\sigma'_m = 300$ kPa; $R = 3.0$; $D_r = 30\%$

ratio across the wall and thus higher β_R values when compared with those for the incremental elastic material. Figs. 3.12 and 3.13 also indicate that β_R[1] for a given (b, α_σ) condition increases with increase in R, for the linear elastic material. For the incremental elastic material on the other hand, β_R values show a much smaller increase, or even a decrease with increase in R for certain combinations of b and α_σ.

The stress non-uniformity coefficients β_R were evaluated in a similar manner at $R = 2$ and 3 for several values of α_σ, but for three selected values of b parameter 0.0, 0.5, and 1.0. The results shown in Fig. 3.14 reveal that for a given stress state, β_R estimated from linear elastic assumption are always higher than those based on incremental elastic assumption. For an increase in R from 2 to 3 for a given α_σ, β_R increases substantially in the case of linear elastic material. For the incremental elastic material on the other hand, β_R at $R = 3$ is less than that at $R = 2$, for most stress states.

In the incremental elastic material, large gradients of R would not exist, as the stresses across the wall of the specimen gradually redistribute as a result of modulus degradation associated with increasing R. In contrast, for the linear elastic material, the elastic moduli remain unaltered with stress level, and therefore no redistribution of stresses can occur resulting in much sharper gradients of R.

It may be argued that the soil is not accurately modelled by an incremental elastic hyperbolic stress strain law. Yet, it is a much superior approximation to the non-linear behaviour of real soils than the linear elastic assumption. The foregoing analyses show that the assessment of stress non-uniformities based on linear elasticity could lead to estimates of β_R which are larger than that actually present in a HCT sand specimen.

The results presented in Figs. 3.12 - 3.14 were restricted to selected combinations of b and α_σ. Figures 3.15 and 3.16 present the contours of β_R encompassing the

[1]Value of β_R is indicated inside the boxes in the figures.

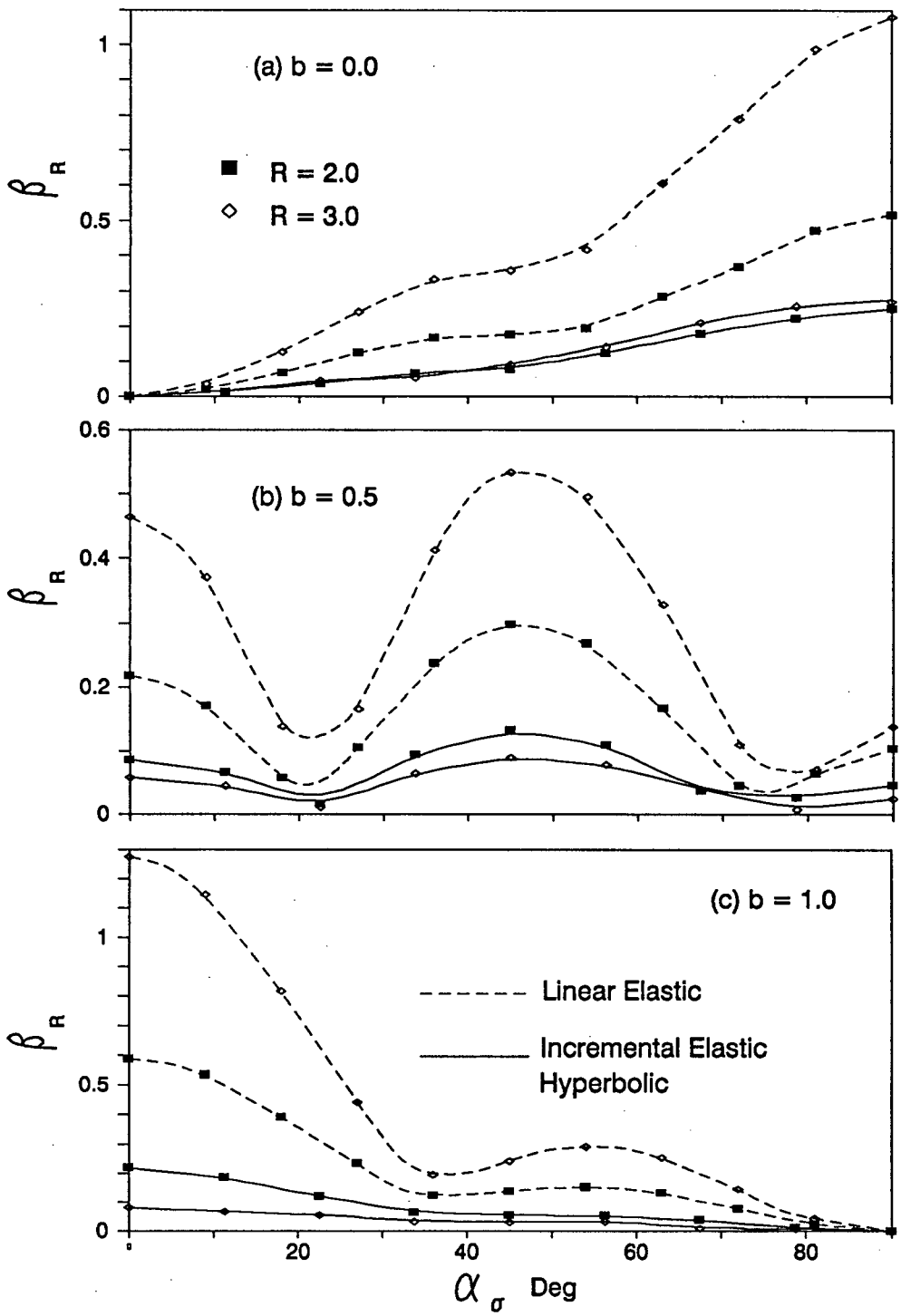

Figure 3.14: Variation of β_R vs R with material behaviour: σ'_m = 300 kPa: D_r = 30%

entire domain of b and α_σ for two R values. The contours for the incremental elastic material are drawn using results of β_R evaluated at several (b, α_σ) locations shown in Fig. 3.11b. The contours of β_R for linear elastic material are reproduced from Sayao (1989). It may be observed that for any stress state within the full domain of (b, α_σ), the linear elastic material law always overestimates the magnitude of β_R, when compared to that obtained using the incremental elastic material law.

Based on the linear elastic analysis, Sayao (1989) suggested that a β_R value less than 0.2 could be considered as an acceptable limit to delineate the domain of stress space that could be reliably explored using the HCT device. Considering the much smaller non-uniformities arising in incremetal elastic material, a much larger domain of the general stress space is available for exploration, even if the acceptable limit of non-uniformity level is restricted to a smaller value of 0.1. This is illustrated by the shaded domains of $\beta_R > 0.1$ and $\beta_R > 0.2$ in Figs. 3.15 and 3.16.

Although the magnitudes of β_R from linear elastic analysis are much larger than those obtained for the incremental elastic material, some similar trends in topographical features in β_R contours can be identified (Figs. 3.15 and 3.16). Excepting the vicinity of ($b = 1.0$, $\alpha_\sigma = 0°$) at $R = 3$ (Fig. 3.16b), the approximate locations of peaks and valleys of β_R in (b, α_σ) space tend to be similar regardless of the material behaviour or R level. It appears that a significant redistribution of stresses has occurred in the neighbourhood of ($b = 1.0$, $\alpha_\sigma = 0°$) at $R = 3$ in the incremental elastic sand (Fig. 3.16b) giving rise to exceptionally low β_R values, compared to those at lower $R = 2$ for the same material.

It has been pointed that stress non-uniformities across the wall of the HCT specimen are caused by the differential pressures across the wall ($P_e - P_i$) and the torque T_h applied to the specimen. In agreement with this, high β_R values would be expected in the vicinity of the corners ($b = 0.0 : \alpha_\sigma = 90°$) and ($b = 1.0 : \alpha_\sigma = 0°$) where the value of ($P_e - P_i$) is high and in the regions where T_h is high (i.e. in the

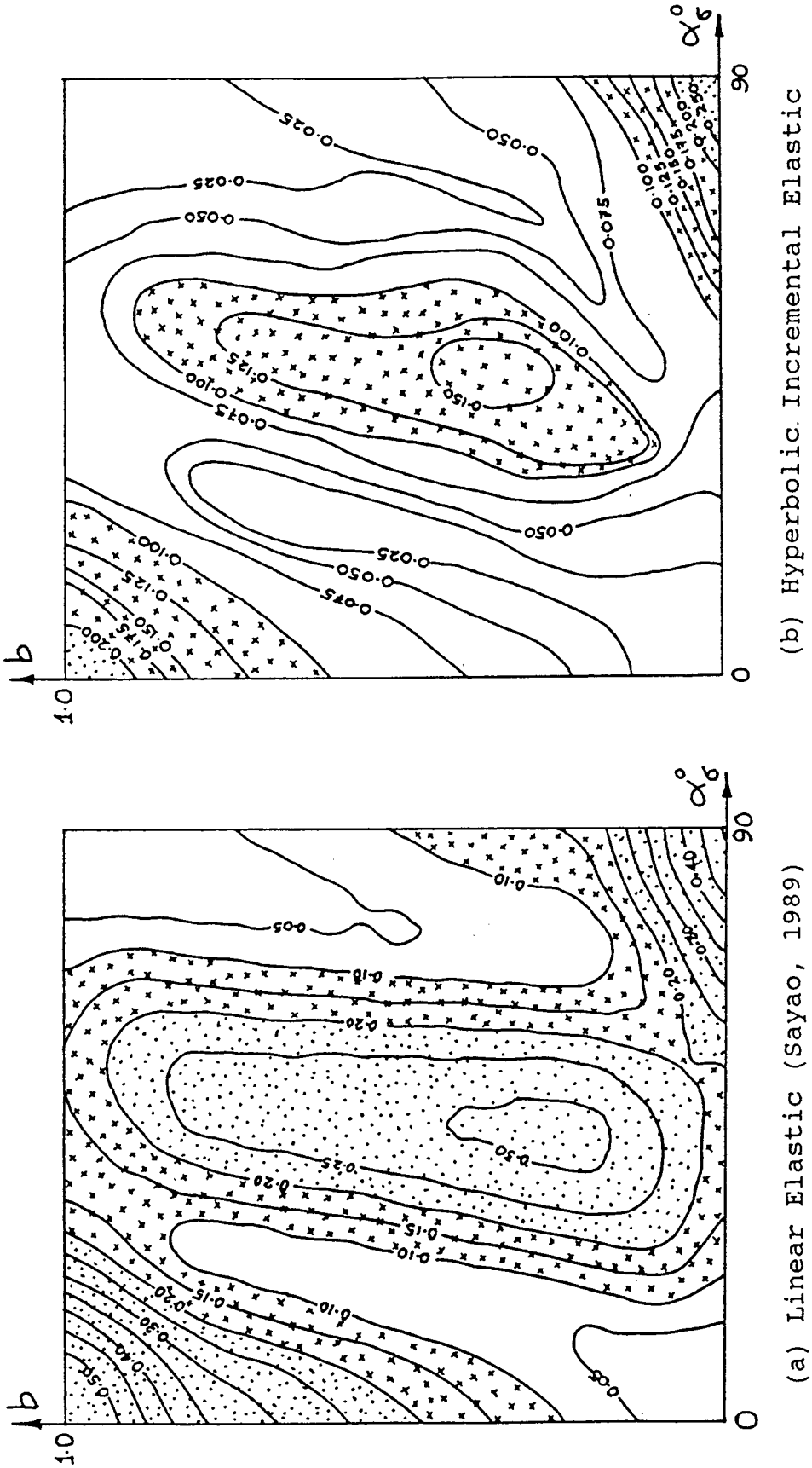

(a) Linear Elastic (Sayao, 1989)

(b) Hyperbolic Incremental Elastic

Figure 3.15: Contours of β_R at $R = 2$, $\sigma'_m = 300kPa$, $D_r = 30\%$

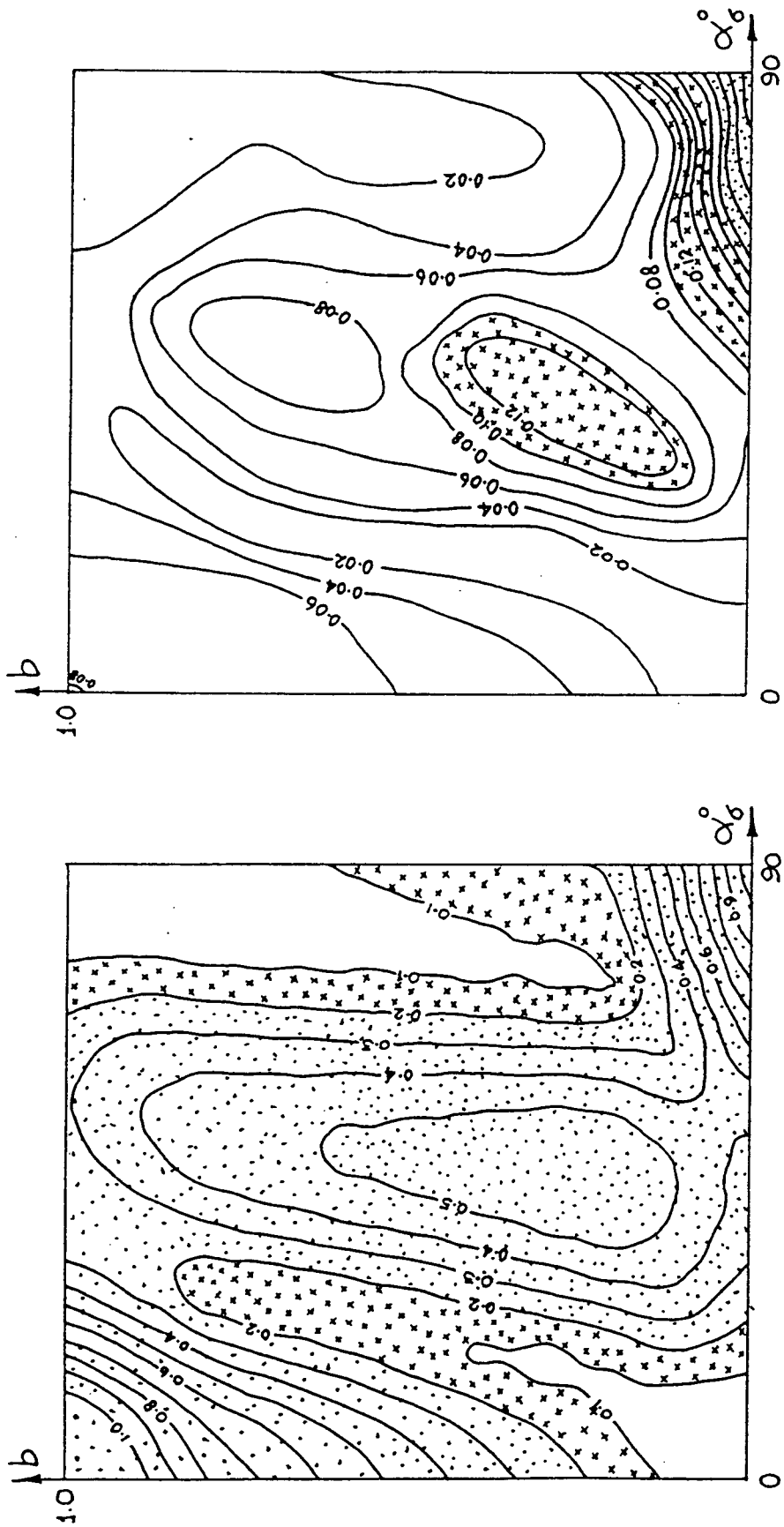

(a) Linear Elastic (Sayao, 1989)

(b) Hyperbolic Incremental Elastic

Figure 3.16: Contours of β_R at $R = 3$, $\sigma'_m = 300kPa$, $D_r = 30\%$

vicinity of $\alpha_\sigma = 45°$). On the other hand, β_R is low in the neighbourhood of the corners ($b = 0.0 : \alpha_\sigma = 0°$) and ($b = 1.0 : \alpha_\sigma = 90°$), where $(P_e - P_i)$ as well T_h have relatively low values.

It is also interesting to note that for some combinations of b and α_σ, β_R is low even when both differential pressure across the wall as well as the torque are applied (e.g. in the vicinity of $b = 0.5$ and $\alpha_\sigma = 25°$; $b = 0.5$ and $\alpha_\sigma = 70°$ etc. See Figs. 3.15 and 3.16). It appears that the effects of $(P_e - P_i)$ and T_h in inducing stress non-uniformities have acted in a compensating manner under these combinations of b and α_σ, thus giving rise to lower β_R values.

3.4.1.2 Influence of Stress Ratio

In the previous section, stress non-uniformity coefficients were shown only for two selected levels of stress ratio $R = 2$ and $R = 3$. The variation β_R with gradual increase in stress ratio for three selected values of b is plotted in Fig. 3.17. β_R is shown as a function of α_σ for several R levels at fixed $D_r = 30\%$ and $\sigma'_m = 300$ kPa. These results show that β_R increases with increasing stress ratio R at lower levels of R. However, with increase in R level, the rate of increase in β_R with R decreases, causing either β_R to reach a maximum or even decrease after reaching a peak value for certain combinations of b and α_σ. This feature becomes clearer in a plot of β_R vs R for selected combinations of b and α_σ, as shown in Fig. 3.18.

A gradually decreasing rate of change of β_R with respect to R can be explained by a gradual redistribution of stresses within the soil specimen as a result of modulus degradation in the non-linear elastic material. Such redistribution of stresses would not occur in a linear elastic material. This effect is further illustrated in Fig. 3.19 where β_R versus R for a linear elastic material is compared with that for the incremental elastic material, for the same stress conditions considered in Fig. 3.18.

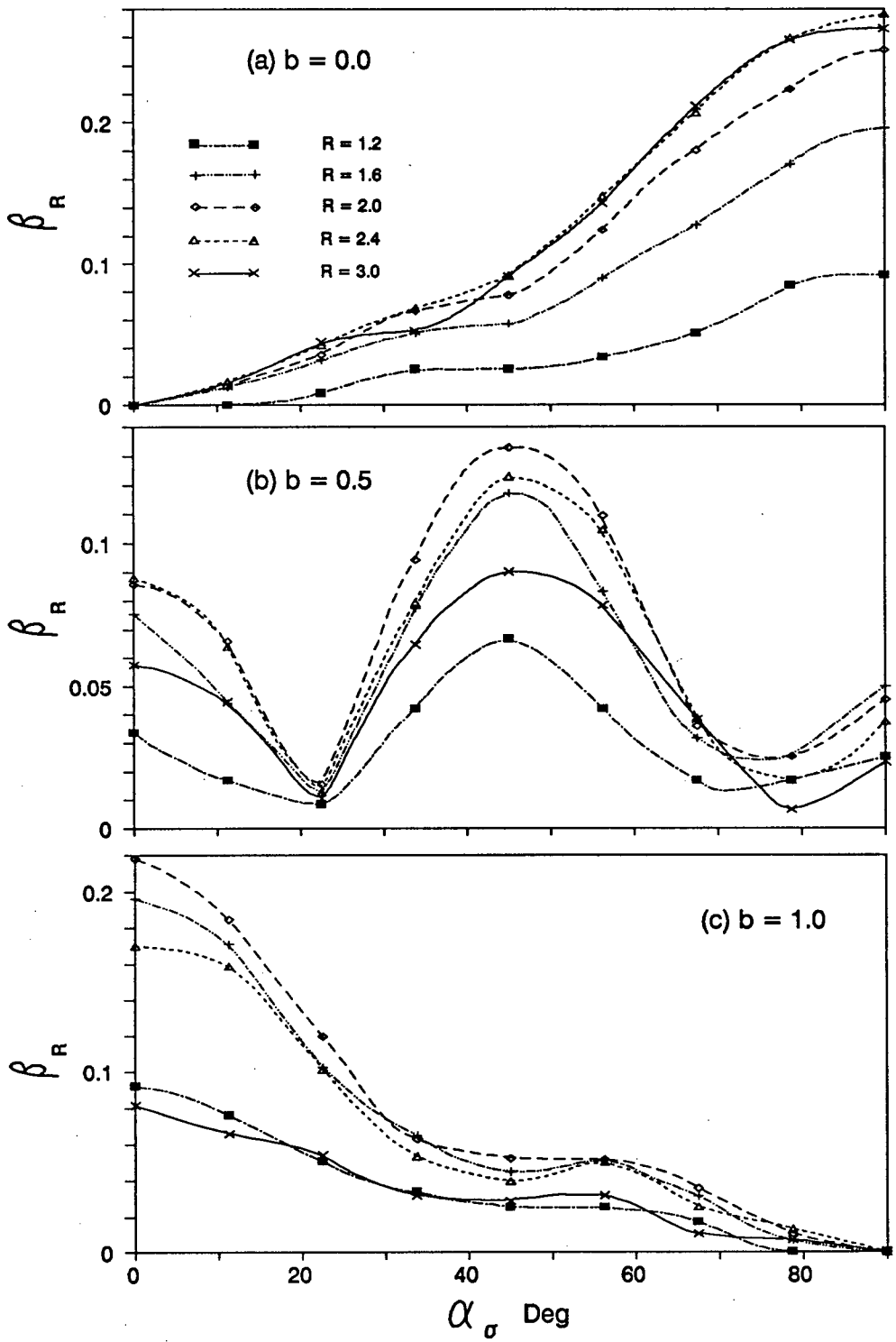

Figure 3.17: Effect of stress ratio on the non-uniformities: σ'_m = 300 kPa: D_r = 30%

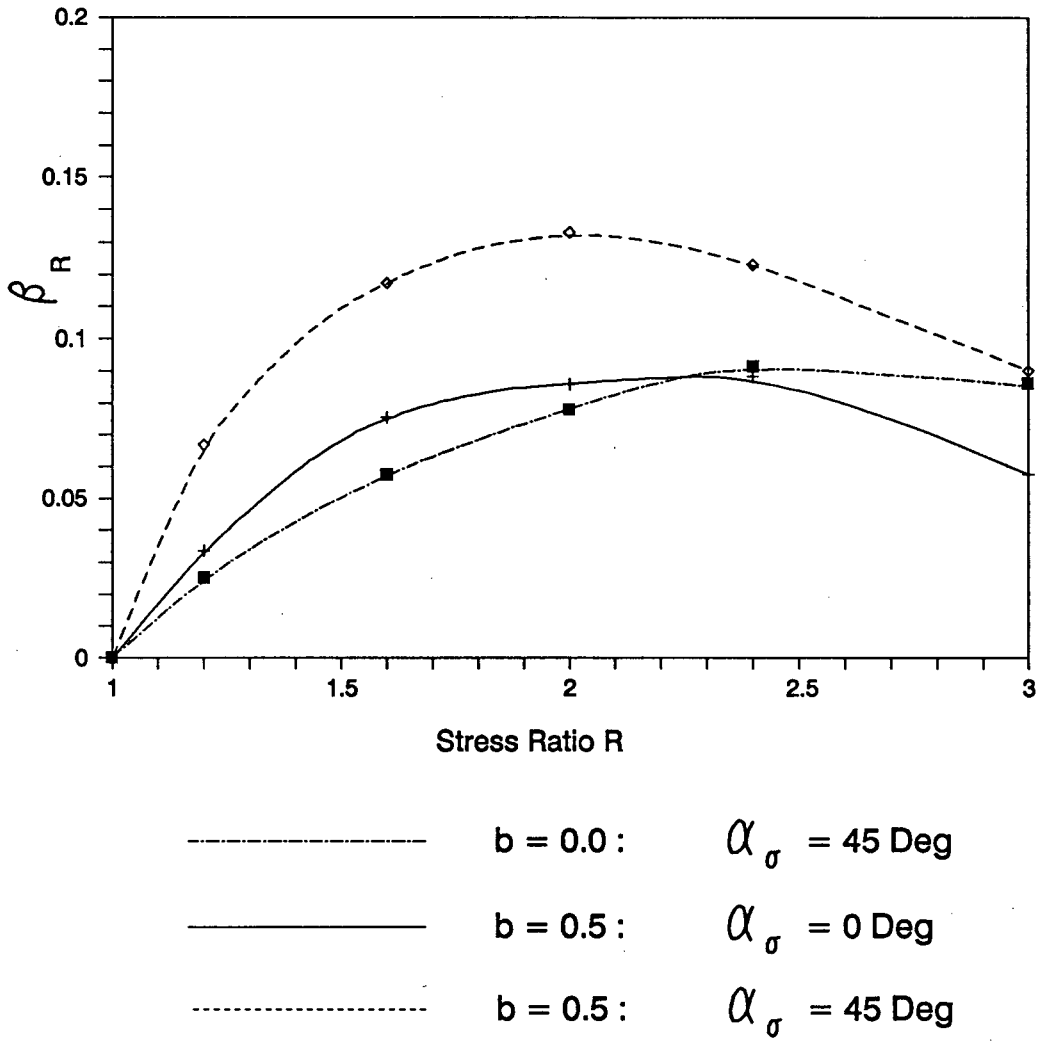

Figure 3.18: Variation of β_R with R: σ'_m = 300 kPa: D_r = 30%

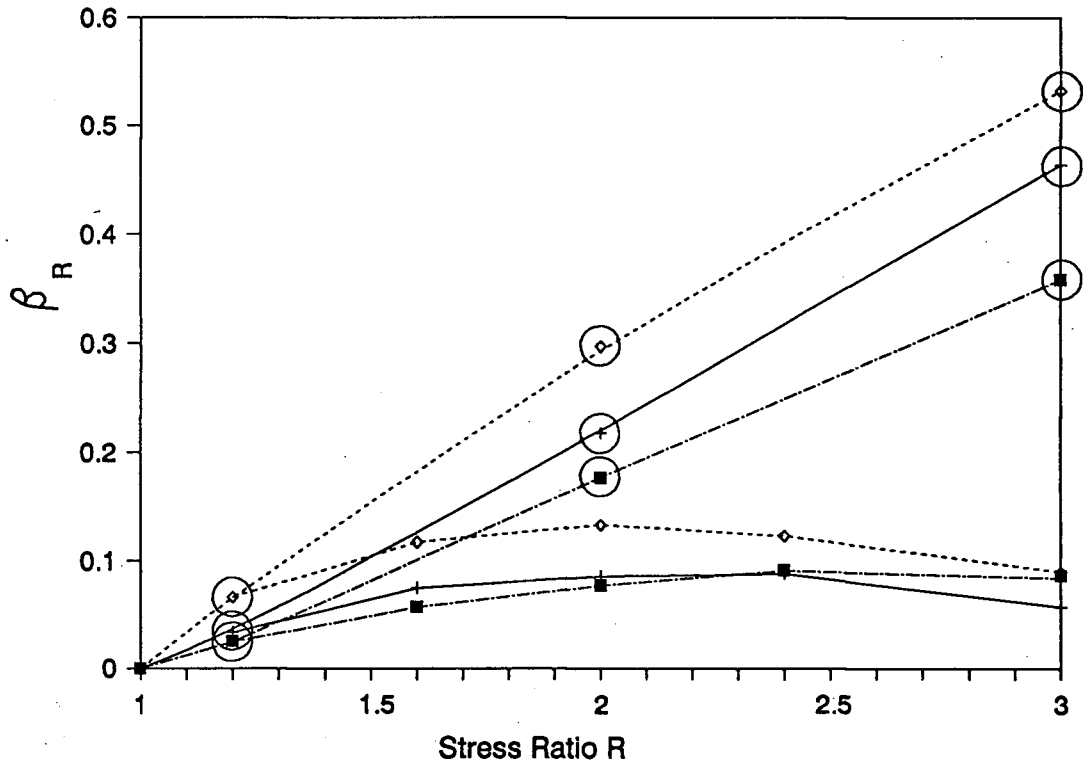

Figure 3.19: Variation of β_R vs R with material behaviour: σ'_m = 300 kPa: D_r = 30%

3.4.1.3 Influence of Mean Normal Stress

Figure 3.20 presents the effects of the level of mean normal effective stress σ'_m on β_R at $R = 2$ and 3, for the same combinations of b and α_σ considered in Fig. 3.19. (viz. $b = 0.0$, $\alpha_\sigma = 45°$; $b = 0.5$, $\alpha_\sigma = 0°$ and $b = 0.5$, $\alpha_\sigma = 45°$). The results show that the influence of σ'_m on stress non-uniformities is very little in the σ'_m range considered (i.e. from 100 kPa to 900 kPa). Therefore, it can be concluded that under moderate stress levels (that would usually be encountered under most field conditions) the effect of σ'_m on β_R is small.

3.4.2 Influence of Relative Density on Stress Non-Uniformities

For a given sand the hyperbolic parameters change with increasing density (see Table 3.1). An immediate consequence of increase in D_r is the increase in E_t, B_t and $(\sigma'_1 - \sigma'_3)_{ult}$ (see Equations 3.9 to 3.12). A limited number of FE analyses were carried out to study the effect of relative density on β_R.

Fig. 3.21 illustrates the effect of relative density D_r, on the variation of β_R with R for one arbitrarily selected stress state $\sigma'_m = 300$ kPa; $b = 0.5$ and $\alpha_\sigma = 45°$. It can be observed that excepting the region of low R, β_R increases with increasing density for a given R . This is because of the increasing stiffness E_t against deformation with increasing density. Consequently the degree of stress redistribution would be less in sand of higher D_r, thus resulting in higher β_R.

It is important to note in Fig. 3.21 that initially β_R increases with increasing R regardless of D_r. With continuing increase in R, the rate of change of β_R with respect to R decreases and β_R reaches a maximum after a certain value of stress ratio. The maximum of β_R occurs at a higher value of R for dense sands than for loose sand. It appears that the occurrence of the maximum of β_R depends more on the ratio of the mobilized stress ratio to the failure stress ratio than on the mobilized stress ratio itself. This is illustrated in Fig. 3.22 in which β_R is plotted against the mobilized

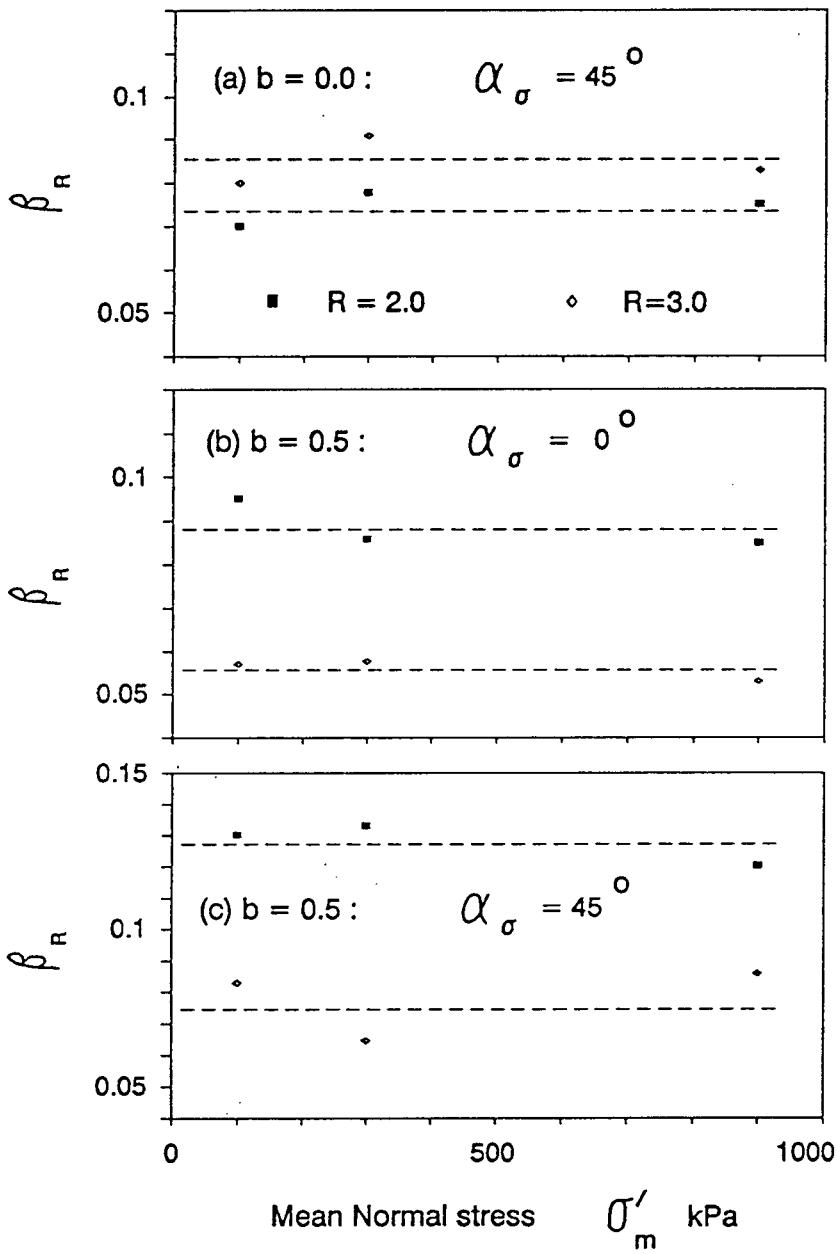

Figure 3.20: Effect of σ'_m on the value of β_R, D_r= 30 %

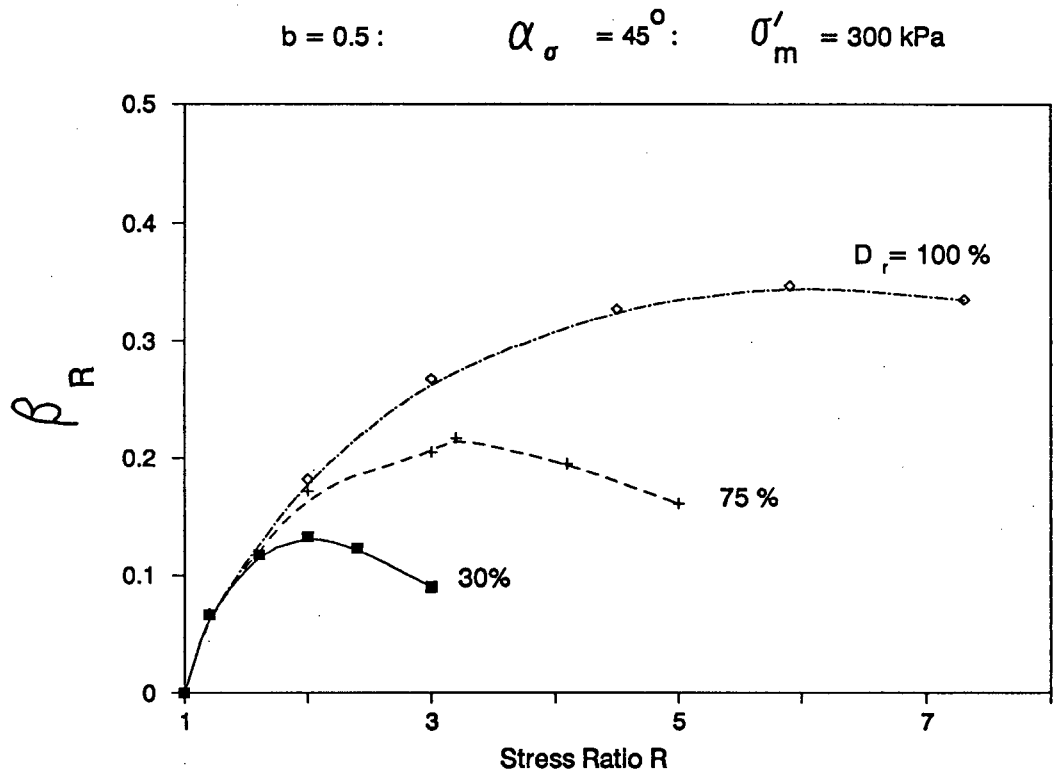

Figure 3.21: Effect of D_r on variation of β_R with R

friction ratio FR. FR is defined as,

$$FR = \frac{(R_{mob} - 1)}{(R_f - 1)} \tag{3.13}$$

where,

R_{mob} - Stress ratio mobilized

R_f - Stress ratio at failure

The Fig. 3.22 shows that peak value of β_R occurs around a FR value of about 60% regardless of density state.

Figure 3.23 shows a plot of β_R vs D_r for three selected stress states: (a) $\sigma'_m = 300$ kPa, $b = 0.0$, $\alpha_\sigma = 45°$; (b) $\sigma'_m = 300$ kPa, $b = 0.5$, $\alpha_\sigma = 0°$; and (c) $\sigma'_m = 300$ kPa, $b = 0.5$, $\alpha_\sigma = 45°$ at two levels of $R = 2$ and 3. β_R may be seen to increase with relative density at a faster rate at higher R value. It is also important to emphasize that for a given R the stress non-uniformities become increasingly large at higher relative densities, indicating a decrease in the size of the domain of stress space available for reliable exploration of generalized stress path behaviour.

The foregoing analyses reveal that for a given stress state, loose sand specimens will have lesser degree of stress non-uniformities across the wall than dense specimens. Therefore, interpretations of HCT test data on very dense specimens at higher stress ratios should be carried out with caution.

3.4.3 Additional Remarks on Stress Non-uniformities

The hyperbolic parameters to represent non-linear sand behaviour were selected based on suggestions by Byrne et al. (1987) for "average sands". Considerable variations in these parameters (especially k_E, k_B and ϕ) can occur depending upon the mineralogical composition, grain shape and gradation of sand. For example, at a given density and confining stress, a carbonate sand could have lower modulus of deformation E_i

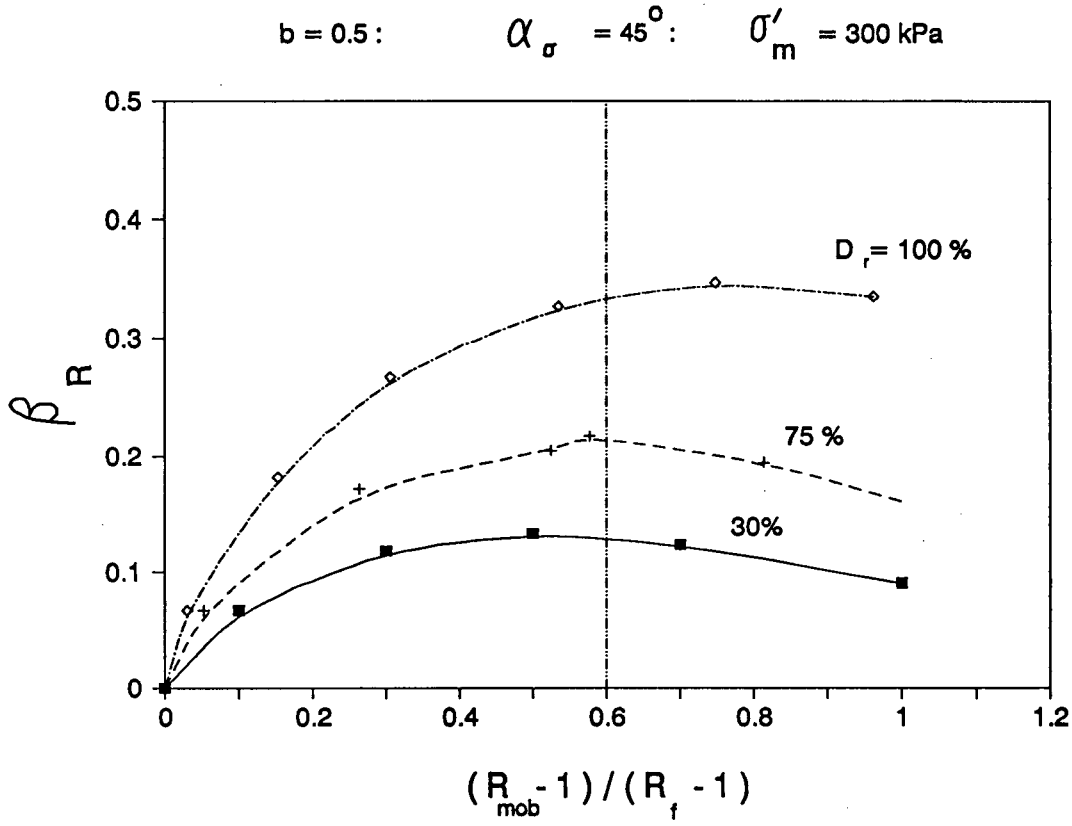

Figure 3.22: Variation of β_R with the mobilized friction ratio

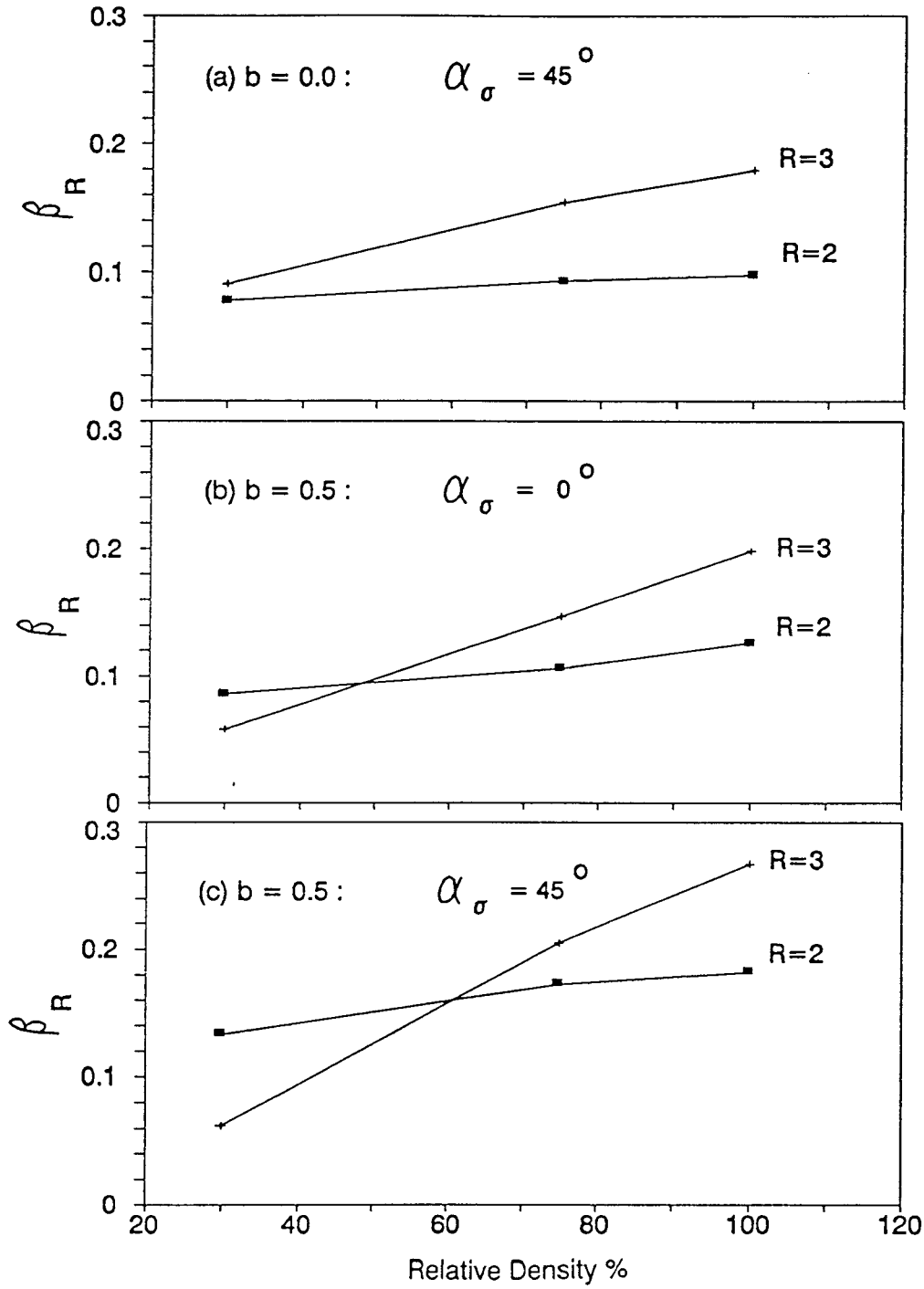

Figure 3.23: Variation of β_R vs D_r for different stress states

but friction angle still identical to that of an "average sand". It is important to assess stress non-uniformities that would arise in specimens of such "non-average" sand. It is clearly not practical to analyse stress non-uniformities for all possible combinations of soil parameters. Nevertheless, some appreciation of β_R changes with different hyperbolic parameters can be inferred from the results already presented.

It has been established that the linear elastic material assumption yields higher β_R at a given stress state when compared to an incremental elastic material assumption. The stress strain behaviour of these two materials can be schematically illustrated by curves A and B in Fig. 3.24. It is clear from this figure that the sole contributing factor in reducing β_R in the incremental elastic material is the degrading modulus of deformation with increasing shear stress. The stress strain curve C in Fig. 3.24 depicts a material having a smaller initial modulus E_i but other hyperbolic parameters identical to curve B. The main difference between curves B and C is that the material represented by curve C will always have lower tangent modulus than that for curve B at a given value of shear stress (or R). Using the already established β_R differences in material representations by curves A and B, it can be inferred that the stress non-uniformities would be smaller in the material having lower initial modulus E_i (e.g. curve C). In other words a softer material will give rise to lesser non-uniformities than a stiffer material.

3.5 Estimation of Average Stresses

In order to interpret test data or to conduct a stress path test in the HCT device, it is necessary to establish a one to one correspondence between the set of surface tractions P_e, P_i, F_z and T_h and the induced average stress components σ_z, σ_r, σ_θ and $\tau_{z\theta}$. The soil is usually assumed to be linear elastic, both for computation of average stresses from the surface tractions or computation of target surface tractions in order to reach the target average stress state. It is important to assess whether this method

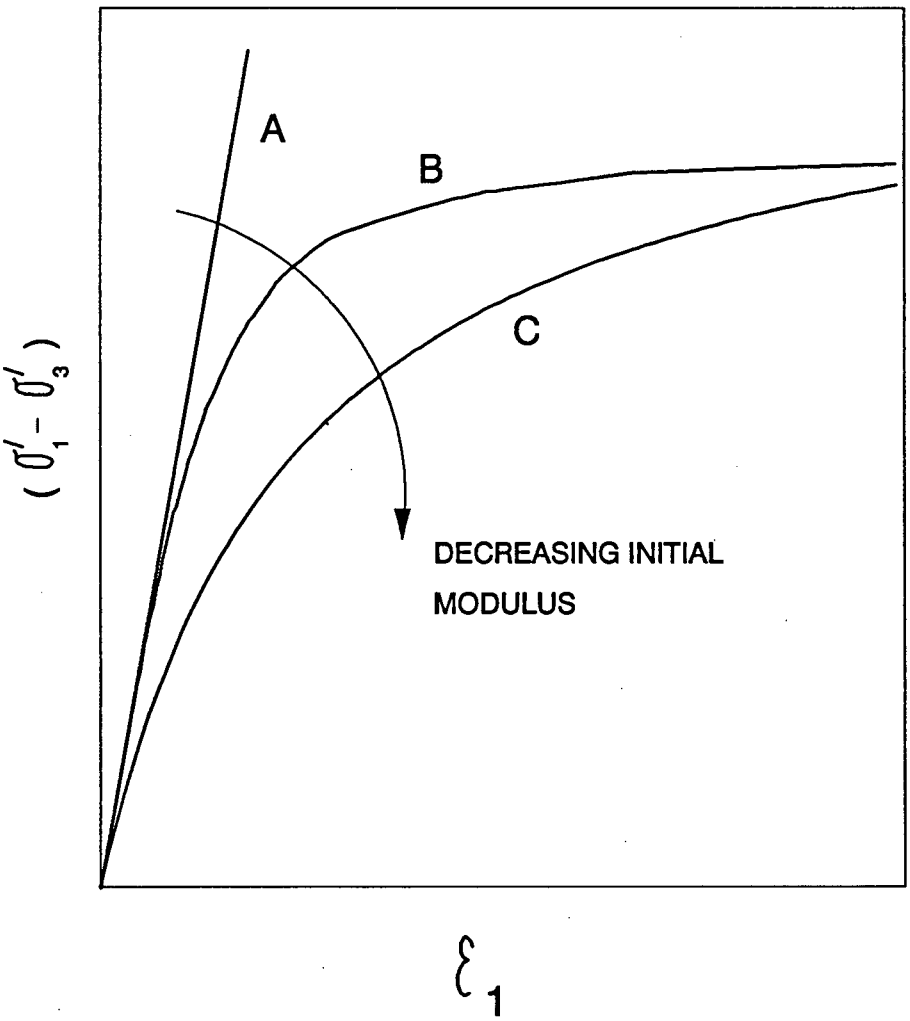

Figure 3.24: Stress strain relations under different initial modulus

of computation is justified considering that the sand behaviour is in fact non-linear.

Comparisons of stress components at identical surface tractions using linear elastic and incremental elastic hyperbolic material approximations, for three selected stress states are presented in Table 3.2. In spite of the differences in stress non-uniformities across the wall, the average values of stresses may be seen to agree remarkably well. This aspect is further examined in Fig. 3.25 by comparing the average stress ratios at several stress states.

The results illustrate that the computed average R values based on hyperbolic incremental elastic behaviour closely agree with those obtained from linear elastic analysis. Thus for a given set of surface tractions, the computed average stresses bear little sensitivity to the material stress strain law, even though the stress distribution is dependent on the material constitutive law. The use of elastic assumption is thus justified for computing average stresses from the applied surface tractions and vice versa.

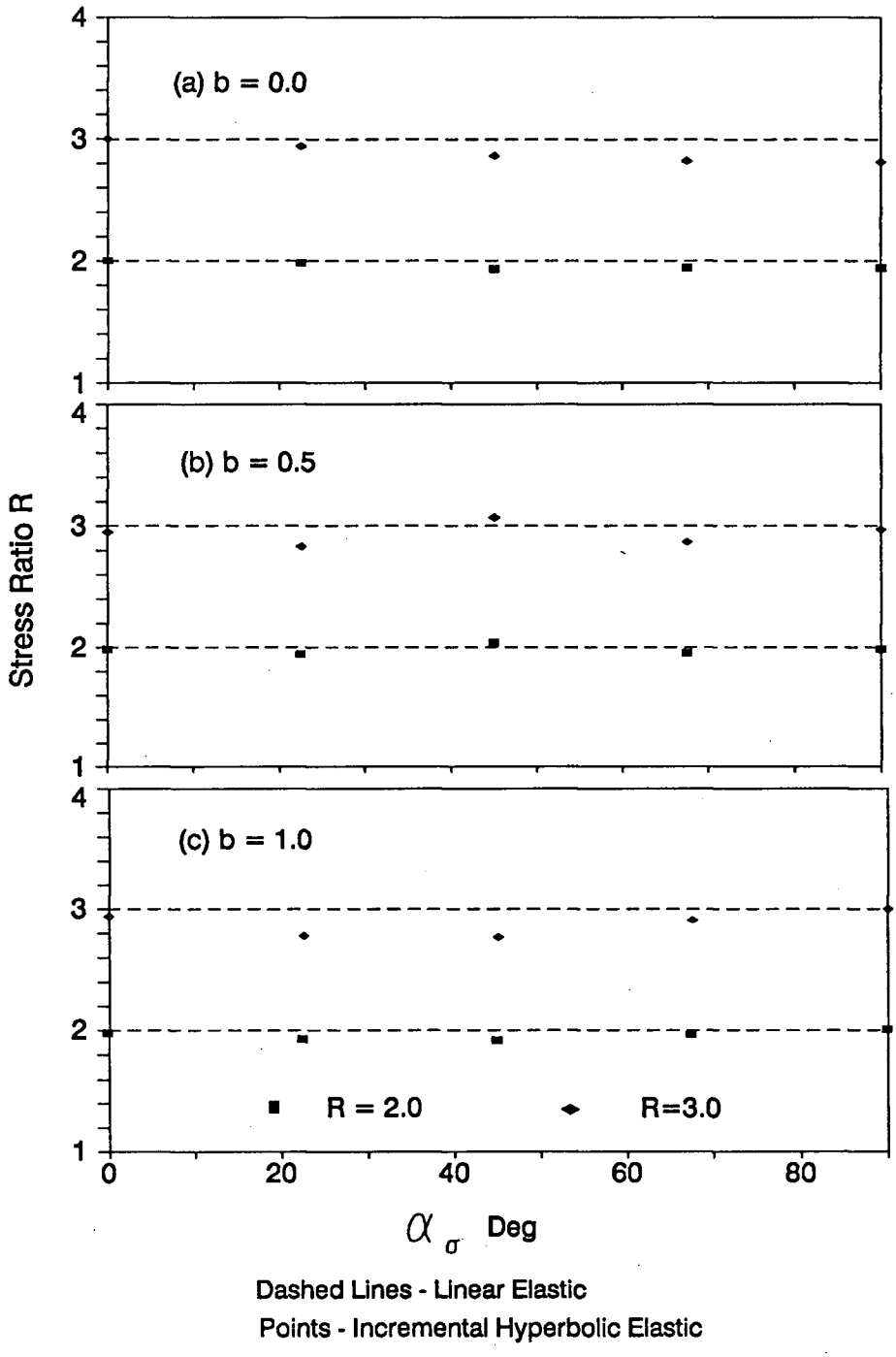

Figure 3.25: Comparison of average stress ratios from incremental vs linear elastic analysis $D_r = 30\%$, $\sigma'_m = 300$ kPa

Table 3.2: Comparison of average stresses

Stress kPa	σ'_m = 300 kPa : R = 2.0: D_r = 30%					
	b = 0.0 : $\alpha_\sigma = 45°$		b = 0.5 : $\alpha_\sigma = 0°$		b = 0.5 : $\alpha_\sigma = 45°$	
	L. Elas.	Inc. Elas.	L. Elas.	Inc. Elas.	L. Elas.	Inc. Elas.
σ_z	337.5	337.4	400.0	400.2	300.0	300.0
σ_r	225.0	228.1	300.0	297.9	300.0	300.0
σ_θ	337.5	335.1	200.0	202.1	300.0	300.0
$\tau_{z\theta}$	112.5	109.5	000.0	000.0	100.0	101.5
σ'_1	450.0	445.2	400.0	400.2	400.0	401.5
σ'_3	225.0	227.2	200.0	202.1	200.0	198.5
R	2.00	1.96	2.00	1.98	2.00	2.02

Chapter 4

UBC Hollow Cylinder Torsional Device and Experimental Aspects

A detailed description of the UBC hollow cylinder torsional (HCT) device has been given by Vaid et al. (1990). Therefore only important features of the apparatus and steps in specimen preparation will be briefly outlined. In order to carry out general stress path tests, a new, fully automated control system was developed. The design considerations, stress path control, and performance of the new system are presented in detail in this chapter.

4.1 The UBC Hollow Cylinder Torsional Apparatus (UBC-HCT)

4.1.1 General Description

The UBC-HCT apparatus is capable of subjecting a hollow cylindrical specimen of soil to an axial load, torque about the vertical axis, and different internal and external pressures. Independent control of these surface tractions enables the specimen to be loaded along a prescribed stress path in the four dimensional stress space (R, σ'_m, b, α_σ). The domain of this stress space that could be explored by the apparatus without introducing serious stress non-uniformities has been discussed in the previous chapter.

A schematic diagram of the UBC-HCT is given in Fig. 4.1. Important details are enlarged and presented in Fig. 4.2. The hollow cylinder specimen is 15.2 cm

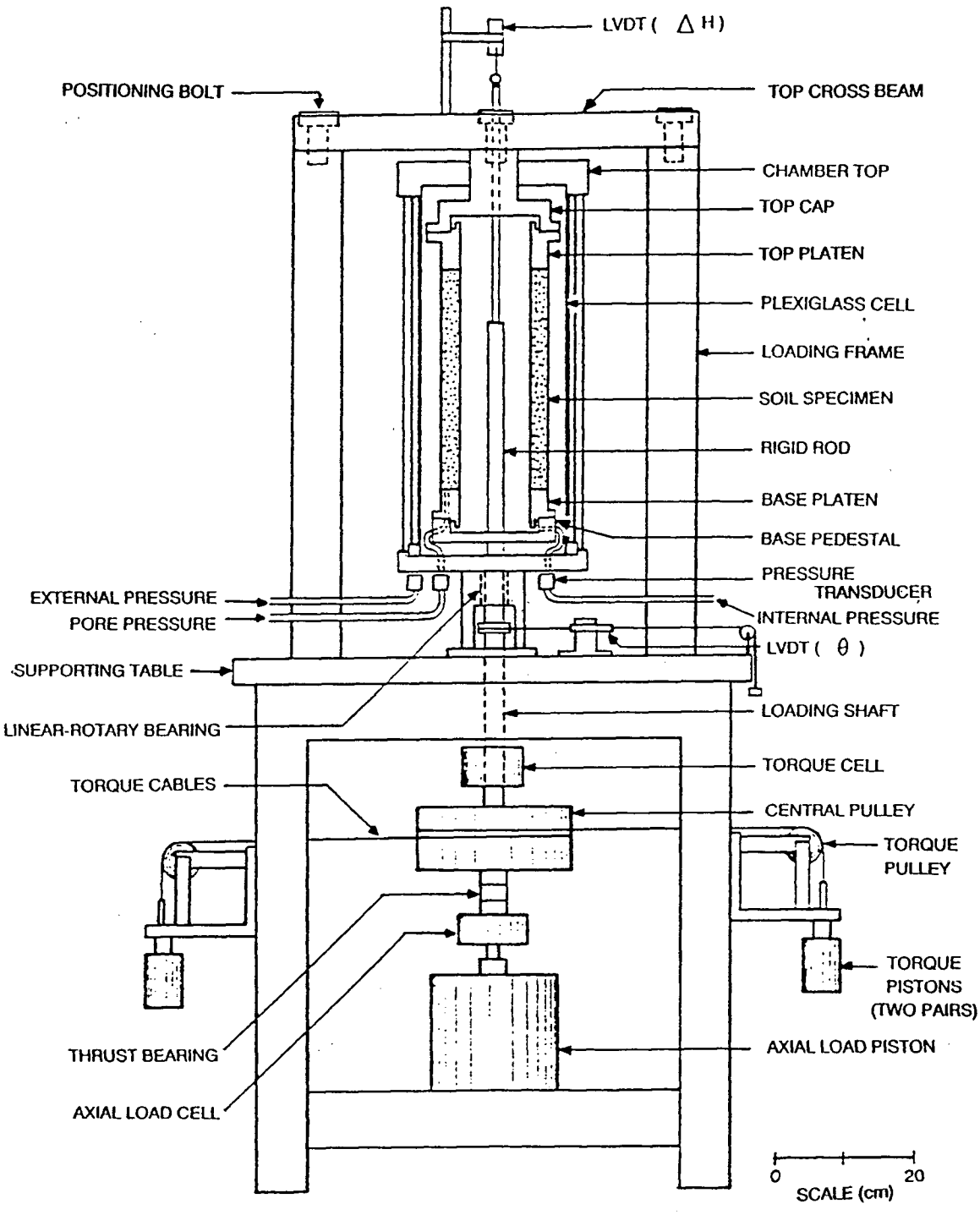

Figure 4.1: Schematic of the UBC-HCT device - after Sayao (1989)

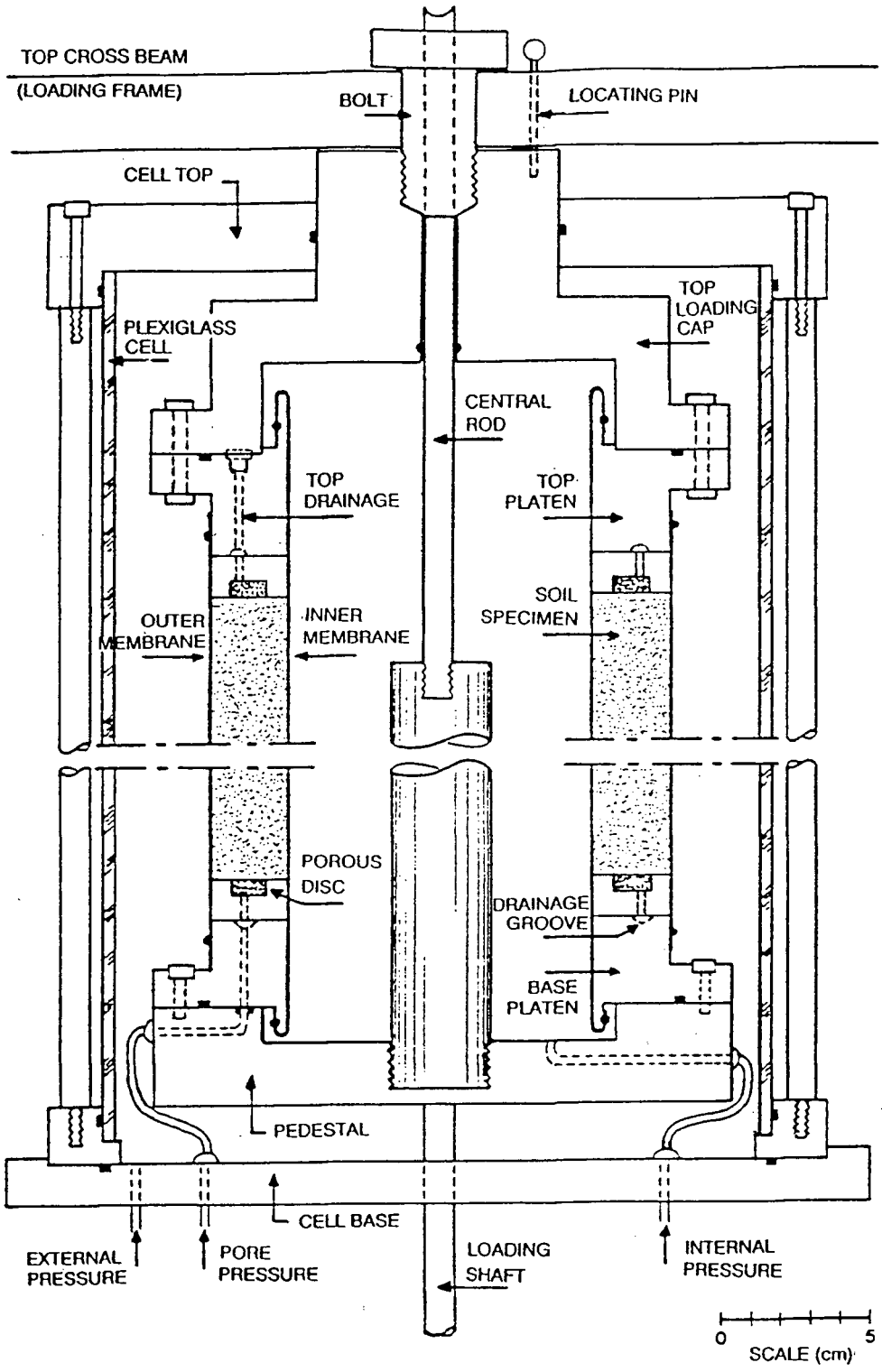

Figure 4.2: Details of the UBC-HCT device - after Sayao (1989)

(6 in) external diameter, 10.2 cm (4 in) internal diameter, and 30.0 ± 0.2 cm long. Considerations involved in the selection of specimen dimensions are described in detail by Sayao (1989).

The test specimen is laterally confined by internal and external water pressures acting on flexible rubber membranes, 0.3 mm thick. The transfer of torsional shear stresses to the specimen end requires that no slip occur between the end platens and the soil, in the circumferential direction. At the same time minimization of end restraint calls for no restraint to deformation in the radial direction. Both these requirements were achieved by using polished anodized aluminum end platens having twelve thin radial ribs (1 mm thick and 2.3 mm deep) machined as an integral part of the platens (Fig. 4.3). The radial ribs prevent the circumferential slip and polished anodized surface provide the low friction condition in the radial direction. Drainage of the specimen is achieved through six 12.5 mm porous discs set 60° apart, flush with each platen surface (Fig. 4.3).

The specimen is fixed at the top. The vertical load is applied at the bottom by means of a double acting air piston. By varying the air pressure on one side of this piston against a fixed back pressure on the other side, a given vertical compressional or extensional load can be applied. In a similar manner torque is applied at the bottom of the specimen by two pairs of identical single acting air pistons and a system of pulleys and cables. A dual thrust bearing isolates the rotary movement of the sample from being transmitted to the bottom vertical loading piston.

4.1.2 Instrumentation of the HCT Device

A choice had to be made between external versus internal measurement of loads and displacements. Both external and internal instrumentation have their own merits and disadvantages. Previous experience at UBC has shown that external measurement of

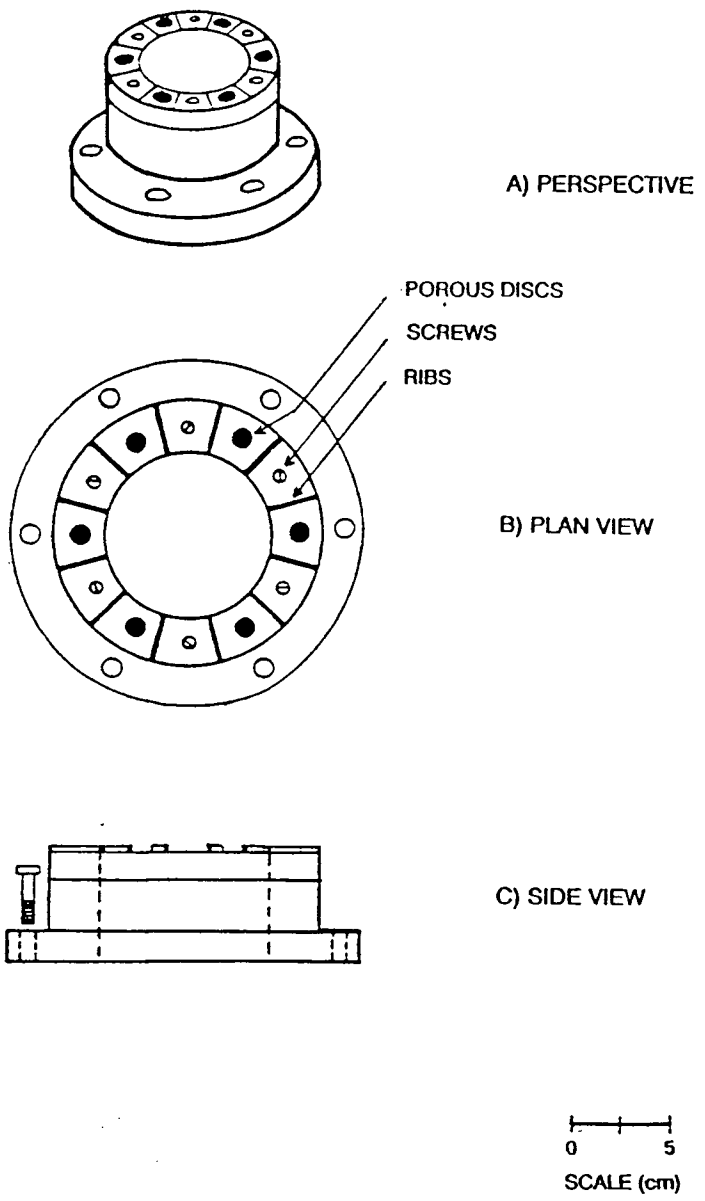

Figure 4.3: Polished end platen with radial ribs - after Sayao (1989)

strains can give very reliable results, provided proper care is taken to eliminate bedding and tilting errors (Negussey, 1984). On the other hand, internal instrumentation gives rise to additional difficulties in terms of specimen preparation and testing procedures etc. Sayao (1989) made a detailed review of these two measuring techniques, and based on that analysis, an external instrumentation system was adopted for the UBC-HCT device.

4.1.2.1 Measurement of Deformations

A minimum of four strain components are needed to describe the complete configuration of the HCT specimen at any given instant. This is achieved by monitoring the vertical and angular displacements of the specimen's base platen, volume change of the specimen, and the volume change of the inner chamber.

The displacement measurements are made with the use of linear variable displacement transducers (LVDT) in order to track the vertical and circumferential movements. The LVDT mounted on the loading frame's top cross beam (Fig. 4.1) measures the height change of the specimen and thus the axial strain ε_z. The rotation of the base platen is converted into linear tangential displacement by using the system shown in Fig. 4.4. This LVDT reading is used to obtain the circumferential shear strain $\gamma_{z\theta}$. Locations of the LVDT's are chosen so as to minimize the compliance errors in the axial LVDT and the cross talk effects in the circumferential LVDT due to axial straining of the specimen. Both LVDT's can reliably detect movements in the order of 1 μm. This results in a resolution of about $5 \times 10^{-4}\%$ in both ε_z and $\gamma_{z\theta}$.

The volume changes of the inner chamber and the soil specimen are obtained by measuring the height of displaced water in graduated pipettes together with sensitive differential pressure transducers (DPT). Measured volume changes are corrected to account the effects of membrane penetration as proposed by Vaid and Negussey (1984a).

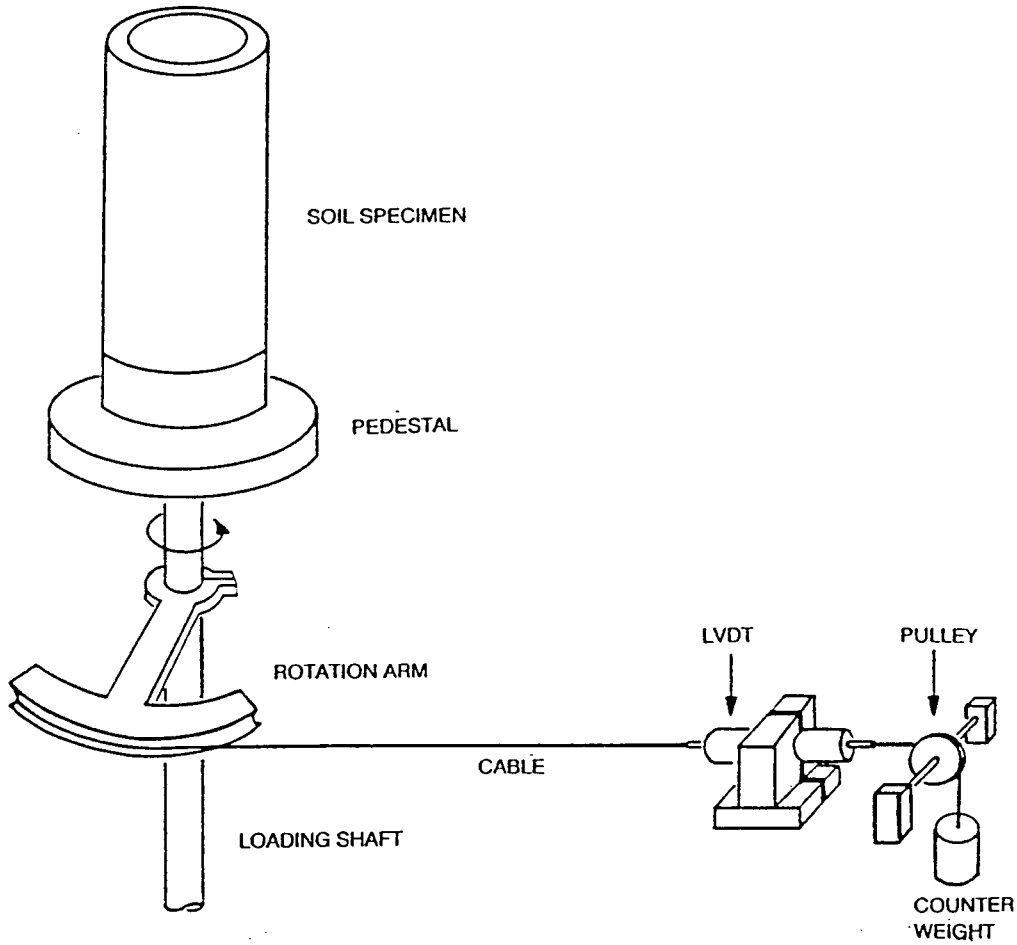

Figure 4.4: Rotational displacement measuring system - after Sayao (1989)

The correction procedure and the magnitude of correction for the test sand are detailed in Appendix B.

For all tests a back pressure of 200 kPa was used to ensure a fully saturated condition. Two pipettes of 5.4 mm inner diameter placed in parallel are used to measure the specimen volume change. When small volume changes occur, only one pipette of this dual system is employed in order to enhance the measurement resolution. The DPT can reliably detect volume changes in the order of 3 mm^3 thus resulting in a resolution of about $5 \times 10^{-4}\%$ in volumetric strain ε_v after correcting for membrane penetration effects.

The volume change of the inner chamber of the HCT apparatus is measured using a single pipette of 7.9 mm inner diameter. The DPT for the inner chamber could thus reliably detect volumetric variations in the order of 10 mm^3 which equals $2 \times 10^{-4}\%$ of the total volume of the inner chamber.

4.1.2.2 Measurement of Surface Tractions

The stress components at a given instant are calculated from the values of four surface tractions applied on the HCT specimen. The four surface tractions consist of vertical load, axial torque, and internal and external chamber pressures.

The pore water pressure and the chamber pressures are monitored using sensitive pressure transducers having a resolution in the order of 0.25 kPa. The vertical load is measured using a force transducer capable of detecting load changes in the order of 230 grams. The resulting resolution in the vertical stress σ_z is about 0.22 kPa. Axial torque measurements are made with a torque transducer possessing a very low cross talk. This transducer can measure torques as low as 0.05 Nm corresponding to a resolution in measurement of shear stress $\tau_{z\theta}$ in the order of 0.1 kPa.

4.2 Stress Path Control and Data Acquisition

In the UBC-HCT apparatus described by Sayao (1989), data acquisition was achieved through a multi-channel scanner and an A/D converter communicating with a personal computer. During a generalized stress path test, the control of the four surface tractions was achieved by manual adjustment of the compressed air pressure regulators. Simultaneous and independent control of these four surface tractions is essential when loading the specimen along complex stress paths. In order to follow a prescribed stress path, smooth changes of surface tractions are needed. These requirements render manual control of surface tractions a time consuming and extremely cumbersome task.

In the case of drained tests, the surface tractions must be applied slow enough to avoid any localized undrained conditions occurring in the specimen. Moreover, subsequent to any applied load increment, sufficient time should be allowed for the specimen to achieve deformation equilibrium. Mejia et al. (1988) observed that creep deformations in sand become increasingly significant at higher stress ratios. As such, more time would be required for deformation equilibrium to be reached at higher R values. The recording of data and the application of the next load increment should be made only after such equilibrium state is reached. Again, manual control of surface tractions possess serious limitations in the achievement of these objectives.

To meet the above requirements a program was undertaken to design a new integrated stress path control and data acquisition system.

4.2.1 Basic Components of the Control System

A schematic layout of the stress path control system is shown in Fig. 4.5. The system consists of four motor set (stepper motor) precision regulators that control surface tractions. Nine transducers monitor various loads, pressures, and deformations (as

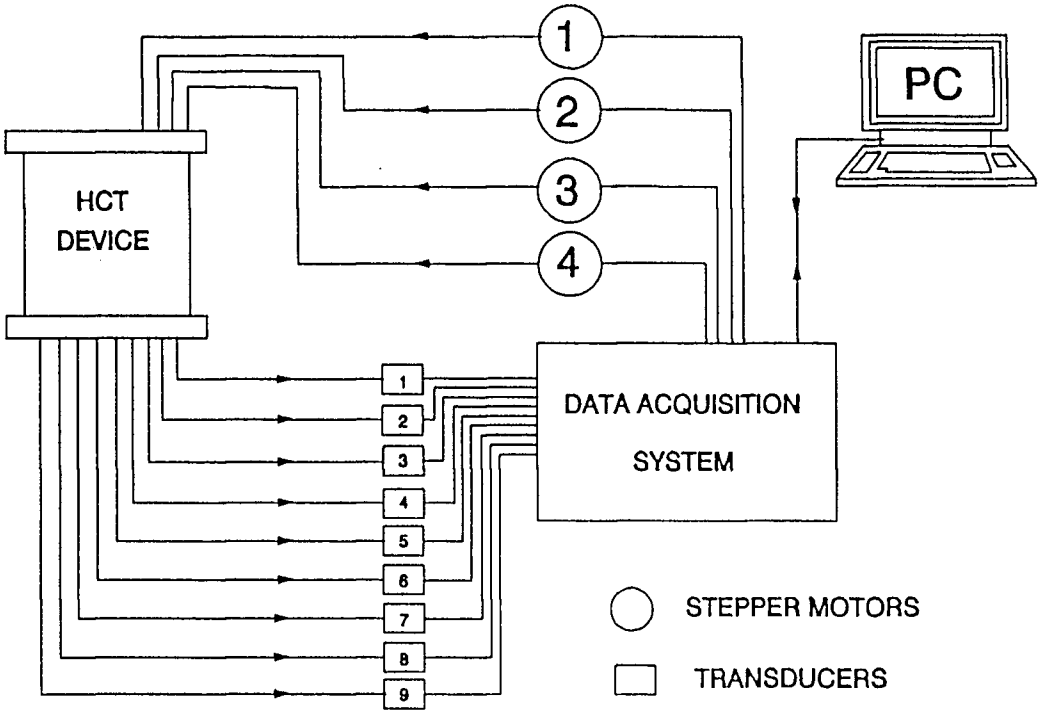

Figure 4.5: Schematic layout of the stress path control system

discussed in section 4.1.2). An IBM personal computer connected to a data acquisition system anchors the input-output control. Basic features of the input-output control are described in the following sections.

4.2.2 Data Acquisition (Input to the Computer)

All transducers were excited with a stable D.C power supply of 6.0 V. The LVDT's being high output devices, did not need any signal amplification. The remaining transducers were of bonded strain gage type with an output of about 3 mV/V. Signal outputs of these transducers were brought upto 2.0 V full scale using variable gain amplifiers.

The feedback control system requires updated values of stress and strain in the specimen, in order to carry out its decision making process. It is therefore important that all transducer readings correspond to the same instant on the time scale. As such, simultaneous reading of transducers became a prime consideration in the development of the data acquisition system.

In the system designed, the scanning is triggered simultaneously on all channels in response to a "start scan" pulse from the computer (Fig. 4.6). The signal from each transducer over a 50 ms period is integrated by an analog circuit and the average value is obtained. This average value is then digitized by the A/D converter and temporarily stored in a memory chip. The digital output from the A/D conversion yields a decimal number ranging from 1 to 40000 ($\approx$ 16 bits in binary) corresponding to an analog range of 0 to 4.0 V. This corresponds to resolution of the tranducer outputs to be in the order of 0.1 mV.

At the end of conversion, the digital voltages are retrieved by the computer in a sequential manner. The system has a low noise level of not exceeding ± 0.1 mV thus making maximum use of the resolution available. With the low noise level and the high sensitivity of the transducers used it was possible to achieve a high precision in

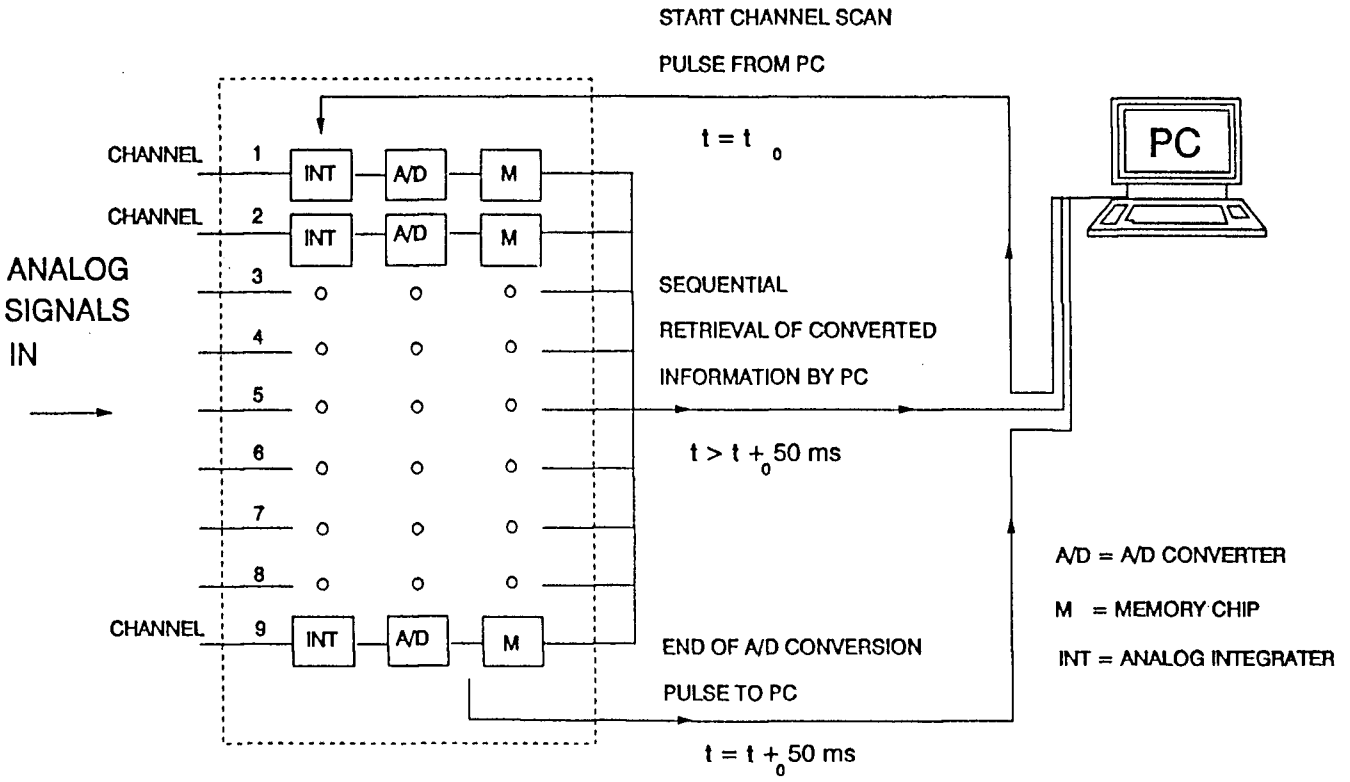

Figure 4.6: Data acquisition process

the acquired data.

4.2.3 Control of Surface Tractions (Output from the Computer)

The surface tractions are controlled by four Fairchild motorset precision regulators powered by a 24 Volt D.C. supply. Regulators have the ability to impose pressures within a range from 0 to 700 kPa ($\approx 0 - 100$ psi).

In response to a logic sequence from the computer, a control chip outputs a series of square pulses to the stepper motors. These pulses change the regulated air supply accordingly. The logic sequence from the computer contains information pertaining to the direction of rotation, and the number of pulses needed to achieve each pressure change. A single pulse advances the motor regulator by one step. Approximately 12 to 13 pulses are needed to obtain a pressure change of 1 kPa, thus enabling the regulators to impose a pressure change as low as 0.1 kPa. Since the motors are operated according to a computer controlled feed back facility, any discrepancies occurring due to factors such as backlash of gear box, etc. are immediately corrected.

Regulator motors can change pressures at a rate of approximately 3.0 kPa/s to 14 kPa/s. In applying a given stress increment in drained tests, the rate of change of pressures should be slow enough to ensure that no localized undrained conditions occur in the sample. Sayao (1989) carried out HCT tests with manual control of surface tractions, in which the pressure changes were imposed in a slow manner so as to ensure fully drained conditions. Fig. 4.7 compares the results of a stress path test from the new automated system with those from an identical test (but manually controlled) by Sayao (1989). To achieve a given stress increment in the automated test, the regulators were set at the slower rate of 3.8 kPa/s. Little difference between deformations in the two tests indicate that fully drained conditions were ensured using the automated system. The rate of pressure change selected was thus confirmed to be

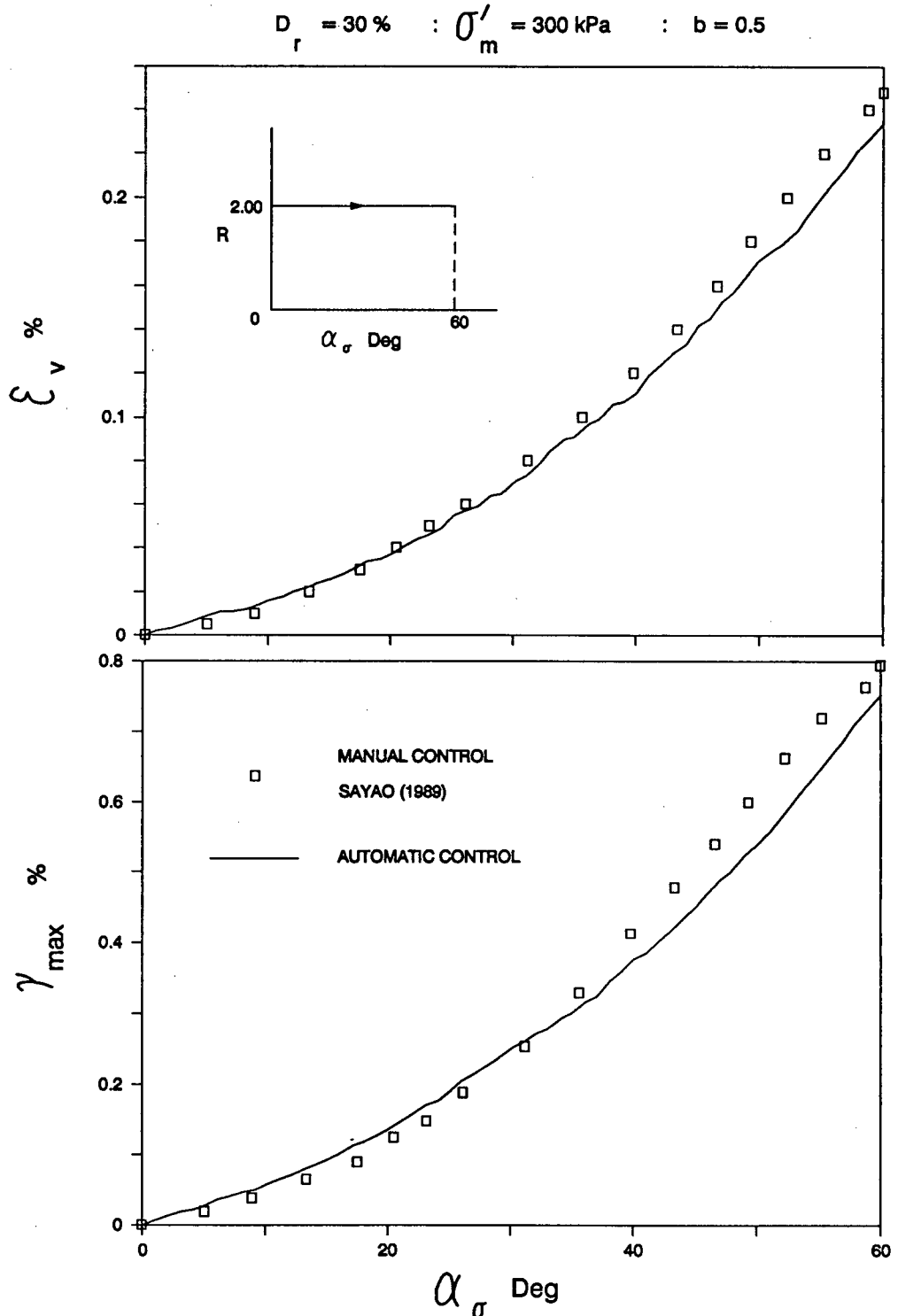

Figure 4.7: Comparison between manually controlled versus automated stress path testing.

slow enough to avoid localized undrained conditions. As such, this rate was selected as the operating rate of regulators for all tests carried out in this research.

4.2.4 Stress Path Control (Software)

The algorithm used for the closed loop controlled stress path testing is presented in Fig. 4.8. Microsoft Quickbasic Version 4.0 was used as the programming language for the main module. For scanning and sending pulses to the stepper motors, subroutines written in assembler language were used.

The program consists of seven major components:

1. Input of initial information : viz. specimen dimensions, reference readings for transducers, etc.
2. Skempton's B value check for saturation
3. Input of stress path to be followed
4. Control of surface tractions
5. Check for deformation equilibrium
6. Data storage
7. Application of next loading increment

Once the initial information is fed into the computer, the specimen is loaded hydrostatically in an incremental manner. Monitoring pore pressure increments during undrained loading enable a check on saturation. If the specimen is saturated (a B value > 0.98 was considered as acceptable), the computer reads a file from the floppy disk containing the information on the desired stress path to be followed. This information contains the $(\sigma'_m,\ R,\ b,\ \alpha_\sigma)$ coordinates of the key turning points in the stress

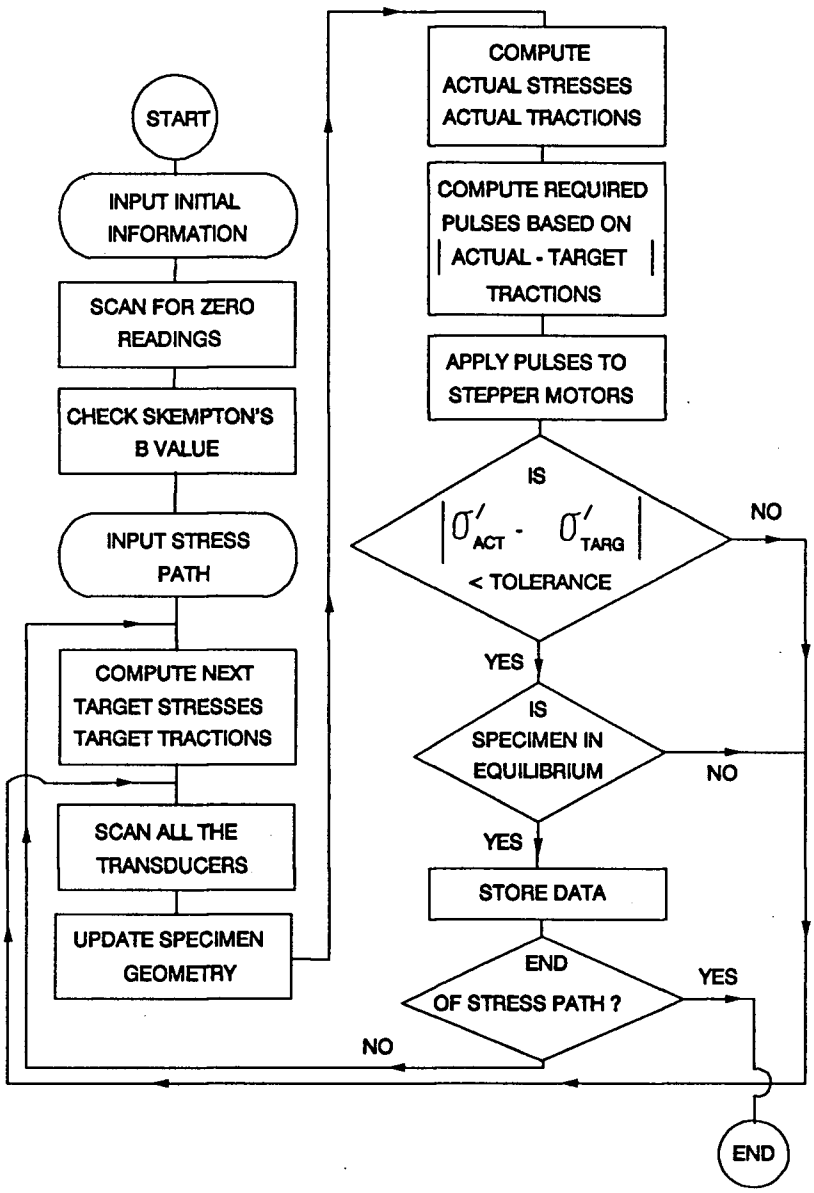

Figure 4.8: Flow chart for the program used in stress path testing

path. The program has the ability to take the specimen from one stress state to the other along a straight line path. The number of increments needed to accomplish this is prescribed so that the computer could linearly interpolate and determine the intermediate stress states. By increasing the number of increments to reach the final stress state, the stress changes within a single increment will decrease. For all tests reported in this thesis, the maximum change in any stress component over a given increment did not exceed 3 kPa.

Pressure control routine governs the incremental changes in the surface tractions to move the stress state along the prescribed stress path. To accomplish a small load increment, the target values of the four surface tractions (viz. external and internal pressures, torque, and vertical load) are calculated. The differences between the current and the target surface tractions are then computed and the number of pulses required to bridge the difference in each regulator is calculated. The pulses are then sent to the stepper motors simultaneously so that all regulators are activated together. Each surface traction is adjusted until the current tractions are within a given tolerance from the target values. The tolerance for the surface tractions were stipulated so that no stress component would deviate more than 0.5 kPa from its target value.

After the increment of loading, deformation equilibrium is checked by monitoring the development of strains ε_v, ε_z, ε_r and γ_{zt}. The specimen is considered to be in deformation equilibrium if the following criteria for strain rate is satisfied by all strain components: i.e. the change in an individual strain component within a minute, does not exceed 5% of the change in the same strain component within the immediately previous minute. If the specimen has not reached equilibrium, further monitoring is continued. Since the specimen dimensions are updated each time the transducers are read, the control decisions could be based on the most recent configuration of the specimen.

Once the specimen has reached deformation equilibrium, all data pertaining to the current stress state is stored on the floppy disk and the next loading increment is applied in a similar manner.

The performance of the control system is demonstrated in Fig. 4.9 by a typical stress path test. In this test the specimen was loaded under simultaneously increasing stress ratio R and rotation α_σ of σ_1' to vertical while σ_m' and b were held constant (Fig. 4.9a). This required the magnitudes of all four boundary tractions to be changed in a controlled manner. Figs. 4.9b and 4.9c present a comparison between the desired and the actually obtained values of all stress components. Close agreement between the desired and the actual data points shows the excellent capability of the automatic control system for carrying out generalized stress path tests.

4.3 Specimen preparation

4.3.1 General Considerations

In the laboratory, a test specimen is assumed to represent an element of soil at a point in the soil mass. Therefore the method of specimen preparation must promote development of homogeneity within the test specimen.

Pluviation is considered to simulate the deposition process and the resulting fabric found in natural sedimentary deposits and artificial deposits such as hydraulic fills (Oda et al., 1978; Miura and Toki, 1984). Laboratory studies on pluviated sands, should therefore give a close indication of the behaviour of these deposits. Furthermore, water pluviation followed by vibration has been found to be the most effective technique of reconstituting homogeneous saturated sand specimens with controlled density (Vaid and Negussey, 1984b). As such, water pluviation was selected as the technique of specimen reconstitution.

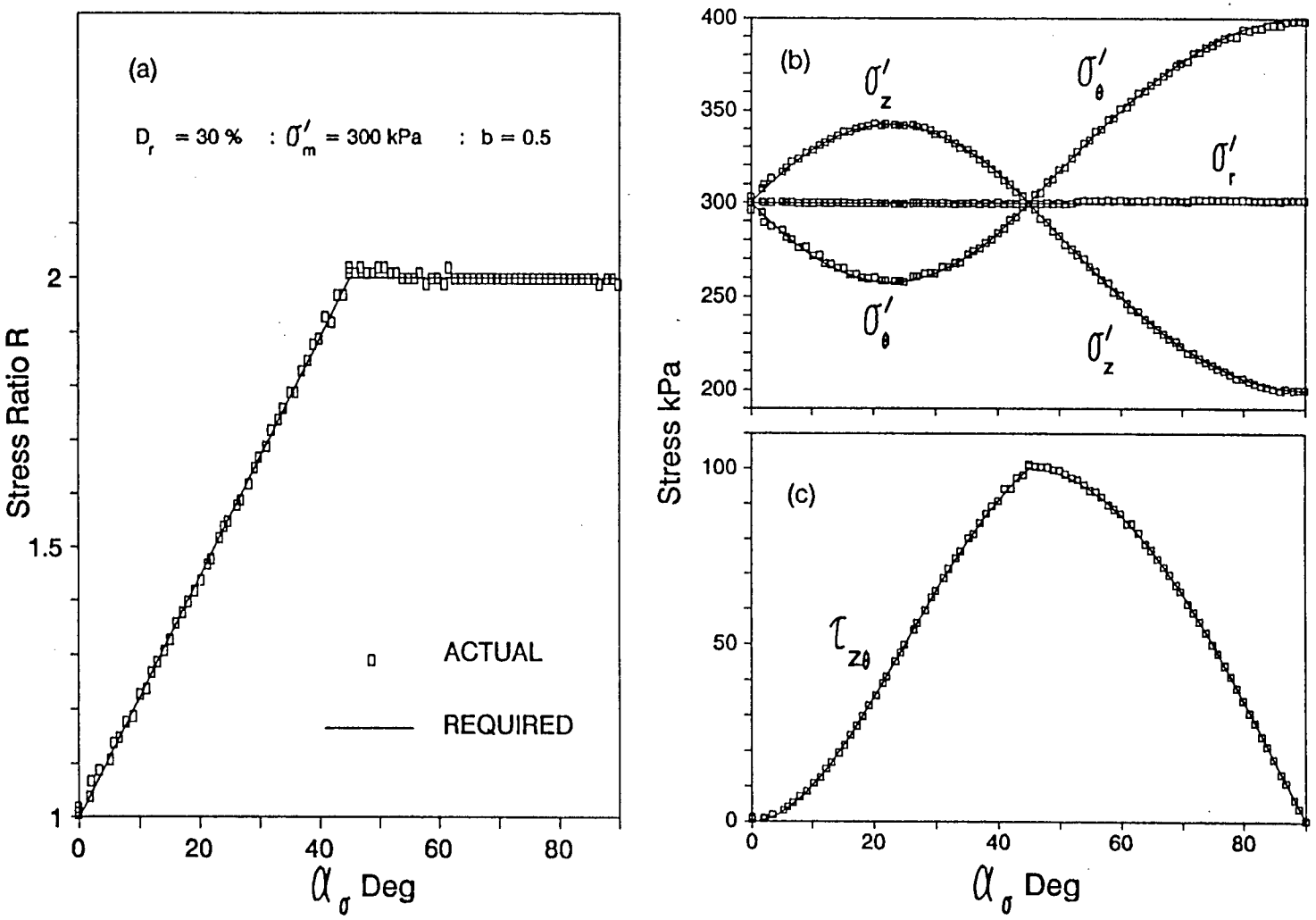

Figure 4.9: Performance of the stress path control system

Both the uniformity of the particle size distribution and density across the specimen is simulated by water pluviation if the sand is uniformly graded. Well graded sands tend to seggregate during pluviation, and for these sands an alternative deposition method suggested by Kuerbis and Vaid (1988) has to be used to ensure specimen homogeneity. In this study a uniform sand was used (as will be found in a later section) and therefore the question of seggregation did not arise.

4.3.2 Preparation Procedure

The procedure adopted for the preparation of HCT test specimens and the assembly of the UBC-HCT device to carry out testing has been described in detail by Sayao (1989). Since the same procedure was employed in this study, only the important steps are presented herein.

Initially a known dry weight (approximately 5 kg) of sand was boiled in several flasks and then left overnight under vacuum. All drainage lines were saturated with deaired water and all the porous stones were boiled and allowed to cool at room temperature.

A reference height was established by placing an aluminum dummy specimen of known height between the bottom and top platens. A dial gage mounted on a movable stand was used to obtain a reference reading on the top platen. This reading was later used for determining the height of the sand sample at the end of preparation.

An annular hollow cylindrical cavity for the placement of sand was formed using inner and outer split moulds with two matching rubber membranes (0.3 mm thick) stretched over them. The annular cavity was first filled with deaired water, followed by pluviation of sand through water. This process is illustrated in Fig. 4.10. During the pluviation process, the flasks containing the deaired sand were traversed over the annular area of the cavity to achieve an approximately level surface at all times. Except in the case of dense samples, no vibrations were imparted to the sample until

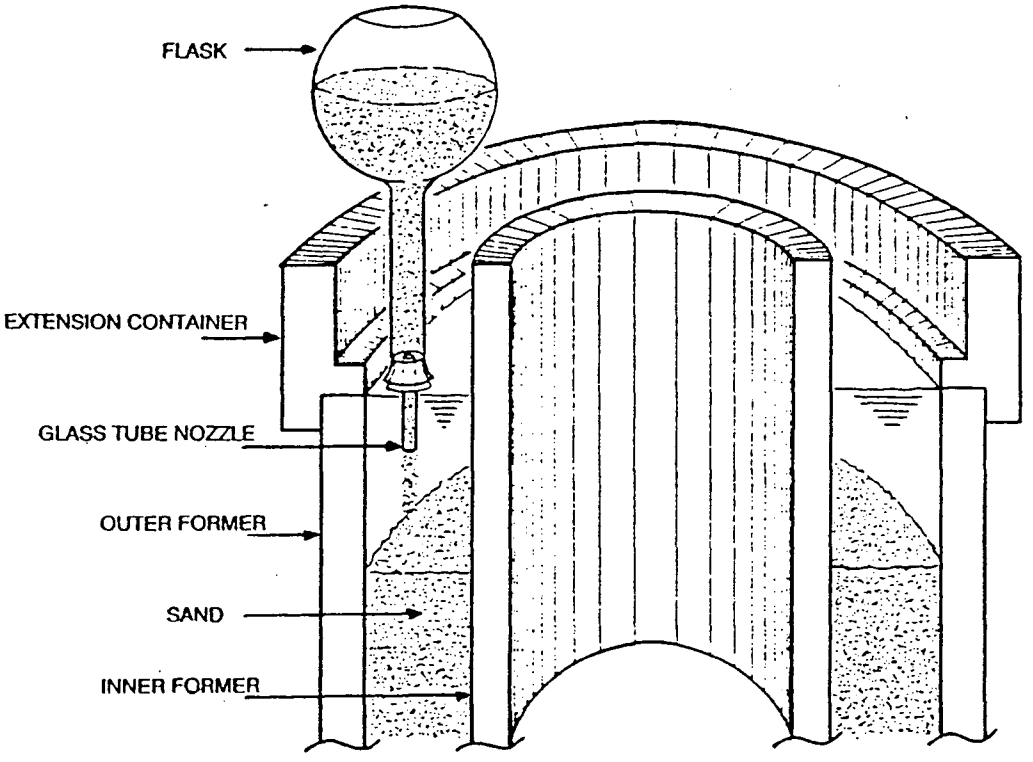

Figure 4.10: Sample preparation by water pluviation - after Sayao (1989)

the top platen was placed on the deposited sand after preparation. However, dense samples had to be partially vibrated during pluviation to avoid excessive descent of the top platen during final densification.

Once the sand was deposited to a level slightly in excess of the target height, the pluviation was terminated. Then the top surface of the specimen was levelled to the desired height by siphoning off excess sand using a low suction head as shown in Fig. 4.11. This siphoning method is a convenient means of levelling which minimizes disturbance to the particles underneath. The siphoned sand was oven dried and weighed in order to obtain the actual dry weight of sand in the specimen.

The top end platen with saturated porous stones was then placed on the levelled surface. Disturbance of the top surface due to penetration of the platen ribs has negligible effects because of the large dimensions of the sample (Tatsuoka et al., 1983) and also because the loose pluviated sand cannnot become any looser (Vaid, 1983).

The sample was then vibrated while monitoring the reference height dial gage, until the target density was reached. A low amplitude high frequency vibrator was used in this densification process and both top and bottom drainage lines were kept open to minimize the generation of any excess pore pressure. Vaid and Negussey (1988) have shown that densification with a small vertical confinement on the top cap promotes a uniform density distribution over the height of the specimen. They have also observed that by this densification technique the possibilty of bedding errors is automatically eliminated, since the top cap smoothly follows the movement of the top suface of the specimen during densification.

After densification, deaired water was percolated (with a low gradient) upward through the specimen to remove any air bubbles entrappped between the rubber membranes and the top platen. Then the membranes were sealed to the top platen using O-rings and a vacuum of 20 kPa was immediately applied to the drainage line at

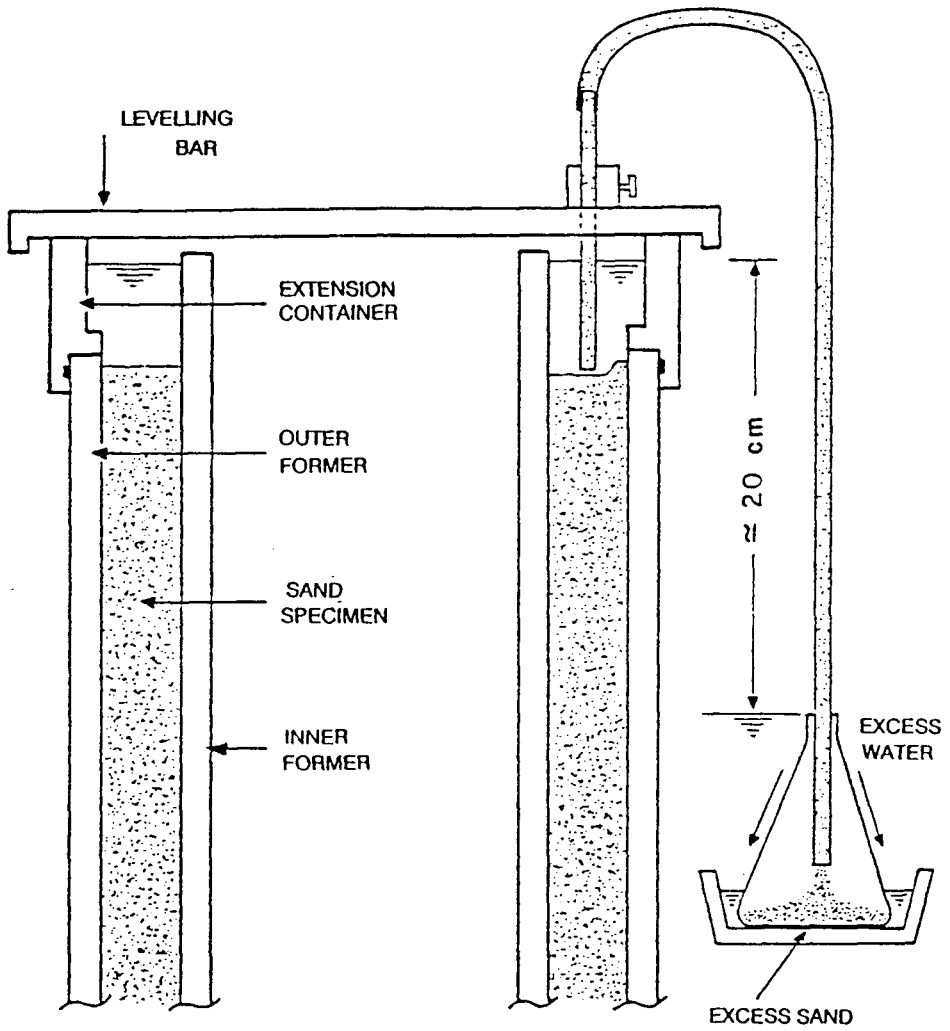

Figure 4.11: Levelling the upper surface of the sample - after Sayao (1989)

the bottom of the specimen. This vacuum provided the effective confinement to the specimen during dismantling of the split moulds. With the split moulds removed, the dimensions of the sample (i.e. height, outer and inner circumferences) are obtained. Height was obtained using the measurement on the reference dial gage. A measuring tape was used to determine the outer circumference. Inner cavity area was derived from the volume needed to raise the water level by 50 mm in the inner chamber. The inner and outer diameters of the sample was then computed after correcting for membrane thickness.

The top loading cap was then clamped to the top platen followed by the assembly of the cell chamber[1]. The top cross beam was then swung into position and bolted to the reaction frame. The specimen was then raised upward by pressurizing vertical loading piston until the top cap is in contact with the cross beam. Using a bolt and a locating pin, the top cap was anchored to the cross beam, thus arresting both vertical and rotational movements of the specimen top. Internal and external chambers were then filled with deaired water. Special care was taken to ensure full saturation of the inner chamber. The central rod for monitoring vertical displacements was then mounted which also sealed the inner chamber.

At the end of assembly, a hydrostatic confining stress of 30 kPa was appplied undrained to bring the pore pressure to a value above zero. Then by increasing the hydrostatic confining pressure incrementally, the Skempton's B value was determined in several steps to check for saturation. Specimens were considered saturated if B value was greater than 0.98. The specimen was then hydrostatically consolidated to an effective stress of 50 kPa against a back pressure of 200 kPa. Stress path loading reported in this study was always initiated from this 50 kPa reference hydrostatic effective stress state.

[1]Refer Figs. 4.1 and 4.2 for details

4.3.3 Repeatability of Test Results

As discussed earlier, it is important to have a specimen preparation procedure which is capable of replicating specimens. Replication of specimens can be achieved only by following identical preparation techniques and test control routines. This aspect was evaluated by repeated testing of several identical samples loaded along identical stress paths.

Results from repeated testing of several identical samples in hydrostatic compression are presented in Fig. 4.12. Excellent repeatability may be observed in both volumetric as well as axial strain responses.

Results of two identical samples subjected to a stress path with simultaneous increase in stress ratio and principal stress rotation are shown in Fig. 4.13. Considering the small magnitudes of the induced strains, again good repeatability is observed in both volumetric and maximum shear strain response.

4.3.4 Experimental Program

4.3.4.1 Material Tested

Medium Ottawa sand ASTM-C-109 was used as the testing material in this program. This sand has been extensively used in laboratory research at UBC and elsewhere. Ottawa sand is a rounded quartz sand with a specific gravity of 2.67. The sand is uniformly graded ($C_u = 1.9$) and has an average particle size D_{50} of 0.4 mm. The particle size distribution is given in Fig. 4.14.

Previous research at UBC has shown that in Ottawa sand the amount of particle crushing under moderate stresses is negligible and thus it could be recycled conveniently for testing purposes (Chern, 1985). Reference maximum and minimum void ratios for the sand are 0.82 and 0.50 respectively.

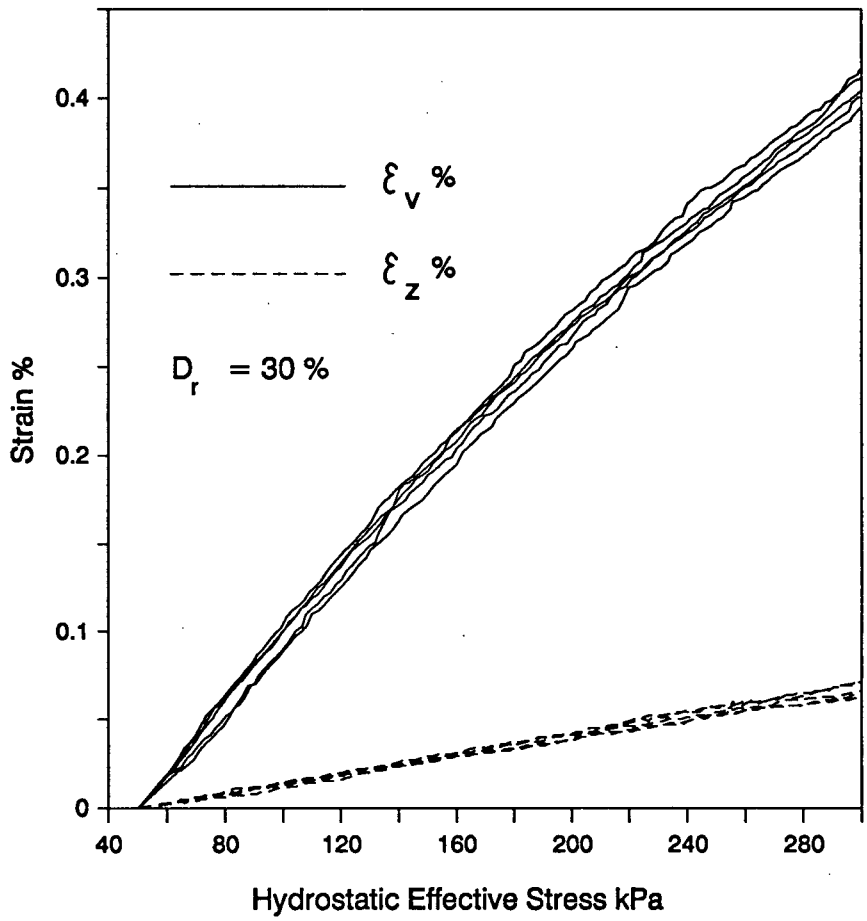

Figure 4.12: Repeatability of HCT test results in a hydrostatic stress path

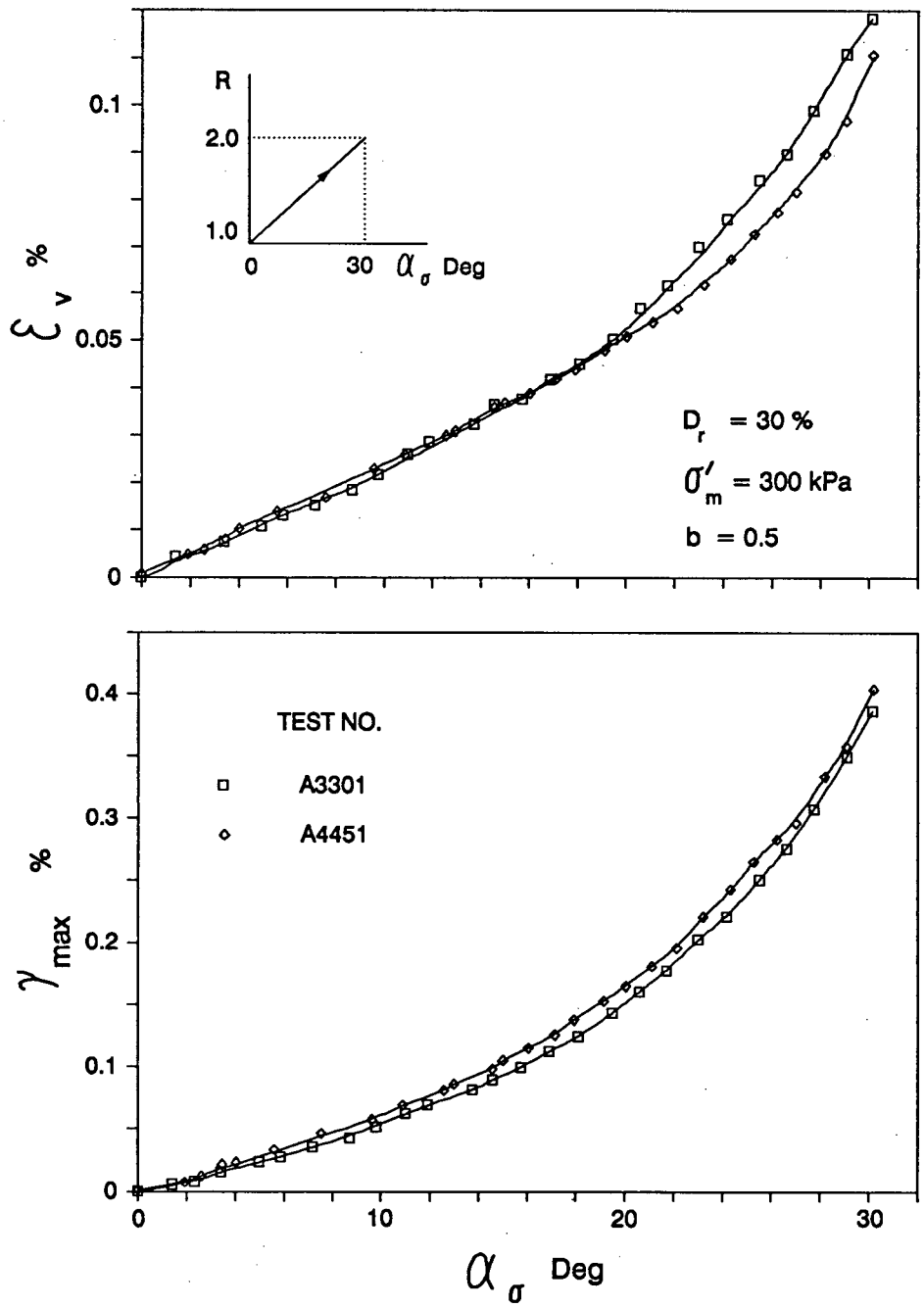

Figure 4.13: Repeatability of HCT test results in a stress path with simultaneous increase of stress ratio and principal stress rotation

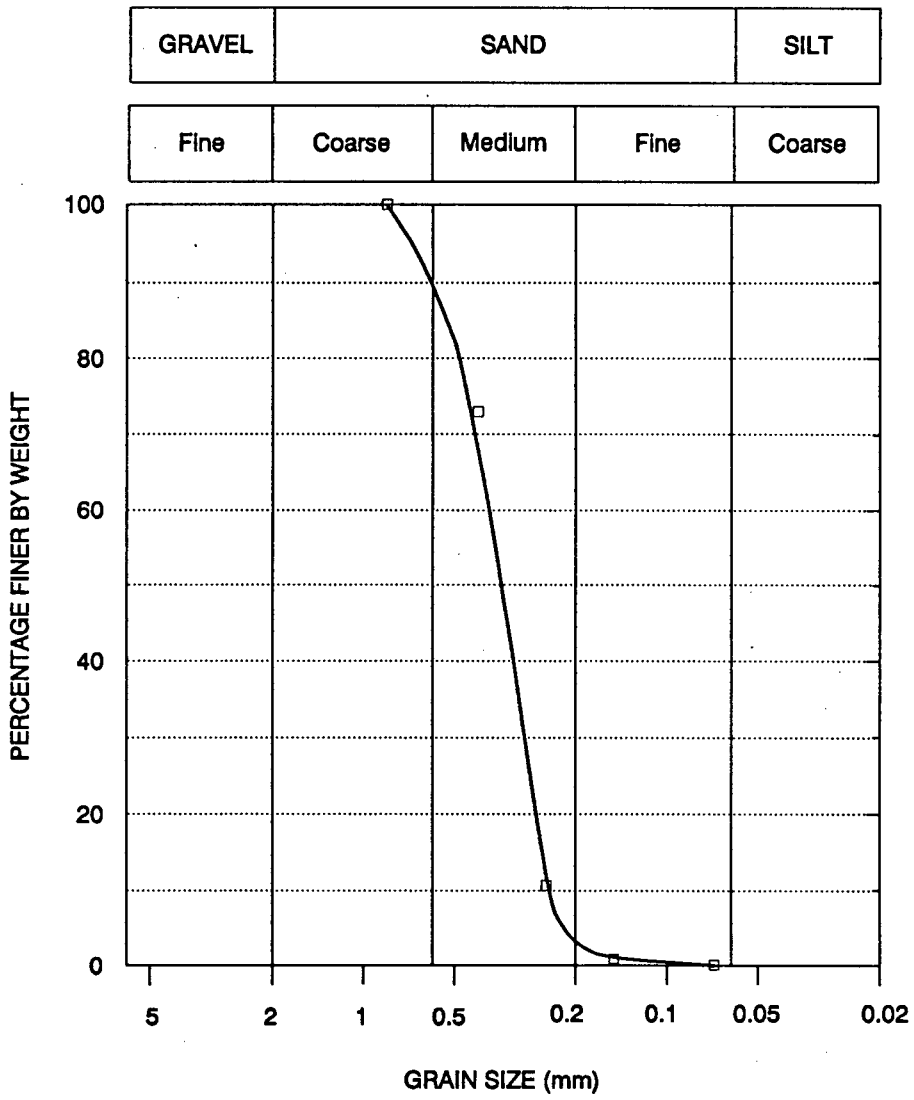

Figure 4.14: Particle size distribution of medium Ottawa sand

4.3.4.2 Testing Program

A testing program was developed with the main objective of studying the behaviour of sand subjected to stress paths involving simultaneous increase in stress ratio R and rotation of principal stresses α_σ. It was intended to compare the behaviour in stress paths with simultaneous increase in R and α_σ with those in which these parameters varied individually. The comparisons of induced strains were aimed at investigating possible stress path independent behaviour that involves principal stress rotation. The stress paths were chosen so that the stress parameters σ'_m, R, b and α_σ were either increasing or remained constant at all times. Stress paths involving decrease of any of the stress parameters are not considered in this study.

The testing program composed of three main types of stress paths. The terminology used to identify these stress paths is given below and illustrated in Fig. 4.15.

R Path : Stress Path with increasing R while other stress parameters σ'_m, b and α_σ are held constant.

α Path : Stress Path with increasing α_σ while other stress parameters σ'_m, b and R are held constant.

R - α Path : Stress Path with increasing R and α_σ while other stress parameters σ'_m and b are held constant.

In order to conveniently identify or make reference to a particular test, each test was given an identification number (Fig. 4.16). This number consist of five characters of which the first is a letter from the alphabet and the remaining four are a sequence of digits from 0 to 9. The first character identifies the series name (eg. all tests in Series A will begin with the character 'A'). The next three characters in the identification number locates the path of the test in the R-α_σ stress space as illustrated in Fig. 4.16. The fifth character was needed for record purposes only.

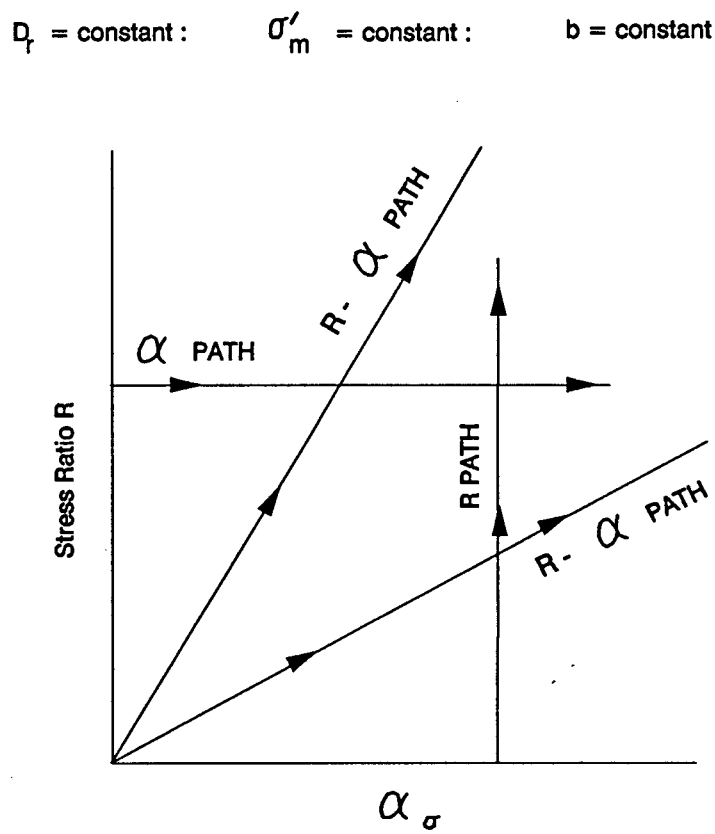

Figure 4.15: Terminology used in identifying a stress path in R-α_σ stress space

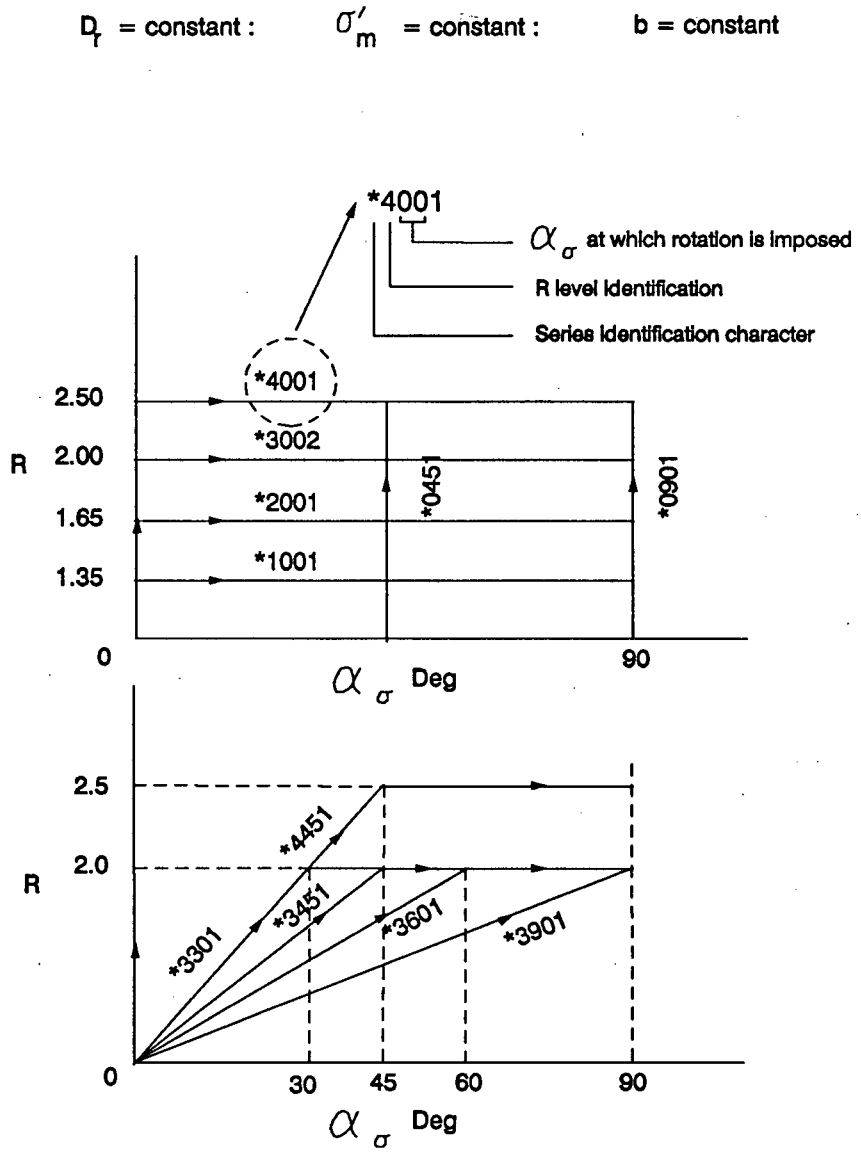

Figure 4.16: Notation used in identifying a stress path in R-α_σ stress space

The details of the testing program developed to meet the above objectives are given in Figs. 4.17 and 4.18. As mentioned in section 4.3.2, stress path loading of all specimens was initiated from an initial hydrostatic stress state of $\sigma'_m = 50$ kPa. From this initial stress state, the specimens were hydrostatically consolidated to the prescribed value of σ'_m. Then R and α_σ were increased as necessary, while maintaining the values of σ'_m and b parameter at constant values. All tests were stress controlled and carried out under fully drained conditions against a back pressure of 200 kPa.

Sand behaviour was examined predominantly at a relative density of 30%. Loose density state was selected because of its greater susceptibility to deformations due to principal stress rotation. Test Series A ($D_r = 30\%$, $\sigma'_m = 300$ kPa, and $b = 0.5$) forms the centre of the testing program (Fig. 4.17). All other test series were built around Series A so that the effects of various stress parameters and relative density on sand behaviour could be investigated in a systematic manner. For example, test Series E and C were complimentary to A, and were conducted to examine the effect of b parameter on behaviour in test Series A. Similarly test Series K and M were performed to investigate the effect of mean normal stress. The behaviour of medium and dense sand was investigated by conducting test Series I and O.

In each test series, deformation response under principal stress rotation was studied at several constant R levels (as illustrated by the right hand side diagram of each series in Figs. 4.17 and 4.18). This was necessary in order to investigate region of possible stress path independent behaviour in R - α_σ space.

Some specific tests were carried out in order to supplement and generalize the characteristic behaviour observed from the main testing program. The stress paths imposed in these tests are illustrated at the bottom of the Fig. 4.18. Test OABCD was carried out in order to examine deformation behaviour under a multi-linear stress path in R - α_σ space, and test AB was intended to investigate the deformation behaviour under simultaneous variation of three stress parameters σ'_m, R, and α_σ as opposed to

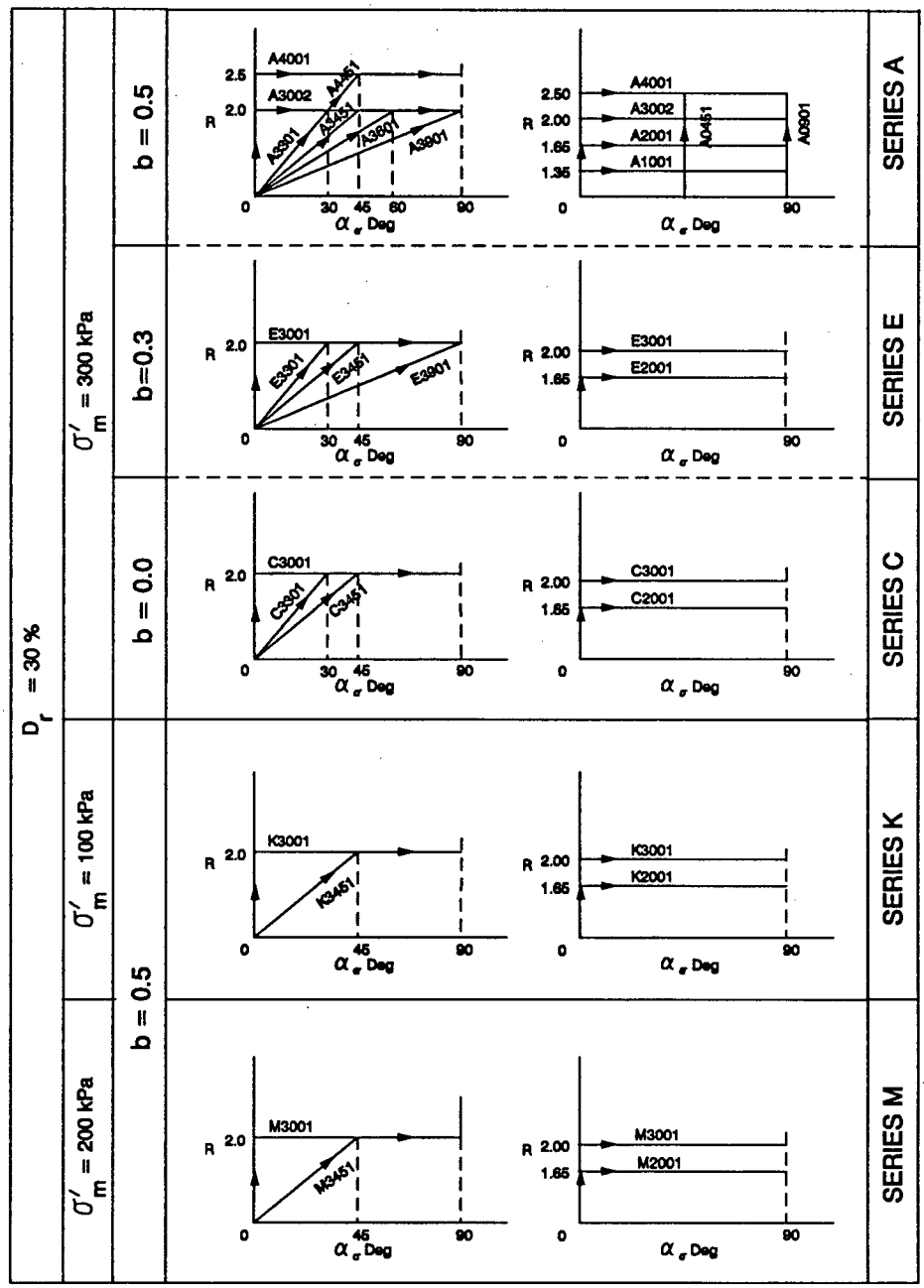

Figure 4.17: HCT testing program - (contd. next page)

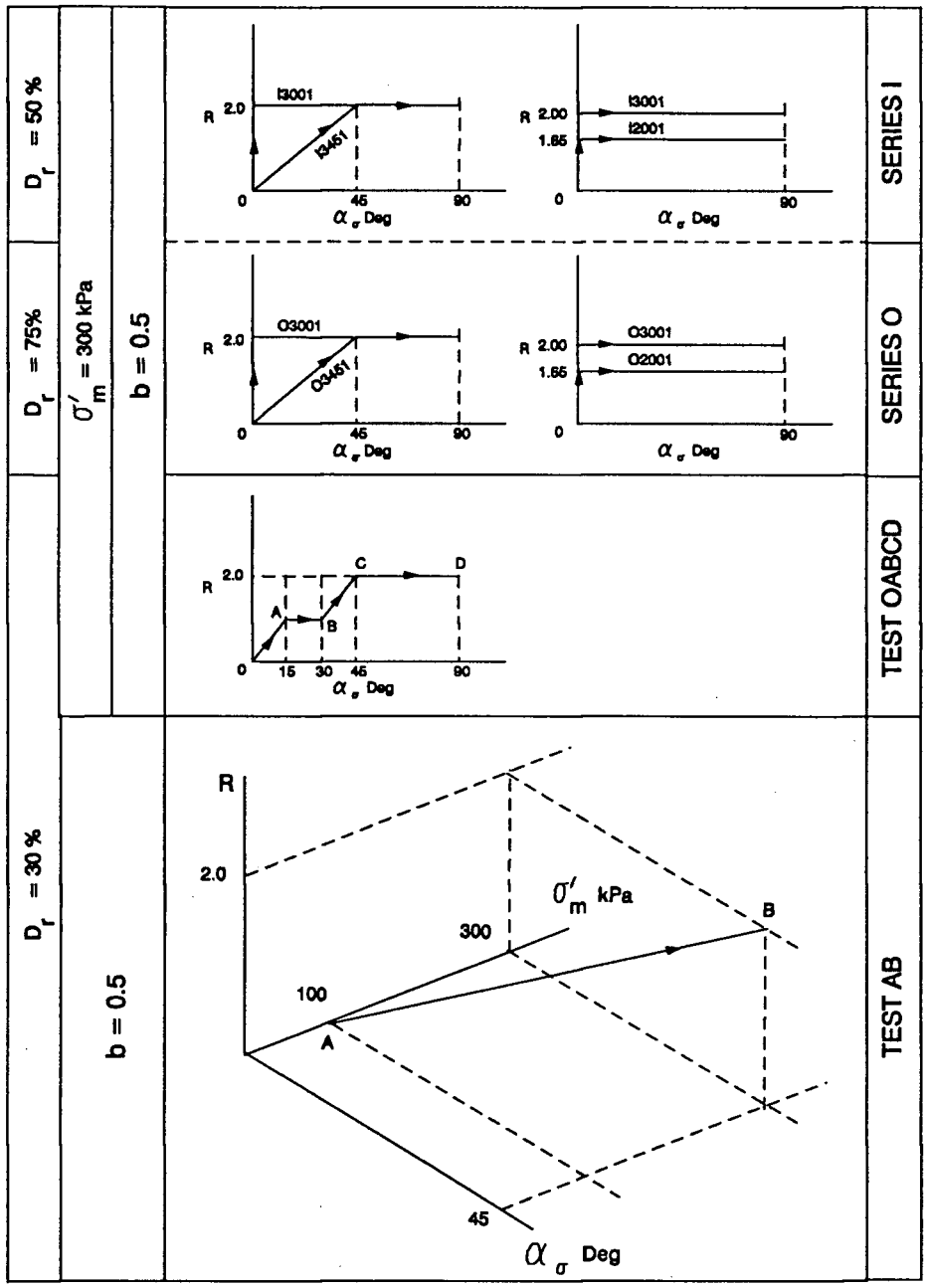

Figure 4.18: HCT testing program (contd. from previous page)

only two parameters R and α_σ in other series.

Chapter 5

Results and Discussion

5.1 Introduction

This chapter presents a detailed examination of the results obtained from the testing program outlined in Chapter 4. Initially, the stress strain behaviour of medium loose Ottawa sand, subjected to stress paths wherein only one stress parameter is varied at a time is presented. These constitute loading under: hydrostatic paths, R paths and α paths [1]. In R paths the stress ratio is increased while other stress parameters σ'_m, b and α_σ are held constant. In α paths the principal stresses σ'_1 and σ'_3 are continuously rotated while σ'_m, b and R are held constant. Effects of the levels of R, b and σ'_m in α tests are systematically assessed. The behaviour under similar stress paths is then examined for different material densities. Deformation characteristics under these stress paths are essential (i) to examine the inherent anisotropic nature of pluviated sand, and (ii) to form a data base for possible prediction of strain response under loadings involving simultaneous increase of several stress parameters, treated as superposition of events in which only one parameter increases.

Then, a comprehensive investigation of sand behaviour under stress paths involving simultaneous increase of stress ratio and principal stress rotation (R - α tests) is presented. This is the main objective of this thesis. Initially, stress paths with linear variation of R versus α_σ are considered. The effects of the levels of σ'_m, b and relative density D_r in R - α path loading are investigated separately in a systematic manner. Possible stress path independence of deformations is initially assessed by comparing

[1] terminology as defined in Chapter 4.

deformations from linear R - α paths with those obtained from increase in R alone and α_σ alone, at common terminal stress states. Such path independence of strain response is also examined at intermediate stress states with the aid of α tests carried out at lower R levels. The influence of stress path history on the deformations along a common principal stress rotation path is also investigated.

Behaviour under a multi-linear R - α path is examined in order to encompass general R - α paths. Finally, deformation response is studied under stress paths involving simultaneous increase in three stress parameters at a time.

Only those stress paths involving increasing values of stress variables (total loading paths) are considered in this thesis. All stress path tests were initiated from the reference hydrostatic stress state of 50 kPa [2]. The deformations are presented in terms of volumetric ($\varepsilon_v\%$) and maximum shear strain ($\gamma_{max}\%$) responses.

In chapter 3, it was shown that the stress non-uniformities in the HCT specimen are much smaller than those estimated previously based on linear elasticity (Sayao, 1989). Therefore a much larger domain of stress space could be explored without introducing unacceptable non-uniformities than considered in previous investigations. The stress non-uniformity coefficient β_R rarely exceeded 0.1 in the region of stress space explored.

5.2 Hydrostatic Loading

Fig. 5.1 presents typical stress-strain response under hydrostatic compression of medium loose Ottawa sand. The associated strain path is given in Fig. 5.2. Shear strains during hydrostatic loading arise as a consequence of the vertical strain smaller than the horizontal. This implies inherent anisotropy typical of water deposited sand (El-Sohby and Andrawes, 1972; Negussey, 1984). A linear strain path between horizontal and vertical strains suggests that the degree of anisotropy is preserved during

[2] N.B. b and α_σ are undefined and $R = 1$ at a hydrostatic stress state

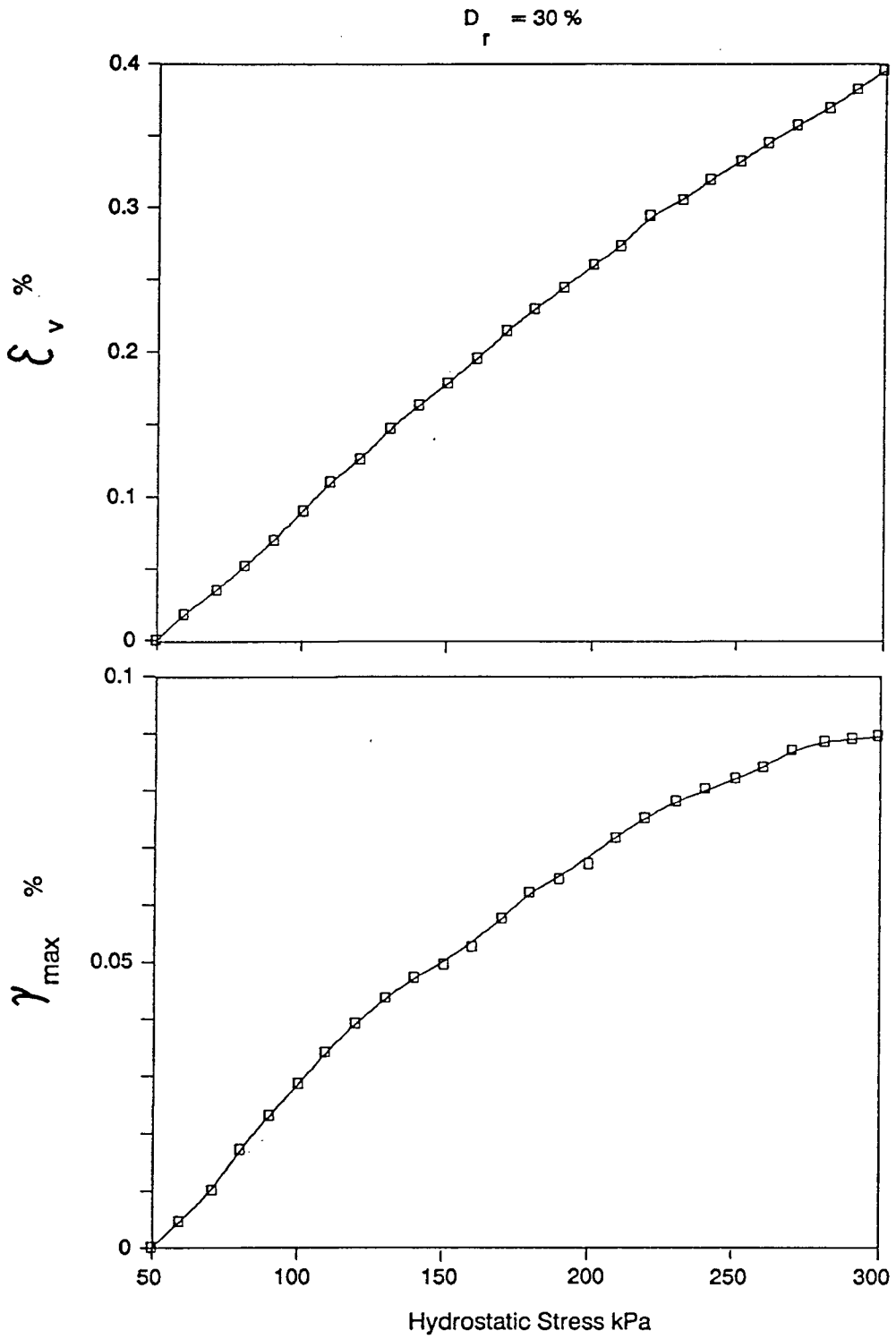

Figure 5.1: Stress-Strain response under hydrostatic loading of medium loose Ottawa sand

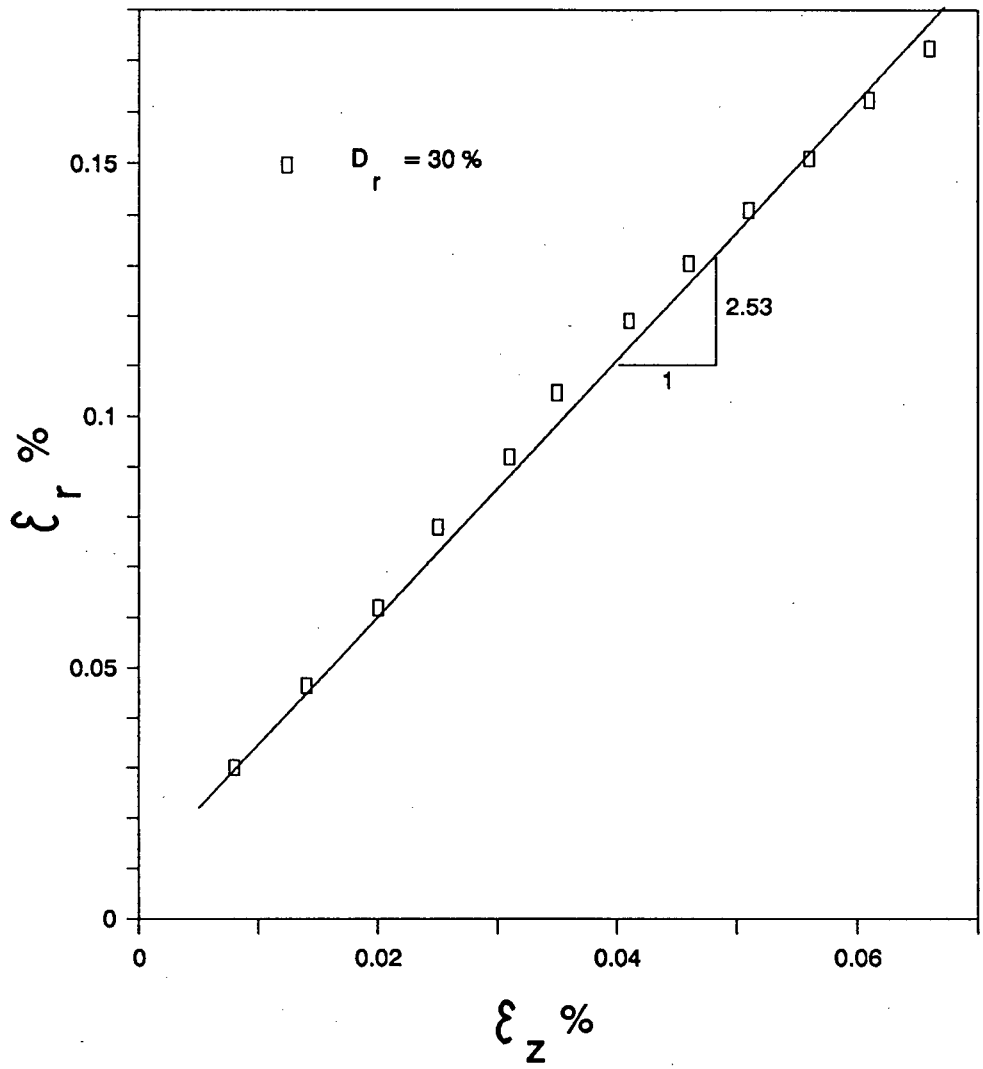

Figure 5.2: Strain path in hydrostatic loading of medium loose Ottawa sand

hydrostatic loading (El-Sohby and Andrawes, 1973).

Strain paths under hydrostatic loading for three different relative densities are shown in Fig. 5.3. With increasing relative density, the degree of inherent anisotropy decrease. Similar observations have been made by El-Sohby and Andrawes (1972). For dense sand (D_r = 70%) the ratio of horizontal to the vertical strain approaches unity, indicating close to isotropic behaviour. These results are in agreement with those reported by Negussey (1984) for hydrostatic loading of Ottawa sand using the conventional triaxial device.

5.3 Deformation Under Increase in a Single Stress Parameter

5.3.1 Shear Loading of Loose Sand with Fixed Principal Stress Directions (R Paths)

5.3.1.1 Stress Strain Behaviour

Figure 5.4 presents results of three R tests on medium loose Ottawa sand at α_σ = 0, 45 and 90 degrees. All samples were initially consolidated to a hydrostatic stress σ'_m = 300 kPa. Stress ratio R was then increased at constant α_σ while values of σ'_m and b were held constant at 300 kPa and 0.5 respectively (R paths A3002, A0451 and A0901 in Fig. 5.4). A marked dependence of deformations on the direction of loading may be noted. The shear stiffness is greatest when major principal stress σ'_1 is coincident with the direction of deposition (α_σ = 0°). With increasing α_σ both volumetric and shear deformations increase, affirming the inherent anisotropic nature of the pluviated sand. These results support the findings on the anisotropy of pluviated sands by previous researchers. (Sayao, 1989; Symes et al., 1982; Arthur and Menzies, 1972; Yamada and Ishihara, 1979; Oda, 1972 and 1976).

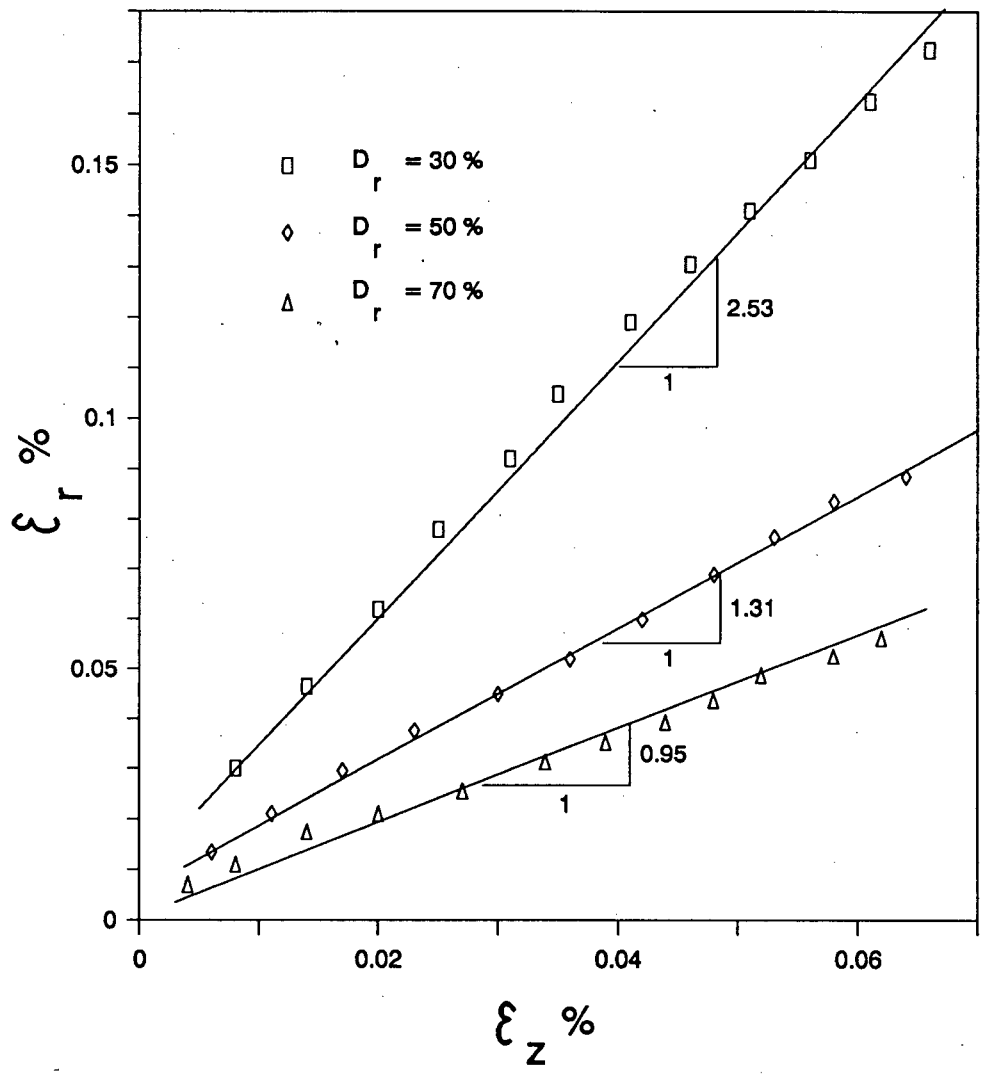

Figure 5.3: Effect of relative density on strain paths in hydrostatic loading

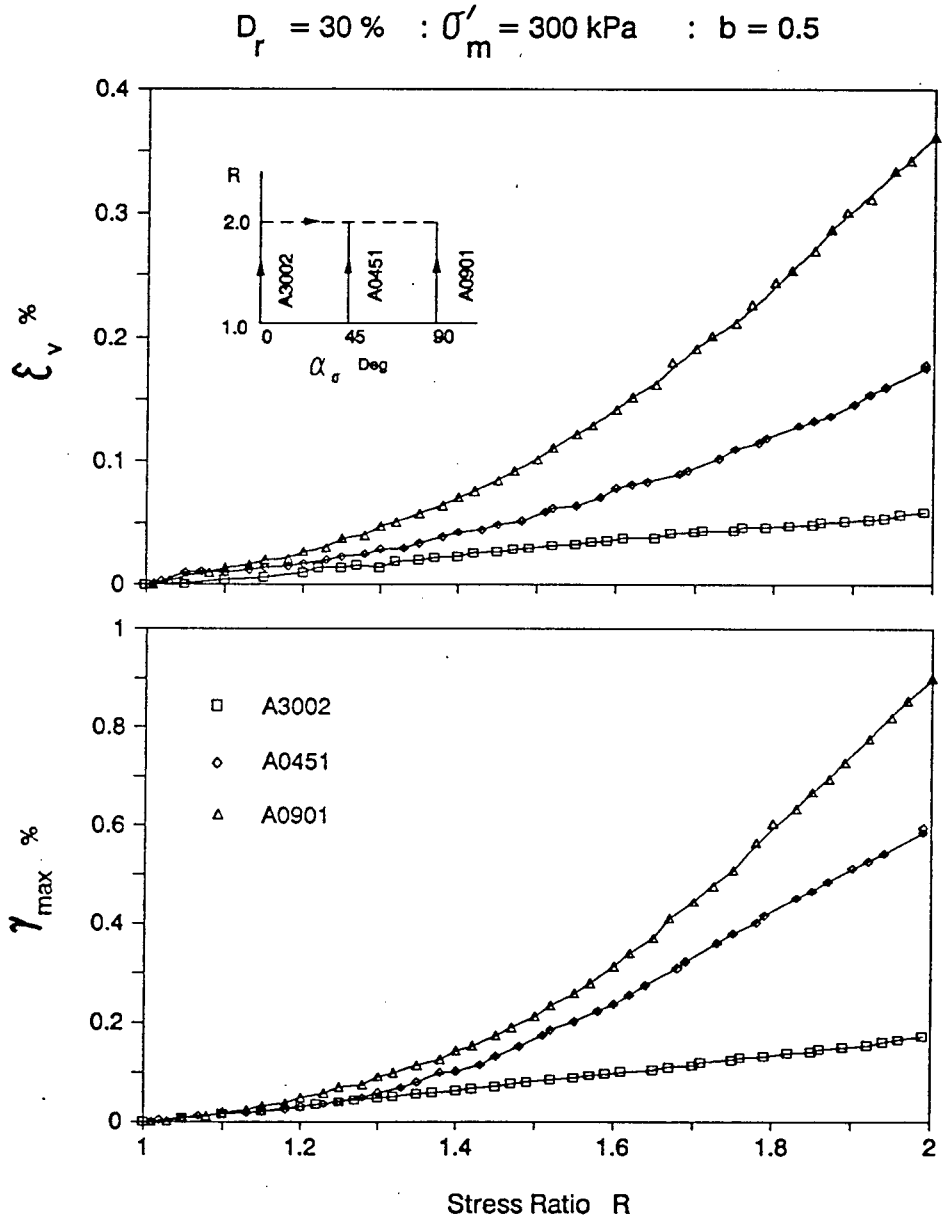

Figure 5.4: Effect of α_σ on the stress strain behaviour in R paths

5.3.1.2 Direction of Strain Increments and Strain Paths

For R tests with $\alpha_\sigma = 0°$ and 90° (i.e. tests A3002 and A0901) the principal stress and stress increment directions coincide with the axes of anisotropy. Hence the directions of principal stresses and strain increments coincide.

Major principal strain increment directions $\alpha_{\Delta\varepsilon}$ for the R test A0451 (with $\alpha_\sigma = 45°$ and the stress increment direction $\alpha_{\Delta\sigma} = 45°$) are presented in Fig. 5.5. It may be noted that the direction of strain increment $\alpha_{\Delta\varepsilon}$ is close to that of stress increment direction $\alpha_{\Delta\sigma}$, with a slight bent towards the bedding plane (i.e. horizontal direction). The results are in agreement with those observed by Sayao (1989) and Symes et al. (1982 and 1988).

Since the strain increment directions $\alpha_{\Delta\varepsilon}$ throughout R paths A3002 and A0901 is constant at 0° and 90° respectively, and in R path A0451 is also essentially constant ($\approx 47°$), the directions of cumulative principal strain vectors in these paths would also remain unchanged. Fig. 5.6 gives the cumulative principal strain paths for the R tests. Initially linear strain paths can be observed regardless of the direction of α_σ. This indicate that under directional shear, the inherent anisotropy is preserved in the small stress ratio region $R \leq 2$. Similar observations of inherent anisotropy have been made by Negussey (1984) and Sayao (1989).

5.3.2 Principal Stress Rotations on Loose Sand at Constant R, b and σ'_m (α Paths)

5.3.2.1 Effect of R Level

In these tests the rotation angle α_σ was varied continuously while values of R, b and σ'_m were held constant. All tests were initiated with samples isotropically consolidated to 300 kPa, and then sheared under identical $\alpha_\sigma = 0°$, $b = 0.5$ and $\sigma'_m = 300$ kPa, until specified values of $R = 1.35$, 1.65, 2.0 and 2.5, prior to principal stress rotation

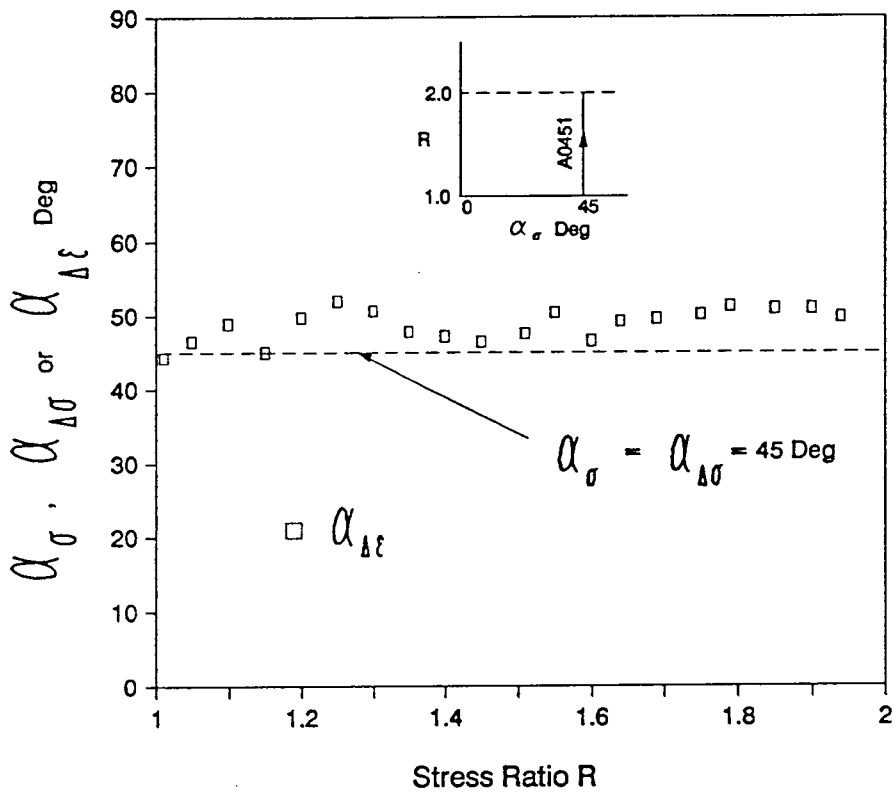

Figure 5.5: Strain increment directions in an R path with $\alpha_\sigma = 45°$

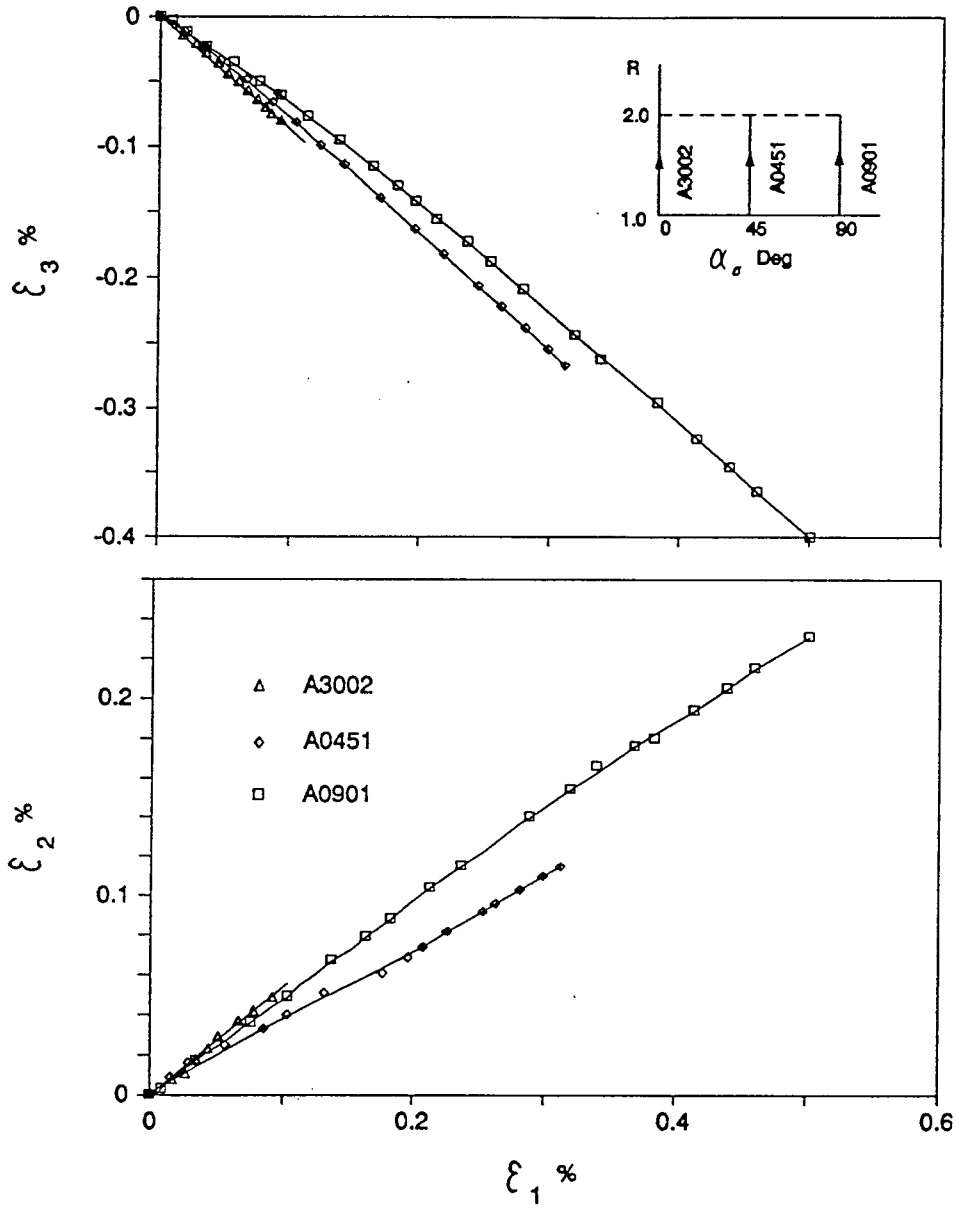

Figure 5.6: Strain paths in directional shear loading

from 0° to 90° (Tests A1001, A2001, A3002 and A4001). The selection of R values particularly encompassed behaviour under principal stress rotation at moderate as well as low R. Behaviour at stress ratios as high as 2.5 can be confidently examined because stress non-uniformities across the specimen wall would still be acceptable (Chapter 3).

Stress Strain Behaviour

Volumetric and maximum shear response due to principal stress rotation in α paths on medium loose Ottawa sand are shown in Fig. 5.7. Principal stress rotation induces contractive deformation that increases with α_σ irrespective of the level of R. For a given α_σ, the volumetric strain increases with the level of R. Similar comments apply to the development of γ_{max}.

The rate of strain development due to principal stress rotation increases with increasing R for a given value of α_σ, and for a given stress ratio, it is dependent on the current value of α_σ. The volumetric strain rate with respect to α_σ for a given R is enhanced further as the major principal stress direction moves from vertical ($\alpha_\sigma = 0°$) towards the bedding plane ($\alpha_\sigma = 90°$). A similar trend may be noted for the rate of change of maximum shear strain with respect to α_σ until $\alpha_\sigma \approx 60°$. However, for rotations involving α_σ greater than about 60°, there is a gradual drop in the rate of maximum shear strain development. In Sayao's (1989) α tests, α_σ was limited to 60° and therefore no such drop in the rate of γ_{max} with respect to α_σ was reported. This indicates that the observations at lower α_σ do not necessarily reflect the behaviour at larger values of principal stress rotation, and extrapolation of data from lower α_σ to larger α_σ should be carried out with caution.

The nature of deformations in α tests have an important implication on the undrained behaviour of anisotropic sands. Contractive deformations under drained conditions suggest significant pore pressure increase under undrained conditions and hence possible liquefaction or large deformations. This concern become more crucial

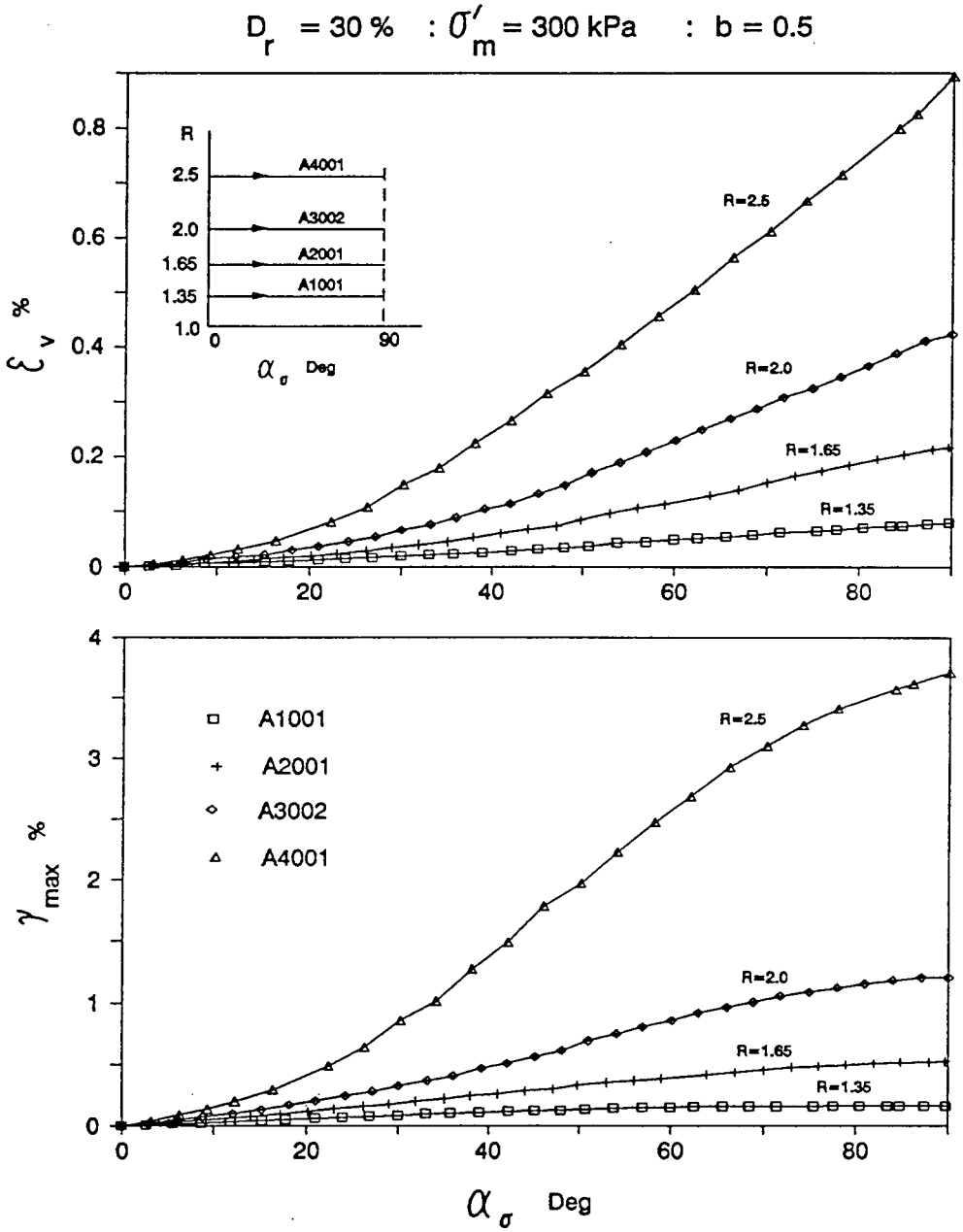

Figure 5.7: Effect of R level on deformation due to principal stress rotation

as the stress ratio increases because of increased contractive deformations that would accompany a given amount of principal stress rotation, as shown in Fig. 5.7.

Direction of Principal Strain Increment

Figure 5.8 shows the direction of major principal strain increment $\alpha_{\Delta\epsilon}$ in response to α loading. Since stress parameters σ'_m, b, and R are fixed and only the direction of σ'_1 changes, the direction of the imposed stress increment $\alpha_{\Delta\sigma}$ must lead the current direction of principal stress α_σ by 45° (Ishihara and Towhata, 1982). This condition is closely achieved by the stress path control as shown in Fig. 5.8. For lower stress ratios $R < 2$, at the beginning of the rotation ($\alpha_{\Delta\sigma} \approx 45°$) the strain increment direction $\alpha_{\Delta\epsilon}$ is close to $\alpha_{\Delta\sigma}$. As the rotation progress, strain increment direction $\alpha_{\Delta\epsilon}$ deviates away from stress increment direction $\alpha_{\Delta\sigma}$, and moves closer to the direction of major principal stress α_σ for rotations up to 90°.

The observed trend in strain increment direction $\alpha_{\Delta\epsilon}$ is also dependent on the level of stress ratio R. At higher R values, there is a larger deviation between $\alpha_{\Delta\epsilon}$ and $\alpha_{\Delta\sigma}$, even at the beginning of rotation. Also, with increasing principal stress rotation, $\alpha_{\Delta\epsilon}$ become much closer to α_σ at higher R, when compared to that under lower R. Similar results have also been experimentally observed by Sayao (1989) and Symes et al. (1988) on rotation tests carried out to limited ranges of α_σ. These observations will be examined again in a later section (section 5.4.1.2) in conjunction with the results under stress paths involving simultaneous increase in R and α_σ.

5.3.2.2 Effect of b Parameter

Stress Strain Behaviour

Deformations in α tests similar to those described in section 5.3.2.1 at $R = 2$ level, but now with $b = 0.0$ and $b = 0.3$ are shown in Fig. 5.9. Results for test A3002 with $b = 0.5$ in Fig. 5.7 are also included. There appears to be no significant influence of the intermediate principal stress parameter on the volumetric strain development

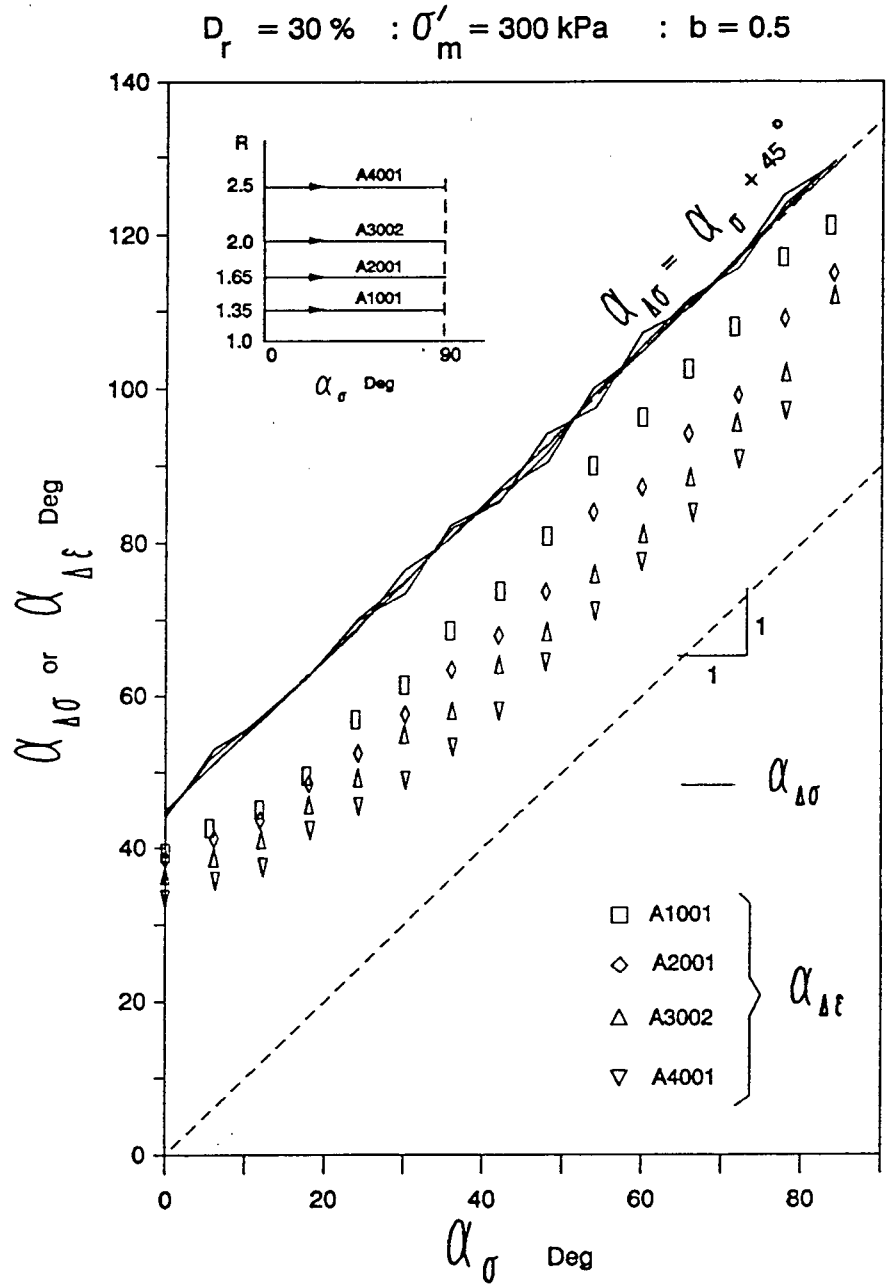

Figure 5.8: Effect of R level on the direction of strain increment

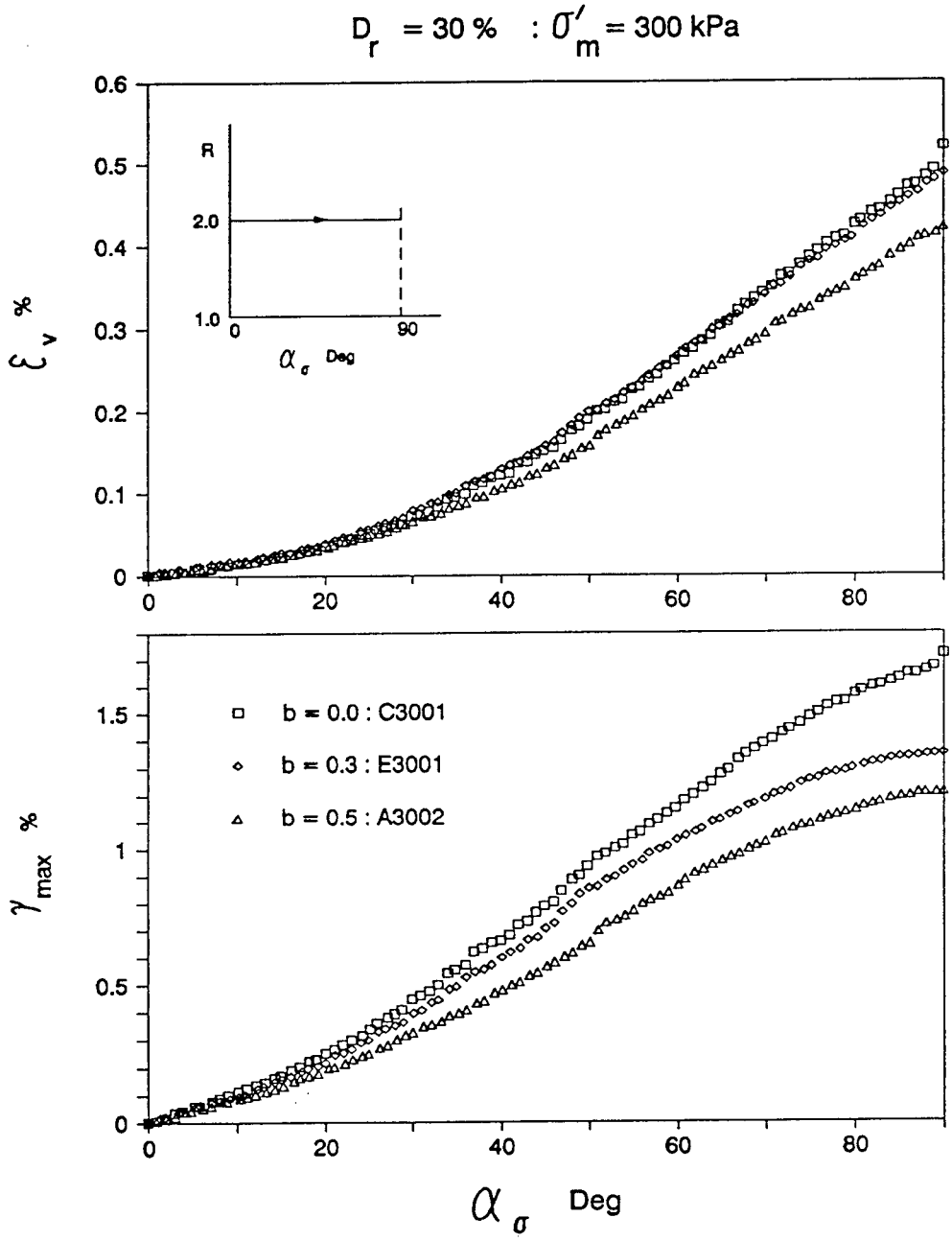

Figure 5.9: Effect of b parameter on deformation due to principal stress rotation

regardless of α_σ. However, significant differences may be observed between maximum shear strain (γ_{max}) induced for a given value of α_σ. Sayao (1989), based on his principal stress rotation tests which were carried up to $\alpha_\sigma = 60°$, concluded that effect of b parameter on strain response under α paths is insignificant. The results in Fig. 5.9 however indicate that although this influence is less significant at smaller α_σ, it does become accentuated at larger values of α_σ.

Direction of Strain Increment

Figure 5.10 shows the effect of b parameter on the relation between the directions of stress increment, strain increment and stress. The direction of the strain increment $\alpha_{\Delta\epsilon}$ seems to be unaffected by the magnitude of b parameter. Thus for any given α_σ, b parameter may be considered to have small effect on strain directions during rotation of principal stresses.

5.3.2.3 Effect of Mean Normal Effective Stress

Stress Strain Behaviour

Figure 5.11 presents results of α tests at $R = 2$ and σ'_m levels of 100 and 200 kPa, but otherwise identical to those described in section 5.3.2.1. The response under σ'_m = 300 kPa (test A3002, Fig. 5.7) is also reproduced. Deformations due to principal stress rotations increase with increasing mean normal stress level. This is consistent with the generally observed behaviour of granular materials, which show increased contractive and deformable response under increasing confining stress levels.

Direction of Strain Increment

The direction of strain increments are presented in Fig. 5.12. Despite significant effects of σ'_m on the magnitudes of volumetric and maximum shear strains, the strain increment direction $\alpha_{\Delta\epsilon}$ is relatively unaffected by the level of σ'_m.

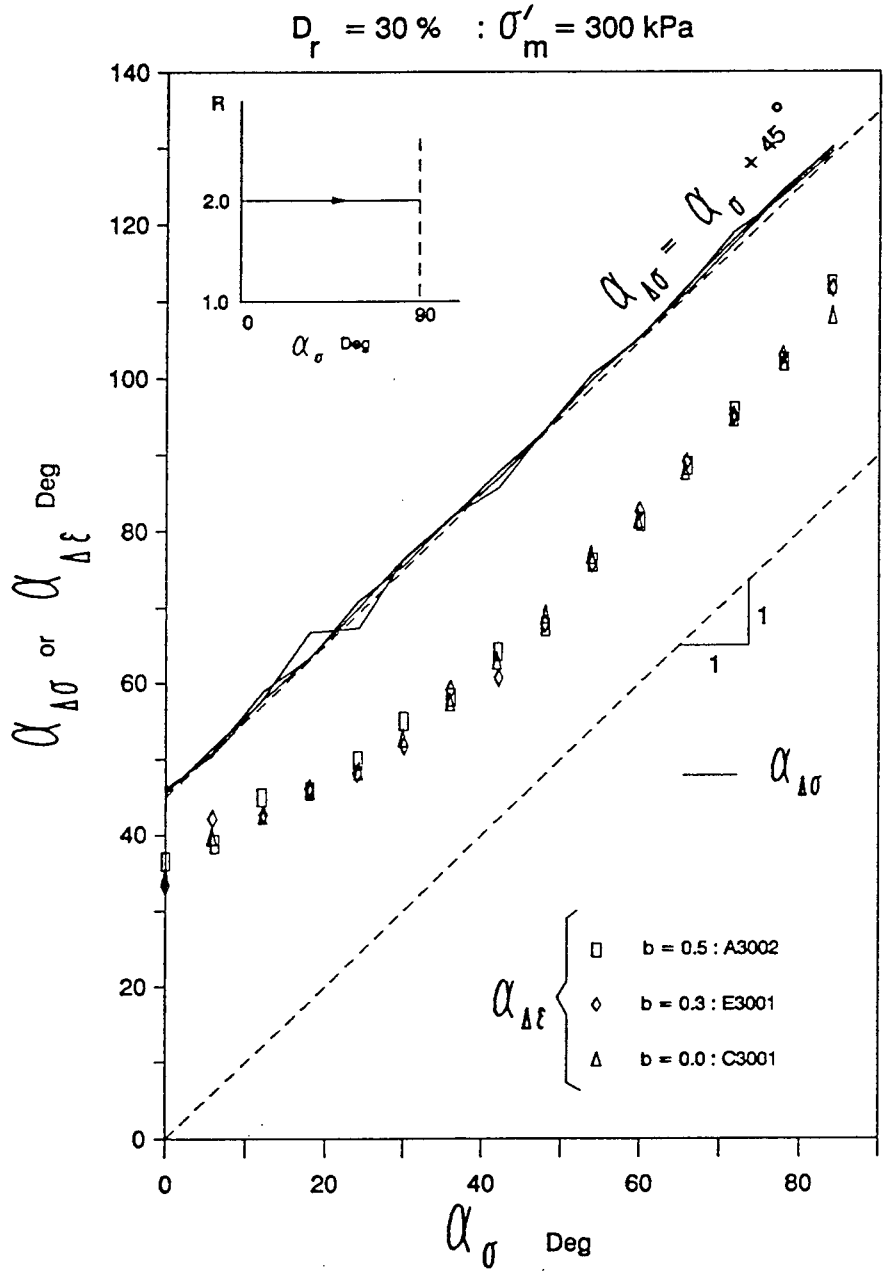

Figure 5.10: Effect of b parameter on the direction of strain increment

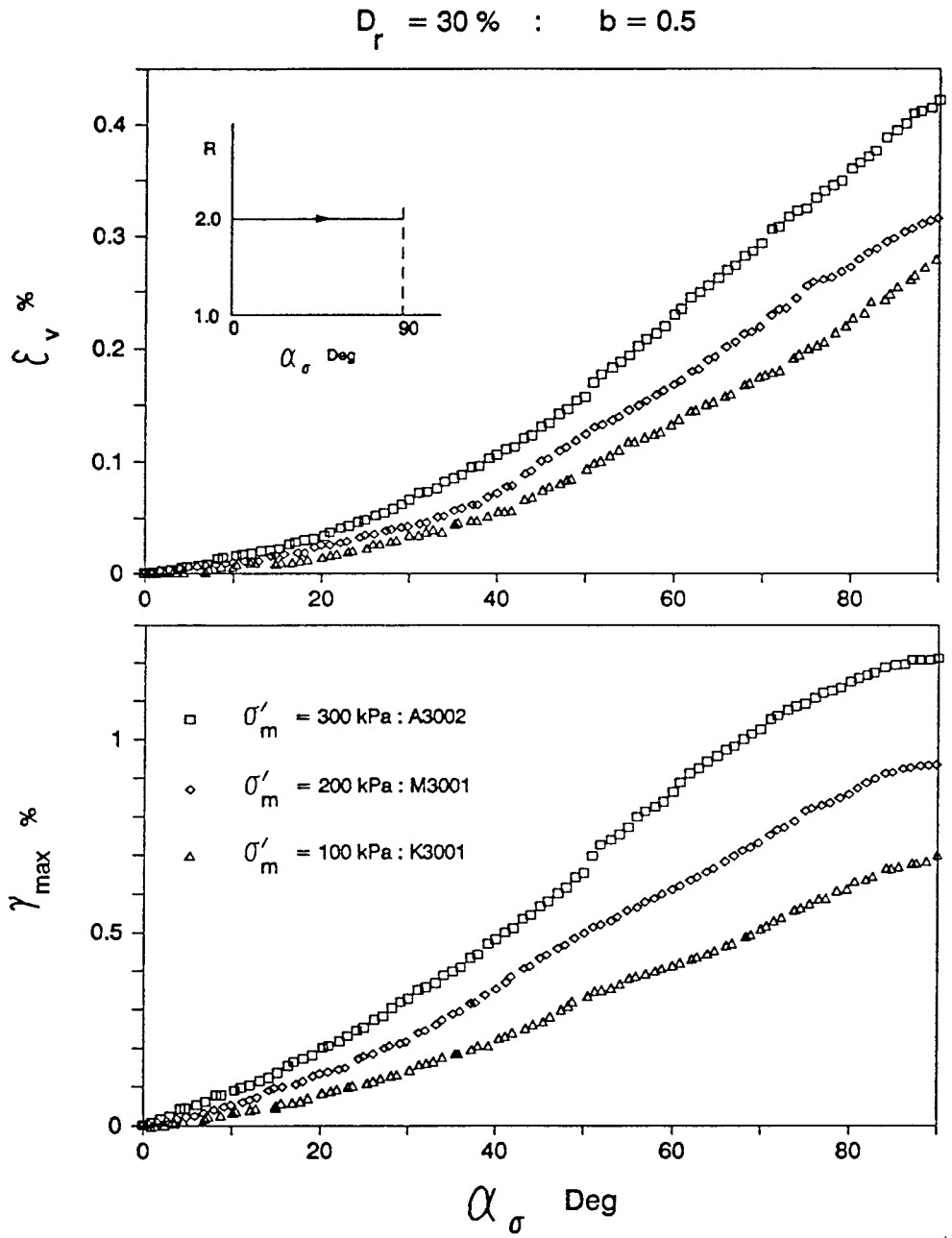

Figure 5.11: Effect of σ'_m on deformation due to principal stress rotation

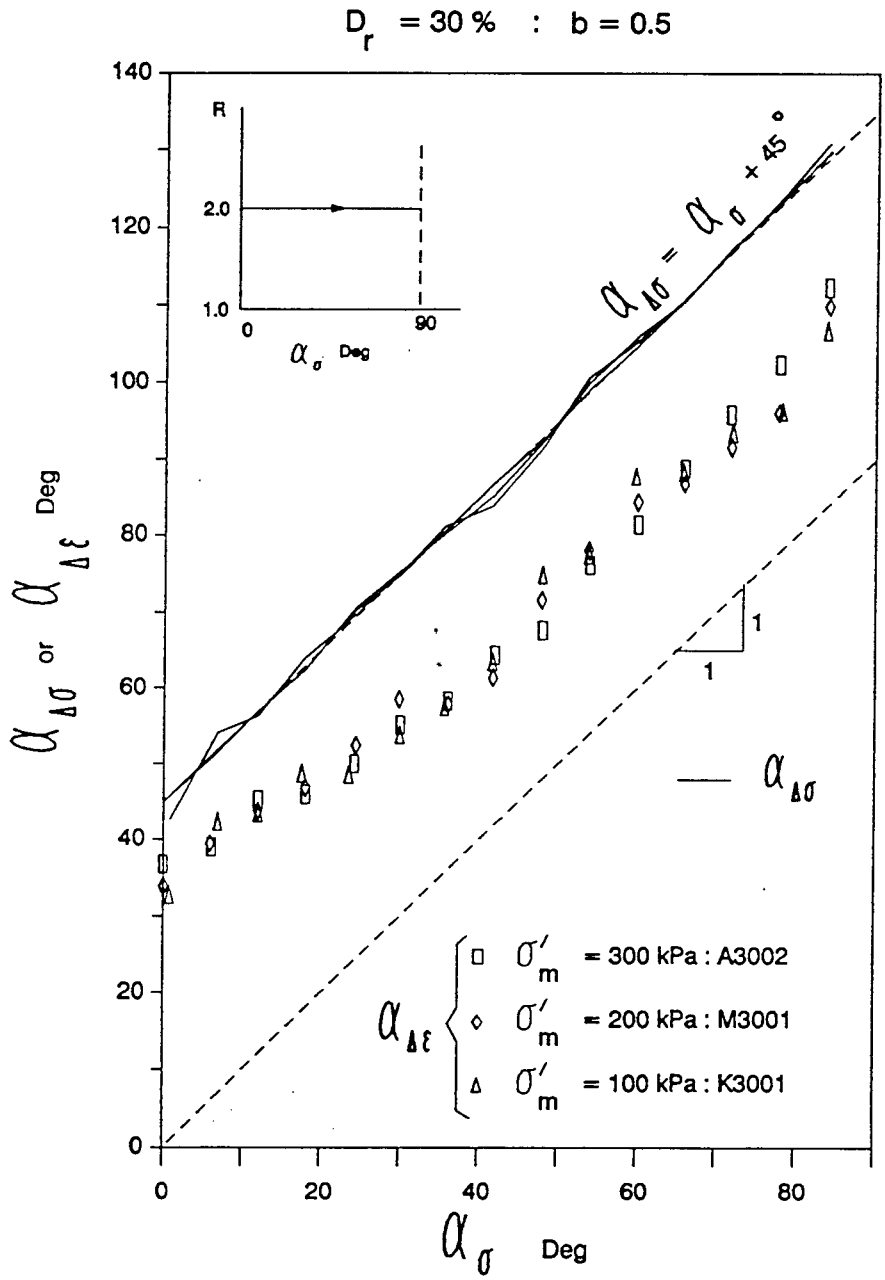

Figure 5.12: Effect of σ'_m on the direction of strain increment

5.3.3 Response to α Loading at Higher Relative Densities

Samples with D_r = 50% and 70% were subjected to α paths identical to that for specimen A3002 at D_r = 30% in Fig. 5.7. Thus stress state of the samples was σ'_m = 300 kPa, b = 0.5 and α_σ = 0° prior to principal stress rotation at R = 2.

5.3.3.1 Stress Strain Behaviour

Both volumetric and shear deformations shown in Fig. 5.13 decrease markedly with increasing relative density. This is due to the reducing degree of inherent anisotropy of sands (getting closer to becoming isotropic) under increasing packing density, as demonstrated in Fig. 5.2. As a result, principal stress rotations induce less deformations in dense sand.

Regardless of density state, the volumetric strains are contractive and increase with increasing principal stress rotation. At higher density levels, however, the value of maximum shear strains (γ_{max}) increases up until a value of $\alpha_\sigma \approx 70°$. With further rotation of principal stresses beyond 70°, γ_{max} starts to decrease indicating a stiffening of the distortional mode of deformation.

5.3.3.2 Direction of Strain Increments

Possible cause behind the decrease in distortional strains at higher α is revealed by examining the directions of strain increments $\alpha_{\Delta\epsilon}$ as shown in Fig. 5.14. For denser sand, $\alpha_{\Delta\epsilon}$ initially is close to $\alpha_{\Delta\sigma}$. As rotation builds up, $\alpha_{\Delta\epsilon}$ moves closer to α_σ. However, with further increase in rotation this trend is changed once again, and $\alpha_{\Delta\epsilon}$ starts to come closer to $\alpha_{\Delta\sigma}$. Since $\gamma_{max} = \varepsilon_1 - \varepsilon_3$ is a vector quantity, both magnitude and directional changes in incremental strains $\Delta\varepsilon_1$ and $\Delta\varepsilon_3$, govern increase or decrease in γ_{max}. Consequently, the observed decrease in γ_{max} at larger α_σ can be attributed to the changing trend in the direction of major principal strain

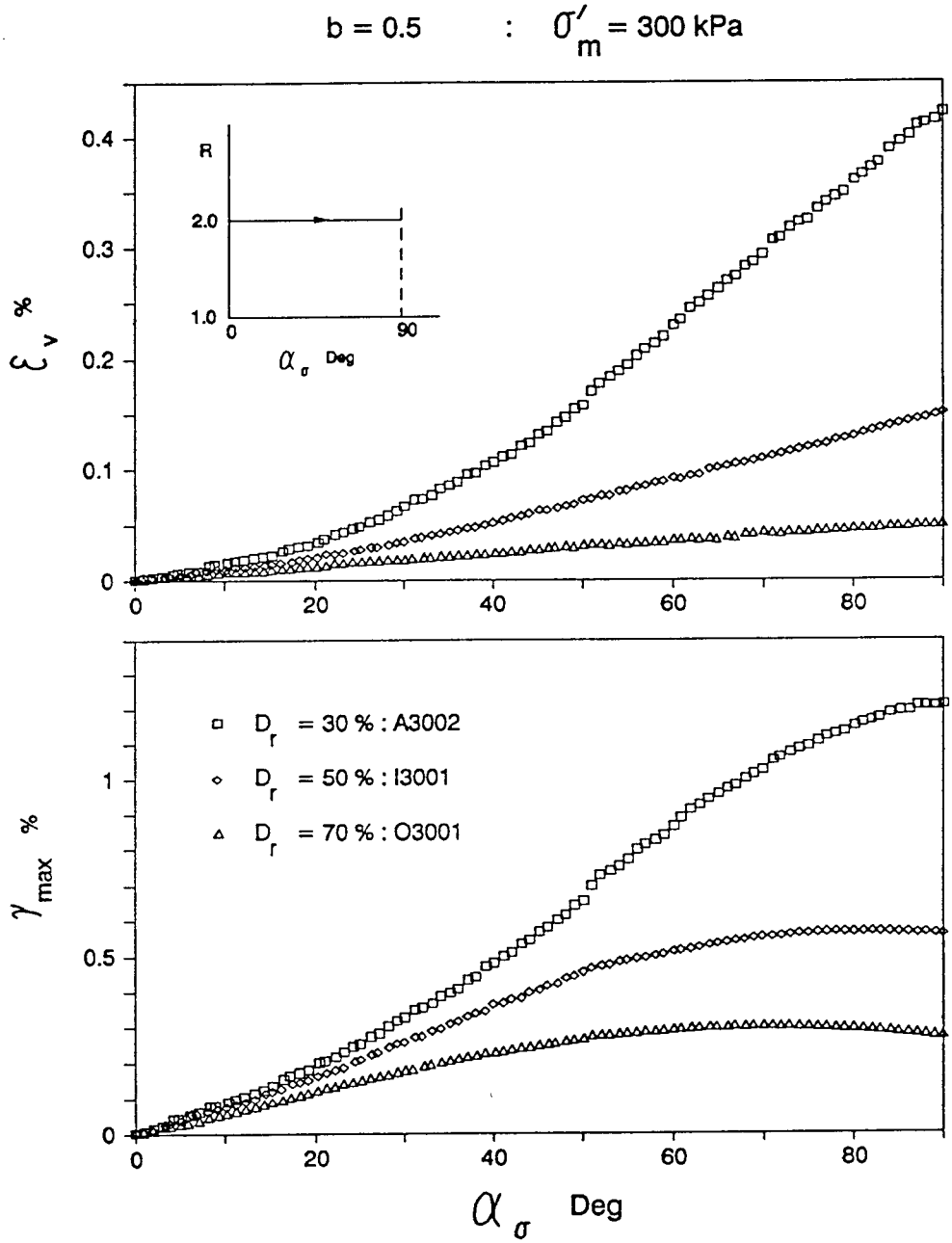

Figure 5.13: Effect of D_r on deformations due to principal stress rotation

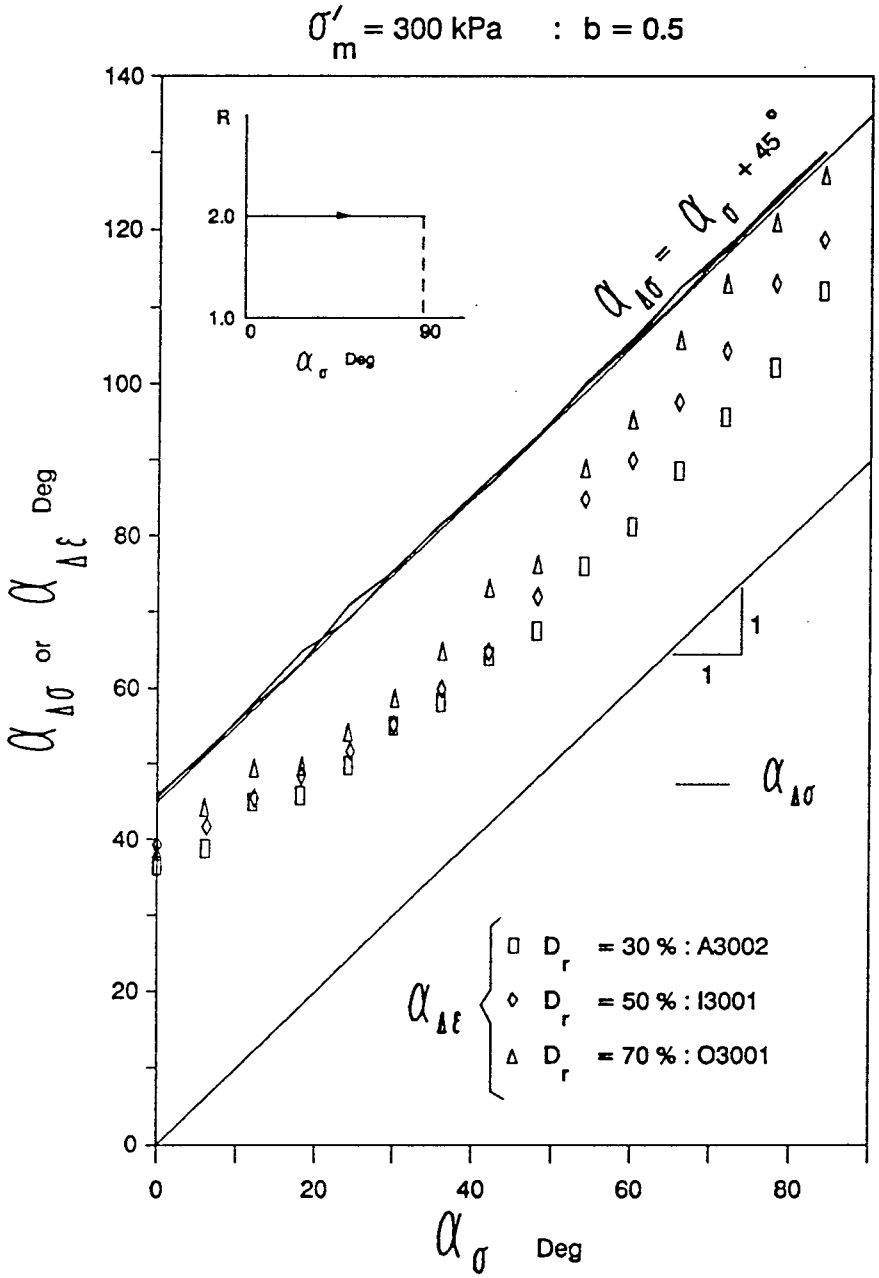

Figure 5.14: Effect of D_r on the direction of strain increment

increment shown in Fig. 5.14.

5.3.4 Stress Path Dependence of Deformations

In loading of medium loose sands along R and α paths under fixed σ'_m = 300 kPa and b = 0.5 (sections 5.3.1 and 5.3.2), stress state (R, α) = (2, 45°)[3] is common to R paths A0451 and α path A3002, and the state (2, 90°) is common to R path A0901 and α path A3002 (Fig. 5.15). Likewise, stress states (1.65, 45°), (1.65, 90°), (1.35, 45°) and (1.35, 90°) can be identified as points of intersections of R paths A0451 and A0901 with α paths A2001 and A1001. It would be of interest to examine stress path dependence of deformation, by comparing deformations accumulated at these common stress states arrived through different stress paths.

Figure 5.15 shows comparison of volumetric and maximum shear strains developed in R paths with those in α paths in medium loose sand. A close match for both volumetric strain ε_v and maximum shear strain γ_{max} may be noted at common stress states (2, 45°), (1.65, 45°) and (1.35, 45°), indicating path independent stress strain behaviour. Note, that strains in α paths must include strains developed during R loading from the starting R = 1 state. At the common stress state (2, 90°), (1.65, 90°) on the other hand, the volumetric as well as maximum shear strains developed through α paths of test A3002 and A2001 respectively are significantly higher than those along R path A0901. This can be explained in terms of the effects of continuous principal stress rotation on deformations, which become much pronounced at higher R and α_σ levels, as observed in Fig. 5.7. α paths A3002 and A2001 experiencing continuous principal stress rotation over the full range of 90° are more prone to development of strains, than path A0901, which involves no principal stress rotation at all. This leads to a wider difference between strains at the common stress points (2, 90°) and (1.65, 90°).

[3]Coordinates (R, α_σ) in the stress space.

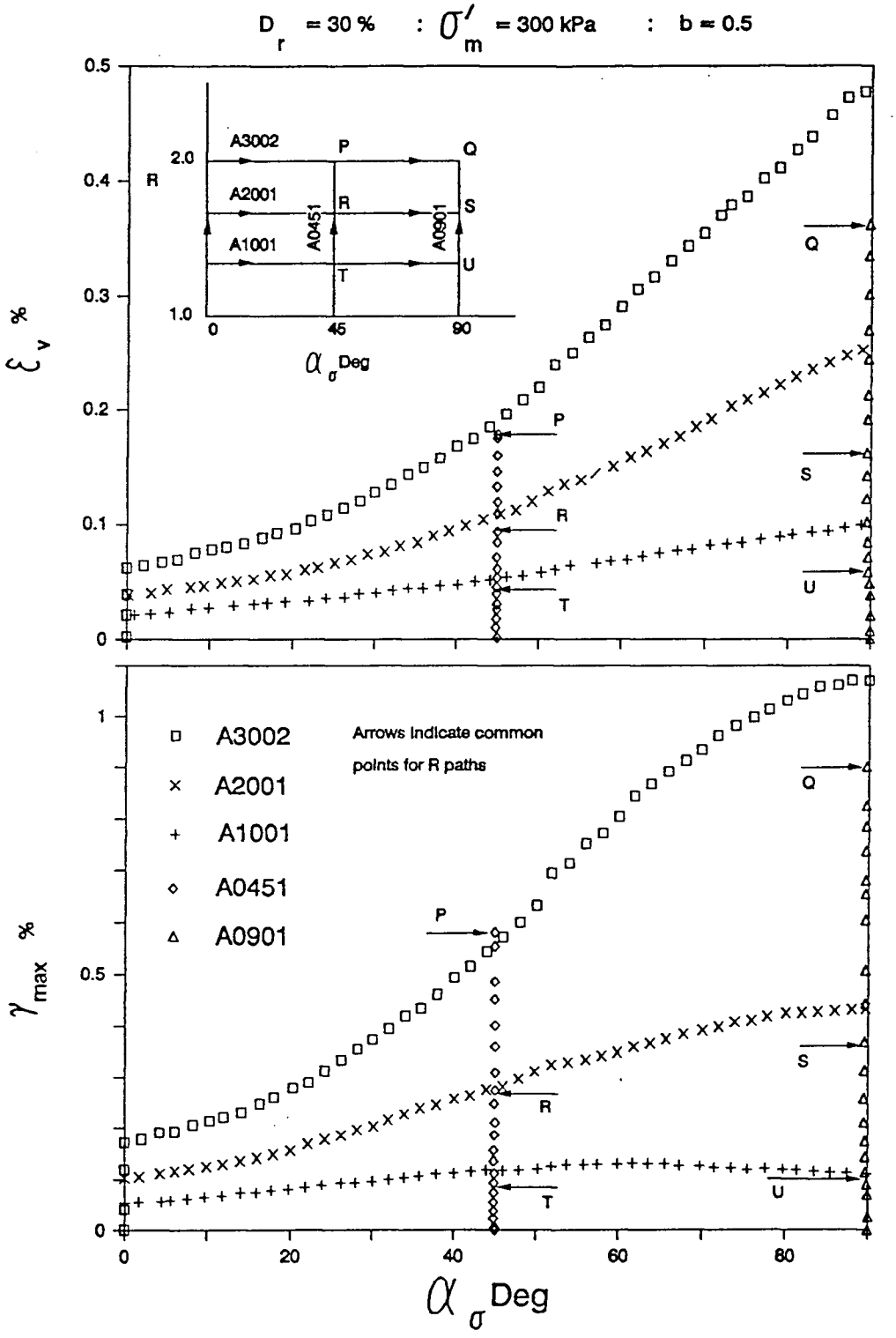

Figure 5.15: Stress path dependence of deformations from R and α tests

The deformations at common stress state (1.35, 90°) show less significant path dependence when compared to those observed at higher R levels at $\alpha_\sigma = 90°$. This can be expected, since the deformations due to principal stress rotations are small at lower levels of stress ratios.

5.4 Deformation Under Simultaneous Increase in Stress Ratio and Principal Stress Rotation

Under constant levels of b and σ'_m it is possible to impose simultaneous increase in R and α_σ along any arbitrary path in the R - α_σ space. A comprehensive investigation was made of deformation under linear R - α paths. A limited study was also carried out under a multi-linear stress path in the R - α_σ space. Effects of levels of b and σ'_m during linear R - α paths and of relative density under identical linear R - α paths was also investigated.

Possible path independence of deformations is initially assessed by comparing strains from α paths with those from R - α paths at common terminal stress states. Later, the investigations on possible path independent deformation response are extended to cover intermediate stress states in R - α_σ domain.

5.4.1 Behaviour of Loose Sand under Linear R - α Paths

Samples of medium loose Ottawa sand ($D_r = 30\%$) were loaded along several linear R - α paths under constant $b = 0.5$ and $\sigma'_m = 300$ kPa (test Series A). Each sample was subjected to a stress path which had two phases. In the first phase R and α_σ were increased simultaneously in a linear manner (i.e. R - α path). This phase ended when the stress ratio R reached a target value of 2.0. Tests in this series differed from each other by the fact that the slope of R - α path was different in each test. As such, the first phase of the tests A3301, A3451, A3601 and A3901 ended at $\alpha_\sigma = 30$,

45, 60 and 90 degrees respectively (Fig. 5.16). At the end of the first phase (after reaching $R = 2$) all samples (except A3901) were subjected to continuous principal stress rotation upto $\alpha_\sigma = 90°$, while the values of σ'_m, R and b were held constant at 300 kPa, 2.0 and 0.5 respectively. This made the second phase of the tests to be of type α and coincident with the α path of test A3002.

5.4.1.1 Stress Strain Behaviour

Figure 5.16 shows the effect of the slope of R - α path on deformation response of medium loose Ottawa sand. Contours of constant R values are also drawn on the same plot to highlight the effects of mobilized stress ratio. For a given value of α_σ, sand in which higher stress ratio is mobilized accumulates larger strains. Deformations at low mobilized R (< 1.5) may be seen to be dependent on R only and largely independent of principal stress rotation α_σ of up to about 30°.

These observations are consistent with the deformation response observed from principal stress rotation tests with constant R, b and σ'_m in Fig. 5.7, wherein the effect of R on the deformations due to principal stress rotations were found to be more pronounced at higher R levels.

5.4.1.2 Direction of Strain Increment

The direction of strain increment $\alpha_{\Delta\epsilon}$ in linear R - α paths is given in Fig. 5.17. Unlike α paths where direction of stress increment $\alpha_{\Delta\sigma}$ leads α_σ by 45°, in R - α paths $\alpha_{\Delta\sigma}$ initially assumes a value close to α_σ. With increasing rotation, $\alpha_{\Delta\sigma}$ diverges more and more from α_σ.

The direction of strain increment $\alpha_{\Delta\epsilon}$ essentially coincide with that of stress increment $\alpha_{\Delta\sigma}$ until $\alpha_{\Delta\sigma}$ approaches approximately 45°. This trend may be noted for all the R - α paths, even though in each stress path the values of R and α_σ are continuously changing in a different manner. For $\alpha_{\Delta\sigma} >$ about 45°, strain increment

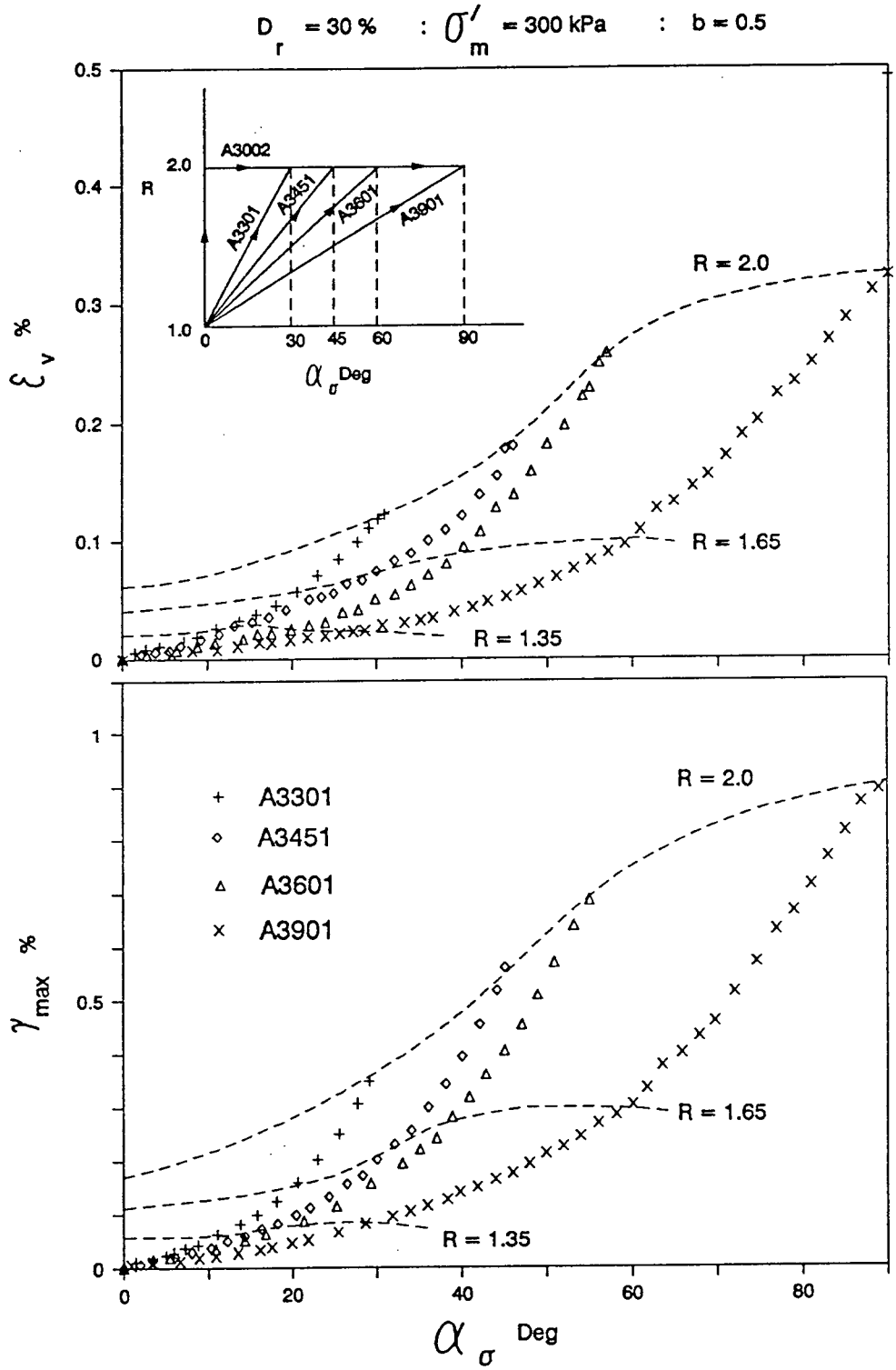

Figure 5.16: Stress strain behaviour under linear R - α loading

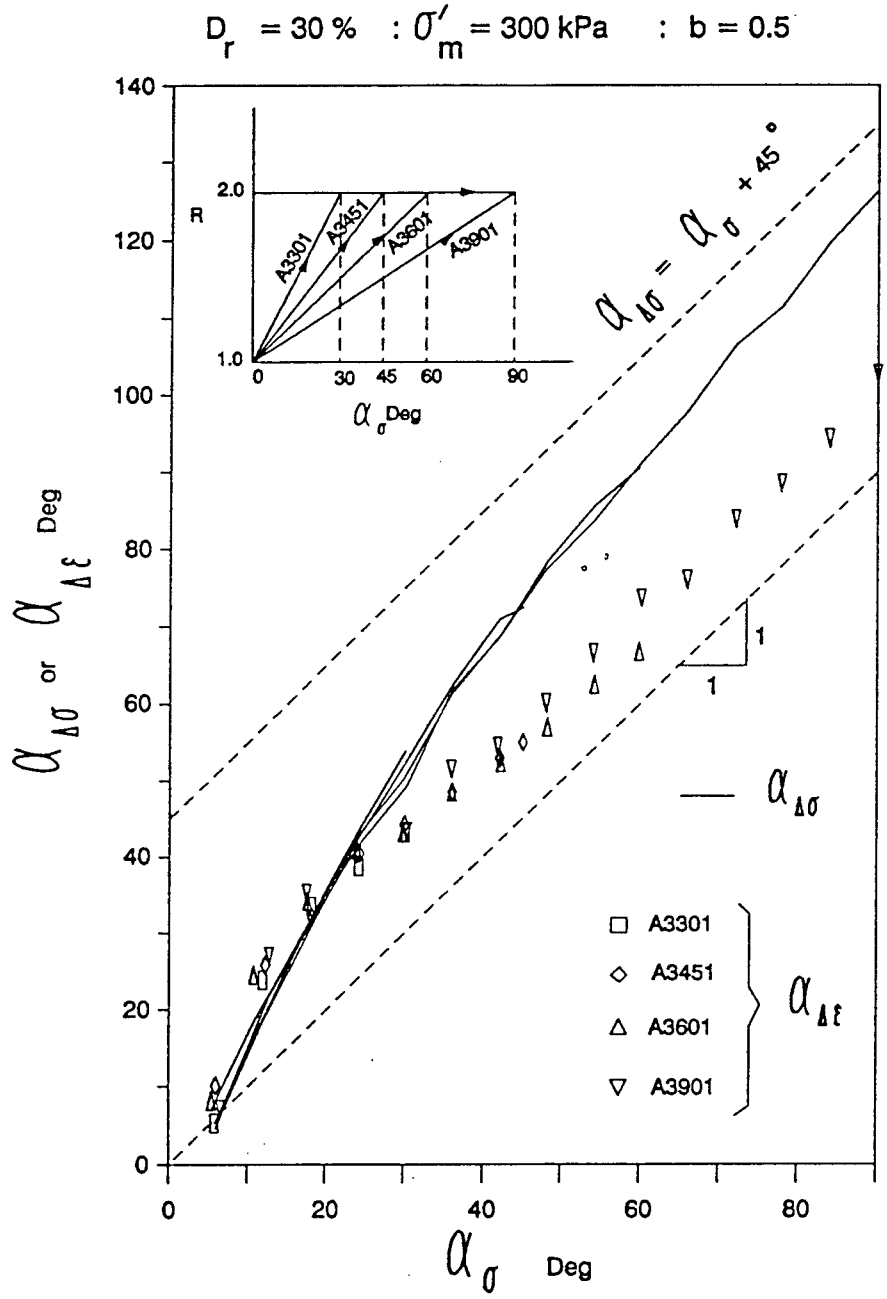

Figure 5.17: Direction of strain increment under linear R - α loading

direction gradually deviates from stress increment direction and moves closer to the direction of stress. It is of interest to examine these results which contrast with the observations from continuous principal stress rotation tests with fixed R, in which the strain increment direction $\alpha_{\Delta\varepsilon}$ was markedly influenced by the level of stress ratio (Fig. 5.8). It is also important to note that in α paths (where $0° \leq \alpha_\sigma \leq 90°$), the applied principal stress increment was always in the region of $45° \leq \alpha_{\Delta\sigma} \leq 135°$. These findings suggest that the direction of strain increment $\alpha_{\Delta\varepsilon}$ is almost totally determined by the direction $\alpha_{\Delta\sigma}$, if the applied stress increment direction $\alpha_{\Delta\sigma}$ is inclined between 0° and 45° (i.e. closer to the direction of deposition). On the other hand, more the direction of the applied stress increment is inclined closer to the bedding plane (i.e. $\alpha_{\Delta\sigma} \geq 45°$), the direction of strain increment appears to be influenced not only by $\alpha_{\Delta\sigma}$ but also by the effects of other parameters such as R and α_σ.

5.4.1.3 Stress Path and Stress History Dependence of Deformations (R - α Paths versus α Paths)

Linear R - α paths A3301, A3451, A3601 and A3901 intersect α path of test A3002 at α_σ = 30, 45, 60 and 90 degrees respectively at common stress points (Fig. 5.18). Strains developed during loading until common stress states (R, α_σ) = (2, 30°), (2, 45°), (2, 60°) and (2, 90°) along R - α and α paths are shown in Fig. 5.18. It may be noted that excepting in test A3901, both volumetric and maximum shear strains that develop along the two paths, match closely at the common stress states. This reflects a stress path independent deformation behaviour.

In the case of test A3901, the strains developed at $\alpha_\sigma = 90°$ along R - α path are significantly less than those accumulated along α path in test A3002. In test A3002 principal stress rotations occur from $\alpha_\sigma = 0°$ to 90°, at $R = 2$ throughout rotation. In test A3901 however, principal stress rotations from 0° to 90° occur while R varies linearly with α_σ from 1 to 2. As such, along path A3901 stress rotation 0° - 90° occur

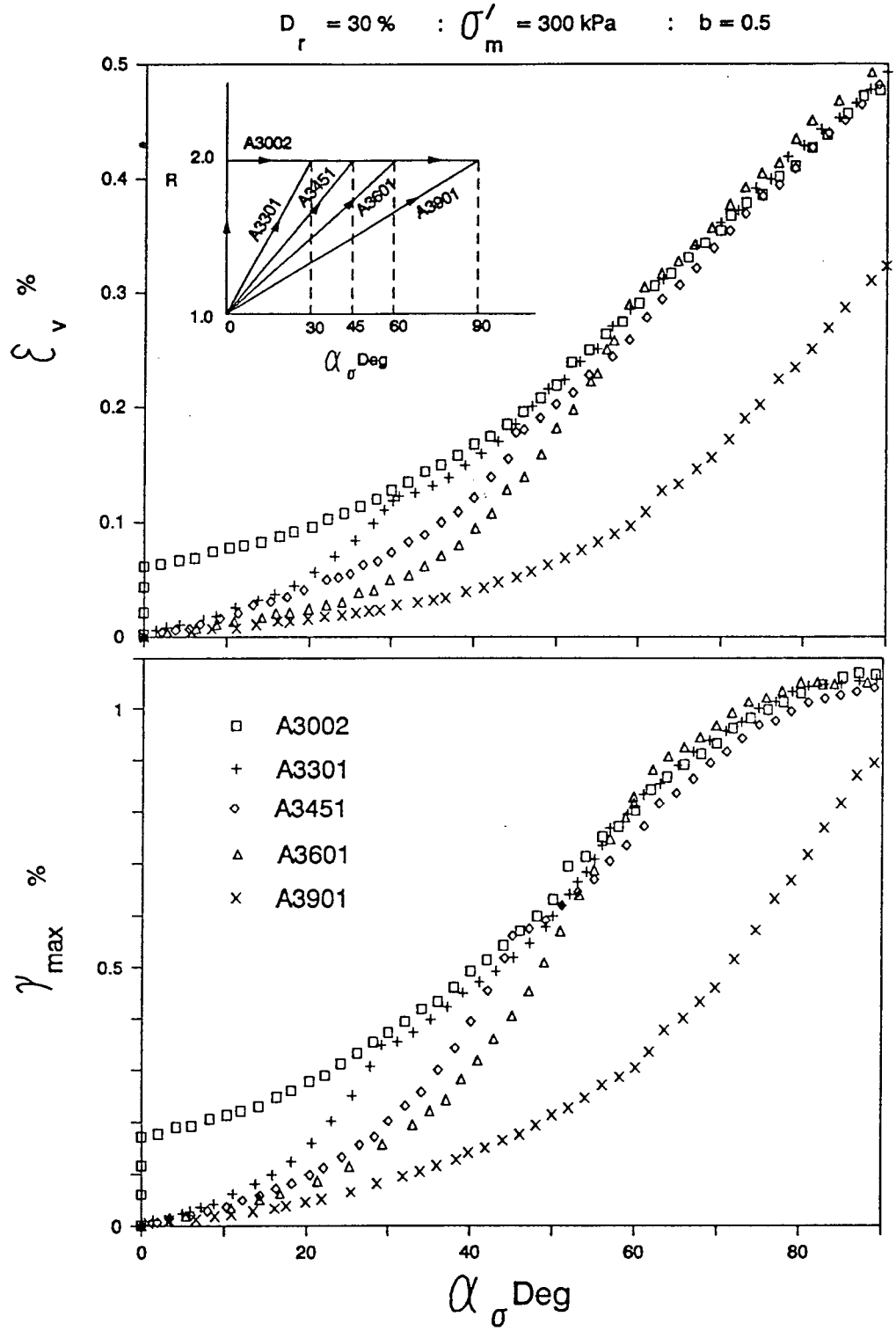

Figure 5.18: Stress path dependence of deformations under principal stress rotation - Test Series A

with R always < 2. Since strain development increases with R level at larger values of α_σ, sand in test A3901 which has little exposure to high R values would develop less strains compared to A3002 which has $R = 2$ throughout principal stress rotation of 0 to 90 degrees.

The foregoing observations therefore suggest that the deformations under stress paths with increasing R and α_σ are essentially path independent upto a stress ratio of 2, if the rotations are moderate (about less than 60 degrees). Under larger principal stress rotation, the deformations gradually become path dependent. Limited observations by Symes et al. (1988) from loadings where R and α_σ was increased in a sequential manner indicate similar path independent behaviour for Ham river sand. The concept of a state boundary surface (BS) by Symes et al. (1984, 1988) and Shibuya and Hight (1987) implies that for "loading" paths, the path independence of deformation should be observed for rotations up to $\alpha_\sigma = 90°$. Test results on Ottawa sand in Fig. 5.18, however do not support this contention at larger values of α_σ.

Once linear R - α phases of tests A3301, A3451, A3601 have been terminated at $R = 2$, the tests follow an α path identical to that of test A3002 (Fig. 5.16). Deformation behaviour in these common α phases of tests A3301, A3451 and A3601 are also presented in Fig. 5.18. It may be noted that the stress strain characteristics of the α phases of tests A3301, A3451 and A3601 closely agree with that of test A3002. This suggest that not only deformations are path independent for loading until a given stress state, the history of previous stress path loading also has no influence on the deformations along a subsequent common stress path.

Effect of Stress Ratio

Deformations in linear R - α path A4451 terminating at $R = 2.5$ and $\alpha_\sigma = 45°$ are compared with deformations in α path A4001 at $R = 2.5$ in Fig. 5.19 for medium loose Ottawa sand. The values of σ'_m, b and D_r for these two tests were 300 kPa, 0.5 and 30% respectively, identical to those for the tests described in the previous

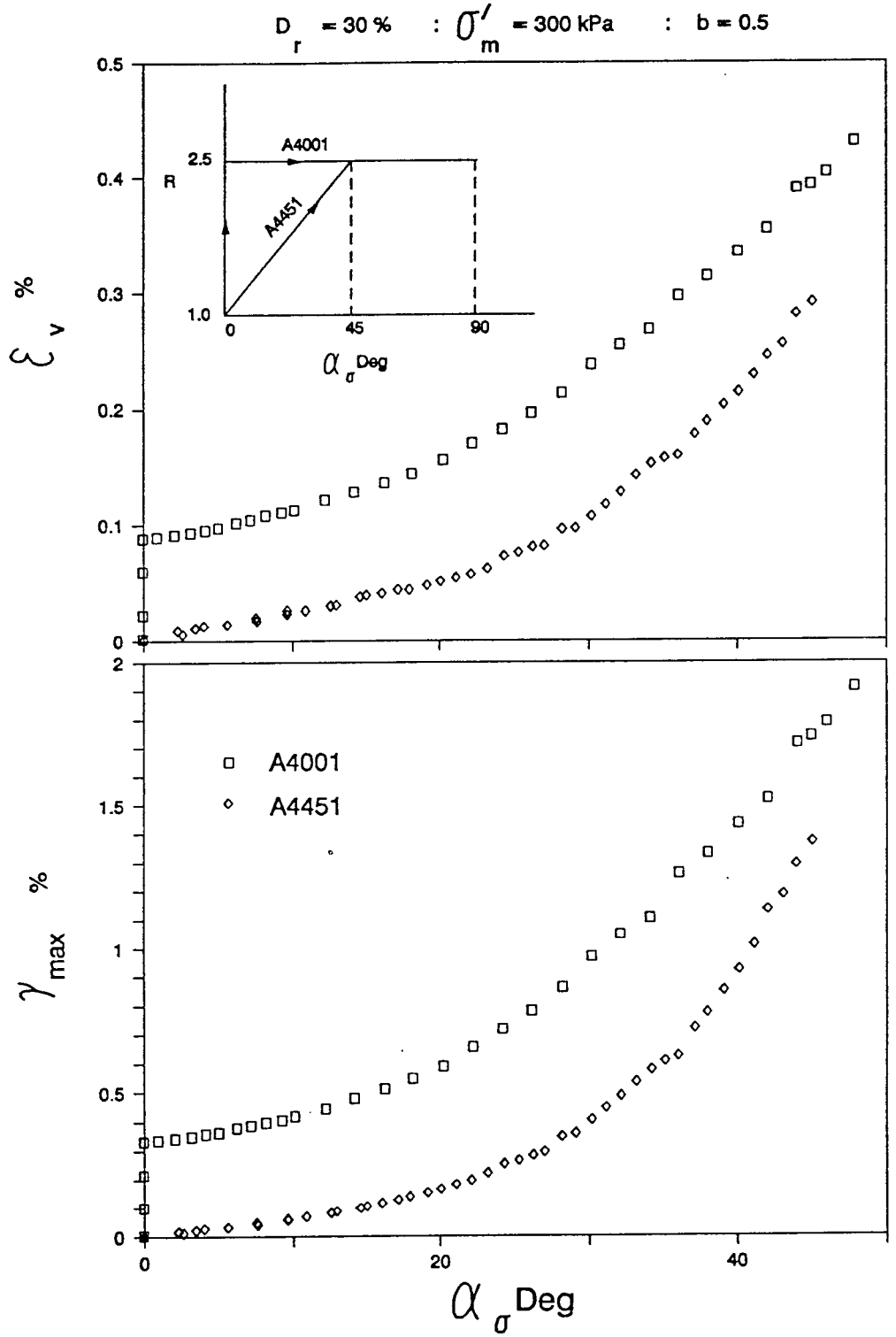

Figure 5.19: Stress path dependence of deformations at higher stress ratios

section. At the common stress state $(R, \alpha_\sigma) = (2.5, 45°)$, the strains accumulated through test A4001 are significantly higher than those developed in test A4451. This difference cannot possibly be attributed to higher stress non-uniformities within the specimen at $R = 2.5$, since β_R is quite low even at this level of stress ratio. It appears that path independent deformation behaviour observed at lower mobilized R levels will not extend to R levels larger than some threshold value.

The results presented so far suggest that loading along stress paths which include principal stress rotations exhibits path independent behaviour, provided principal stress rotations and mobilized stress ratios are held below certain threshold values. In order to establish these threshold bounds precisely, extensive stress path testing need to be done in R - α_σ space. Nevertheless, based on the test results presented for medium loose Ottawa sand, it can be concluded that path independent deformation response is found for stress states defined by $\sigma'_m = 300$ kPa; $b = 0.5$; $0° \leq \alpha_\sigma \leq 60°$ and $R \leq 2$.

Strain and stress increment directions during test A4451 are given in Fig. 5.20. Approximate coincidence of stress and strain increment directions may still be observed for $\alpha_{\Delta\sigma} < 45°$. With increasing rotation, the direction of strain increment $\alpha_{\Delta\epsilon}$ moves closer and closer to the major principal stress direction α_σ. These results are similar to the observations on strain increment directions given in Fig. 5.17 at lower levels of R.

It is to be noted that the above observations have been made from a test series with values of intermediate principal stress parameter b and mean normal effective stress σ'_m fixed at 0.5 and 300 kPa respectively. Furthermore, the results were restricted only to medium loose Ottawa sand. Stress path independence at other values of b parameter, σ'_m and relative density D_r is examined in the next sections. As noted earlier, it is not practical to perform a large number of tests in order to establish precisely the domain of path independent strain response. Therefore, in the following sections possible

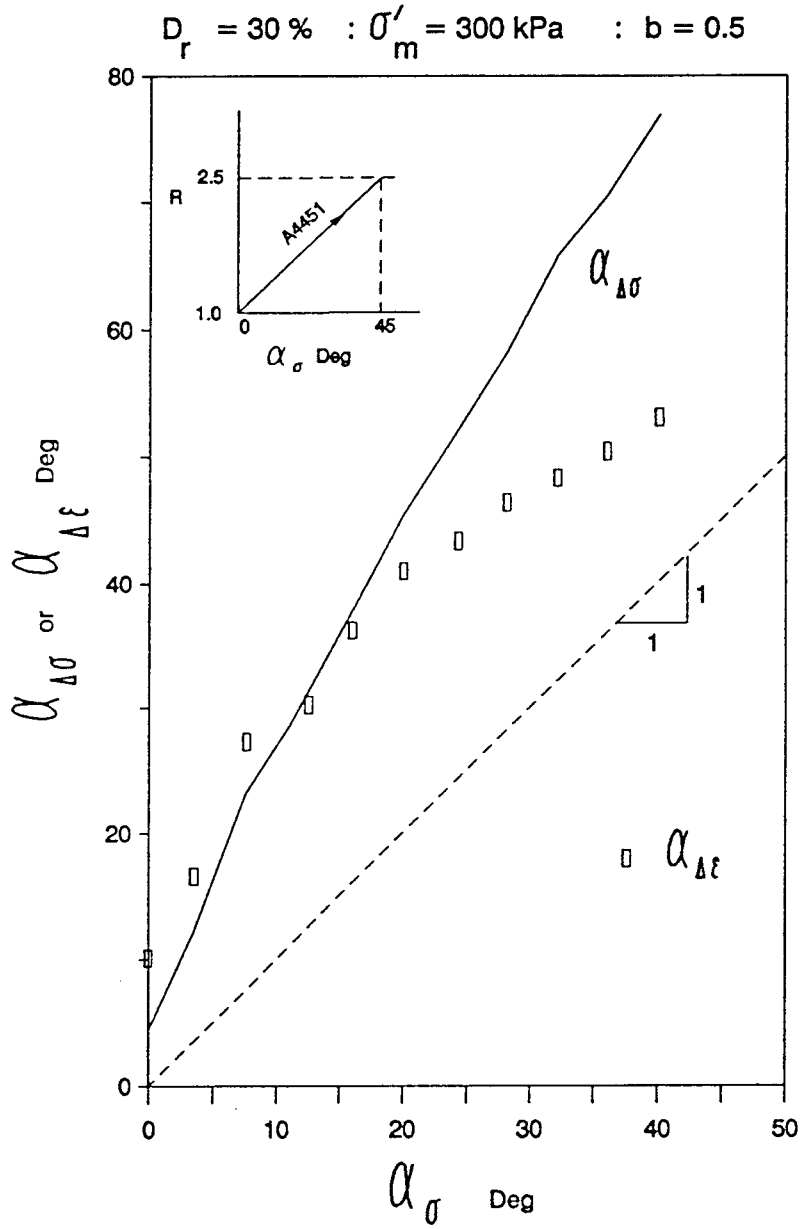

Figure 5.20: Direction of strain increments under linear R - α loading leading to higher stress ratios

path independence is investigated predominantly within the bounds of $R \leq 2$ and $\alpha_\sigma \leq 45°$. These bounds were chosen mainly because most field situations are likely to fall within these stress ranges under general loading conditions.

5.4.2 Effect of b Parameter during R - α Loading of Loose Sand

In order to investigate possible path independent behaviour under different b parameters, two additional series of tests were performed at fixed b values of 0.3 (Series E) and 0.0 (Series C) respectively (Fig. 4.17). Except for the difference in b values, the tests in each series were conducted at identical fixed values of σ'_m = 300 kPa, and D_r = 30%, the conditions identical to those imposed in Series A. Somewhat lesser number of linear R - α paths were explored when compared to those in Series A. All R - α paths in Series E and C were such that once a stress ratio of 2.0 was reached, further loading was carried along the α path of tests E3001 and C3001 respectively.

5.4.2.1 Stress Strain Behaviour

Deformation response under a selected R - α loading on medium loose Ottawa sand at three different levels of b, but identical σ'_m = 300 kPa (paths A3451, E3451 and C3451) is presented in Fig. 5.21. The b parameter does not appear to influence deformations in a significant manner for the selected R - α path in which maximum values R and α_σ are limited to 2 and 45° respectively. These results regarding the influence of b on deformation are consistent with those observed under α paths within a similar domain of R and α_σ (Fig. 5.9), and also in previous findings of Sayao (1989). However, it is cautioned that the effect of b level could be significant if principal stress rotations are relatively large.

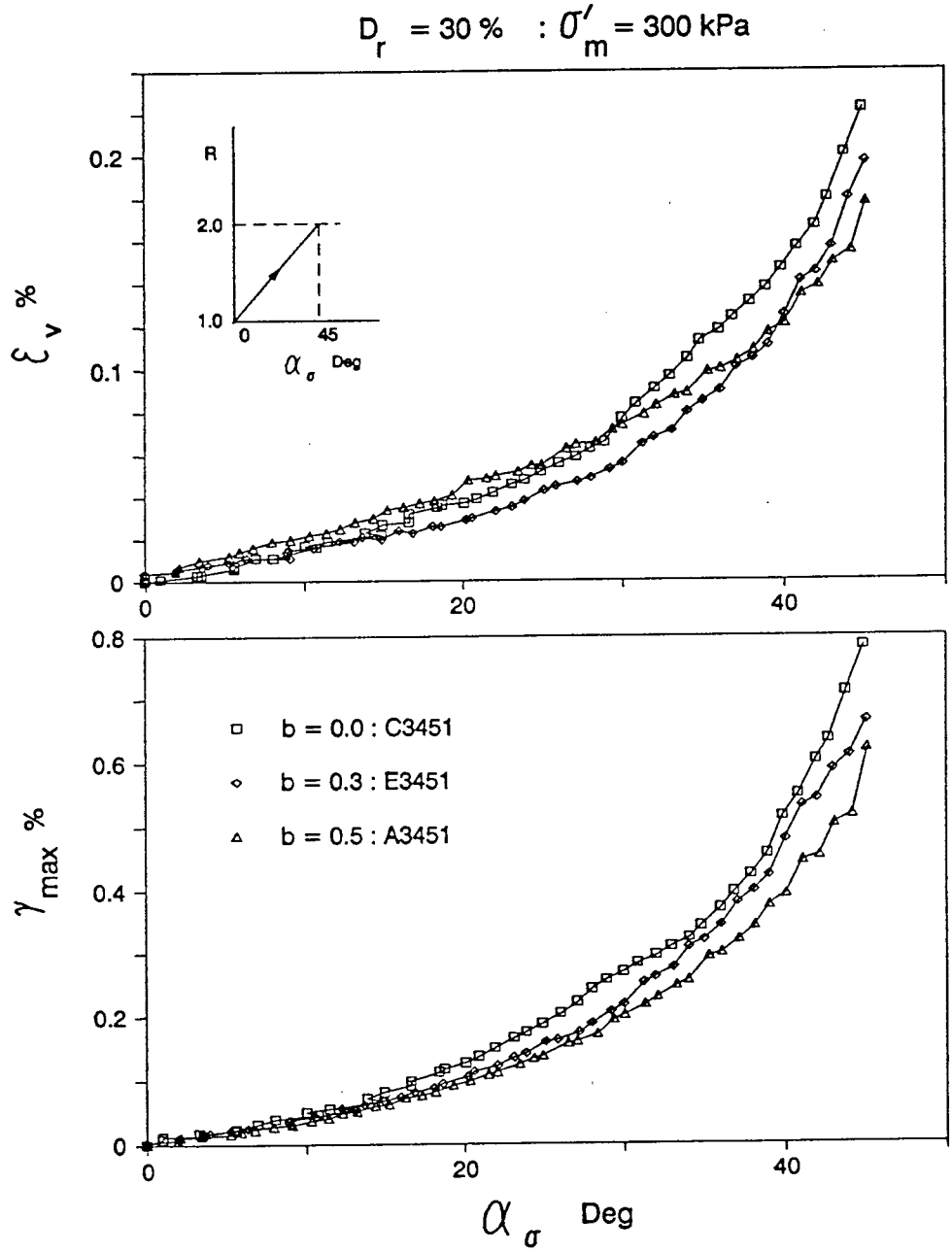

Figure 5.21: Effect of b parameter on the behaviour under linear R - α loading

5.4.2.2 Direction of Strain Increment

Directions of stress and strain increment for the same stress paths considered in the previous section are plotted in Fig. 5.22. There is no significant effect of b parameter on the direction of strain increment $\alpha_{\Delta\varepsilon}$. A near coincidence of stress and strain increment directions occurs in the domain of $0° \leq \alpha_{\Delta\sigma} \leq 45°$. When $\alpha_{\Delta\sigma}$ exceeds approximately 45°, the direction of strain increment tends to move gradually towards the direction of major principal stress α_σ. These results support further the observations in Figs. 5.17 and 5.20, that if $\alpha_{\Delta\sigma}$ is closer to the direction of deposition, $\alpha_{\Delta\sigma} \approx \alpha_{\Delta\varepsilon}$ regardless of the current values of R and α_σ.

5.4.2.3 Stress Path and Stress History Dependence of Deformations

Figure 5.23 compares deformations along R - α stress paths (Series E) with those along α paths at common stress states for fixed b value of 0.3. The strains developed along linear R - α stress paths of tests E3301 and E3451 match closely the strains accumulated along α path of test E3001 at the common stress states (R, α_σ) = (2, 30°) and (2, 45°). Thus path independence of deformations is also noted under a b value of 0.3. R - α loading along path E3901, however resulted in significantly lower deformations when compared with that along α path of test E3001 at the common stress state (R, α_σ) = (2, 90°). Therefore, likewise the results in test Series A, for paths involving larger rotations of principal stresses (Fig. 5.18) the behaviour gradually changes from path independent to path dependent.

Figure 5.24 which presents results similar to those in Fig. 5.23 but under $b = 0.0$ (Series C), also shows essentially identical deformations at common stress points regardless of the stress path. Thus, deformations are path independent in the domain $R \leq 2.0$ and $0° \leq \alpha_\sigma \leq 45°$.

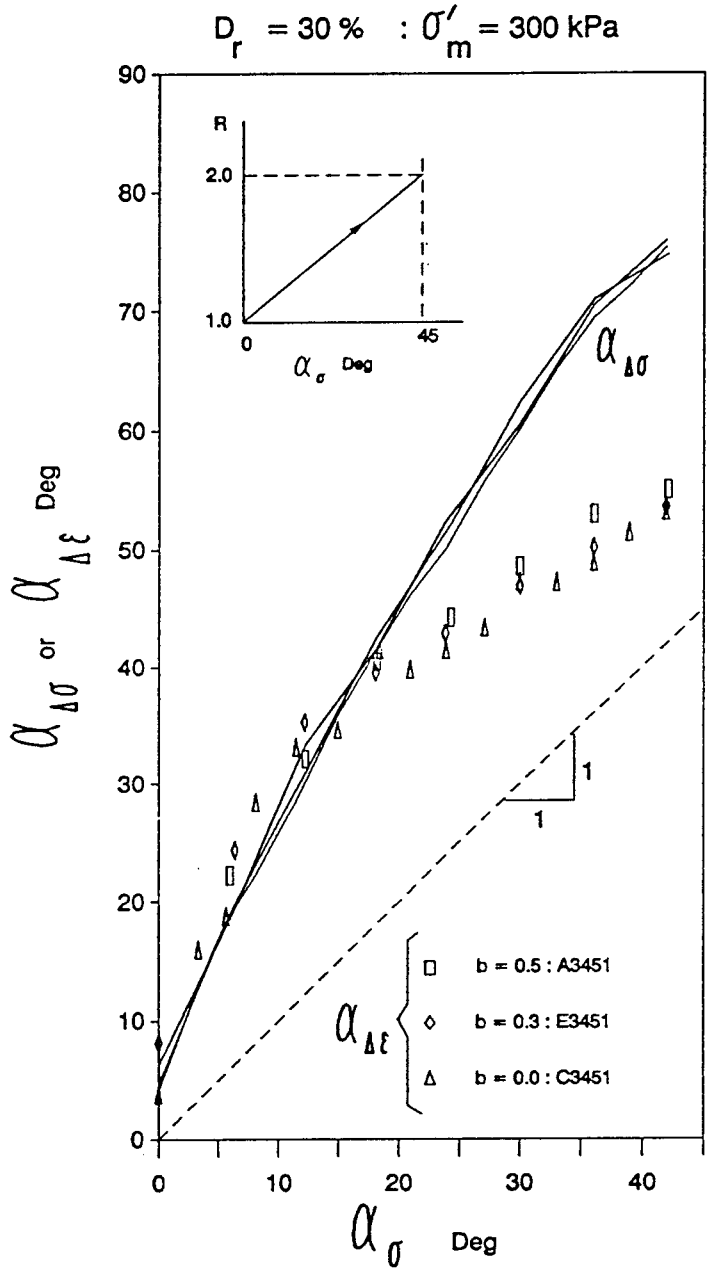

Figure 5.22: Effect of b parameter on the direction of strain increment in linear R - α loading

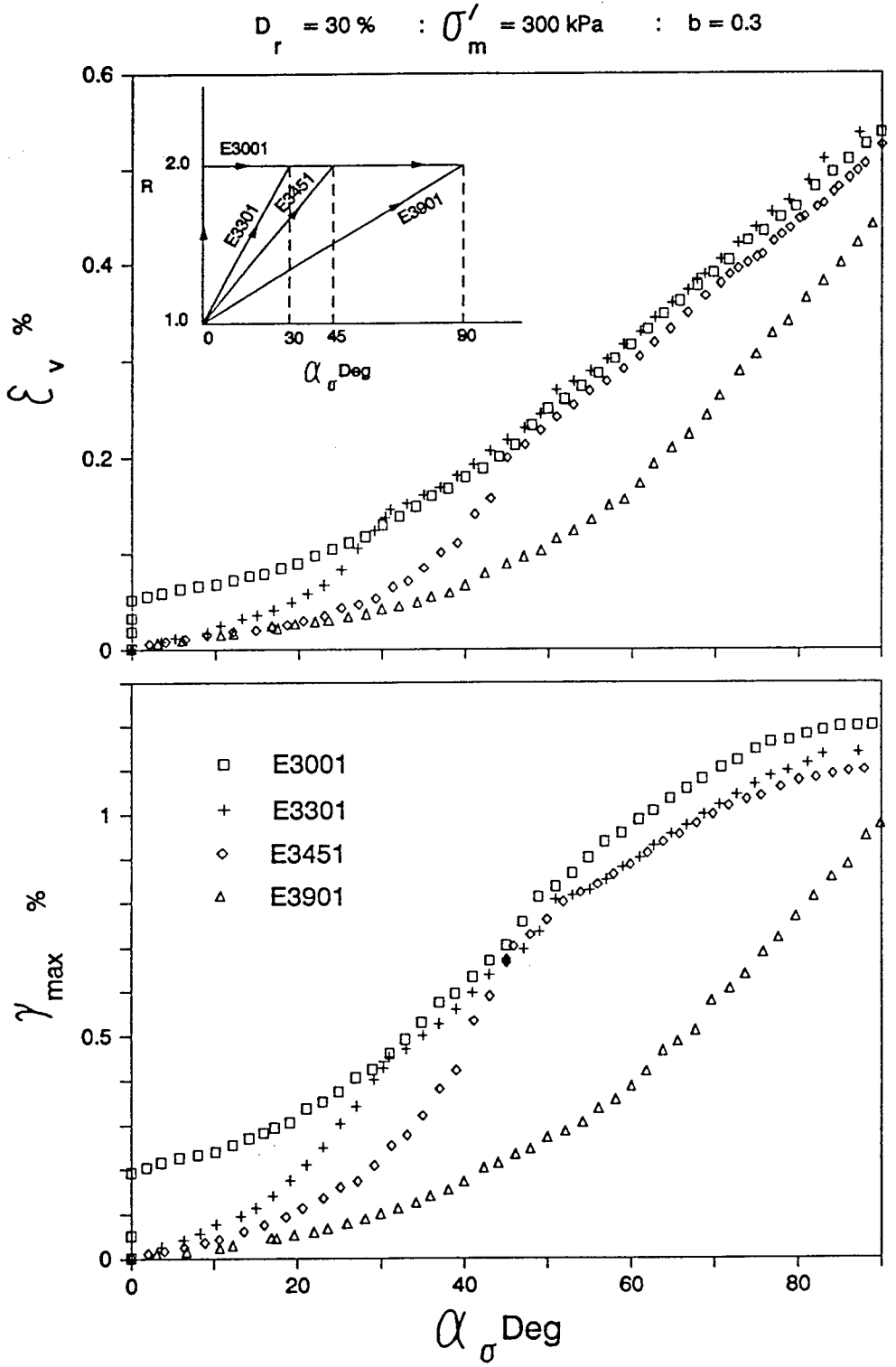

Figure 5.23: Effect of b parameter on stress path dependence of deformations - Test Series E

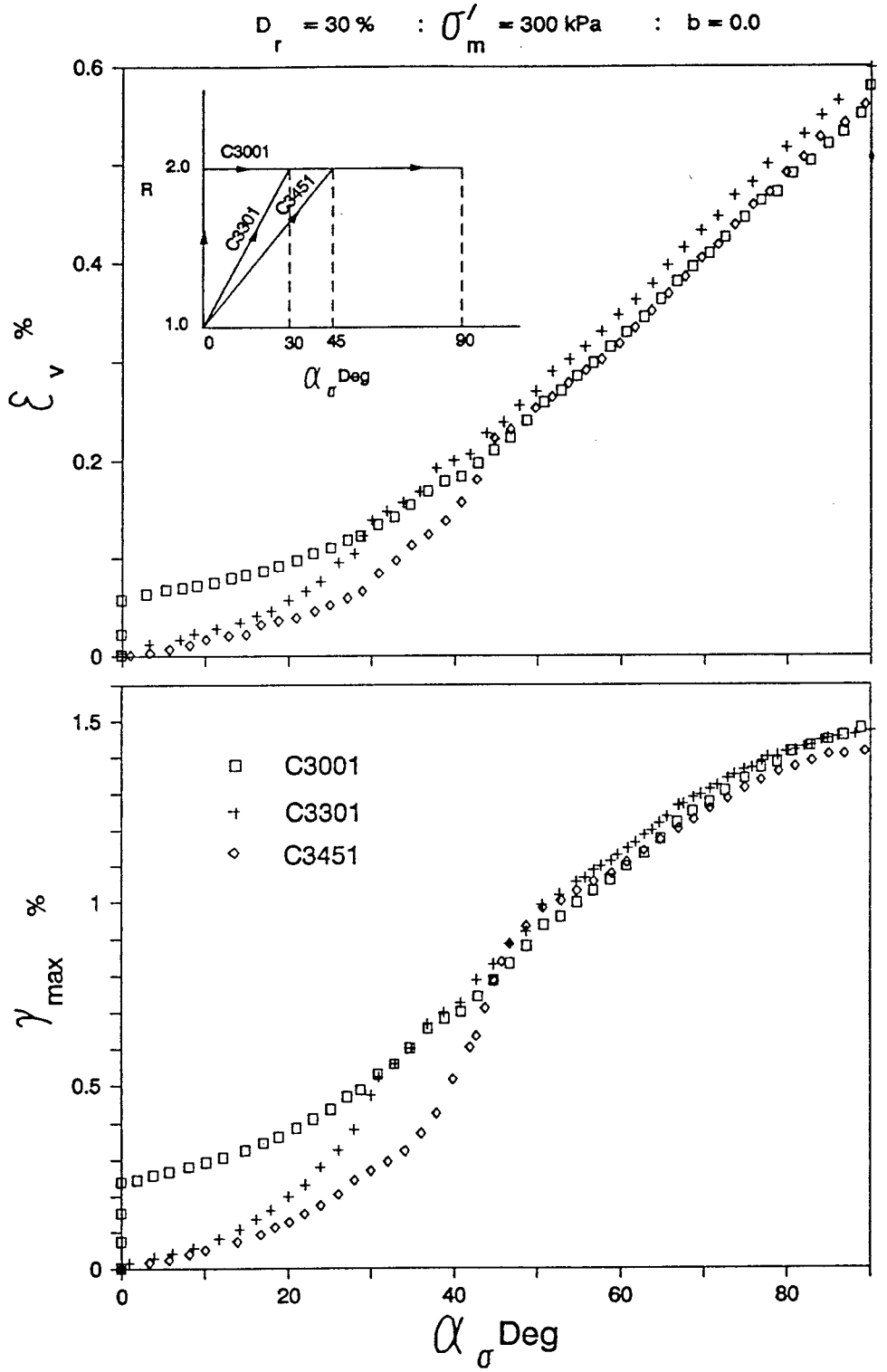

Figure 5.24: Effect of b parameter on stress path dependence of deformations - Test Series C

Tests E3301 and E3451 ($b = 0.3$) after reaching $R = 2$ follow an α path identical to that of test E3001 (Fig. 5.23). The sand response along common legs of these α paths of tests E3301, E3451 and E3001 are nearly identical. This implies that R - α path stress history has no influence on the subsequent deformation behaviour. A similar, essentially stress history independent behaviour may be noted from test results of Series C ($b = 0.0$) illustrated in Fig. 5.24.

5.4.3 Effect of σ'_m during R - α Loading of Loose Sand

Two series of tests with $\sigma'_m = 200$ kPa (Series M) and $\sigma'_m = 100$ kPa (Series K) were carried out to examine the influence of σ'_m. A constant value of $b = 0.5$ and a medium loose condition ($D_r = 30\%$) for the density was chosen for these two series so that the results from Series A (which also had a b parameter equal to 0.5 and $D_r = 30\%$) could be conveniently supplemented. For both the series, only one R - α path moving from (R, α_σ) = (1.0, 0°) to (2.0, 45°) (tests M3451 and K3451, see Fig. 4.17) was considered in order to investigate possible path independent strain response.

5.4.3.1 Stress Strain Behaviour

The strain response under identical R - α paths, but different σ'_m values (paths A3451, M3451 and K3451) is presented in Fig. 5.25. It may be noted that for a given R - α_σ state, volumetric and shear strains induced in the sand increase with increasing mean normal stress σ'_m. This behaviour is consistent with observations made from α paths (Fig. 5.11), and also with the generally observed granular material behaviour reflecting increasing contractancy and shear deformability with increasing confinement.

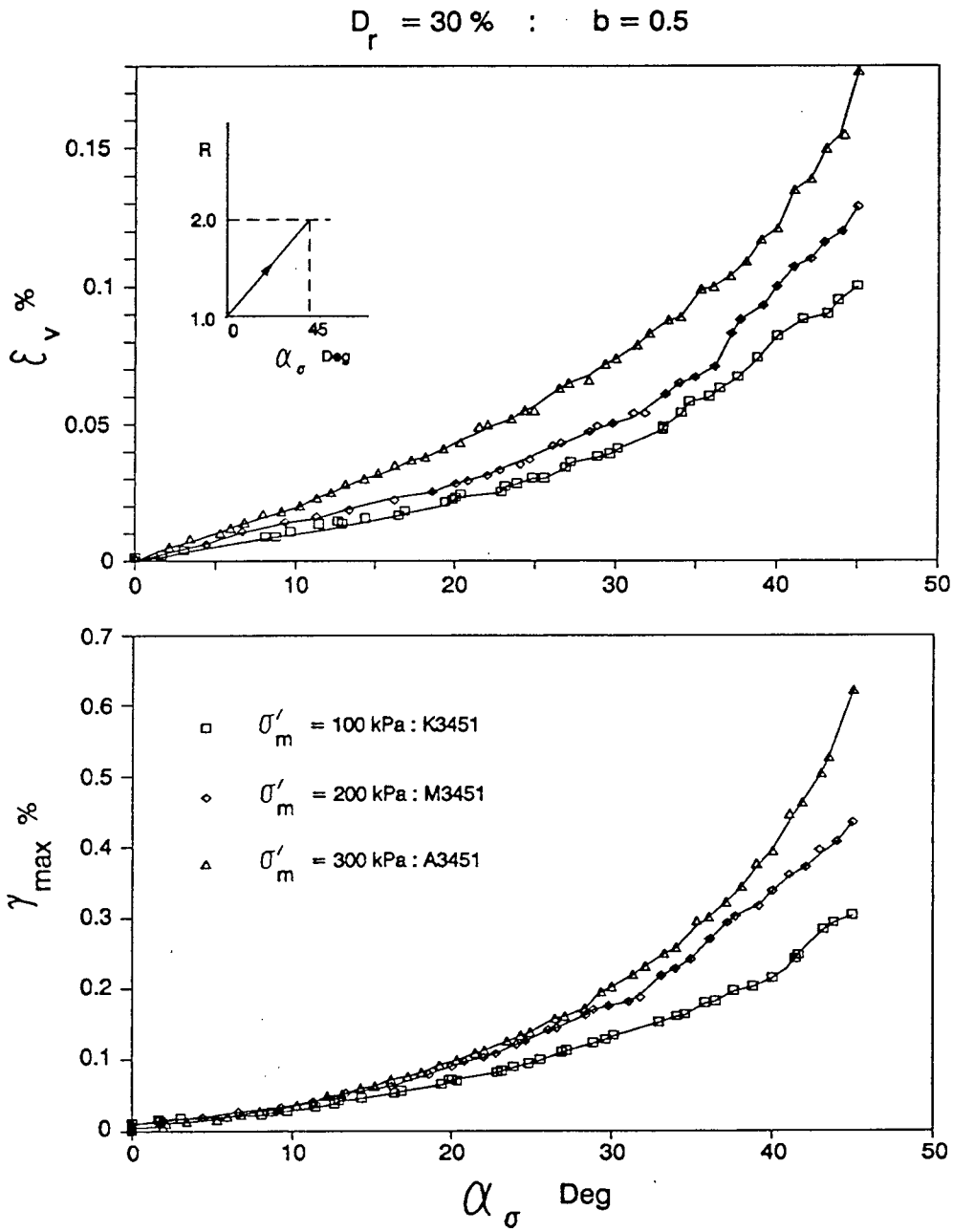

Figure 5.25: Effect of σ'_m on the behaviour under linear R - α loading

5.4.3.2 Direction of Strain Increment

The dependence of strain increment direction $\alpha_{\Delta\epsilon}$, on σ'_m level during R - α paths is illustrated in Fig. 5.26. There seems no noticeable effect of mean normal stress state on $\alpha_{\Delta\epsilon}$. Coincidence of stress and strain increment directions observed for $\alpha_{\Delta\sigma} \leq 45°$ in the previous sections, still remain unaltered even under different values of σ'_m. Thus the direction of strain increment $\alpha_{\Delta\epsilon}$ is coincident with and totally governed by the direction of stress increment, regardless of the values of R, b, σ'_m and α_σ, provided $\alpha_{\Delta\sigma} \leq 45°$.

5.4.3.3 Stress Path and Stress History Dependence of Deformations

The comparison of strains induced through different stress paths for Series M ($\sigma'_m = 200$ kPa) is presented in Fig. 5.27. The deformations accumulated through stress path M3451 very nearly agree with those observed from stress path M3001, thus exhibiting a path independent strain response at a stress state of (R, α_σ) = (2.0, 45°). An identical behaviour pattern is revealed from the comparison of results of tests K3001 and K3451 (Fig. 5.28) at $\sigma'_m = 100$ kPa.

These observations when considered along with the previous results from test Series A, E and C, it is possible to arrive at a very general conclusion with regard to path independent deformation behaviour of medium loose Ottawa sand. The conclusion is that, the deformation behaviour of medium loose Ottawa sand under increasing α_σ and R ("total loading") is path independent irresepective of the values of b parameter or σ'_m, provided the final stress conditions are within the domain of $R \leq 2.0$ and $0° \leq \alpha_\sigma \leq 45°$.

Moreover, the stress strain behaviour under α paths subsequent to the R - α paths of tests M3451 and K3451 tend to closely follow the results from α paths of

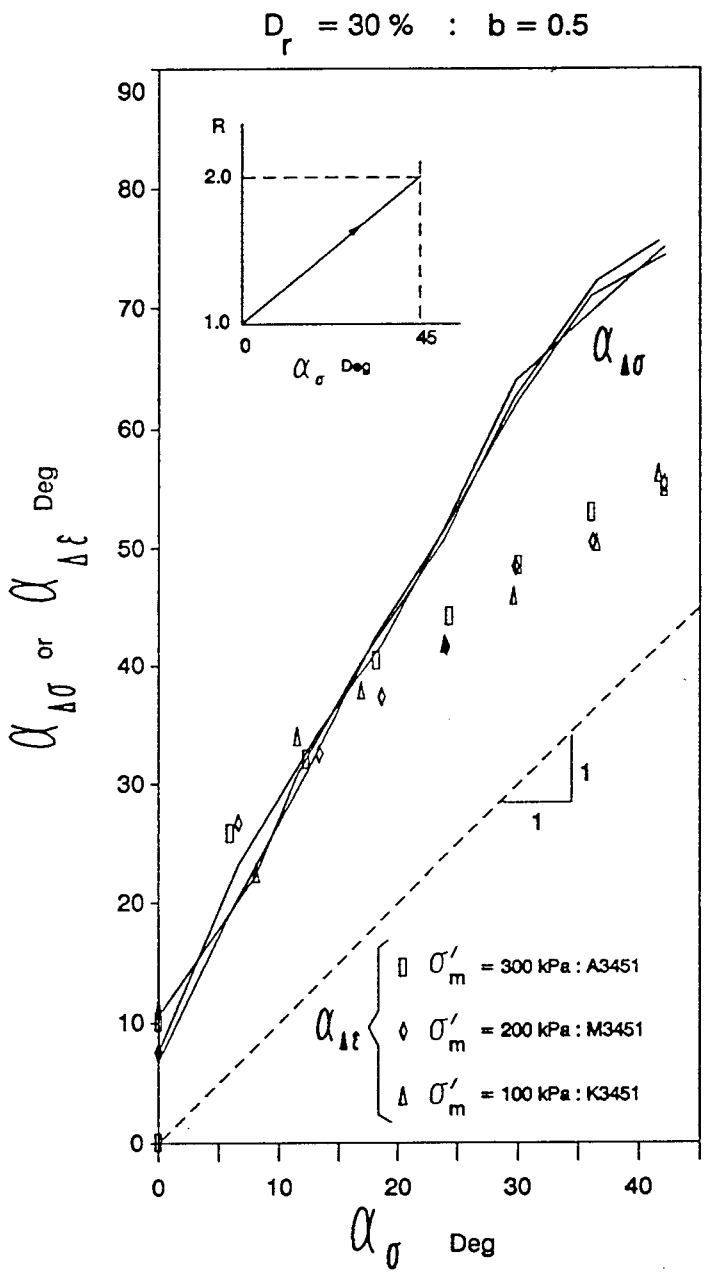

Figure 5.26: Effect of σ'_m on the direction of strain increment in linear R - α loading

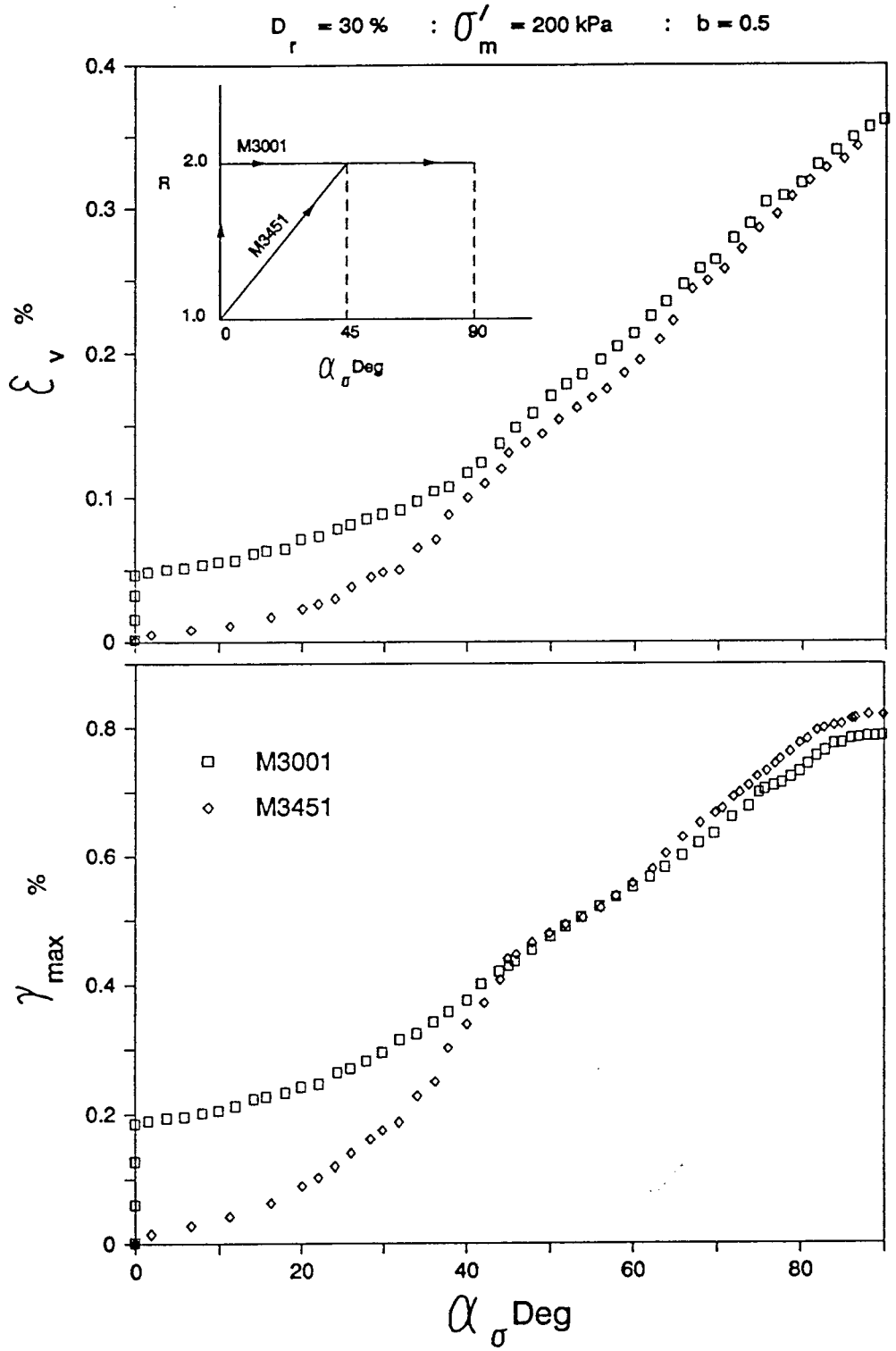

Figure 5.27: Effect of σ'_m on stress path dependence of deformations - Test Series M

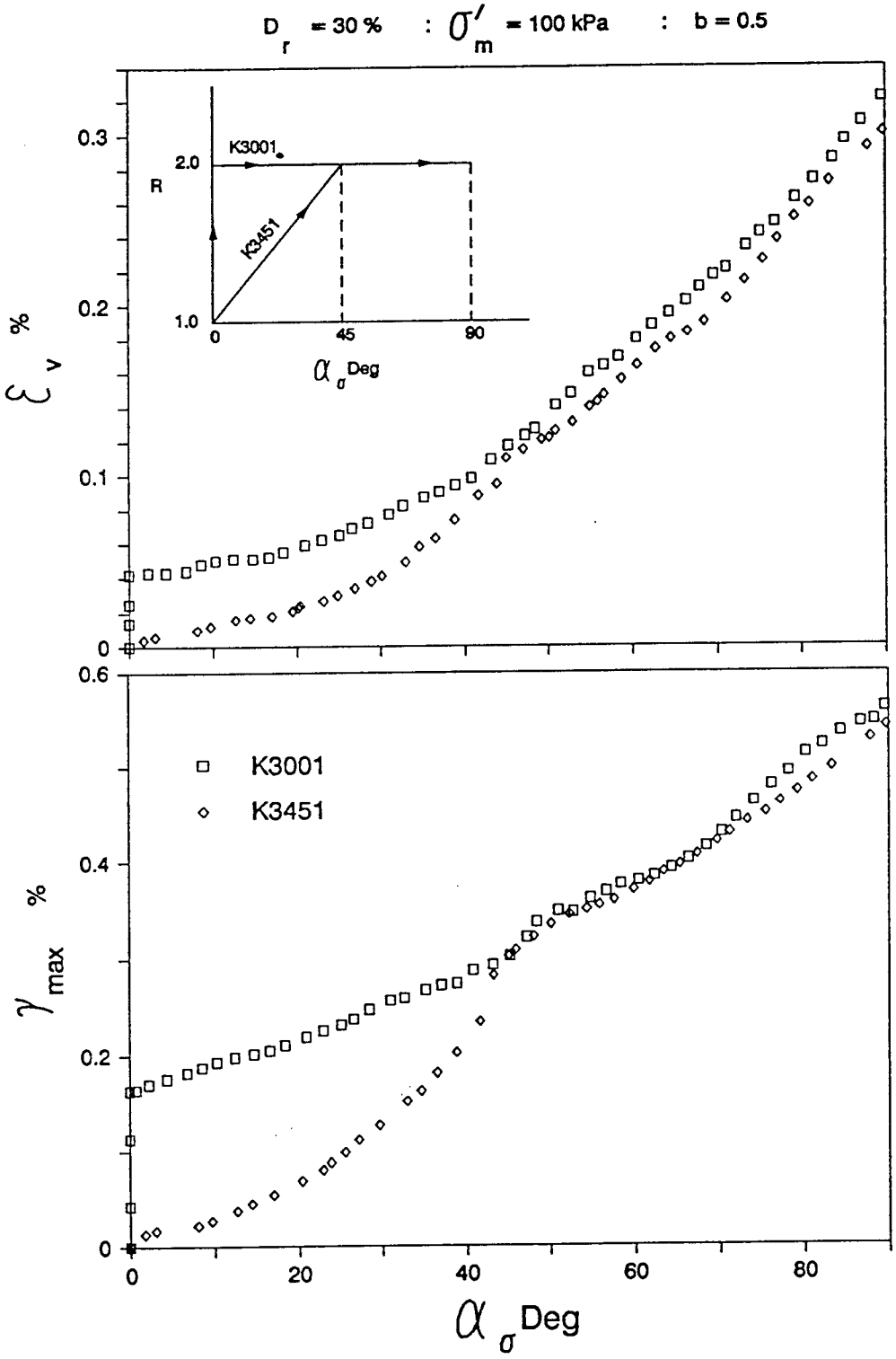

Figure 5.28: Effect of σ'_m on stress path dependence of deformations - Test Series K

tests M3001 and K3001 respectively, thus indicating no effect of stress path history (Figs. 5.27 and 5.28). These results corroborate the previous findings from test series A, E and C, that for increasing R - α paths, deformations at a given stress state is determined by the current (R, α_σ) value and not by the actual path taken to reach that stress state.

5.4.4 Response to R - α Loading at Higher Relative Densities

In order to examine the influence of packing density on stress strain behaviour under linear R - α paths, two tests were conducted with initial relative densities of 50% (test I3451) and 70% (test O3451) respectively. Both samples were initially isotropically consolidated to 300 kPa and then subjected to an R - α path (as shown in the key diagram of Fig. 5.29), with b and σ'_m held constant at 0.5 and 300 kPa respectively. This is identical to the stress path of test A3451 at D_r = 30% (Fig. 5.16).

5.4.4.1 Stress Strain Behaviour

A comparison of volumetric and maximum shear strains induced at the three different relative densities but under identical R - α loading is given in Fig. 5.29. A retardation in strain development with increasing relative density may be noted. This is in agreement with the previous observations on the sand behaviour reflecting decreasing strains with increasing density.

5.4.4.2 Direction of Strain Increment

Directions of strain increment in relation to the directions of applied stress increment and stresses, for the above tests are presented in Fig. 5.30. The direction of strain increment $\alpha_{\Delta\epsilon}$ is approximately coincident with the stress increment direction $\alpha_{\Delta\sigma}$

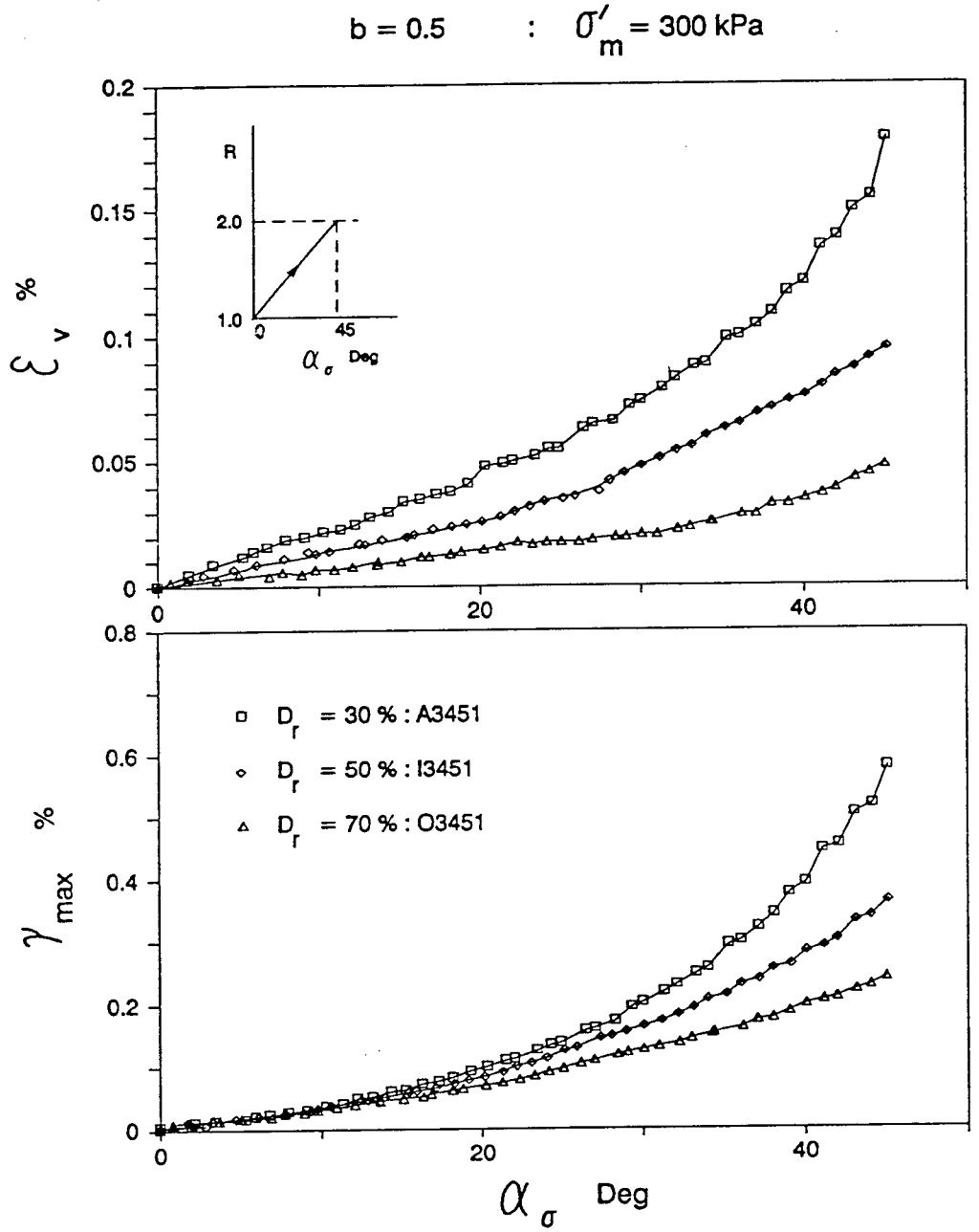

Figure 5.29: Effect of D_r on the behaviour under linear R - α loading

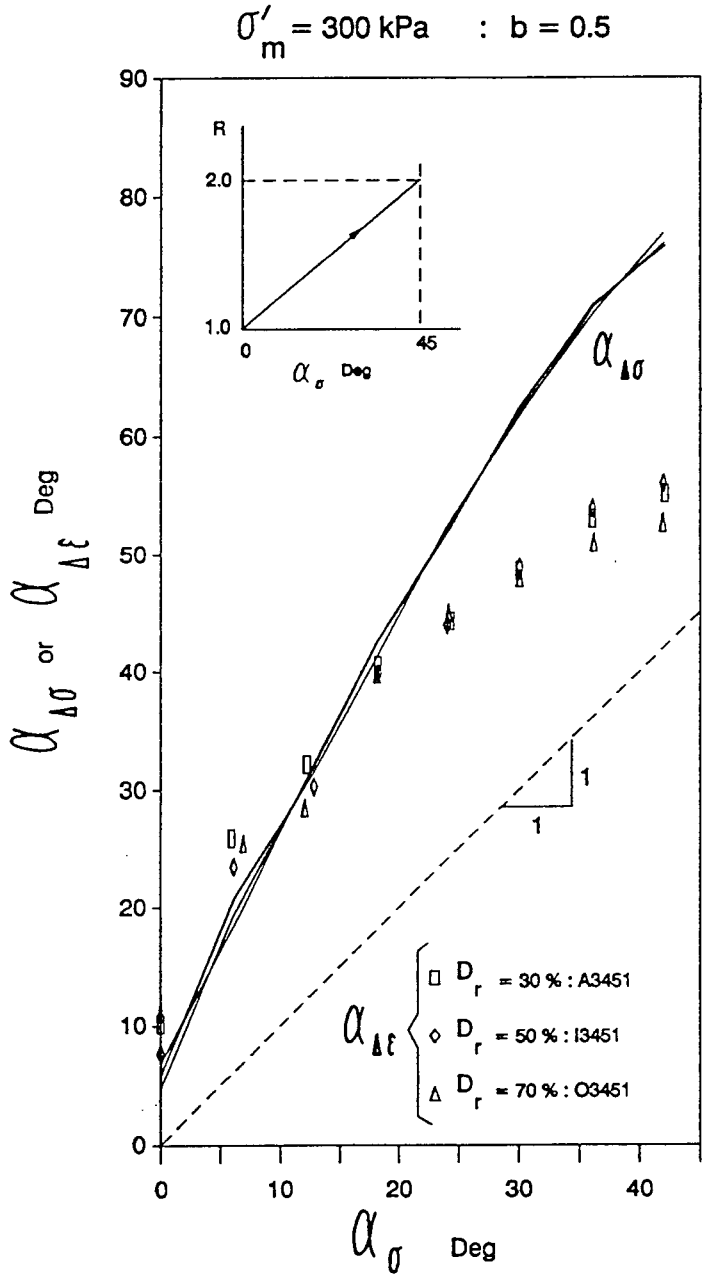

Figure 5.30: Effect of D_r on the direction of strain increment in linear R - α loading

for $\alpha_{\Delta\sigma} < 45°$. This is in agreement with the previous findings (Figs. 5.17, 5.22 and 5.26) in that the direction of strain increment is governed entirely by the direction of stress increment, if the applied stress increment is inclined less than 45° to the vertical.

Figure 5.30 also shows that under identical R - α paths relative density D_r has no appreciable effect on the directions of strain increment. It is much in contrast to the significant effects of relative density on $\alpha_{\Delta\varepsilon}$, observed under α paths where principal stress rotations were imposed with constant R (see Fig. 5.14). This difference in strain increment direction presumably arises due to difference in the directions of the imposed stress increment under the two stress paths. For the selected R - α path (Fig. 5.30) $\alpha_{\Delta\sigma}$ was in the range of $0° - 70°$, whereas in α paths $\alpha_{\Delta\sigma}$ ranged between $45° - 90°$ (Fig. 5.14). These ranges of $\alpha_{\Delta\sigma}$ are such that, for α paths, the applied stress increment is more inclined towards the direction of bedding plane, but for R - α paths, the applied stress increment is more inclined towards the direction of deposition, during the entire loading path. The previous finding that strain increment direction approximately coincides with stress increment direction (Figs. 5.17, 5.22, and 5.26) if $\alpha_{\Delta\sigma} < 45°$, now appears to be valid regardless of the relative density state of sand.

5.4.4.3 Stress Path and Stress History Dependence of Deformations

Possible stress path dependence of deformations at different relative densities is examined in Figs. 5.31 and 5.32 (Test Series I and O). Strains developed along R - α stress paths in both test series I and O are compared with strains along stress paths in which R and α_σ vary individually.

Approximately equal deformations at common stress state $(R, \alpha_\sigma) = (2, 45°)$ indicate path independence for both test Series I ($D_r = 50\%$, Fig. 5.31) and Series

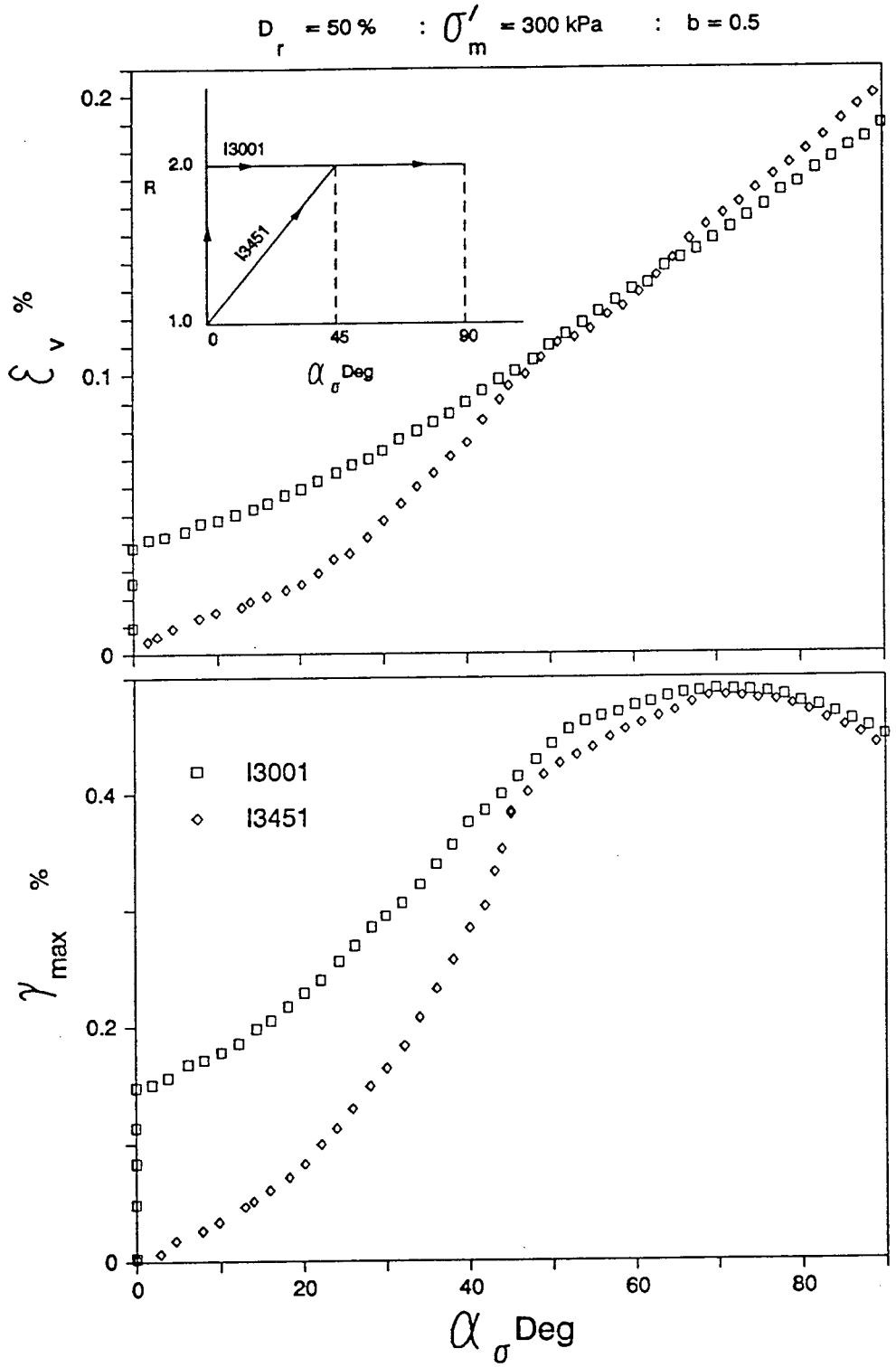

Figure 5.31: Effect of D_r on stress path dependence of deformations - Test Series I

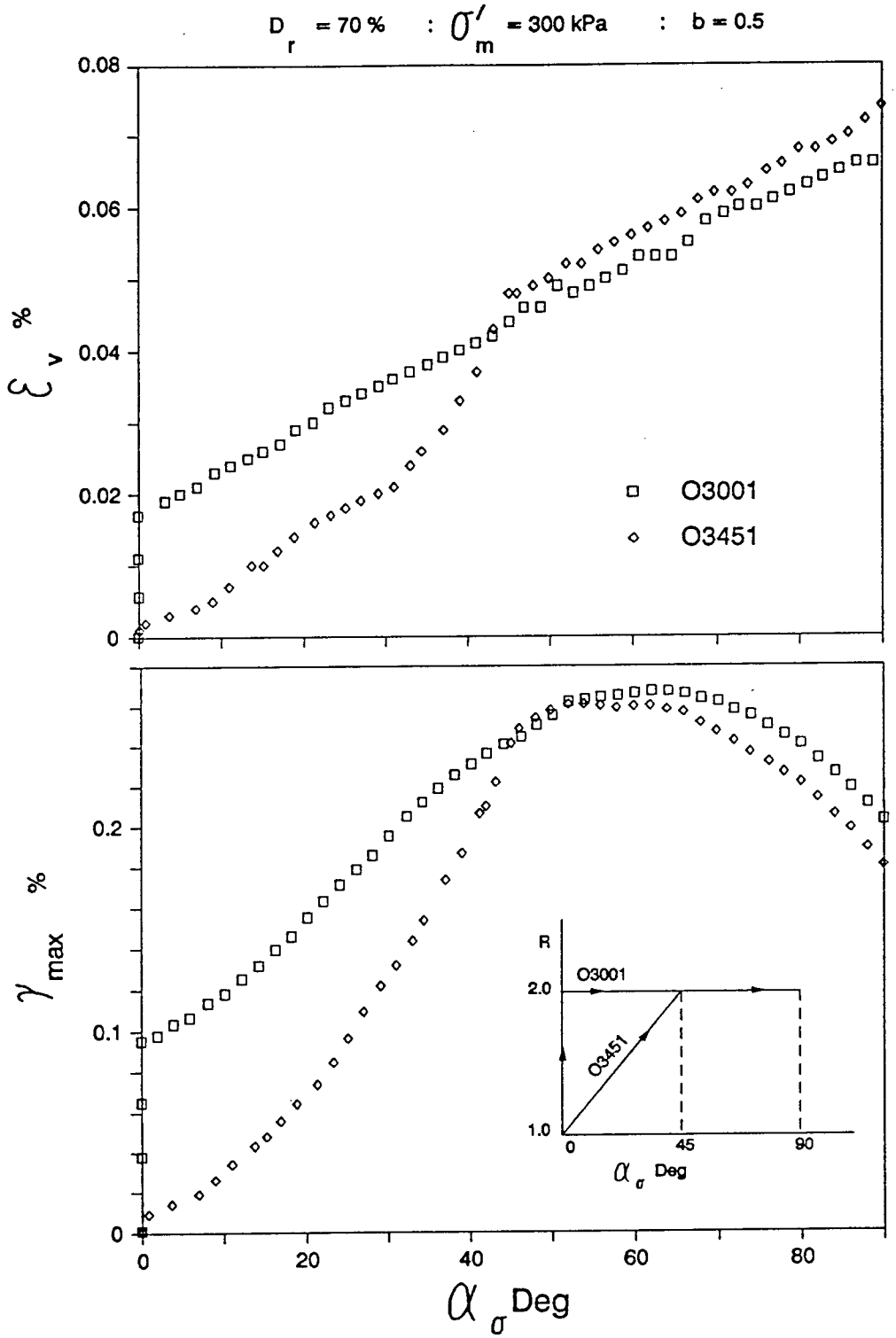

Figure 5.32: Effect of D_r on stress path dependence of deformations - Test Series O

O (D_r = 70%, Fig. 5.32). Behaviour of Ottawa sand under total loading paths can therefore be regarded as path independent regardless of b, σ'_m, and D_r provided $R \leq 2.0$ and $0° \leq \alpha_\sigma \leq 45°$.

Following linear R - α loading, deformations under common α paths in tests I3451 and O3451 (α_σ from 45° to 90°) match closely with those in α tests I3001 and O3001 respectively. These results further support the insignificant effect of stress path history observed earlier in test Series A, E, C, M and K.

5.4.5 Deformations under Multi-Linear R - α Loading

5.4.5.1 Stress Strain Behaviour

Linear variation of R - α_σ, selected so far is only one method of varying R and α in an increasing manner. This was mainly chosen because of its simplicity. A medium loose Ottawa sand sample was loaded under a tri-linear R - α stress path (OABCD) as shown in Fig. 5.33. Other stress parameters σ'_m and b were held constant at 300 kPa and 0.5 respectively, so that a direct comparison could be made between deformations under this stress path and those under α path A3002 at $R = 2$ at common stress state C.

Figure 5.33 shows deformations under this tri-linear R - α stress path. The results strongly corroborate the proposed notion of path independent deformation response of Ottawa sand under stress paths involving increasing R and α_σ in the domain of $R \leq 2.0$ and $0° \leq \alpha_\sigma \leq 45°$. Beyond the stress point C (α_σ = 45°) the sample was loaded along the stress path CD identical to that for test A3002. Near identical strain response on further loading along CD with that of test A3002 suggests little effect of stress path history.

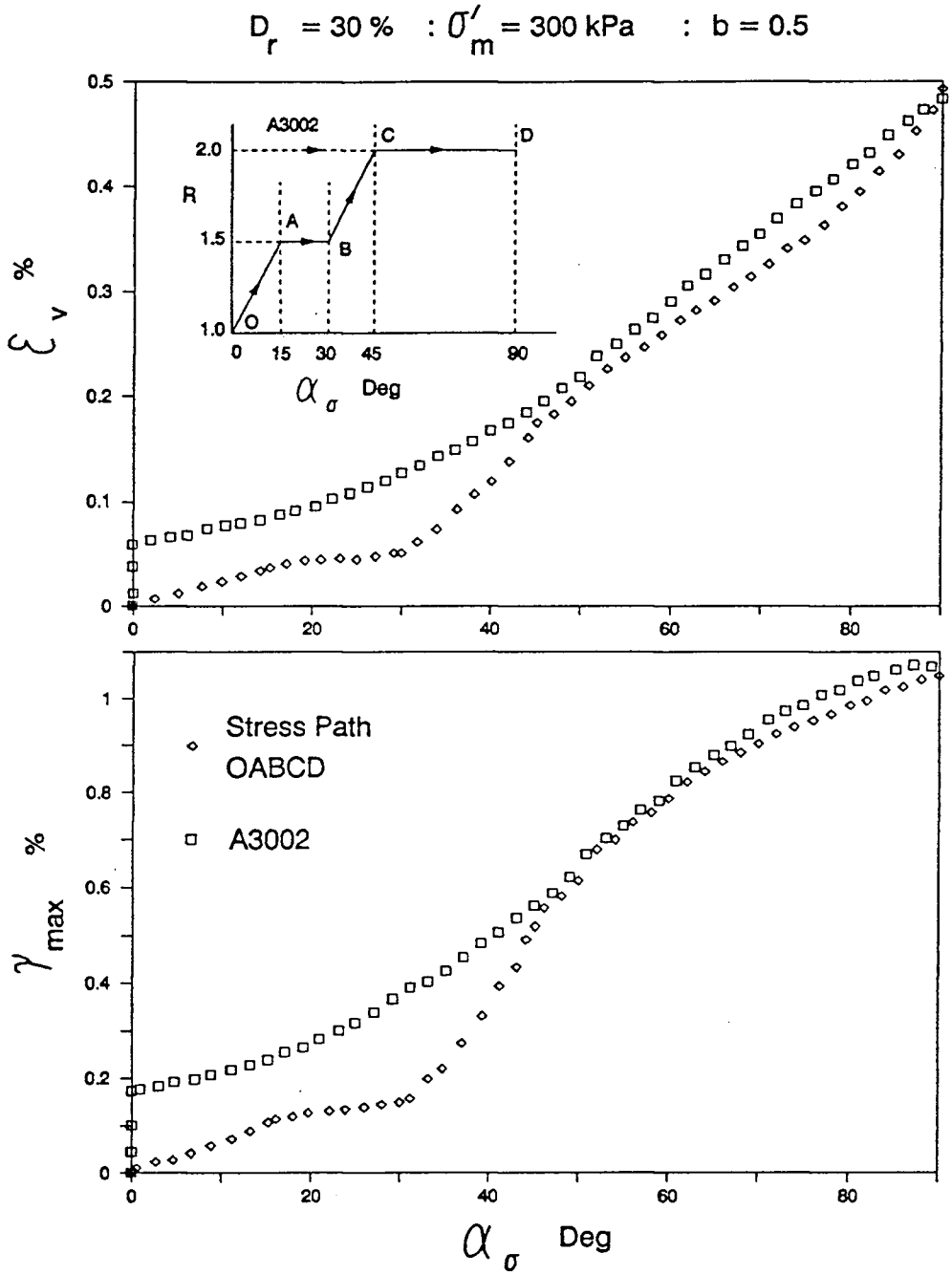

Figure 5.33: Stress path independence observed in a tri-linear R - α loading path

5.4.5.2 Direction of Strain Increment

The strain increment directions for the multi-linear R - α path are illustrated in Fig. 5.34. In order to achieve the tri-linear variation of R and α_σ the direction of stress increment $\alpha_{\Delta\sigma}$ varied in a discontinuous manner. During the stress path segment OA, stress and strain increment directions are nearly coincident as observed earlier under all previous linear R - α stress paths (Figs. 5.17, 5.22, 5.26 and 5.30) for $\alpha_{\Delta\sigma} \leq 45°$. Along segment AB the stress increment direction $\alpha_{\Delta\sigma}$ equals $\alpha_\sigma + 45°$, and hence lie within 60° to 75° (i.e. $\alpha_{\Delta\sigma} > 45°$). According to the findings in the previous sections (Figs. 5.17, 5.22, 5.26 and 5.30) the strain increment direction $\alpha_{\Delta\varepsilon}$ along this constant R segment (α loading) should deviate from the stress increment direction towards the stress direction α_σ. A sudden jump reflecting changes in $\alpha_{\Delta\sigma}$ and $\alpha_{\Delta\varepsilon}$ are clearly apparent in Fig. 5.34 at A, where sudden changes in loading path from R - α to α occurs.

The very initiation of the third phase BC of the tri-linear stress path is associated with another jump in the directions of stress and strain increments resulting in the stress increment direction $\alpha_{\Delta\sigma}$ oriented very close to 45°. It is interesting to note that the direction of strain increment $\alpha_{\Delta\varepsilon}$ is once again almost coincident with stress increment direction at this initiation point B of this linear R - α segment of the tri-linear path. The results demonstrate that the near coincidence of stress and strain increment directions for $\alpha_{\Delta\sigma} < 45°$ is not only restricted to linear R - α paths, but also valid under more complex loading involving swift changes in R vs α_σ.

5.5 Deformation Under Simultaneous Increase in Three Stress Parameters

The preceding investigations have focussed on stress paths involving simultaneous increases in R and α_σ only, and no change in σ'_m or b parameter was allowed during

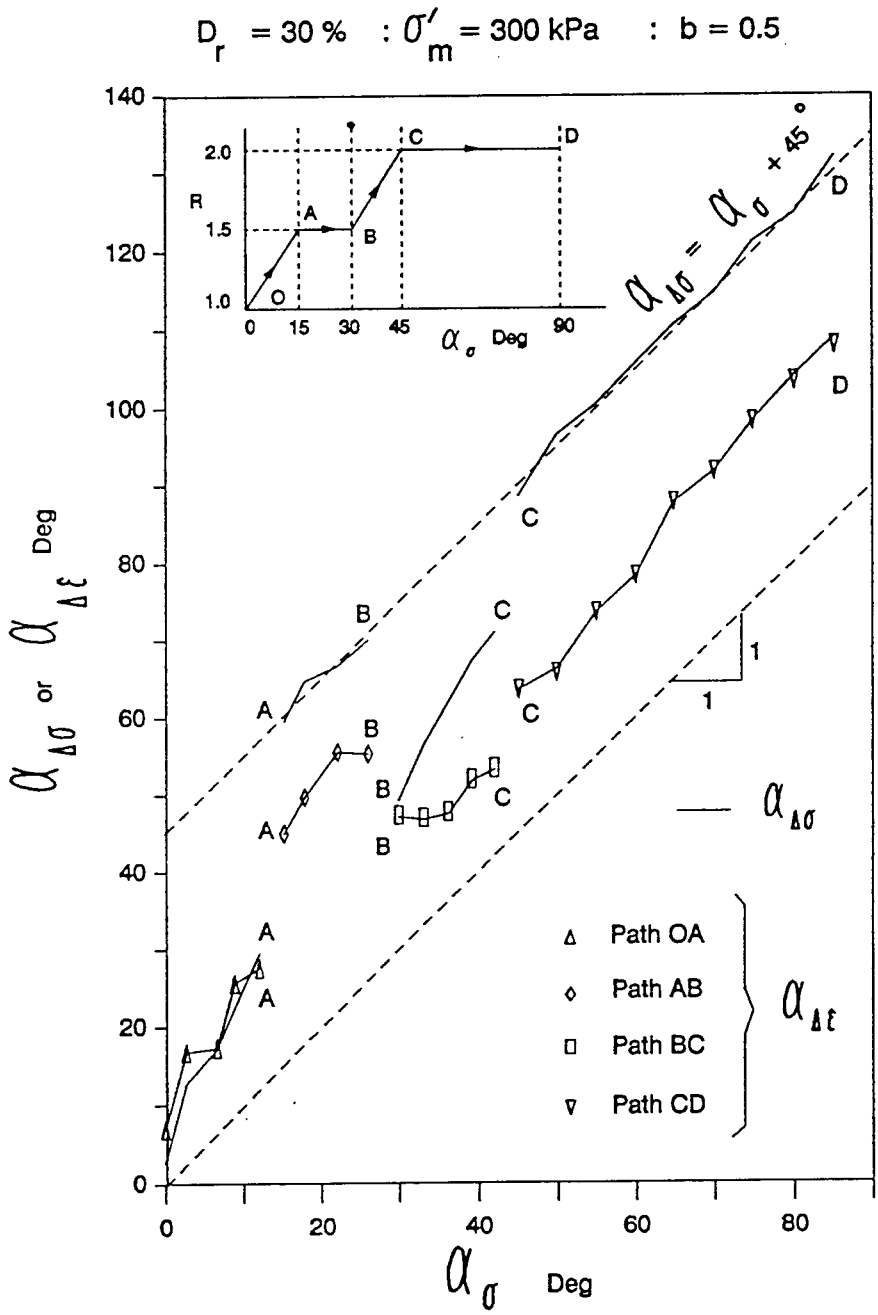

Figure 5.34: Strain increment directions under a tri-linear R - α loading path

loading. It is of fundamental as well as practical interest to examine, whether the observed behaviour patterns from these results will also be valid for loading along stress paths in which more than two stress parameters vary at a given time. This aspect was probed in a test which involved simultaneous increase in σ'_m, R and α_σ (path AB, Fig. 5.35; defined as σ'_m - R - α_σ path). A medium loose sample was initially isotropically consolidated to a hydrostatic stress of 100 kPa, and then subjected to a linear variation of σ'_m, R and α_σ until (σ'_m, R, α_σ) = (300 kPa, 2.0, 45°). During the course of loading b was maintained at a fixed value of 0.5. In this manner the strains developed until the final stress state could be directly compared with those which develop along α path A3002, which also passes through the same stress state (σ'_m, R, α_σ) = (300 kPa, 2.0, 45°).

5.5.1 Stress Strain Behaviour

Deformations along σ'_m - R - α_σ path AB are presented in Fig. 5.35. Strains induced until the terminal state (σ'_m, R, α_σ) = (300 kPa, 2.0, 45°) along σ'_m - R - α_σ stress path may be seen to be in close agreement with those in α test A3002. This indicates that the stress path independent behaviour observed under R - α paths could be extended to those paths in which three stress parameters vary simultaneously. It may be pointed out that very elaborate investigations are needed before such stress path independent behaviour and the domain of its validity is generalized to all loading paths lying in the 3 dimensional σ'_m - R - α_σ space, or even the 4 dimensional stress space σ'_m, R, α_σ and b.

5.5.2 Direction of Strain Increment

The direction of strain increment along stress path AB is plotted in Fig. 5.36. It is interesting to note that even with simultaneous increase in three stress parameters, the characteristic that strain increment direction $\alpha_{\Delta\varepsilon} \approx \alpha_{\Delta\sigma}$ for $\alpha_{\Delta\sigma} \leq 45°$ still

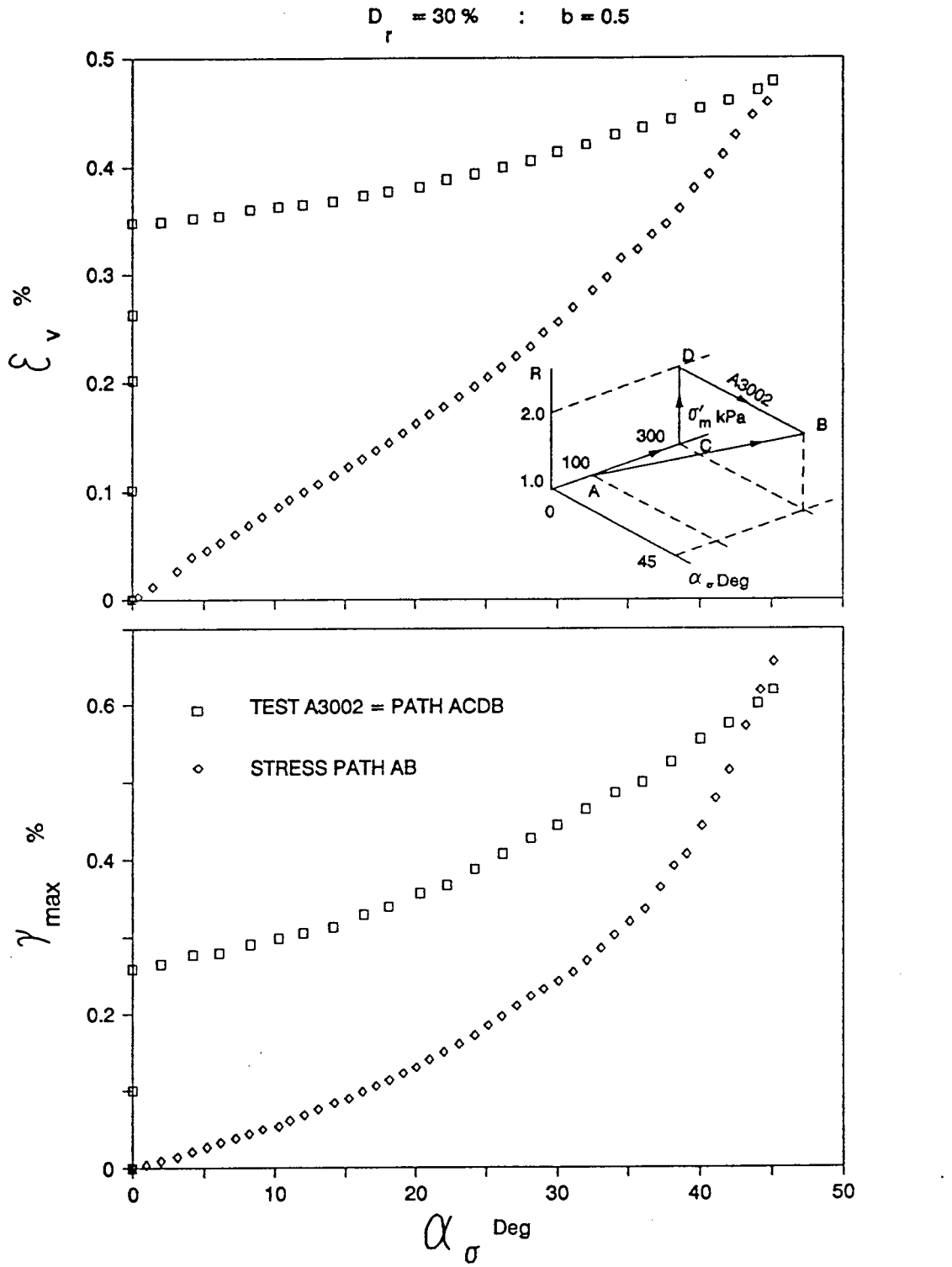

Figure 5.35: Deformation under simultaneous increase in three stress parameters σ'_m, R and α_σ

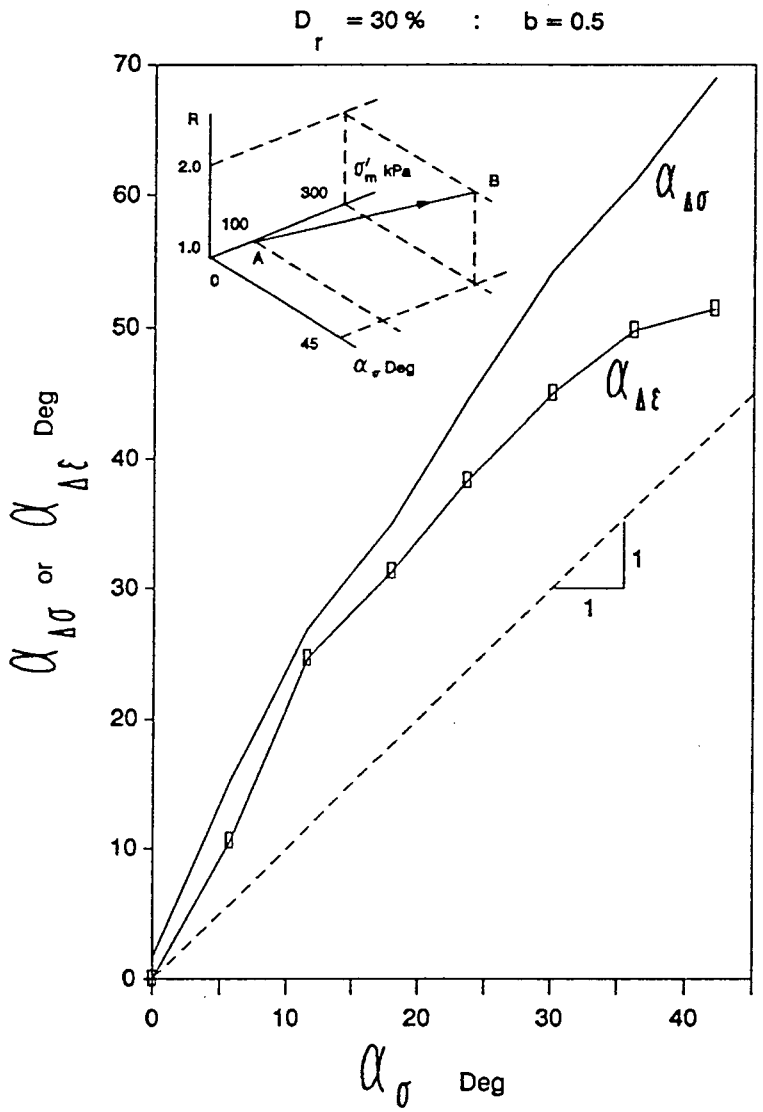

Figure 5.36: Strain increment directions under a σ'_m - R - α path

remains valid. For $\alpha_{\Delta\sigma} > 45°$, a gradual deviation of $\alpha_{\Delta\epsilon}$ from $\alpha_{\Delta\sigma}$ towards α_σ is observed which is also consistent with the results from previous R - α paths.

5.6 Prediction of Deformations Under Simultaneous Increase in Stress Ratio and Principal Stress Rotation

5.6.1 Introduction

Experimental investigations presented so far in this chapter have shown that the stress strain behaviour of sand under simultaneous increase of shear and principal stress rotation is path independent provided the final stress state is within the domain $R \leq 2.0$ and $0° \leq \alpha_\sigma \leq 45°$. Therefore it should be possible to estimate the deformation at any given stress state within the above domain, by carrying out a single test which would pass through that particular state of stress. Although there are many options for selecting such a stress path, a simple choice would be to use a sequential stress path wherein each sequence consists of increase in only one stress variable (e.g. increase R to the desired amount with α_σ fixed at 0° followed by increase in the value of α_σ at constant R)[4].

It is practically not possible to conduct a test each time deformations at a given (R, α_σ) stress state are needed. Since the stress path independence has already been demonstrated, it would be of interest to investigate the posssibility of characterizing material behaviour in the domain $R \leq 2.0$ and $0° \leq \alpha_\sigma \leq 45°$ for fixed σ'_m and b conditions, using a finite number of tests traversing this stress domain. As discussed in the previous paragraph, a reasonable choice would be to perform tests wherein principal stress rotation occur under constant R (with constant σ'_m and b values), at different levels of R, as shown in Fig. 5.37.

Using the observation that the material behaviour is path independent, strains

[4]the values of σ'_m and b parameter are held constant throughout the test.

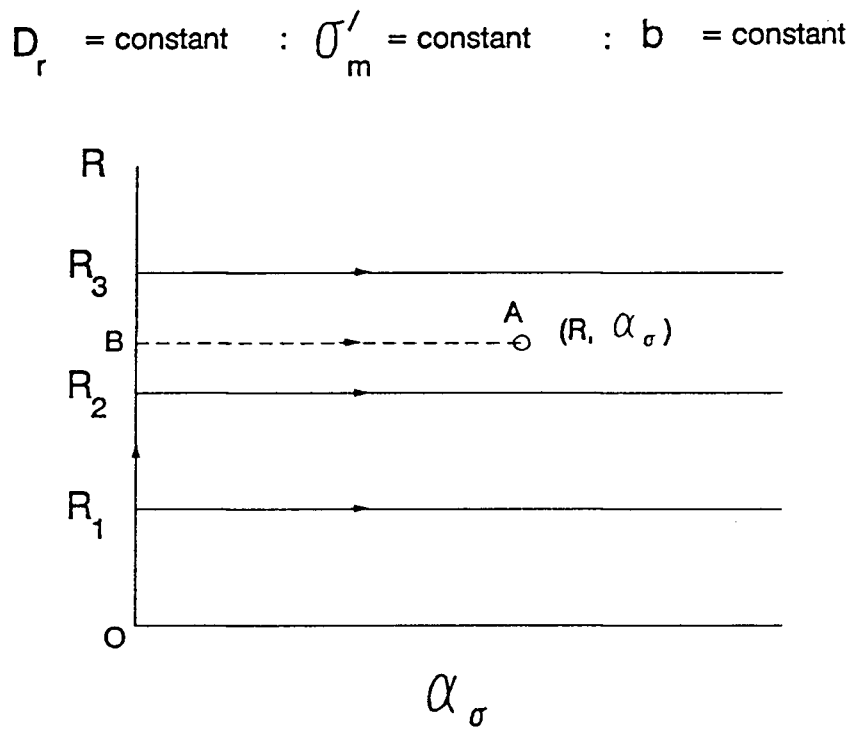

Figure 5.37: Constant R principal stress rotation loading to characterize material behaviour.

accumulated at any given (R, α_σ) stress state A (for a certain combination of b and σ'_m) can be considered as the superposition of strains due to:

- increase in R from hydrostatic stress state to the desired value with $\alpha_\sigma = 0°$ and constant σ'_m and b (Path OB).
- increase in α_σ with σ'_m, R and b fixed at the desired value (Path BA).

Using this concept, the volumetric strain ε_v and maximum shear strain γ_{max} under R - α stress paths were predicted for the domain of $R \leq 2$ and $0° \leq \alpha_\sigma \leq 45°$, using test results from stress paths which involved increase in one stress parameter only at a time (Fig. 5.37). The details of the procedure developed for these predictions are presented in the next section.

Deformation predictions were made for all series of tests (Series A through O) presented in the previous sections of this chapter. These predictions were then compared with the measured results. In order to characterize the behaviour for each test series, a minimum of two principal stress rotation tests at different R levels had to be performed with relevant constant σ'_m, b and D_r conditions for that series.

It is also important to point out that the comparison of the predicted and experimental results for the R - α paths would not only check the success of the superposition of strains but also affirm the validity of the stress path independence at all stress points along a given stress path.

5.6.2 Prediction Method

The concept of prediction of strains begins with the basic assumption that the superposition of strains is valid[5]. This assumption can be expressed in terms of the following equations:

[5] **All the strain components are considered with reference to hydrostatic stress state immediately prior to R - α loading.**

$$\{\varepsilon_v\}_{total} = \{\varepsilon_v\}_R + \{\varepsilon_v\}_\alpha \tag{5.1}$$

$$\{\gamma_{max}\}_{total} = \{\gamma_{max}\}_R + \{\gamma_{max}\}_\alpha \tag{5.2}$$

where,

Subscript R denotes strains due to changes in R only, with $\alpha_\sigma = 0°$.

Subscript α denotes strains due to changes in α_σ only, with R = constant.

The prediction of strains at a given stress state requires that all strain components on the right hand side of the above equations be evaluated. In order to demonstrate the method of prediction more effectively, the procedure is applied to the test series A (i.e. σ'_m = 300 kPa; b = 0.5; D_r = 30%). Test data is presented in parallel with the general explanation of the method.

Values of $\{\varepsilon_v\}_R$ and $\{\gamma_{max}\}_R$ are established from the experimental results along the stress path where R is increased with $\alpha_\sigma = 0°$. It is important to note that these strains are dependent only on the stress ratio, since all other stress parameters σ'_m, b and α_σ are fixed. Results for series A, are given in Fig. 5.38. These results constitute the R path with $\alpha_\sigma = 0°$ of test A3002.

Values of $\{\varepsilon_v\}_\alpha$ and $\{\gamma_{max}\}_\alpha$ are however dependent on both R as well as α_σ (see Fig. 5.39). These strains for the example case of Series A are presented in Fig. 5.39. These results are identical to those in Fig. 5.7 except for the fact that the strains are now expressed with reference to the hydrostatic stress state of 300 kPa. Strains are plotted only for $0° < \alpha_\sigma < 45°$, which is the domain of interest, and represent α phases of tests A1001, A2001, A3002 in which principal stresses were rotated at fixed R values of 1.35, 1.65 and 2.0 respectively. Since the experimental results for $\{\varepsilon_v\}_\alpha$ and $\{\gamma_{max}\}_\alpha$ were developed only for finite values of R, a method of interpolation was required to obtain these strains at intermediate values of R. Interpolation could

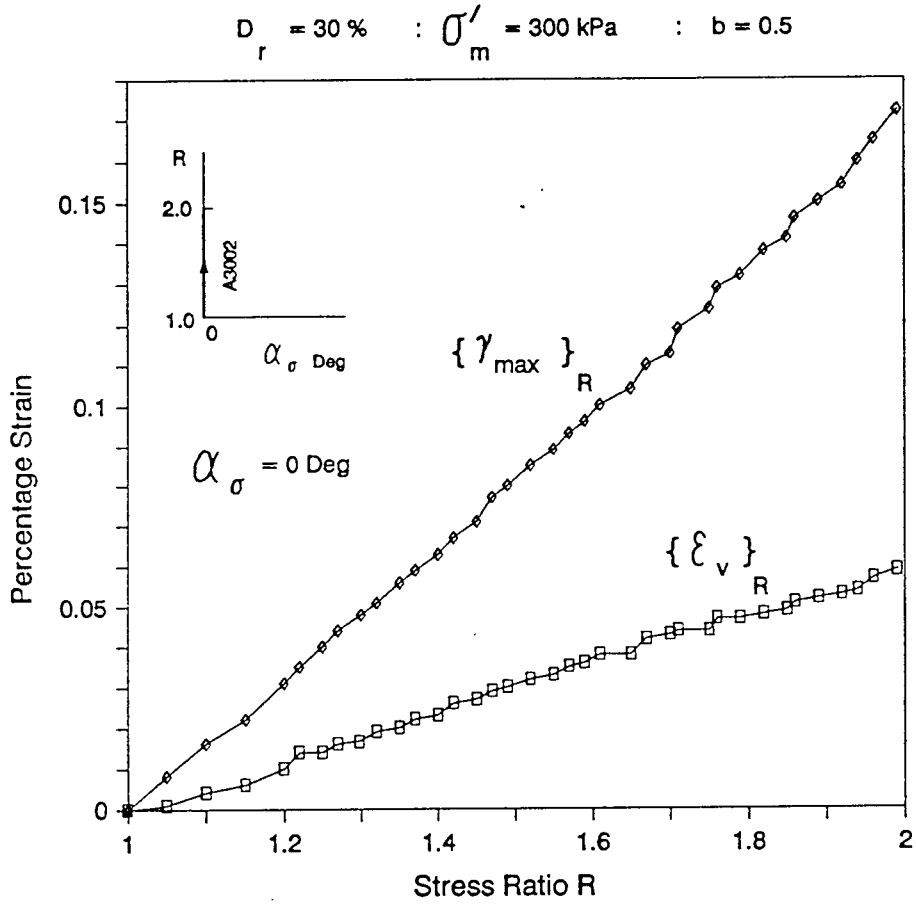

Figure 5.38: Deformations under shear loading with $\alpha_\sigma = 0°$ for medium loose Ottawa sand - Series A

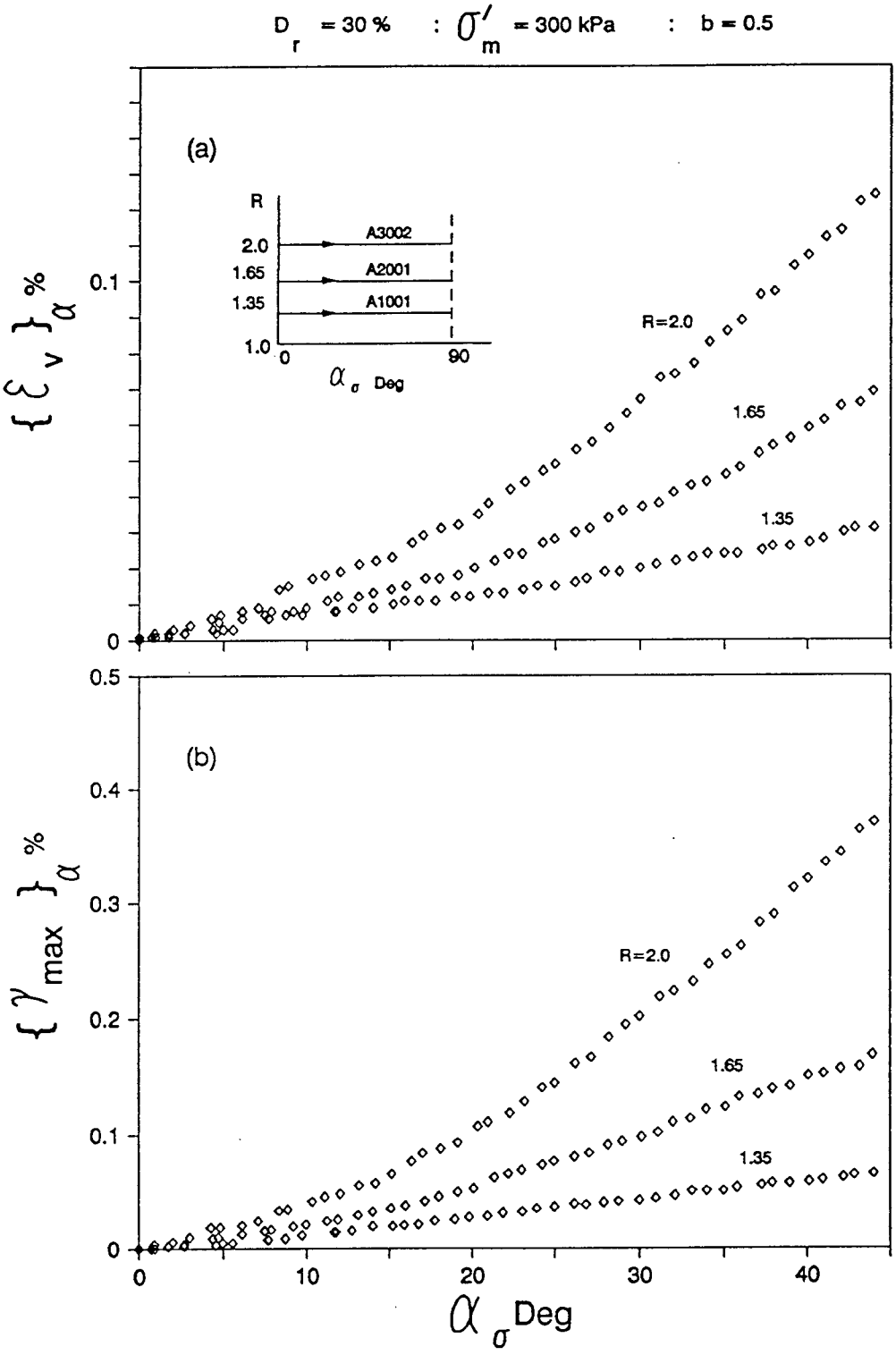

Figure 5.39: Strains from α paths with R = constant for medium loose Ottawa sand - Series A

be achieved in two ways. The first is to use a graphical method, and the second choice is to use a curve fitting technique. Since the graphical method proved to be cumbersome and time consuming, the second alternative of curve fitting was adopted. Use of power functions of the form given below could adequately approximate the $\{\varepsilon_v\}_\alpha$ and $\{\gamma_{max}\}_\alpha$ characteristics for any desired value of α and R.

$$\{\varepsilon_v\}_\alpha = k_1(R-1)^{m_1}{\alpha_\sigma}^{n_1} \tag{5.3}$$

$$\{\gamma_{max}\}_\alpha = k_2(R-1)^{m_2}{\alpha_\sigma}^{n_2} \tag{5.4}$$

where k_1, m_1, n_1 and k_2, m_2, n_2 are constants obtained from curve fitting for $\{\varepsilon_v\}_\alpha$ and $\{\gamma_{max}\}_\alpha$ respectively. (Units of α_σ in the above equations are degrees and the resulting strain components are in percentage strains). Suitability of curve fit for the results of test series A is illustrated in Fig. 5.40. A satisfactory representation of both volumetric and maximum shear strain characteristics of α paths may be noted. It is emphasized that the curve fitting exercise was used only as a tool for continuous interpolation, and no physical significance is attached to the parameters derived for the mathematical expression for the curves.

The predictions were made for deformation under R - α loading paths A3301, A3451, A3601 and A3901 (see Fig. 5.16) in the domain $0° \leq \alpha_\sigma \leq 45°$ and $1 \leq R \leq 2$, using equations 5.1 through 5.4. The predicted and experimentally observed results are compared in Fig. 5.41. It can be seen that the prediction of strains at any given stress state (R, α_σ) is succesfully achieved by superposition of the results obtained from stress paths wherein only one stress parameter is allowed to increase at a time.

It is also important to reiterate that the close match between the predicted and the measured behaviour confirms stress path independence of deformations in the domain of $R \leq 2.0$ and $0° \leq \alpha_\sigma \leq 45°$.

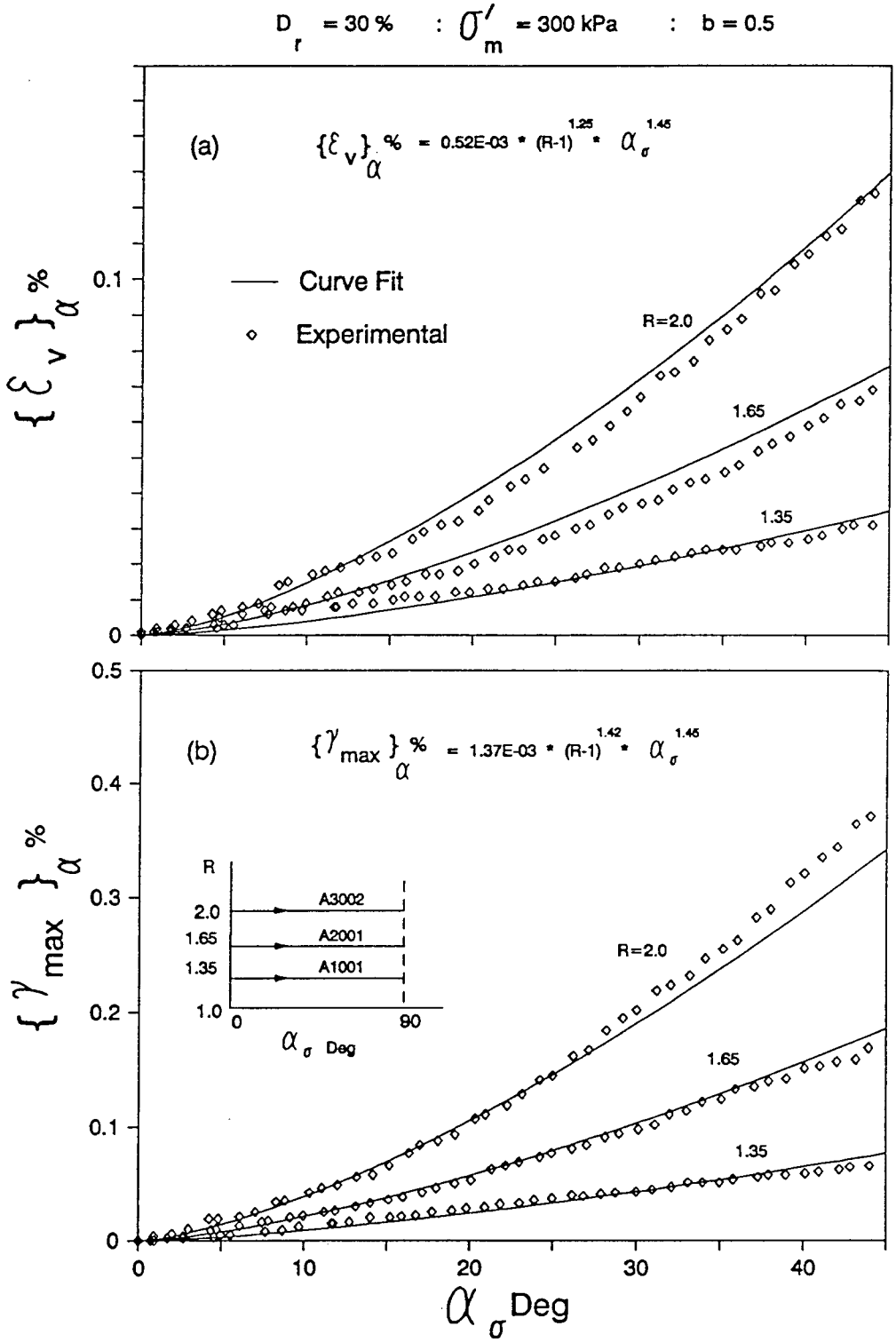

Figure 5.40: Curve fitting technique illustrated for test Series A

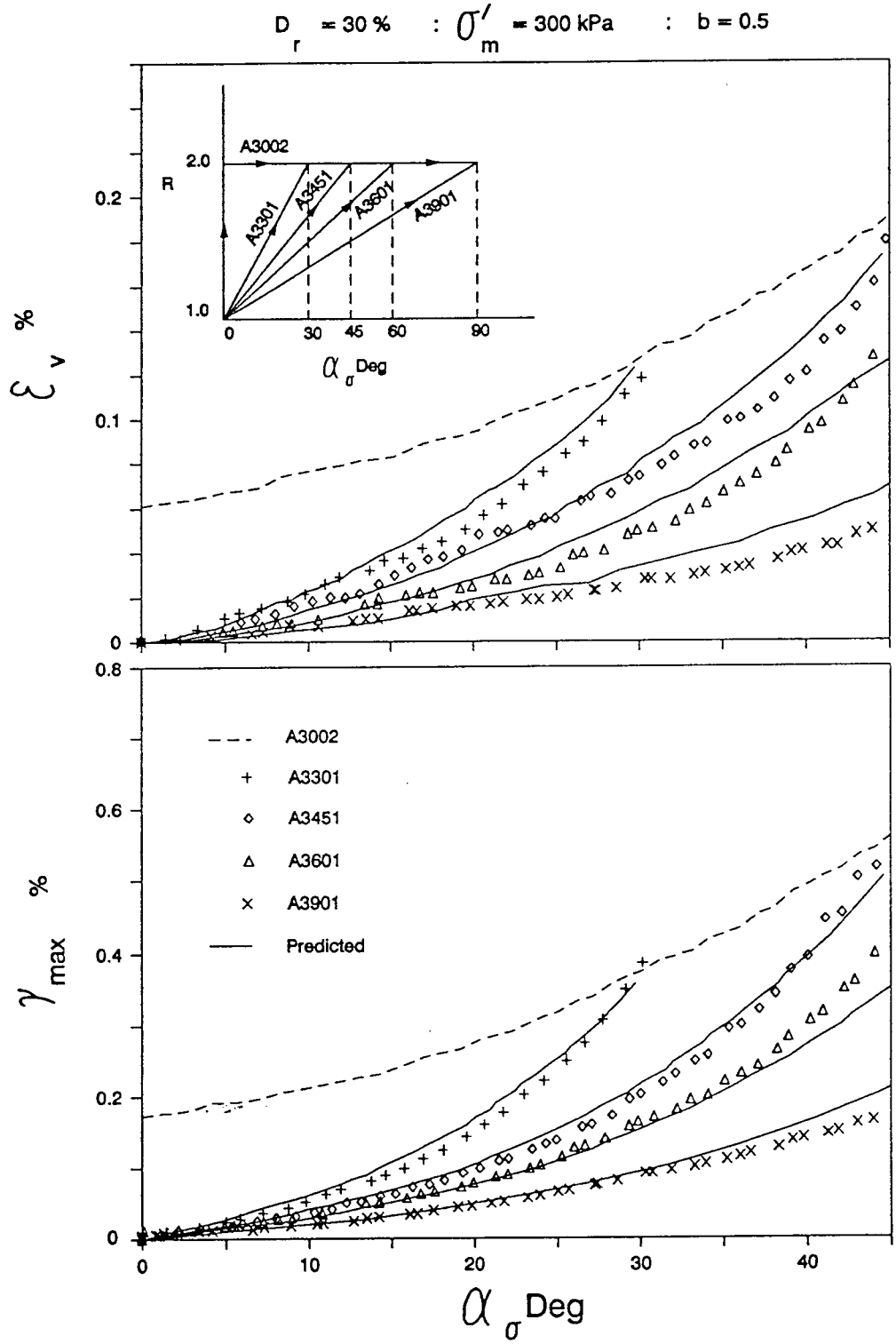

Figure 5.41: Predicted and observed stress strain behaviour - Series A

Deformation predictions similar to those for series A were also made for R - α paths in several other test series E, C, M, K, I, O and also for the tri-linear stress path. In order to characterize the behaviour in each series, at least two principal stress rotation tests (α tests) under different but fixed levels of R and the R test at $\alpha_\sigma = 0°$ are needed at the specified σ'_m, b and D_r conditions of that series. Test data for characterizing behaviour in the Series E, C, M, K, I and O (along with the fitted curves for interpolation) are given in Appendix C.

Comparison between the predicted and experimentally observed strains for each test series E, C, M, K, I, O including the tri-linear R - α path are presented in Figs. 5.42 through 5.48 respectively. Excellent agreement between predicted and measured results confirms that the stress strain behaviour for given σ'_m, b values, in the R - α space can be predicted successfully with the use of a limited number of principal stress rotation tests performed at different stress ratios. The underlying principles behind such predictions is the experimentally demonstrated path independent deformation behaviour in the domain of $R \leq 2.0$ and $0° \leq \alpha_\sigma \leq 45°$.

5.7 Prediction of Deformations Under Simultaneous Increase of σ'_m, R and α_σ

The stress-strain response under σ'_m - R - α path AB (Fig. 5.35) was predicted by an approach similar to the one used in the prediction of strains under R - α loading in the previous section. Along this stress path, values of σ'_m, R and α_σ were simultaneously increased in a linear manner from an initial hydrostatic stress state $\sigma'_m = 100$ kPa until $\sigma'_m = 300$ kPa; $R = 2$; and $\alpha_\sigma = 45°$ was achieved. A path independent strain response would imply that the strains at any given σ'_m, R, α_σ state along path AB could be evaluated by following any loading path ending at that state. Since the data base characterizing the material behaviour consisted of hydrostatic paths and R and

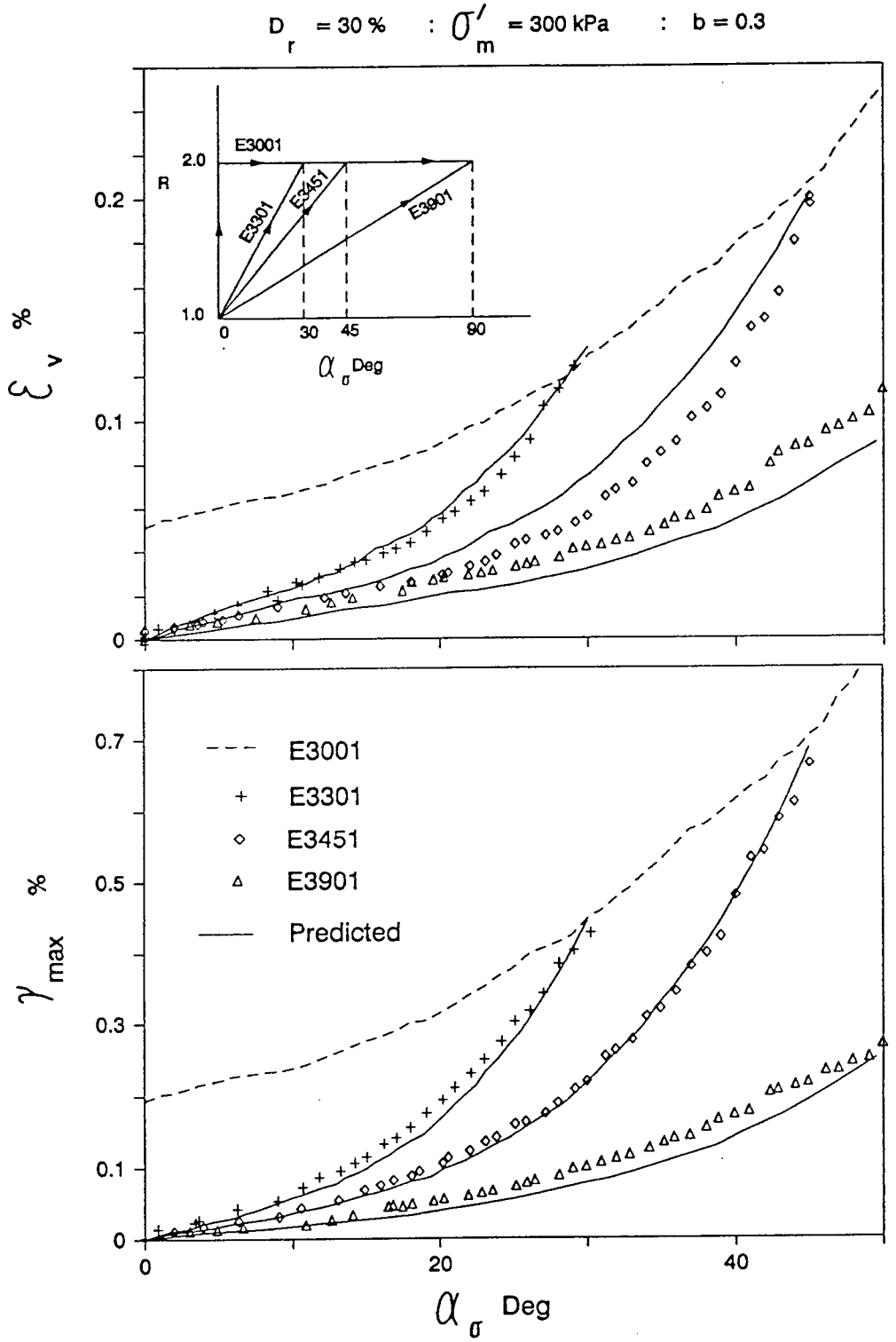

Figure 5.42: Predicted and observed stress strain behaviour - Series E

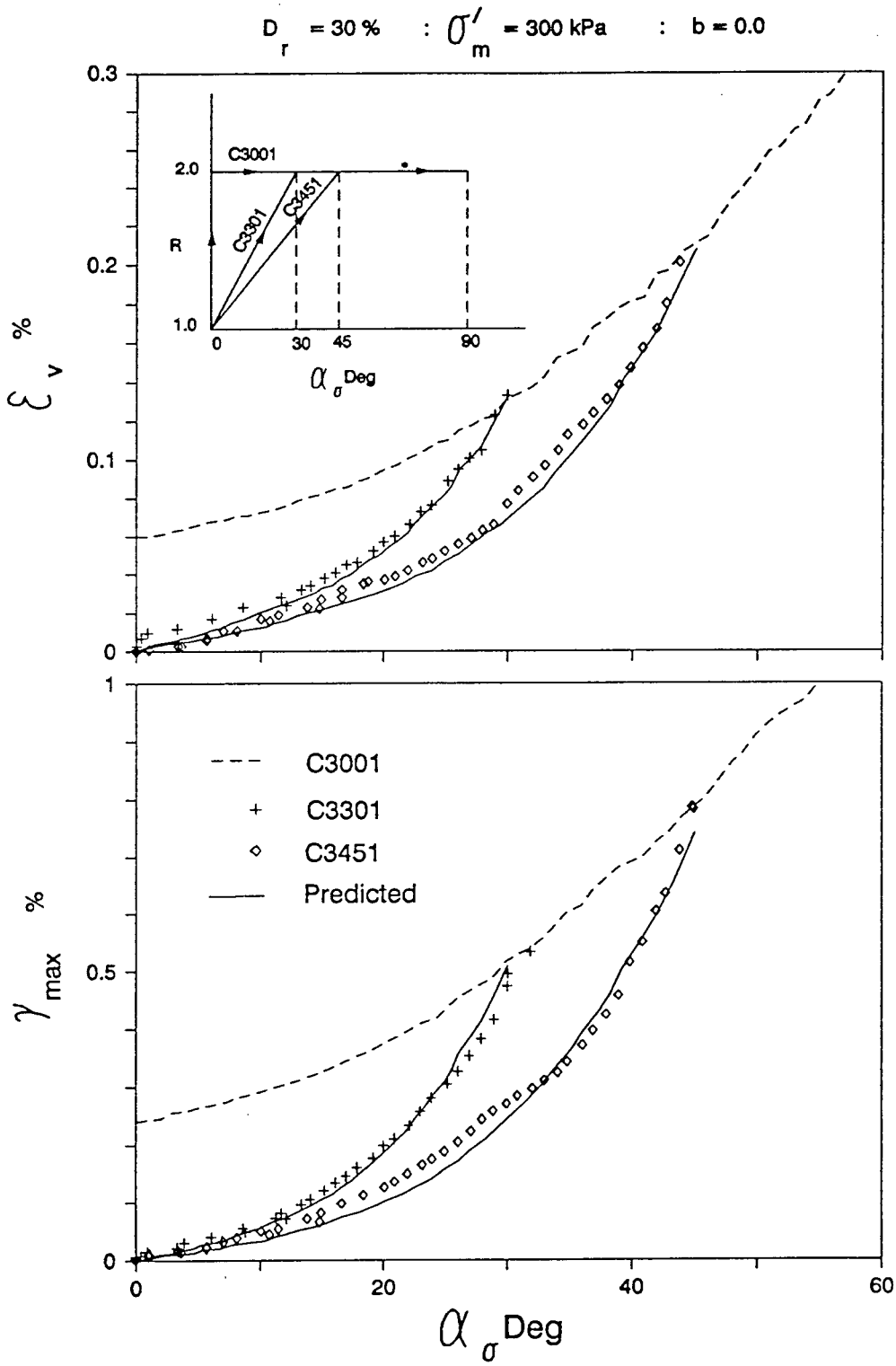

Figure 5.43: Predicted and observed stress strain behaviour - Series C

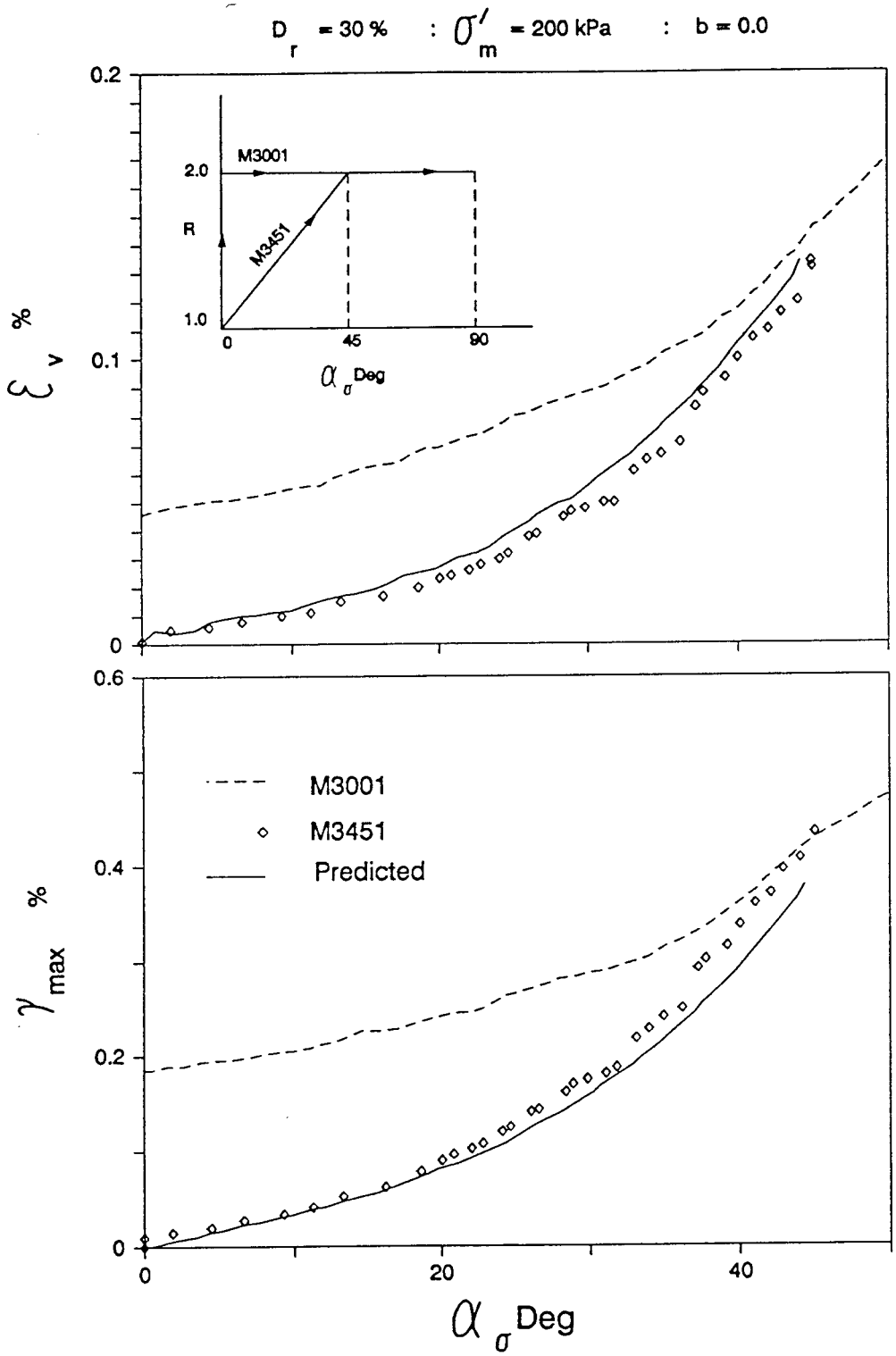

Figure 5.44: Predicted and observed stress strain behaviour - Series M

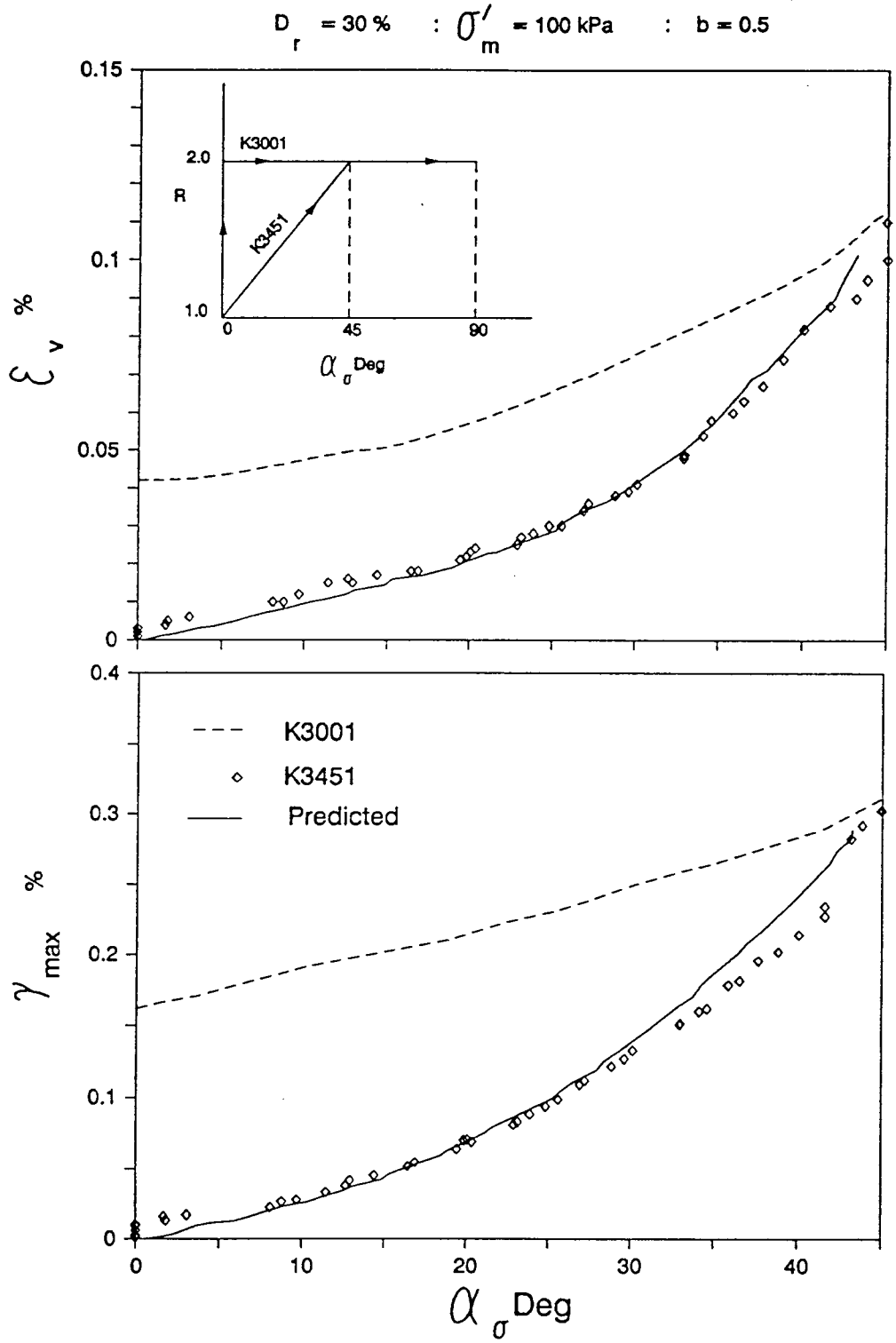

Figure 5.45: Predicted and observed stress strain behaviour - Series K

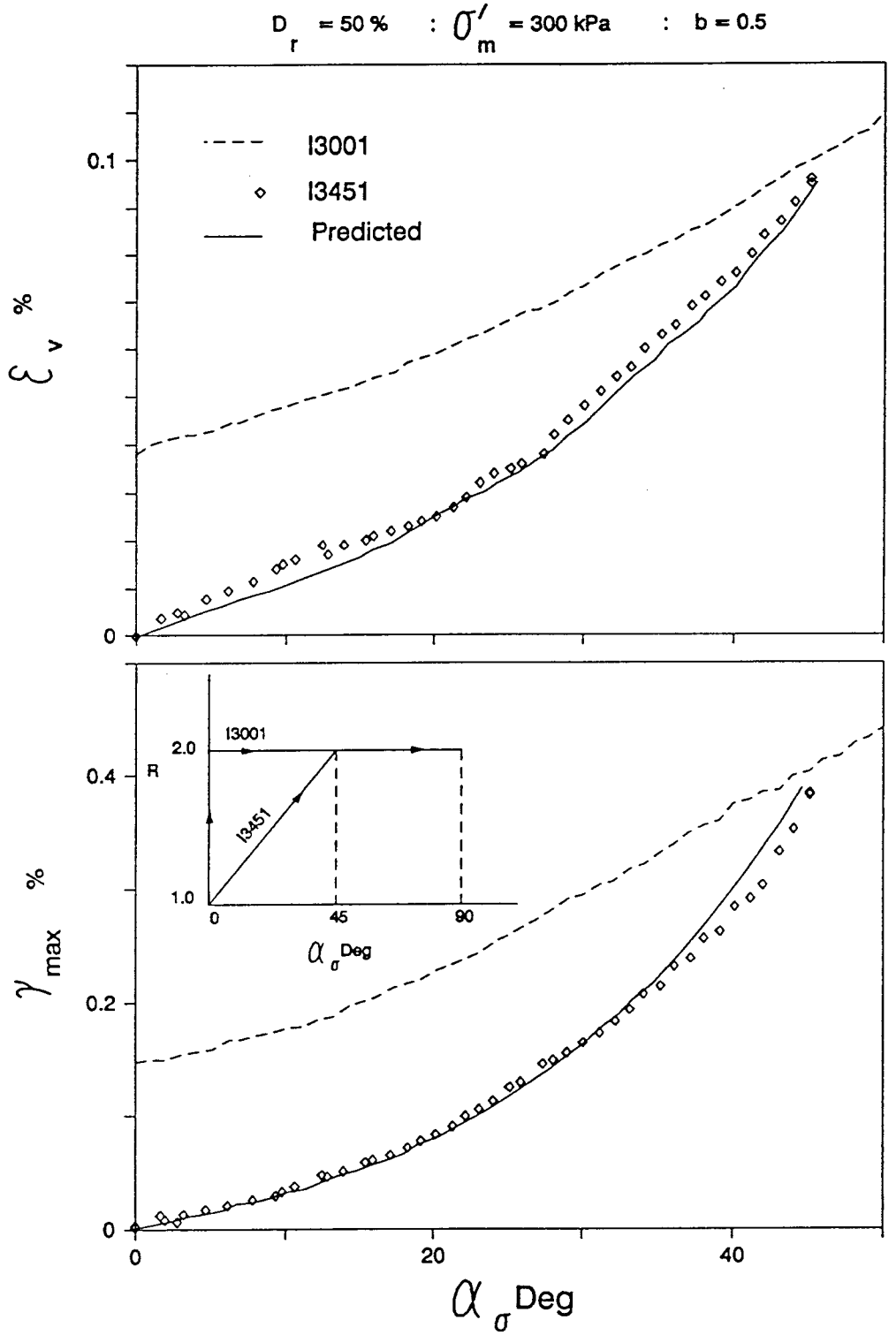

Figure 5.46: Predicted and observed stress strain behaviour - Series I

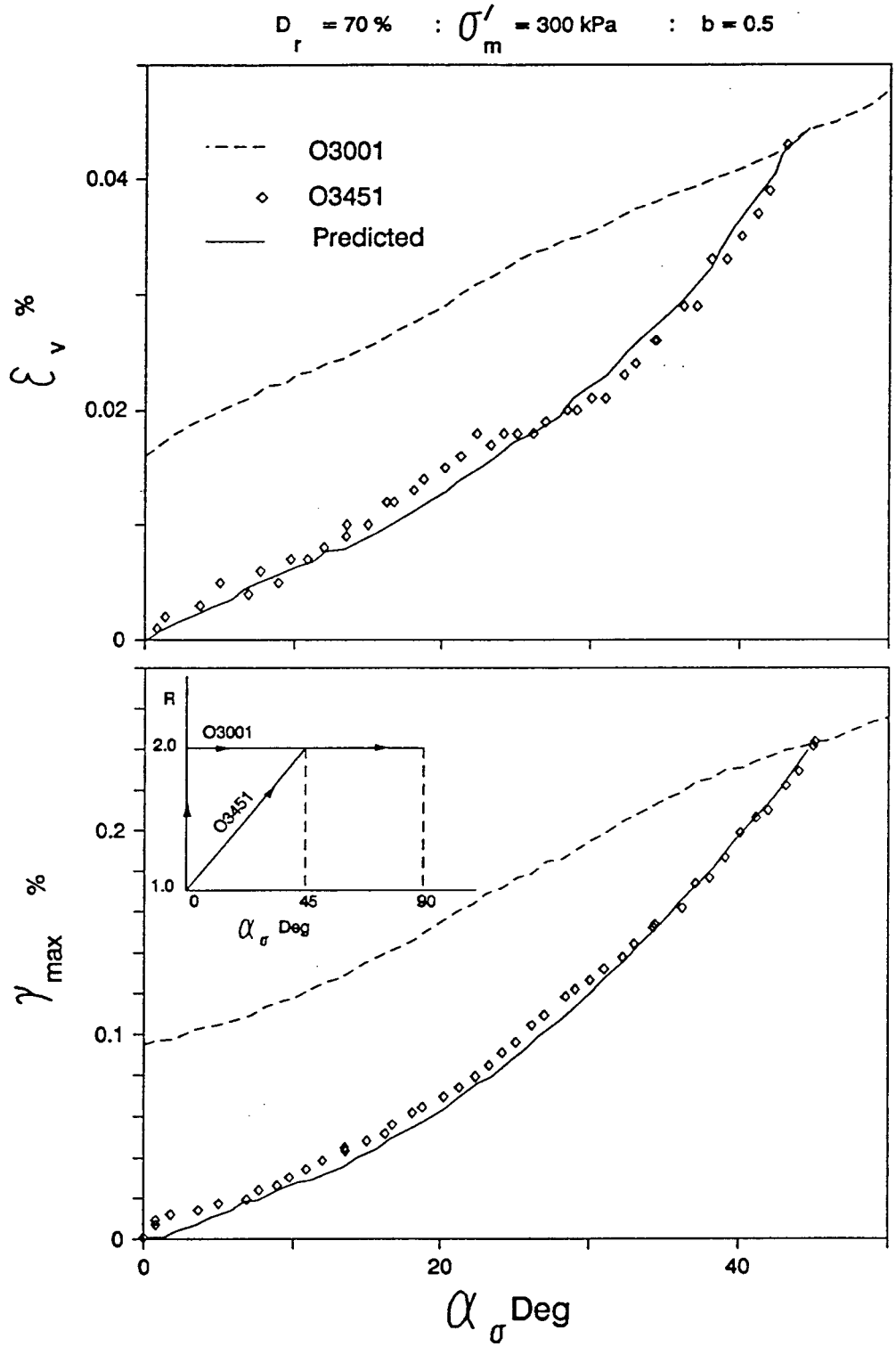

Figure 5.47: Predicted and observed stress strain behaviour - Series O

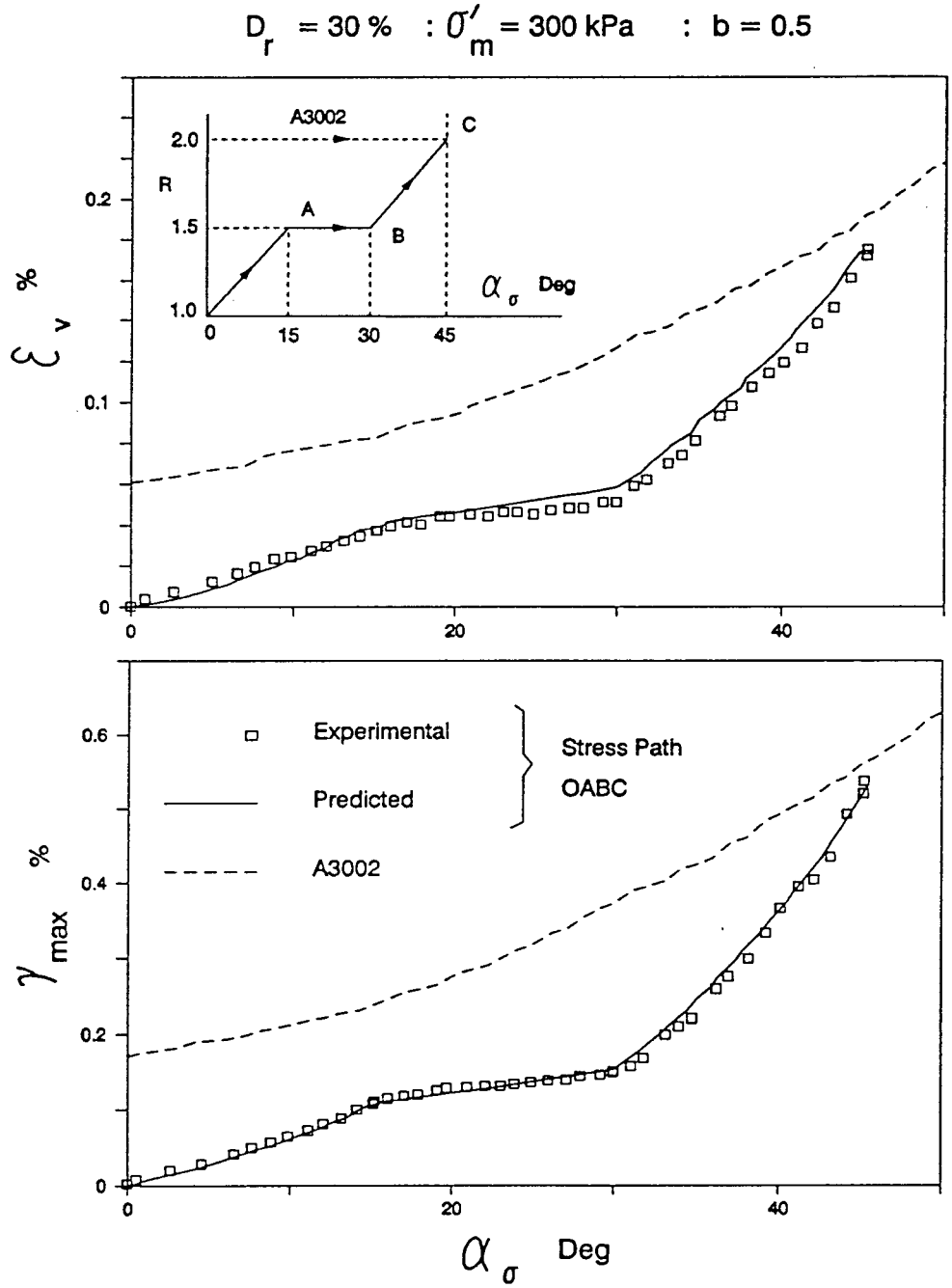

Figure 5.48: Predicted and observed stress strain Behaviour - tri-linear stress path OABC

α paths carried out at several constant σ'_m conditions (Series A, M and K) as shown in Fig. 5.49, the strains at a given σ'_m, R, α_σ stress state P was obtained by the superposition of strains due to:

- hydrostatic loading from initial to the desired value σ'_m (path OC).
- increase in R from above hydrostatic stress state to the desired value with α_σ = 0° and constant σ'_m and b (path CB).
- increase in α_σ with σ'_m, R and b held constant at the desired value (path BP).

This can be expressed mathematically,

$$\{\varepsilon_v\}_{total} = \{\varepsilon_v\}_{\sigma'_m} + \{\varepsilon_v\}_R + \{\varepsilon_v\}_\alpha \tag{5.5}$$

$$\{\gamma_{max}\}_{total} = \{\gamma_{max}\}_{\sigma'_m} + \{\gamma_{max}\}_R + \{\gamma_{max}\}_\alpha \tag{5.6}$$

where, subscript σ'_m indicate strains under hydrostatic loading from initial to the required σ'_m state. For the superposition to be applied for the prediction of strain response under σ'_m - R - α path AB, all strains were referenced to the initial 100 kPa hydrostatic stress state of the path.

$\{\varepsilon_v\}_{\sigma'_m}$ and $\{\gamma_{max}\}_{\sigma'_m}$ are obtained from hydrostatic compression test results.

Values $\{\varepsilon_v\}_R$ and $\{\gamma_{max}\}_R$ are dependent on R as well as σ'_m level. R tests at α_σ = 0° from test series A, M and K gives the strain components $\{\varepsilon_v\}_R$ and $\{\gamma_{max}\}_R$ as functions of R, only for three distinct values of σ'_m (= 300, 200 and 100 kPa). $\{\varepsilon_v\}_R$ and $\{\gamma_{max}\}_R$ at any intermediate σ'_m is obtained by interpolating between these known R path results.

Strain components $\{\varepsilon_v\}_\alpha$ and $\{\gamma_{max}\}_\alpha$ are dependent on all three stress parameters σ'_m, R and α_σ. Again, the α test results from series A, M and K provide the data

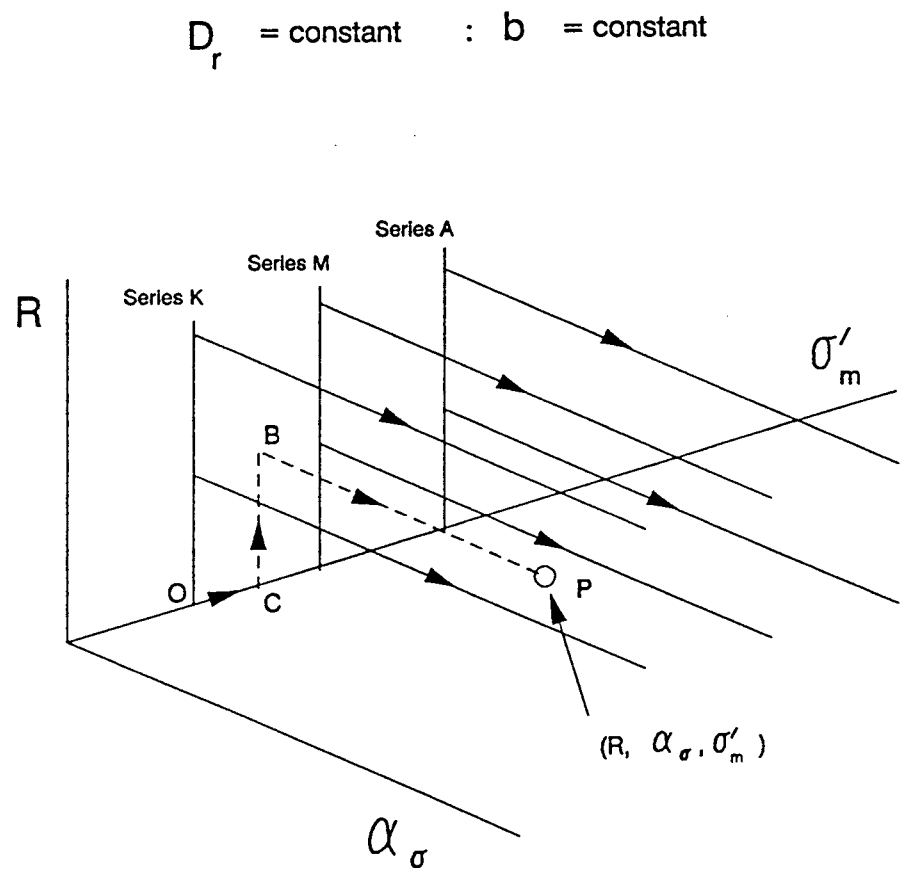

Figure 5.49: Characterization of material behaviour under σ'_m - R - α_σ loading using test series A, M and K

base to characteristize these strain components. Therefore, in this case the values of $\{\varepsilon_v\}_\alpha$ and $\{\gamma_{max}\}_\alpha$ at the given σ'_m, R, α_σ state is derived after interpolation between all these three variables.

The strain response under σ'_m - R - α path (path AB) was predicted using a graphical interpolation, and the comparison between predicted and measured strain responses is given in Fig. 5.50. Very good agreement between the predicted and observed results further corroborates the previously demonstrated stress path independent deformation behaviour of sand under general "total loading" paths involving principal stress rotation.

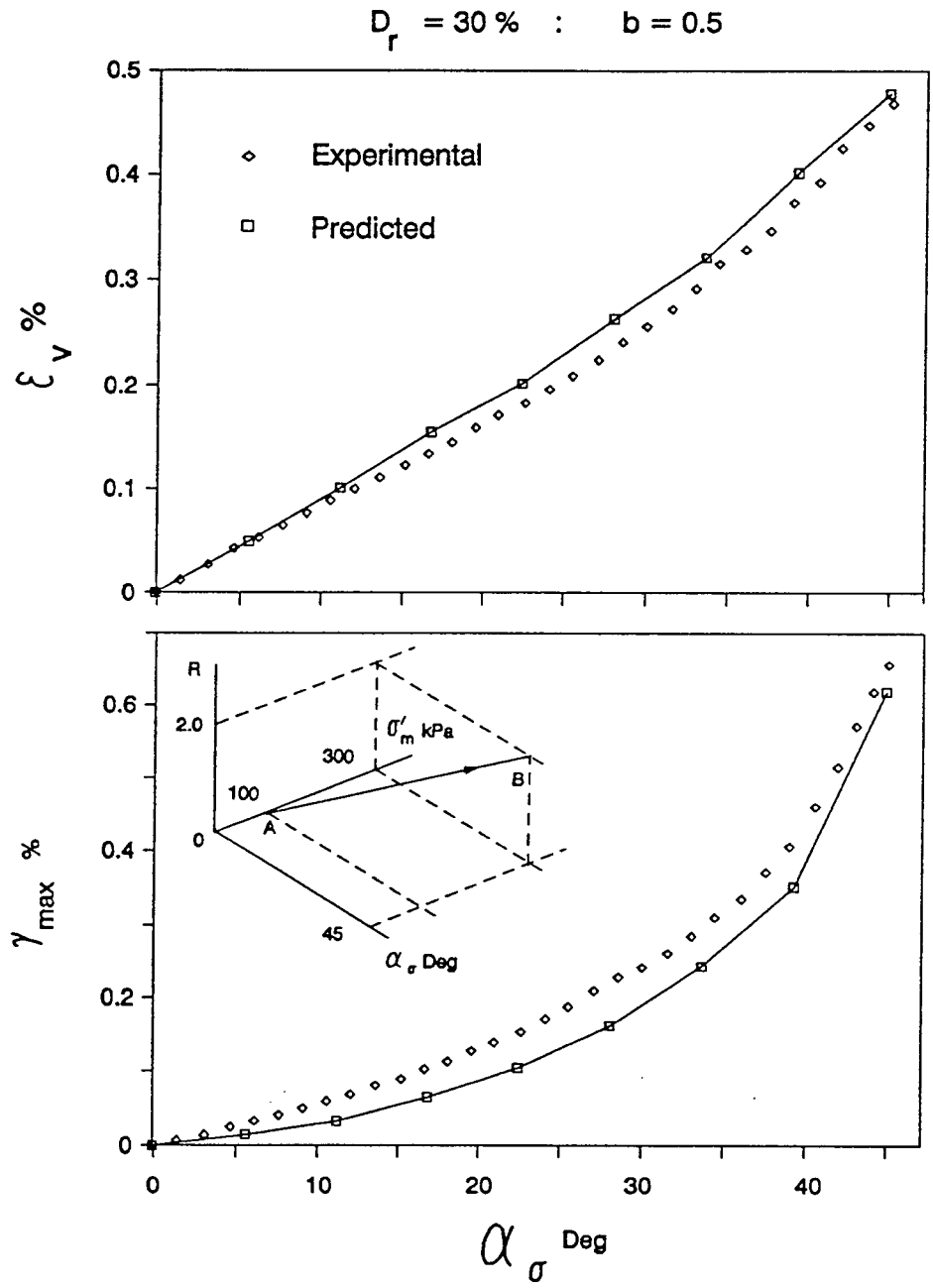

Figure 5.50: Predicted and observed stress strain behaviour - σ'_m - R - α path (path AB)

Chapter 6

Summary and Conclusions

The main objective of this research was to study the drained behaviour of sand under simultaneous increase in stress ratio and principal stress rotation. Hollow cylinder torsional (HCT) device was adopted in this study, due to its inherent advantage of being the only apparatus which is capable of independently controlling the four stress parameters: mean normal effective stress σ'_m, stress ratio R, intermediate principal stress parameter b, and the direction of major principal stress α_σ. These four parameters adequately describe any stress state involving two dimensional principal stress rotation and have been found to influence the behaviour of inherently anisotropic materials.

Manual control of surface tractions in the HCT device is extremely cumbersome, especially in the case of complex stress path tests. In view of this, an automatic stress path control system was developed as a part of the research program.

During stress path loading, stress non-uniformities develop across the walls of the HCT specimen due to its curvature. Therefore a good understanding of the non-uniformities was essential before carrying out stress path testing in the HCT device. It was noted that the stress non-uniformities have been assessed mainly based on the assumptions of linear elastic material behaviour. A finite element simulation of the HCT specimen was performed to study the stress non-uniformities during general stress path tests. The sand behaviour was represented by an incremental elastic hyperbolic model in the analysis. It was revealed that for any given stress state, the linear elastic assumptions overestimates the stress non-uniformity coefficient β_R in

the HCT specimen. The results showed that β_R did not continuously increase with increasing R as in the case of linear elastic material. Instead, β_R values reached a plateau or sometimes even suffered a drop after the peak with increasing stress ratio. The domain of stress space that could reliably be explored using the HCT device was found to be much larger than that previously suggested based on linear elastic considerations. For a given stress state, β_R values increased with increasing density of the specimen. Therefore, the available domain of stress space for reliable exploration decreases for denser sand specimens.

The experimental program was designed to systematically examine the sand response under simultaneous increase of stress ratio R and the direction of major principal stress α_σ. Tests were also carried out where the stress parameters R and α_σ increased individually. Only the stress paths with increasing stress parameters ("loading paths") were considered in this study. No tests were carried out where any of the parameters σ'_m, R, b and α_σ experienced a decrease during loading. All tests were performed on saturated samples of pluviated sand under drained conditions. Emphasis was placed on examining the response of medium loose sand ($D_r = 30\%$) under linear R - α loading paths. Additional investigations were also made on the sand behaviour under multi linear R - α paths and loading with simultaneously increasing σ'_m, R and α_σ.

Deformations from stress paths with individual variations of stress parameters were compared with those from simultaneously increasing R - α_σ at common stress states. The results showed that the strain response of the medium loose sand is path independent provided the final stress state is within the domain of approximately $R \leq 2$ and $0° \leq \alpha_\sigma \leq 45°$. At higher stress ratios and/or larger principal stress rotation angles the deformations were clearly path dependent. In such situations, sand which was subjected to principal stress rotation at a higher stress ratio was observed to develop the largest strains. Furthermore, sand initially loaded to a stress

state within the confines of $R \leq 2$ and $0° \leq \alpha_\sigma \leq 45°$, exhibited no signs of previous stress history effects on the strain response under a subsequent common loading path.

This observed stress path and stress history independent deformation behaviour of loose sand was found to be valid irrespective of the levels of intermediate principal stress parameter b or the mean normal effective stress σ'_m. Similar tests performed at higher densities corroborated these findings, thus extending the validity of the observations to the general sand behaviour.

The major principal strain increment direction $\alpha_{\Delta\varepsilon}$ and the major principal stress increment direction $\alpha_{\Delta\sigma}$ were approximately coincident when $\alpha_{\Delta\sigma} < 45°$. This was found valid regardless of the magnitudes of stress parameters R, α_σ, σ'_m and b or relative density D_r. However, for $\alpha_{\Delta\sigma} > 45°$, strain increment direction $\alpha_{\Delta\varepsilon}$ moved towards the major principal stress direction α_σ with increasing R or principal stress rotation. In other words, the strain increment direction $\alpha_{\Delta\varepsilon}$ was almost totally governed by and coincident with the stress increment direction $\alpha_{\Delta\sigma}$, when $\alpha_{\Delta\sigma}$ was inclined closer to the direction of deposition. When $\alpha_{\Delta\sigma}$ was inclined closer to the direction of bedding plane, the strain increment direction was dependent not only on $\alpha_{\Delta\sigma}$ but also on other parameters such as α_σ, R and D_r etc.

The strain response under tri-linear R - α loading and simultaneous increase in three stress parameters also supported the notion of stress paths and stress history independent behaviour in the domain of $R \leq 2$ and $0° \leq \alpha_\sigma \leq 45°$. It was demonstrated that the sand response under "loading paths" within the above domain could be predicted by the results of a limited number of stress path tests characterizing the strain response in that stress domain.

It was also observed that the effect of b parameter on strain response is insignificant only for small principal stress rotations ($\alpha_\sigma < 45°$). However with increasing principal stress rotation ($\alpha_\sigma \rightarrow 90°$) the influence of b on deformation gradually increase. The distortional strains were more sensitive to b level at larger rotations and larger

deformations occurred with decreasing b. Both increasing mean normal stress σ'_m and decreasing relative density D_r made the deformations under principal stress rotations to increase.

Bibliography

[1] **Arthur, J.R.F. and Menzies, B.K. (1972)**. "Inherent Anisotropy in a Sand", *Geotechnique, Vol. 22, No. 1, pp. 115-128.*

[2] **Arthur, J.R.F., Chua, K.S. and Dunstan, T. (1977)**. "Induced Anisotropy in a Sand", *Geotechnique, Vol. 27, No. 1, pp. 13-30.*

[3] **Arthur, J.R.F., Chua, K.S. and Dunstan, T. (1979)**. "Dense Sand Weakened by Continuous Principal Stress Direction Rotation" *Geotechnique, Vol. 29, No. 1, pp. 92-96.*

[4] **Arthur, J.R.F., Chua, K.S., Dunstan, T. and del Camino, J.R. (1980)**. "Principal Stress Rotation : A missing Parameter", *Journal of the Geotech. Eng. Div., ASCE, Vol. 106, No. GT4, pp. 419-433.*

[5] **Arthur, J.R.F., Bekenstein, S., Germaine, J.T. and Ladd, C.C. (1981)**. "Stress Path Tests with Controlled Rotation of Principal Stress Directions", *Symp. on Laboratory Shear Strength of Soil, ASTM STP 740, pp. 516-540.*

[6] **Bishop, A.W. (1966)**."The Strength of Soils as Engineering Materials", *6th Rankine Lecture, Geotechnique, Vol. 16, No. 2, pp. 91-128.*

[7] **Byrne, P.M., Cheung, H. and Yan, L. (1987)**. "Soil Parameters for Deformation Analysis of Sand Masses", *Canadian Geotech. Journal, Vol. 24, No. 3, pp. 366-376.*

[8] **Casagrande, A. and Carillo, N. (1944)**. "Shear Failure of Anisotropic Materials", *Journal of Boston Society of Civil Engineers, Vol. 31, No. 4, pp. 122-135.*

[9] **Chern, J.C. (1985)**. "Undrained Response of Saturated Sands with Emphasis on Liquefaction and Cyclic Mobility", *Ph. D. Thesis, Dept. of Civil Enginerring, University of British Columbia, Canada.*

[10] **Duncan, J.M., Byrne, P.M., Wong, K.S. and Mabry, P. (1980)**. "Strength, Stress-Strain and Bulk Modulus Parameters for Finite Element Analysis of Stresses and Movements in Soil Masses", *University of California, Berkeley, CA, Report No. UCB/GT/80-01.*

[11] **El-Sohby, M.A. and Andrawes, K.Z. (1972)**. "Deformation Characteristics of Granular Materials Under Hydrostatic Compression", *Canadian Geotech. Journal, Vol. 9, No. 4, pp. 338-350.*

[12] **El-Sohby, M.A. and Andrawes, K.Z. (1973)**. "Experimental Examination of Sand Anisotropy", *Proc. 8th Int. Conf. on Soil Mech. and Found. Eng., Vol. 1, pp. 103-109.*

[13] **Green, G.E. (1971)**. "Strength and Deformation of Sand Measured in an Independent Stress Control Cell", *Proc. of Roscoe Memorial Symp. on Stress-Strain Behaviour of Soils, Cambridge University, pp. 285-323.*

[14] **Habib, P. (1953)**. "Influence of the Variation of the Average Principal Stress Upon the Shearing Strength of Soils", *Proc. 3rd. Int. Conf. on Soil Mech. and Found. Eng., Vol. 1, pp. 131-136.*

[15] **Haruyama, M. (1981)**. "Anisotropic Deformation - Strength Characteristics of an Assembly of Spherical Particles Under 3-D Stresses", *Soils and Foundations, Vol. 21, No. 4, pp. 41-55.*

[16] **Hight, D.W., Gens, A. and Symes, M.J. (1983)**. "The Development of a New Hollow Cylinder Apparatus for Investigating the Effects of Principal Stress Rotation in Soils", *Geotechnique, Vol. 33, No. 4, pp 355-383.*

[17] **Ishihara, K. and Towhata, I. (1982)**. "Cyclic Behaviour of Sand During Rotation of Principal Stress Axes", *Proc. of the U.S./Japan Seminar on New Models and Constitutive Relations in the Mechanics of Granular Materials, Ithaca, N.Y., pp. 53-73.*

[18] **Kjellman, W. (1936)**. "Report on an Apparatus for Consummate Investigation of the Mechanical Properties of Soil", *Proc. 1st Int. Conf. on Soil Mech. and Found. Eng., Vol. 2, pp 16-20.*

[19] **Kuerbis, R. and Vaid, Y.P. (1988)**. "Sand Sample Preparation: The Slurry Deposition Method", *Soil Mech. Series No. 121, Dept. of Civil Engineering, University of British Columbia, Canada.*

[20] **Lee, K.L. and Seed, H.B. (1967)**. "Drained Strength Characteristics of Sands", *Journal of the Soil Mech. and Found. Eng. Division, ASCE, Vol. 93, No. SM6, pp. 117-141.*

[21] **Ladd, C.C., Foott, R., Ishihara, K., Schlosser, F. and Poulos, H.G. (1977)**."Stress-Deformation and Strength Characteristics", *State of the Art Report, Proc. 9th Int. Conf. on Soil Mech. and Found. Eng., Vol. 2, pp. 421-494.*

[22] **Lade, P.V. and Duncan, J.M. (1973)**. "Cubical Triaxial Tests on Cohesionless Soil", *Journal of the Soil Mech. and Found. Div., ASCE, Vol. 99, No. SM10, pp. 793-812.*

[23] **Matsuoka, H. (1974)**. "Stress-Strain Relationships of Sands Based on the Mobilized Plane", *Soils and Foundations, Vol. 14, No. 2, pp. 47-61.*

[24] **Mejia, C.A., Vaid, Y.P. and Negussey, D. (1988)**. "Time Dependent Behaviour of Sand", *Proc. of the Int. Conf. on Rheology and Soil Mechanics, Coventry, UK, pp. 312-326.*

[25] **Miura, K. (1985)**."Study on the Deformation Behaviour of Anisotropic Sand Under Principal Stress Axes Rotation", *Ph. D. Thesis, Hokkaido University, Japan.*

[26] **Miura, S. and Toki, S. (1984)**. "Anisotropy in Mechanical Properties and its Simulation of Sands Sampled from Natural Deposits", *Soils and Foundations, Vol. 24, No. 3, pp. 69-84.*

[27] **Mould, J.C., Sture, S. and Ko, H.Y. (1982)**. "Modelling of Elastic-Plastic Anisotropic Hardening and Rotating Principal Stress Directions in Sand", *IUTAM Conf. on Deformation and Failure of Granular Materials, Delft, pp. 431-439.*

[28] **Negussey, D. (1984)**. " An Experimental Study of the Small Strain Response of Sand", *Ph.D Thesis, Dept. of Civil Engineering, University of British Columbia, Canada.*

[29] **NSF/NSERC Workshop (1980)**. "On Limit Equilibrium, Plasticity and Generalized Stress-Strain in Geotechnical Engineering". Montreal, Canada.

[30] **Oda, M. (1972)**. "Initial Fabrics and Their Relations to Mechanical Properties of Granular Material", *Soils and Foundations, Vol. 12, No. 1, pp. 17-36.*

[31] **Oda, M. (1976)**. "Fabrics and Their Effects on the Deformation Behaviour of Sand", *Report, Dept. of Foundation Engineering, Saitama Univ., Japan, Special Issue.*

[32] **Oda, M. (1981)**. "Anisotropic Strength of Cohesionless Sands", *Journal of the Geot. Eng. Div., ASCE, Vol. 107, No. GT9, pp. 1219-1231.*

[33] **Oda, M., Koishikawa, I. and Higuchi, T. (1978)**. "Experimental Study of Anisotropic Shear Strength of Sand by Plane Strain Test", *Soils and Foundations, Vol. 18, No. 1, pp. 25-38.*

[34] **Oda, M., Nemat-Nasser, S. and Konishi, J. (1985)**. "Stress-Induced Anisotropy in Granular Masses", *Soils and Foundations, Vol. 25, No. 3, pp. 85-97.*

[35] **Roscoe, K.H., Schofield, A.N. and Wroth, C.P. (1958)**. "On the Yielding of Soils", *Geotechnique, Vol. 8, No. 1, pp. 25-53.*

[36] **Saada, A.S. (1981)**. Discussion on "Undrained Deformation Characteristics of Loose Sand Under Three Dimensional Stress Conditions", *Soils and Foundations, Vol. 21, No. 4, pp. 121-122.*

[37] **Saada, A.S. and Townsend, F.C. (1981)**. "State of the Art: Laboratory Strength testing of Soils", *Symp. on Laboratory Shear Strength of Soils, ASTM STP 740, pp. 7-77.*

[38] **Salgado, F. M. G. A. (1990)**. "Analysis Procedures for Caisson - Retained Island Type Structures.", *Ph.D Thesis, Dept. of Civil Engineering, University of British Columbia, Canada.*

[39] **Sayao, A.S.F. (1989)**. "Behaviour of Sands Under General Stress Paths in the Hollow Cylinder Torsional Device.", *Ph.D Thesis, Dept. of Civil Engineering, University of British Columbia, Canada.*

[40] **Sayao, A.S.F. and Vaid, Y.P. (1988)**. "A Critical Assessment of Stress Distribution on Hollow Cylinder Test Specimens", *Soil Mech. Series, No. 132, Dept. of Civil Engineering, Univ. of British Columbia, Canada.*

[41] **Sayao, A.S.F. and Vaid, Y.P. (1989)**. Discussion on "Drained Principal Stress Rotation in Saturated Sand", *Geotechnique, Vol. 39, No. 3, pp. 549-552.*

[42] **Shibuya, S. and Hight, D.W. (1987)**. "A Bounding Surface for Granular Materials", *Soils and Foundations, Vol. 27, No. 4, pp. 123-136.*

[43] **Sutherland, H.B. and Mesdary, M.S. (1969)**. "The Influence of the Intermediate Principal Stress on the Strength of Sand", *Proc. 7th Int. Conf. on Soil Mech. and Found. Eng., Vol. 1, pp. 391-399.*

[44] **Symes, M.J., Hight, D.W. and Gens, A. (1982)**. "Investigating Anisotropy and the Effects of Principal stress Rotation of the Intermediate Principal Stress Using a Hollow Cylinder Apparatus", *IUTAM Conf. on Deformation and Failure of Granular Materials, Delft, pp. 441-449.*

[45] **Symes, M.J., Gens, A. and Hight, D.W. (1984)**. "Undrained Anisotropy and Principal Stress Rotation in Saturated Sand", *Geotechnique, Vol. 34, No. 1, pp. 11-27.*

[46] **Symes, M.J., Gens, A. and Hight, D.W. (1988)**. "Drained Principal Stress Rotation in Saturated Sand", *Geotechnique, Vol. 38, No. 1, pp. 59-81.*

[47] **Tatsuoka, F., Muramatsu, M. and Sasaki, T. (1983)**. Discussion Closure on "Cyclic Undrained Stress-Strain Behaviour of Dense Sands by Torsional Simple Shear Test", *Soils and Foundations, Vol. 23, No. 3, pp. 142-145.*

[48] **Vaid, Y.P. (1983)**. Discussion on "Cyclic Undrained Stress-Strain Behaviour of Dense Sands by Torsional Simple Shear Test", *Soils and Foundations, Vol. 23, No. 2, pp. 172-173.*

[49] **Vaid, Y.P. and Negussey, D. (1984a)**. "A Critical Assessment of Membrane Penetration in Triaxial Test", *Geotechnical Testing Journal, ASTM, Vol. 7, No. 2, pp. 70-76.*

[50] **Vaid, Y.P. and Negussey, D. (1984b)**. "Relative Density of Pluviated Sand Samples", *Soils and Foundations, Vol. 24, No. 2, pp. 101-105.*

[51] **Vaid, Y.P. and Negussey, D. (1988)**. "Preparation of Reconstituted Sand Specimens", *Symp. on Advanced Triaxial testing of Soil and Rock, ASTM STP 977, pp. 405-417.*

[52] **Vaid, Y.P., Sayao, A., Enhuang, H. and Negussey, D., (1990)**. "The UBC Holow Cylinder Torsional Apparatus", *Soil Mech. Series, No. 118, Dept. of Civil Engineering, Univ. of British Columbia, Canada.*

[53] **Vesic, A.S. and Clough, G.W. (1968)**. "Behaviour of Granular Materials Under High Stresses", *Journal of the Soil Mech. and Found. Eng. Division, ASCE, Vol. 94, No. SM3, pp. 661-688.*

[54] **Yamada, Y. and Ishihara, K. (1979)**. "Anisotropic Deformation Characteristics of Sand Under Three Dimensional Stress Conditions", *Soils and Foundations, Vol. 19, No. 2, pp. 79-94.*

[55] **Wong, R.K.S and Arthur, J.R.F. (1985)**. "Induced and Inherent Anisotropy in Sand", *Geotechnique, Vol. 35, No. 4, pp. 471-481.*

Appendix A

Cross Anisotropic Elastic Material Behaviour

Cross anisotropic elastic material exhibits a rotational symmetry about one of the coordinate axes. Let Z be the axis of elastic symmetry and $X-Y$ be the plane of isotropy as shown in Fig. A.1a.

The incremental stress strain relation for a cross anisotropic elastic material (under 2-D principal stress rotation in $X-Z$ plane) can be written as,

$$\begin{Bmatrix} \Delta\varepsilon_x \\ \Delta\varepsilon_y \\ \Delta\varepsilon_z \\ \Delta\gamma_{xz} \end{Bmatrix} = \begin{bmatrix} \frac{1}{E} & -\frac{\nu}{E} & -\frac{\nu'}{E'} & 0 \\ -\frac{\nu}{E} & \frac{1}{E} & -\frac{\nu'}{E'} & 0 \\ -\frac{\nu'}{E'} & -\frac{\nu'}{E'} & \frac{1}{E'} & 0 \\ 0 & 0 & 0 & \frac{1}{G'} \end{bmatrix} \begin{Bmatrix} \Delta\sigma_x \\ \Delta\sigma_y \\ \Delta\sigma_z \\ \Delta\tau_{xz} \end{Bmatrix} \tag{A.1}$$

where,

E - Young's modulus in the plane $X-Y$

E' - Young's modulus in the Z direction

G' - Shear modulus in the plane $X-Z$

ν - Poisson's ratio in the plane $X-Y$

ν' - Poisson's ratio in the plane $X-Z$

This leads to,

$$\Delta\varepsilon_x = \frac{1}{E}\Delta\sigma_x - \frac{\nu}{E}\Delta\sigma_y - \frac{\nu'}{E'}\Delta\sigma_z \tag{A.2}$$

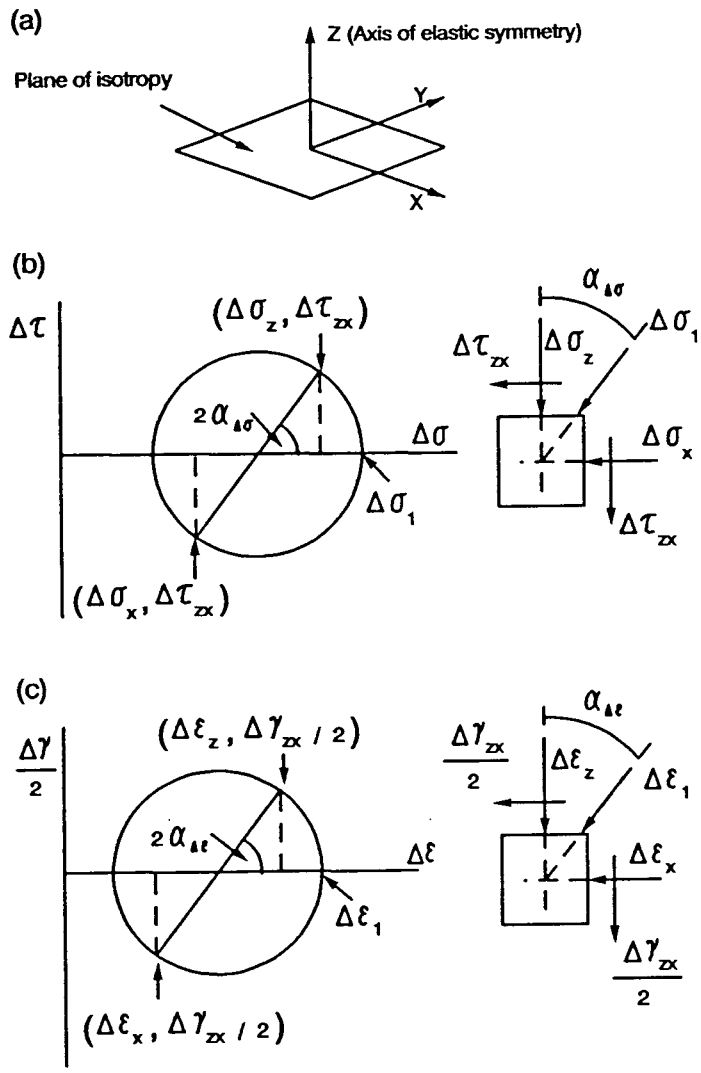

Figure A.1: Cross anisotropic elastic material

$$\Delta\varepsilon_z = -\frac{\nu'}{E'}\Delta\sigma_x - \frac{\nu'}{E'}\Delta\sigma_y + \frac{1}{E'}\Delta\sigma_z \tag{A.3}$$

$$\Delta\gamma_{xz} = \frac{1}{G'}\Delta\tau_{xz} \tag{A.4}$$

From equations A.2 and A.3,

$$\frac{(\Delta\varepsilon_z - \Delta\varepsilon_x)}{(\Delta\sigma_z - \Delta\sigma_x)} = \left[\frac{\nu'}{E'} + \left\{\frac{\left(\frac{\Delta\sigma_z}{\Delta\sigma_x}\right)\frac{1}{E'} - \frac{1}{E}}{\left(\frac{\Delta\sigma_z}{\Delta\sigma_x}\right) - 1}\right\} + \left\{\frac{\nu}{E} - \frac{\nu'}{E'}\right\}\left\{\frac{\left(\frac{\Delta\sigma_y}{\Delta\sigma_x}\right)}{\left(\frac{\Delta\sigma_z}{\Delta\sigma_x}\right) - 1}\right\}\right] \tag{A.5}$$

Defining $\frac{\Delta\sigma_z}{\Delta\sigma_x} = k_{zx}$ and $\frac{\Delta\sigma_y}{\Delta\sigma_x} = k_{yx}$, and substituting in Eqn. A.5 yields,

$$\frac{(\Delta\varepsilon_z - \Delta\varepsilon_x)}{(\Delta\sigma_z - \Delta\sigma_x)} = \left[\frac{\nu'}{E'} + \left\{\frac{\frac{k_{zx}}{E'} - \frac{1}{E}}{k_{zx} - 1}\right\} + \left\{\frac{\nu}{E} - \frac{\nu'}{E'}\right\}\left\{\frac{k_{yx}}{k_{zx} - 1}\right\}\right] \tag{A.6}$$

Using Mohr circle for stress increments in Fig. A.1b, the direction of stress increment $\alpha_{\Delta\sigma}$ with respect to Z direction can be written as,

$$\tan 2\alpha_{\Delta\sigma} = \frac{2\Delta\tau_{xz}}{\Delta\sigma_z - \Delta\sigma_x} \tag{A.7}$$

Similarly using Mohr circle for strain increments in Fig. A.1c, the direction of strain increment $\alpha_{\Delta\varepsilon}$ with respect to Z direction can be written as,

$$\tan 2\alpha_{\Delta\varepsilon} = \frac{\Delta\gamma_{xz}}{\Delta\varepsilon_z - \Delta\varepsilon_x} \tag{A.8}$$

Coincidence of stress increment and strain increment directions implies, $\tan 2\alpha_{\Delta\sigma} = \tan 2\alpha_{\Delta\varepsilon}$. Therefore, from Eqns. A.7 and A.8,

$$\frac{\Delta\gamma_{xz}}{\Delta\tau_{xz}} = 2\left\{\frac{\Delta\varepsilon_z - \Delta\varepsilon_x}{\Delta\sigma_z - \Delta\sigma_x}\right\} \tag{A.9}$$

Combining Eqns. A.4, A.6 and A.9 we get the condition for coincidence of stress increment and strain increment directions as,

$$\frac{1}{G'} = 2\left[\frac{\nu'}{E'} + \left\{\frac{\frac{k_{xx}}{E'} - \frac{1}{E}}{k_{zx} - 1}\right\} + \left\{\frac{\nu}{E} - \frac{\nu'}{E'}\right\}\left\{\frac{k_{yx}}{k_{zx} - 1}\right\}\right] \tag{A.10}$$

For a given cross anisotropic linear elastic material the parameters E, E', G', ν and ν' are constants. Therefore, the condition expressed by Eqn. A.10 would be satisfied only under certain values of k_{zx} and k_{yx}, which is related to the applied loading conditions. This implies that the coincidence of stress and strain increment directions would not occur under any arbitrary loading condition, even if the material is cross anisotropic elastic. Conversely, the coincidence of stress and strain increments along an arbitrary loading path in an anisotropic material is not a sufficient condition to conclude that the material is elastic.

Appendix B

Membrane Penetration Corrections

A minimum of four strain components are required to define the complete configuration of a hollow cylindrical specimen. In the UBC-HCT device, two strain components ε_r and ε_θ are estimated indirectly from the measured volume changes of the specimen and the internal confining chamber. (See section 3.2 for details).

Both inside and outside vertical surfaces of the HCT specimen are covered by 0.3 mm thick rubber membranes. In testing granular materials, when drained stress paths of varying cell pressures are imposed, the measured volume changes are subject to error resulting from membrane penetration. Therefore it is important to correct the measured volume changes for membrane penetration effects before the values are employed in strain computations.

The test results in this thesis have been presented after correcting for membrane penetration effects, using the method proposed by Vaid and Negussey (1984). Vaid and Negussey observed a linear variation between the unit membrane penetration ε_m and the logarithm of effective confining stress. Unit membrane penetration results for Ottawa sand ASTM-C-109 (with a 0.3 mm thick rubber membrane) are reproduced in Fig. B.1.

The measured volume change of the sand specimen was corrected as follows.

$$\Delta V_S = \{\Delta V_S\}_t - \{\Delta V_M\}_t \tag{B.1}$$

$$\{\Delta V_M\}_t = \{\Delta V_M\}_i + \{\Delta V_M\}_e \tag{B.2}$$

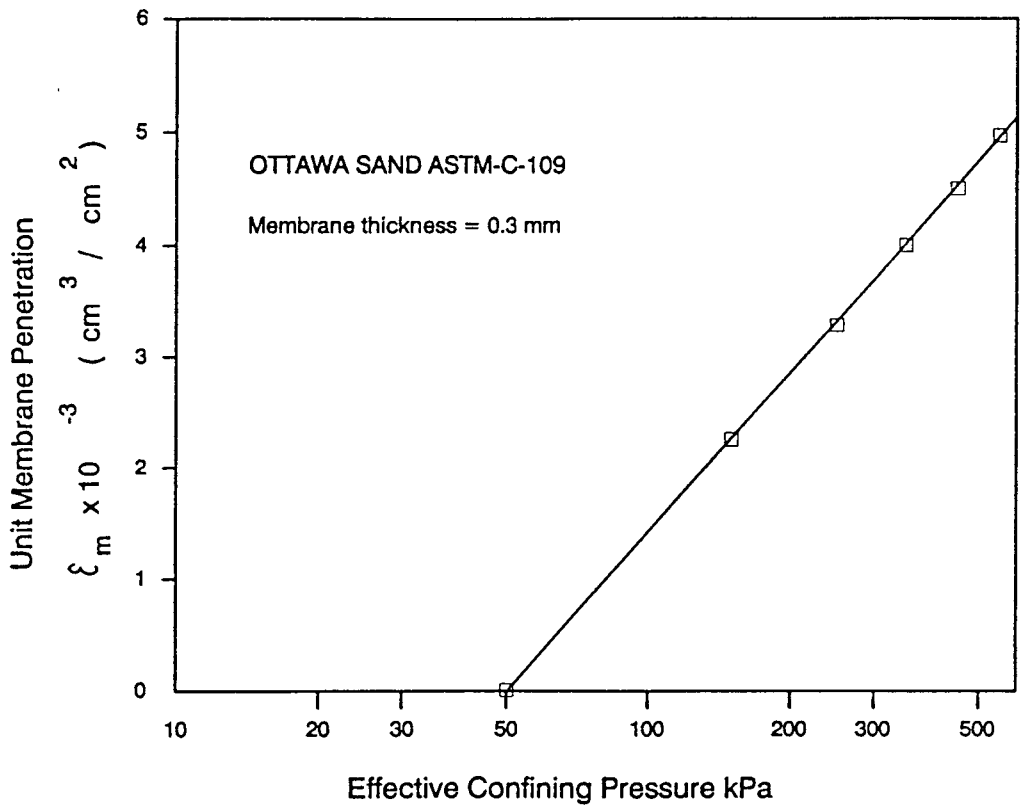

Figure B.1: Membrane penetration correction curve - after Vaid and Negussey (1984)

where,

ΔV_S - Corrected volume change of the specimen

$\{\Delta V_S\}_t$ - Measured total volume change of the specimen

$\{\Delta V_M\}_t$ - Total membrane penetration volume change

$\{\Delta V_M\}_i$ - Volume change due to penetration of internal membrane

$\{\Delta V_M\}_e$ - Volume change due to penetration of external membrane

For the current values of internal (or external) effective confining pressure and the imposed increments $\Delta P_i'$ (or $\Delta P_e'$), the change in corresponding unit membrane penetration $\{\Delta\varepsilon_m\}_i$ (or $\{\Delta\varepsilon_m\}_e$) [1] were obtained from the curve in Fig. B.1. The values of $\{\Delta V_M\}_i$ and $\{\Delta V_M\}_e$ were then obtained using the following equations.

$$\{\Delta V_M\}_i = \{\Delta\varepsilon_m\}_i A_i \tag{B.3}$$

$$\{\Delta V_M\}_e = \{\Delta\varepsilon_m\}_e A_e \tag{B.4}$$

where,

A_i - Surface area of the internal membrane covering the specimen

A_e - Surface area of the external membrane covering the specimen

In a similar manner the volume change of the internal chamber was corrected as given below.

$$\Delta V_I = \{\Delta V_I\}_t + \{\Delta V_M\}_i \tag{B.5}$$

where,

[1] N.B. the value of $\{\Delta\varepsilon_m\}$ is positive, for positive $\Delta P'$.

ΔV_I - Corrected volume change of the internal chamber

$\{\Delta V_I\}_t$ - Measured total volume change of the internal chamber

Appendix C

Deformation Characteristics of Test Series E, C, M, K, I and O

As discussed in Chapter 5 (Section 5.6), in order to predict deformations under R - α paths, the characteristic behaviour is obtained by means of several α paths and an R path with $\alpha_\sigma = 0°$. Such characterization was demonstrated for the test Series A (Figs. 5.37 and 5.39).

Similar tests were carried out on several test series (Series E through O) and the resulting deformation data are presented in this appendix. The data were utilized to predict the strain response under R - α paths for these test series presented in Figs. 5.42 through 5.47.

For each series the volumetric and maximum shear strain responses under following loading conditions are presented.

- R loading with $\alpha_\sigma = 0°$
- α loading under different R levels ($R = 1.65$ and 2.0)

Test results are presented in Figs. C.1 through C.12. The contents of each figure are summarized in Table C.1.

In prediction of response under R - α paths, the data from α paths were interpolated using a curve fitting technique as described in section 5.6.2. In order to examine the suitability of fit, the fitted curves are superimposed on the experimentally observed volumetric and maximum shear strain data.

Table C.1: Index - Deformation Characteristics of Test Series E, C, M, K, I and O

Series No.	Figure No.	
	R path	α paths
E	C.1	C.2
C	C.3	C.4
M	C.5	C.6
K	C.7	C.8
I	C.9	C.10
O	C.11	C.12

All strain components are referenced to the hydrostatic stress state immediately before R loading.

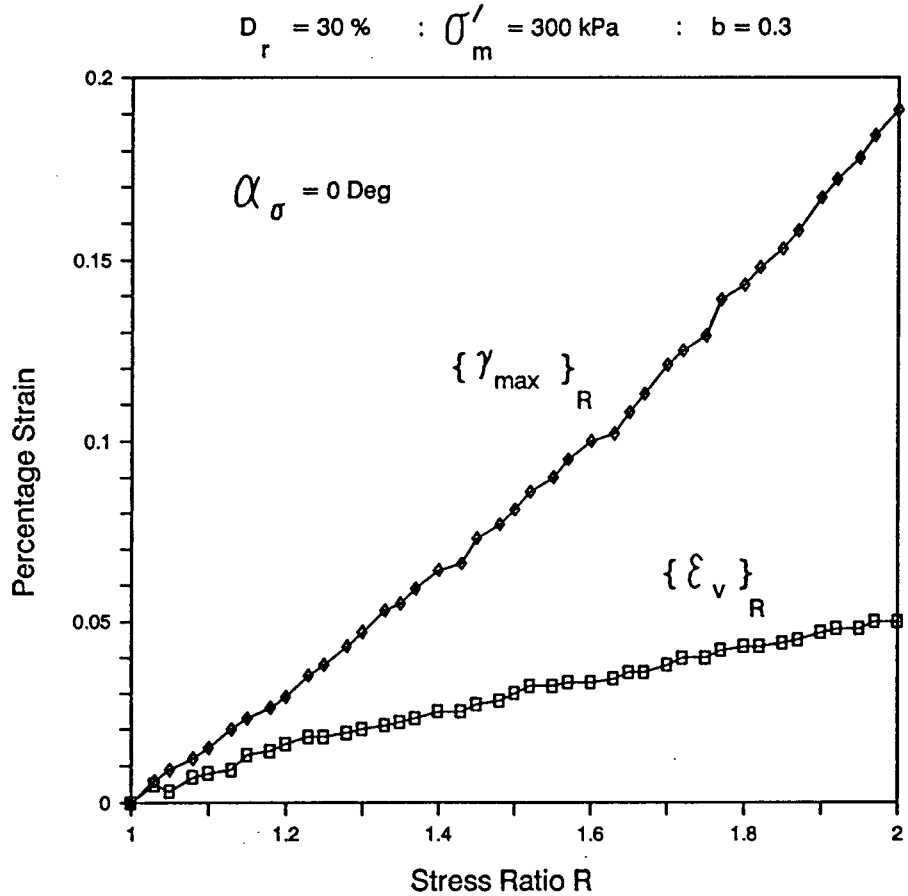

Figure C.1: Deformations under shear loading with $\alpha_\sigma = 0°$ - Test Series E

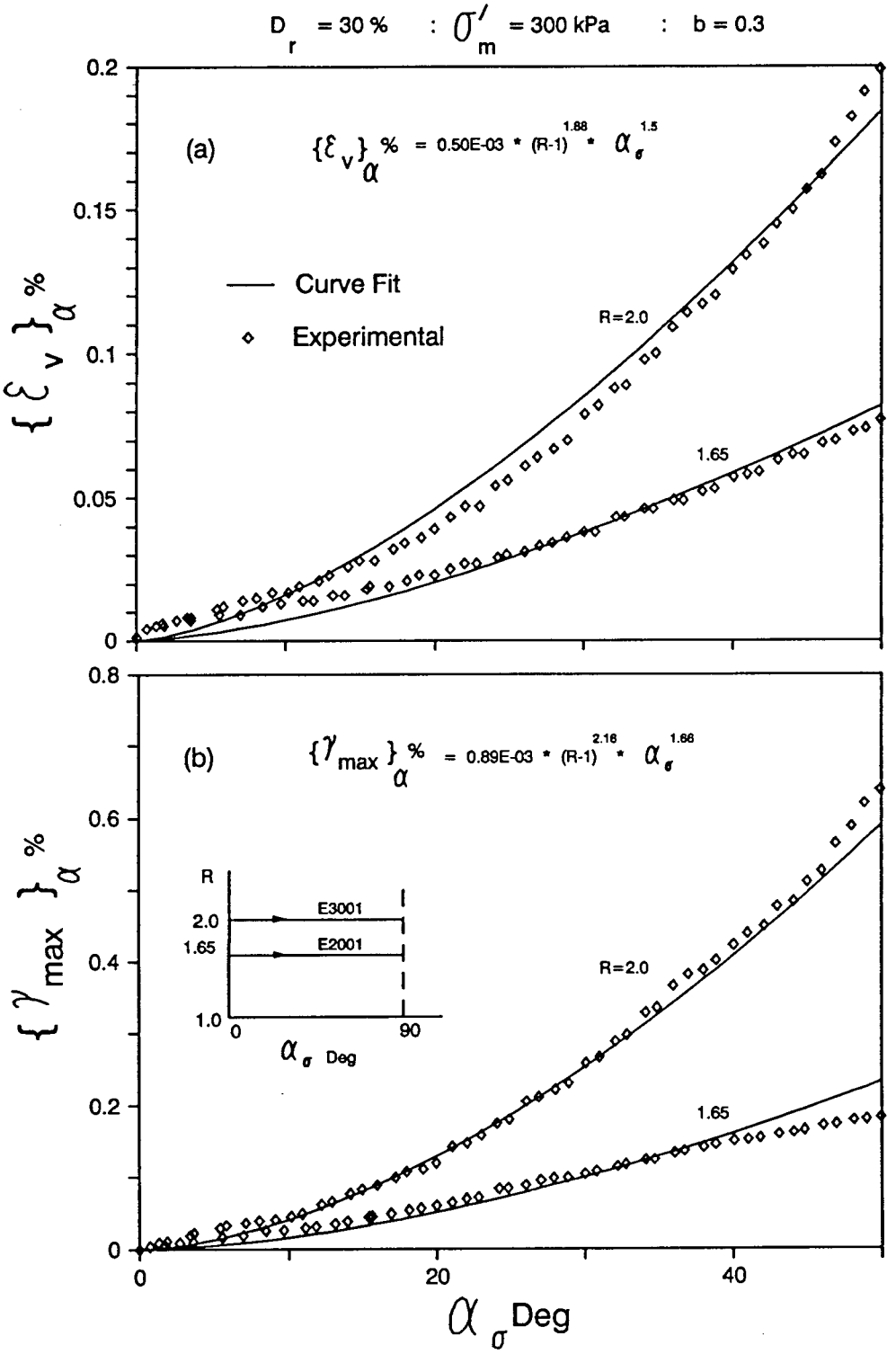

Figure C.2: Deformations under α paths with R = constant - Test Series E

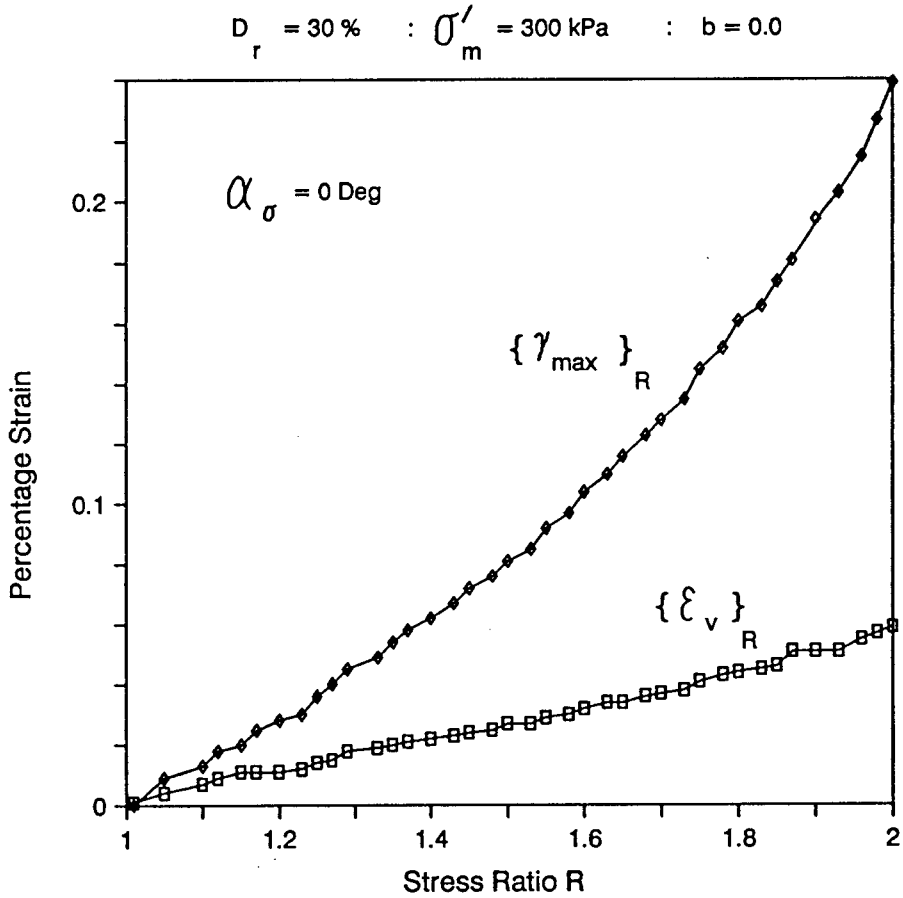

Figure C.3: Deformations under shear loading with $\alpha_\sigma = 0°$ - Test Series C

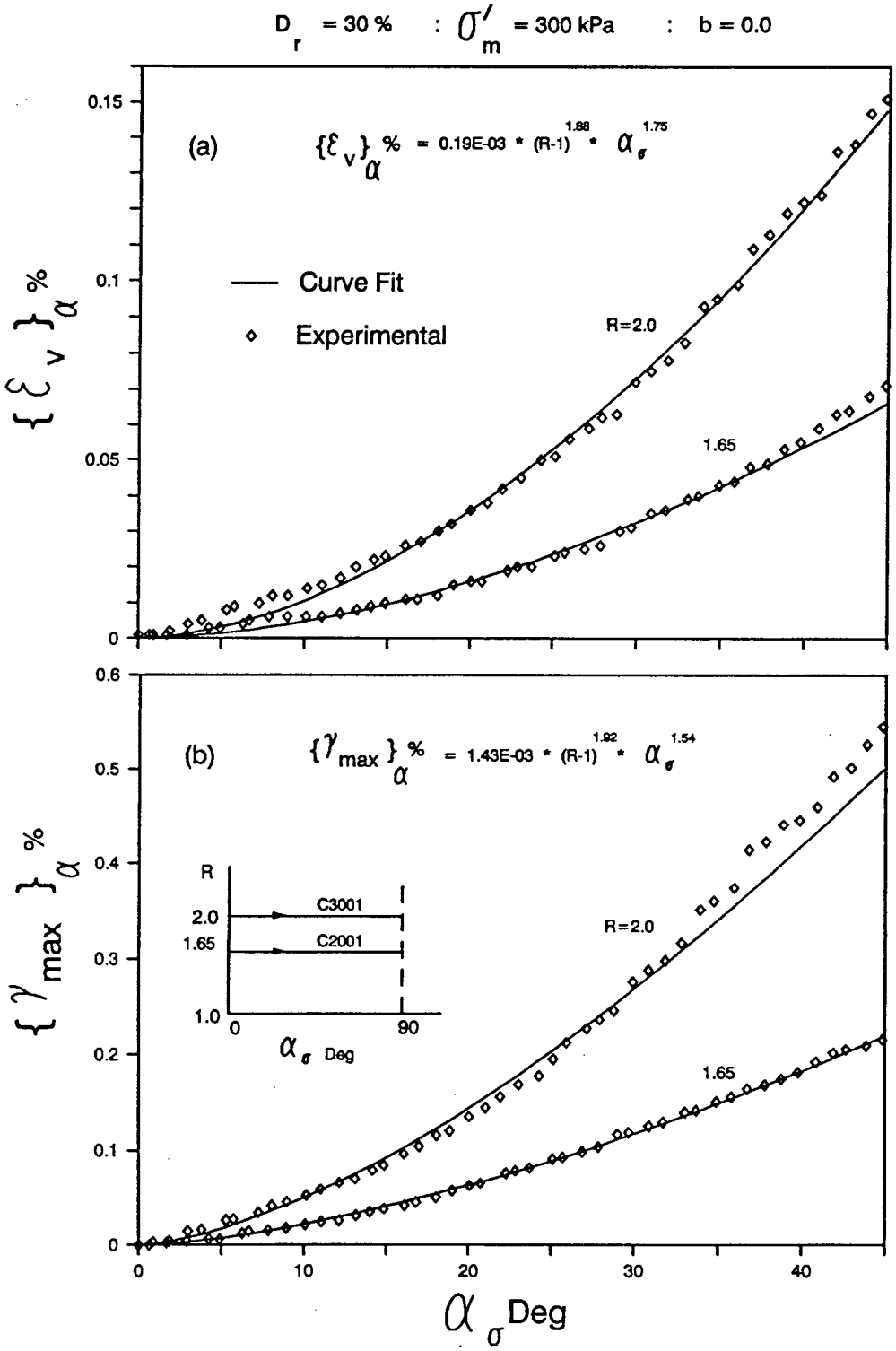

Figure C.4: Deformations under α paths with R = constant - Test Series C

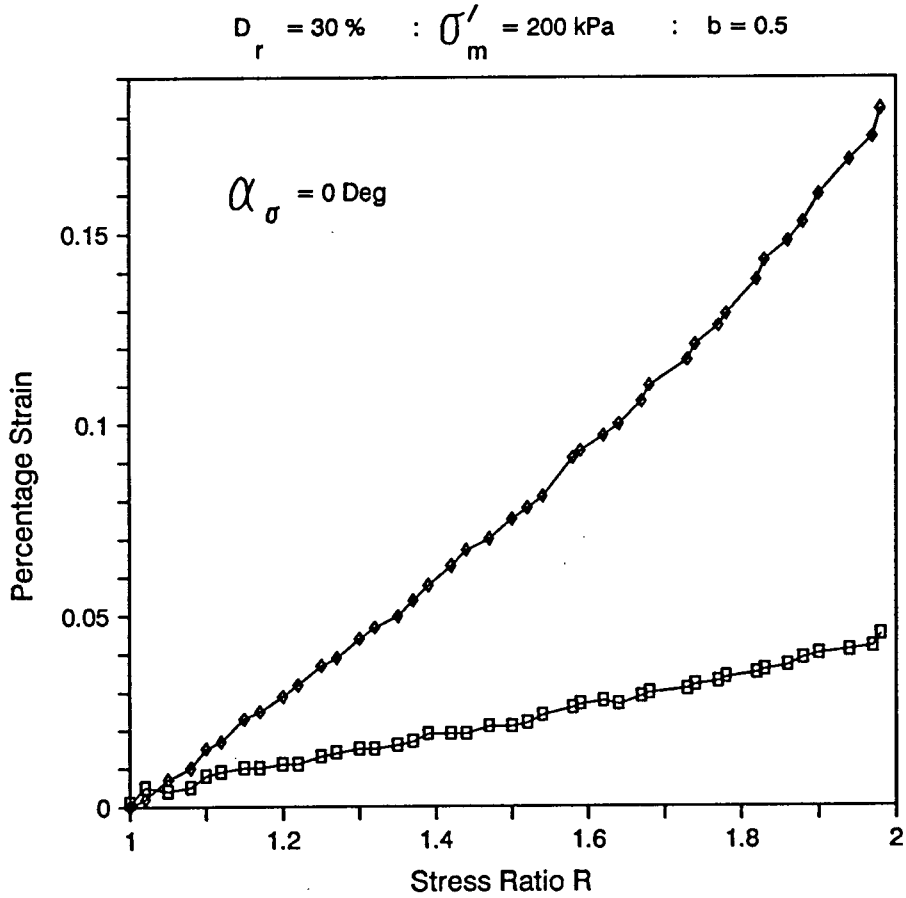

Figure C.5: Deformations under shear loading with $\alpha_\sigma = 0°$ - Test Series M

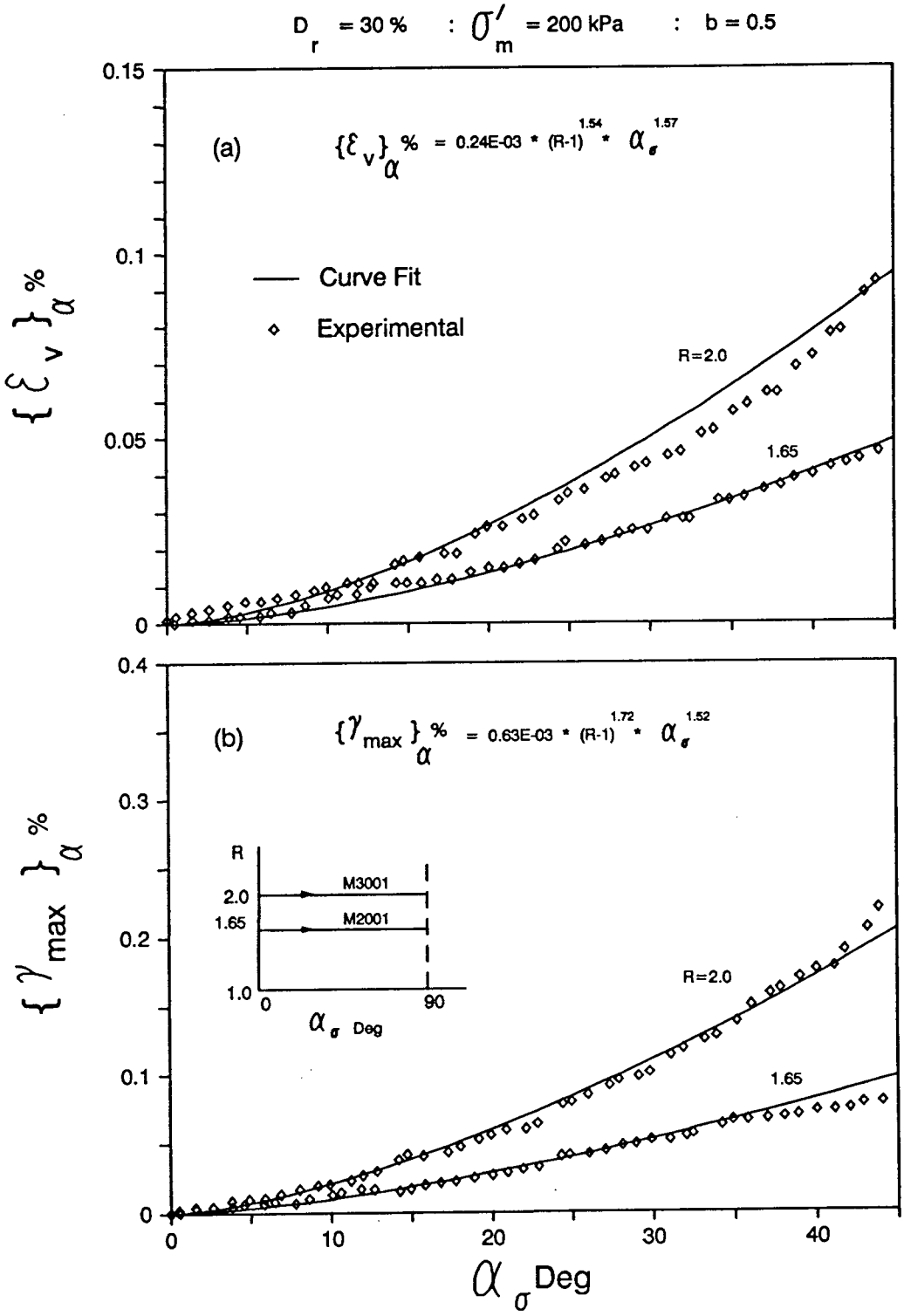

Figure C.6: Deformations under α paths with R = constant - Test Series M

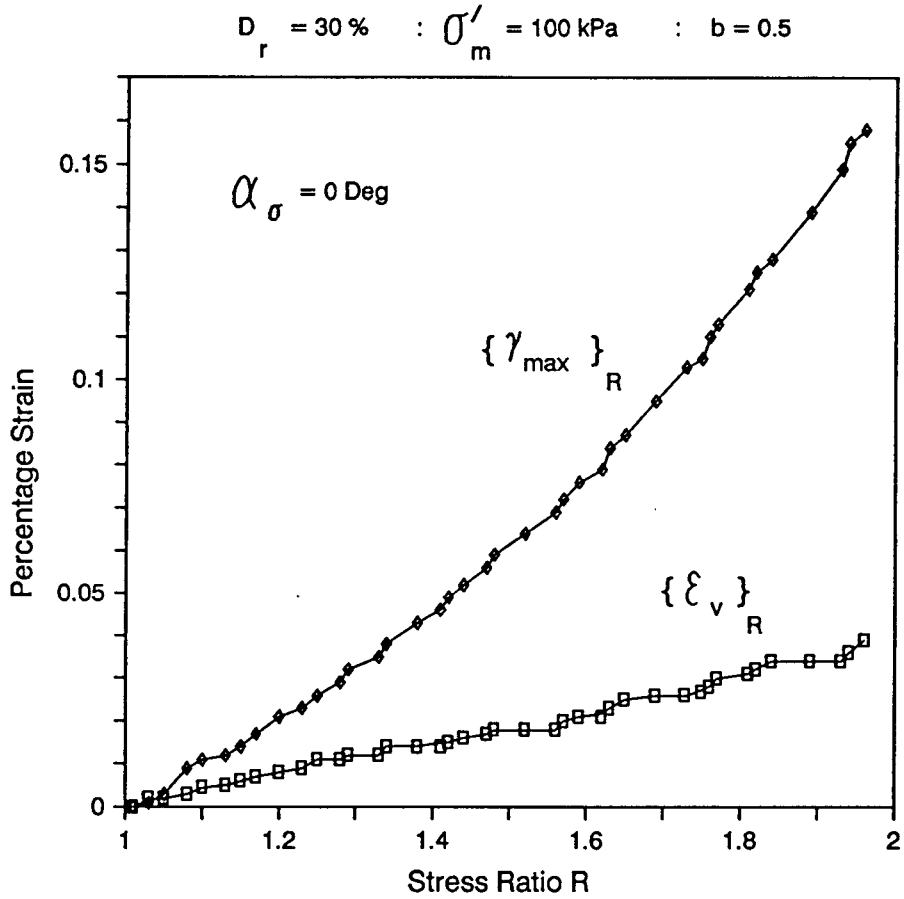

Figure C.7: Deformations under shear loading with $\alpha_\sigma = 0°$ - Test Series K

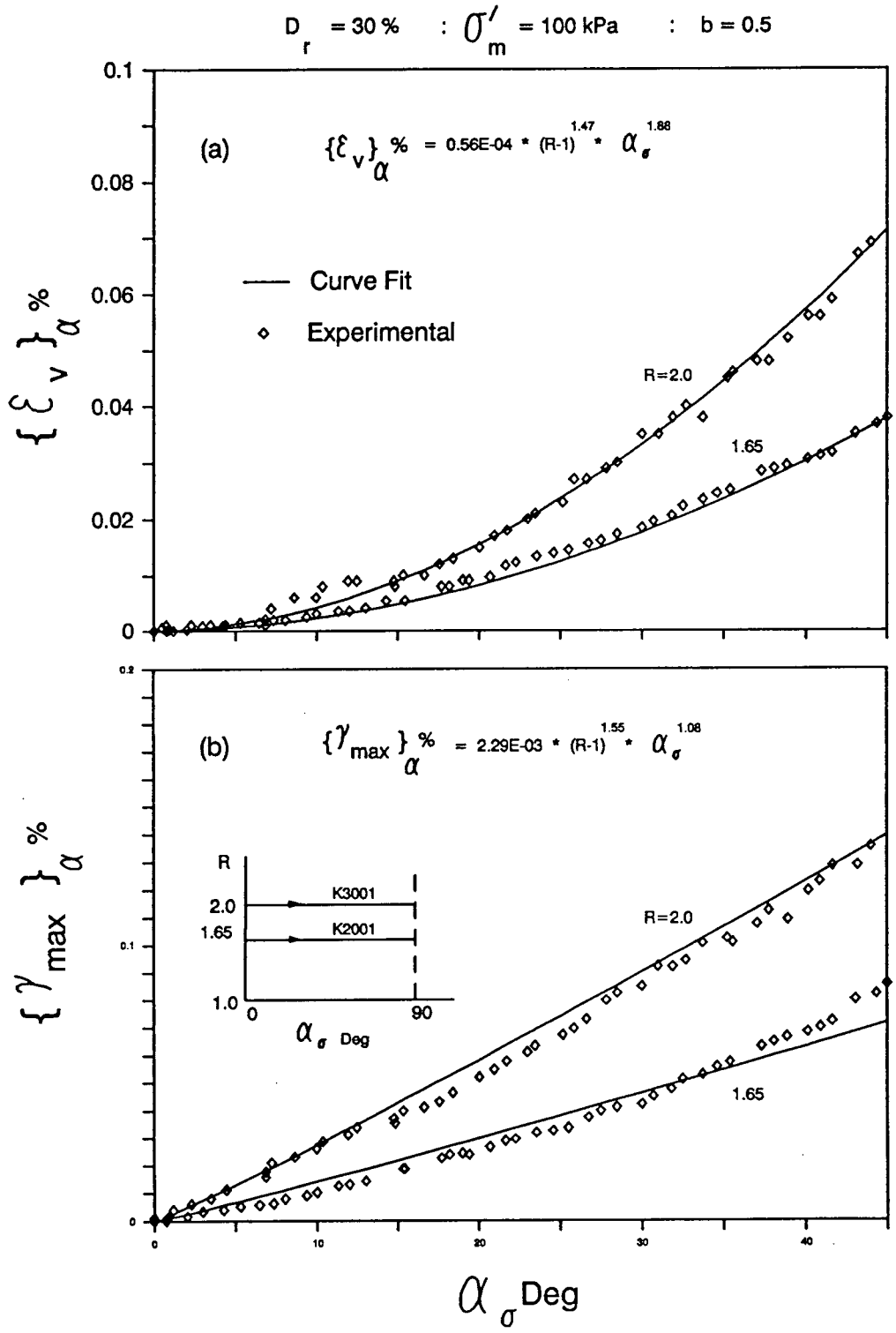

Figure C.8: Deformations under α paths with R = constant - Test Series K

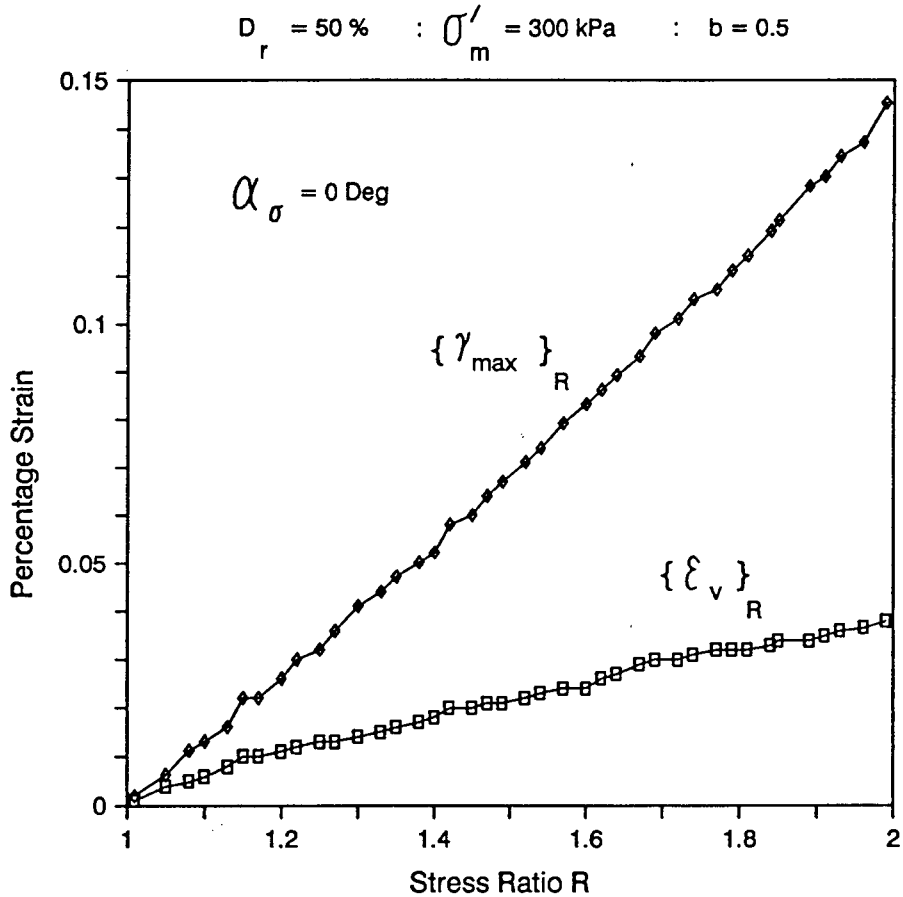

Figure C.9: Deformations under shear loading with $\alpha_\sigma = 0°$ - Test Series I

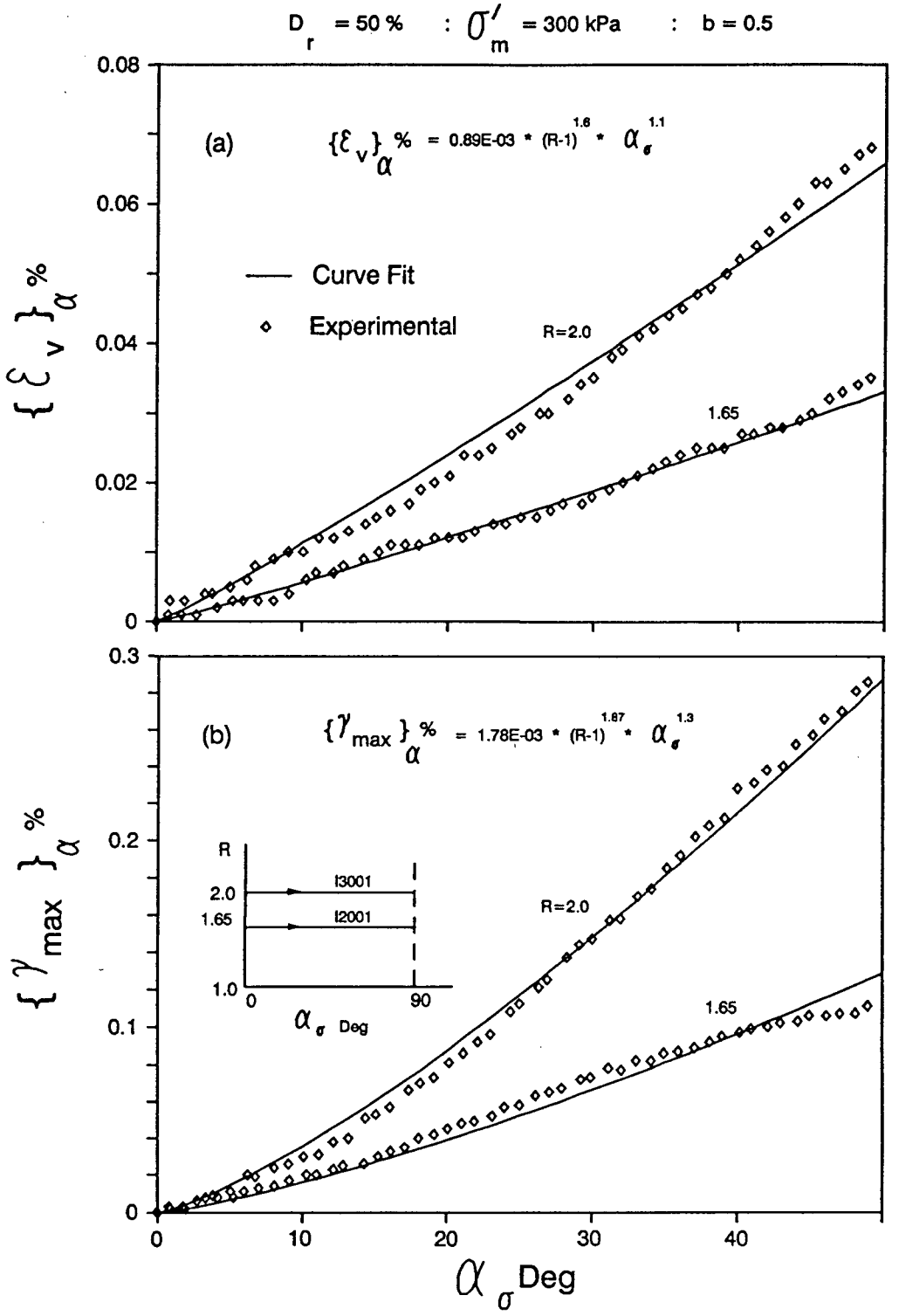

Figure C.10: Deformations under α paths with R = constant - Test Series I

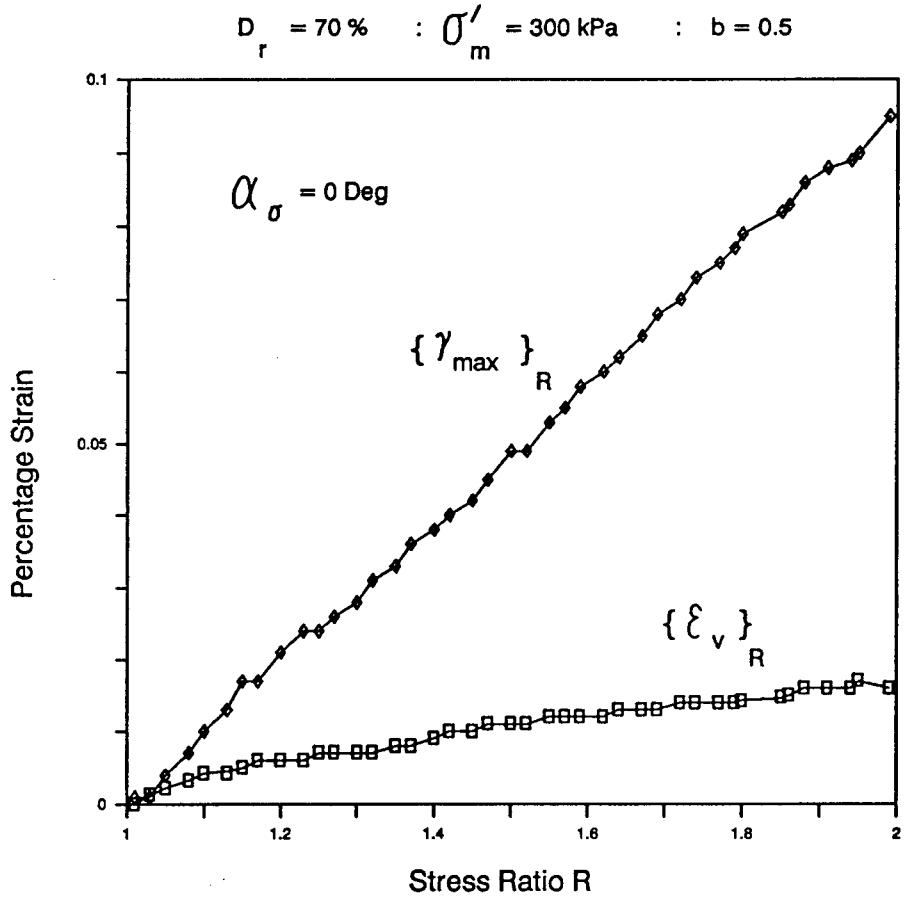

Figure C.11: Deformations under shear loading with $\alpha_\sigma = 0°$ - Test Series O

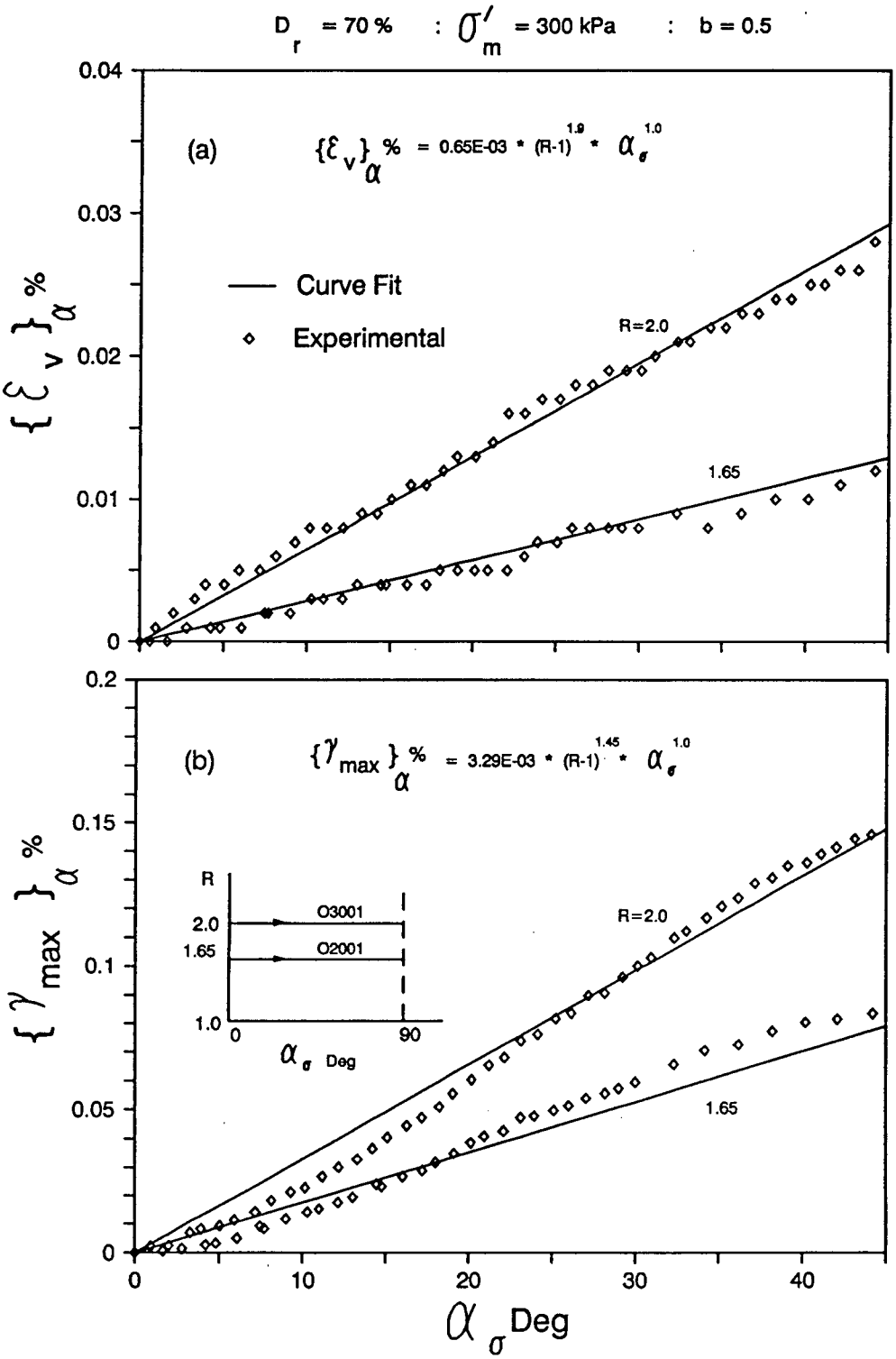

Figure C.12: Deformations under α paths with R = constant - Test Series O